SRI International

Final Report • July 1993

NOVEL NONLINEAR LASER DIAGNOSTIC TECHNIQUES

Gregory W. Faris
Jay B. Jeffries
David L. Huestis
Molecular Physics Laboratory

Prepared for:

Air Force Office of Scientific Research
110 Duncan Avenue, Suite B115
Bolling Air Force Base, DC 20332-0001

Attn: Dr. Julian M. Tishkoff

SRI Project 1187
Contract No. F49620-90-C-0044
MP 93-137

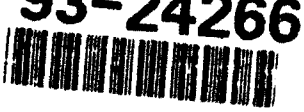

333 Ravenswood Avenue • Menlo Park, CA 94025-3493 • (415) 326-6200 • FAX (415) 326-5512 • Telex 334 486

Final Report• July 1993

NOVEL NONLINEAR LASER DIAGNOSTIC TECHNIQUES

Gregory W. Faris
Jay B. Jeffries
David L. Huestis
Molecular Physics Laboratory

Prepared for:

Air Force Office of Scientific Research
110 Duncan Avenue, Suite B115
Bolling Air Force Base, DC 20332-0001

Attn: Dr. Julian M. Tishkoff

SRI Project 1187
Contract No. F49620-90-C-0044
MP 93-137

Approved:

Donald J. Eckstrom, Laboratory Director
Molecular Physics Laboratory

David M. Golden
Vice President
Physical Sciences Division

SRI International 333 Ravenswood Avenue • Menlo Park, CA 94025-3493 • (415) 326-6200 • FAX (415) 326-5512 • Telex. 334486

REPORT DOCUMENTATION PAGE

Form Approved OMB No. 0704-0188

1. AGENCY USE ONLY *(Leave blank)*	2. REPORT DATE	3. REPORT TYPE AND DATES COVERED
	July 1993	Final 6-1-90 to 7-31-93

4. TITLE AND SUBTITLE
Novel Nonlinear Laser Diagnostic Techniques

5. FUNDING NUMBERS
PE-61102F
PR-2308
SA-B5
C-F49620-90-C-0044

6. AUTHOR(S)
Gregory W. Faris, Jay B. Jeffries, and David L. Huestis

7. PERFORMING ORGANIZATION NAME(S) AND ADDRESS(ES)
SRI International
333 Ravenswood Avenue
Menlo Park, CA 94025

8. PERFORMING ORGANIZATION REPORT NUMBER
MP 93-137

9. SPONSORING/MONITORING AGENCY NAME(S) AND ADDRESS(ES)
AFOSR/NA
110 Duncan Avenue Suite B115
Bolling AFB, DC 20332-0001

10. SPONSORING/MONITORING AGENCY REPORT NUMBER

11. SUPPLEMENTARY NOTES

12a. DISTRIBUTION/AVAILABILITY STATEMENT
Approved for public release; distribution is unlimited

12b. DISTRIBUTION CODE

13. ABSTRACT *(Maximum 200 words)*

Research on novel laser-based diagnostic techniques in two areas is described: (1) extension of laser-based diagnostics to shorter wavelengths for two-photon detection of atomic ions and other detection techniques requiring high powers in the vuv and (2) investigation of quantitative concentration, temperature, and velocity measurements using two-photon-excited amplified spontaneous emission (ASE) of atomic oxygen and hydrogen. For the first task, a broadly tunable high power vuv source based on two-photon-resonant difference frequency mixing in hydrogen and krypton gas was developed. Up to 65 mJ at 133 nm was generated and wavelengths as short as 122 nm were produced. This radiation was applied to multiphoton spectroscopy at vuv wavelengths below 150 nm, including two-photon-excited fluorescence in neon at 133 nm. Research on Task 2 included demonstration measurements of the bandwidth of ASE signals from both oxygen and hydrogen atoms in low-pressure flames. A model of the ASE signal shows gas temperature determination from ASE bandwidth measurements is possible. Gain on a cw diode probe laser from two-photon-excited oxygen atoms has been demonstrated in low-pressure flames; from such direct gain measurements, quantitative atom concentration measurements are feasible.

14. SUBJECT TERMS
Laser-based diagnostics, multiphoton excitation, atomic ions, vuv generation, four-wave mixing, amplified spontaneous emission, velocity measurement, temperature measurement, concentration measurement

15. NUMBER OF PAGES
161

16. PRICE CODE

17. SECURITY CLASSIFICATION OF REPORT	18. SECURITY CLASSIFICATION OF THIS PAGE	19. SECURITY CLASSIFICATION OF ABSTRACT	20. LIMITATION OF ABSTRACT
Unclassified	Unclassified	Unclassified	Unlimited

CONTENTS

F. COMPARING LASER-INDUCED FLUORESCENCE MEASUREMENTS AND COMPUTER MODELS OF LOW-PRESSURE FLAME CHEMISTRY

G. AMPLIFIED SPONTANEOUS EMISSION MEASUREMENTS OF ATOMIC OXYGEN

ILLUSTRATIONS

RESEARCH ACCOMPLISHMENTS

OBJECTIVES AND SUMMARY

The research for Task 1 was centered on extending laser-based diagnostics to shorter wavelengths. The objectives of this task were to develop new vuv laser sources and techniques, with emphasis on widely tunable radiation with high powers, and to apply this vuv radiation to diagnostics of species not accessible with current visible and near ultraviolet laser sources.

Task 2 investigated the feasibility of laser-excited amplified spontaneous emission (ASE) measurements for gas species concentration, gas temperature, and velocity. Gain measurements on a probe laser from atoms excited via two-photon transitions demonstrated the feasibility of concentration measurements. Bandwidth determinations were used to probe the gas velocity and/or gas temperature in reacting flows. The goal of this work was to determine the feasibility of the ASE technique from demonstration measurements.

TASK 1: DEVELOPMENT AND APPLICATION OF NEW VUV LASER SOURCES AND TECHNIQUES

Advances in laser techniques and technology have been a strong driving force in the development of nonintrusive diagnostics techniques. The production and use of higher laser powers at shorter wavelengths have been particularly fruitful throughout the 1980s and have led to the now well-established techniques of planar laser-induced fluorescence (LIF), two-photon-excited fluorescence, and resonantly enhanced multiphoton ionization (REMPI). More recent advances in nonlinear crystals, such as β-BaB_2O_4 (BBO) and LiB_3O_5 (LBO), allow use of these techniques on species requiring shorter wavelengths.

Below 200 nm, the generation and application of laser radiation become more difficult, for two reasons: the lack of suitable nonlinear frequency-converting crystals and the increasing absorption of background gases in this region. However, a number of diagnostic problems can be solved only in the vuv. Detection of atomic ions is important for applications including plasma propulsion, the study of highly ionized flows, plasma lithography, and magnetically confined fusion. The very high photon energies for excitation of light atomic ions require that two-photon excitation using vuv radiation be used for detection of these species.

For light atoms and molecules, single-photon vuv excitation offers several advantages over two-photon excitation. Because high intensities are not required, photodissociation or other

perturbing processes can be avoided. Quantitative results are simpler to obtain because the process is linear and the transition strengths are often well known. The single-photon sensitivity is higher, and planar imaging may be possible. Through 1+1 multiphoton ionization (MPI) or single-photon ionization coupled with mass spectrometry, ultrasensitive measurements can be made, comparable to those achievable with a gas chromatograph-mass spectroscopy system, except with a much faster response time. Another potential application for vuv diagnostics is single-photon calibration of multiple-photon diagnostic techniques. VUV diagnostics will be useful for plasma diagnostics, the study of chemical dynamics and kinetics of processes important in combustion and fluid flow, the calibration of other diagnostic techniques, and the study of shock-heated flows.

A key part of this research is the production of high power vuv radiation suitable for diagnostics measurements. Because of the lack of suitable nonlinear crystals for vuv generation, frequency conversion must be performed in gases. Because gases are centrosymmetric, four-wave-mixing is the lowest order frequency conversion process that may be used. To obtain high powers, techniques using resonances are required, such as multi-order anti-Stokes Raman shifting and two-photon-resonant sum- and difference-frequency mixing.

Under a previous contract, Faris and coworkers investigated multi-order Raman shifting for the two-photon excitation of atomic and molecular fluorine.[1,2] Wavelengths as short as 132 nm and energies up to 1 mJ at 170 nm have been produced.[3,4] However, the Raman shifting has limitations for vuv generation, including low efficiency for shorter vuv wavelengths, large intensity fluctuations when shifting dye lasers, and limited tuning range when shifting excimer lasers. Raman shifting can be the most appropriate source for certain applications—for example, when the wavelengths required lie within the tuning range of one of the Raman orders for shifting the ArF laser. An example of such a fortuitous overlap is shown as the middle curve in Figure 1, which shows a two-photon spectrum of the $F^1\Pi_g$ (v'=3) state of molecular fluorine excited from the ground state by using the first Stokes radiation from Raman shifting an ArF laser in D_2. The upper curve shows the first Stokes energy and the lower curve is a two-photon calibration spectrum. The ArF laser is tunable through only 1 nm, yet a spectrum of the full band of this vibrational level is possible. This tuning of the ArF laser, although limited, is important for the four-wave-mixing process we currently use for vuv generation.

The two-photon-resonant difference and sum process is shown in Figure 2. Because of the two-photon resonance, this mixing process can provide efficiencies of about 10^{-4}, significantly better than frequency tripling. However, unlike frequency tripling, this process has the disadvantage that two lasers are required. For vuv generation, the difference frequency process is preferable because much of the vuv spectral region may be covered and negative dispersion of the medium is not required. The difference frequency process has been demonstrated using

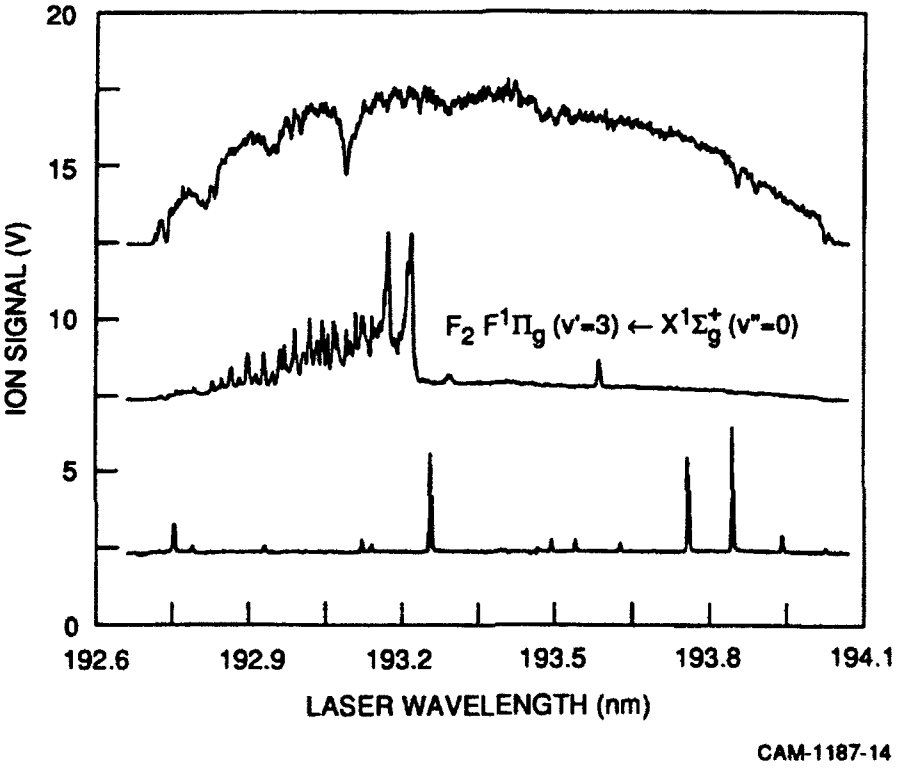

Figure 1. Two-photon spectrum of the $F^1\Pi_g(v'=3) \leftarrow X^1\Sigma_g^+(v'=0)$ transition of F_2.

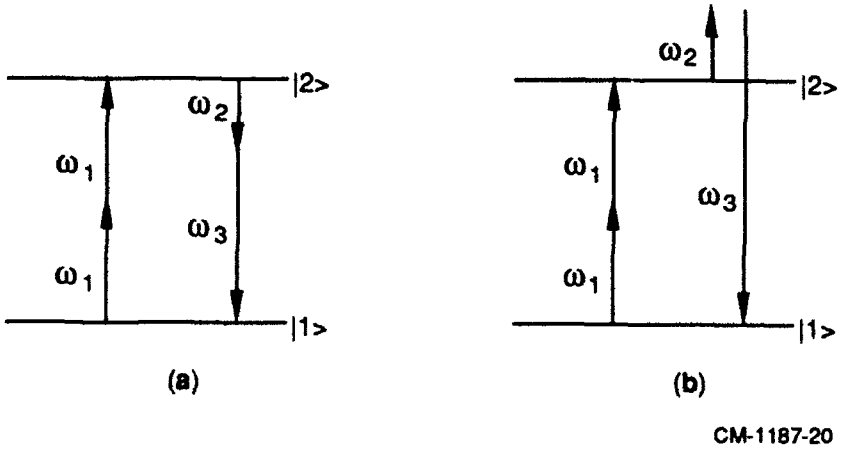

Figure 2. Two-photon resonant difference- (a) and sum- (b) frequency mixing.

krypton with frequency-doubled dye laser radiation as the two-photon pump laser. Because the vuv output power scales as the square of the two-photon pump laser intensity, and minimal tuning of the pump laser is required, a frequency-doubled dye laser may not be the best pump laser. By coincidence, there are two-photon resonances in krypton, H_2, and HD that are within the tuning range of the ArF laser. Because of the very high powers attainable with the ArF laser, this is an attractive pump laser for two-photon resonant difference frequency generation. Use of the $6p[3/2,2]\leftarrow 4p^6\ ^1S_0$ transition in krypton for vuv-xuv generation with an ArF laser was proposed in 1986 by Hilbig et al.[7] Two-photon-resonant sum-frequency mixing using the $E,F(v'=6)\ ^1\Sigma_g^+ \leftarrow X^1\Sigma_g^+(v''=0)$ Q(1) transition of H_2 with an ArF laser has been demonstrated for xuv generation.[8]

Two-photon resonant difference-frequency generation of vuv using an ArF laser was not demonstrated until 1991, when it was reported by Faris and Dyer[3] and Strauss and Funk.[9] The advantages of this technique over mixing techniques using frequency-doubled dye lasers as the two-photon pump laser include the higher power available from the ArF excimer laser, the ability to tune to shorter wavelengths (tuning from 110 nm to 180 nm is possible), and the lower sensitivity to phase mismatch due to the shorter two-photon pump wavelength.

For our work on two-photon-resonant difference-frequency mixing, we take advantage of previous work on Raman shifting, for which we have performed a number of modifications to a Lambda Physik 150 dual discharge excimer laser to obtain better spatial mode quality.[4] We use the same laser for two-photon-resonant difference-frequency generation. The apparatus is shown in Figure 3. The ArF excimer laser is run as an oscillator-triple pass amplifier. A lens, a pinhole, and a curved mirror between the oscillator and amplifier are used to filter the beam spatially. The output, up to 100 mJ in a beam five times over the diffraction limit, is combined on a dichroic beamsplitter with the frequency-doubled output of a dye laser (Quanta-Ray PDL) pumped by a Nd:YAG laser (Quanta-Ray DCR II). The timing of the two laser pulses is synchronized to about 1 ns. The two beams are focused together with a 1-m fused silica lens into a gas cell. The beam path of the ArF laser is purged with argon to minimize the effects of oxygen Schumann Runge absorption. From the beam splitter on, the beam path is evacuated. Light passing through the gas cell is collimated with a MgF_2 lens and continues into a vacuum spectrometer or is dispersed with a MgF_2 Pellin Broca prism.

Our initial characterization of the two-photon resonant difference frequency generation process was made using the $6p[3/2,2]\leftarrow 4p^6\ ^1S_0$ transition in krypton.[3] VUV generation in H_2 by using the $E,F(v'=6)\ ^1\Sigma_g^+ \leftarrow X^1\Sigma_g^+\ (v'=0)$ Q(1) transition is hampered by amplified spontaneous emission (ASE) in the vuv on $B\rightarrow X$ transitions, as has been seen previously.[10] The emission we

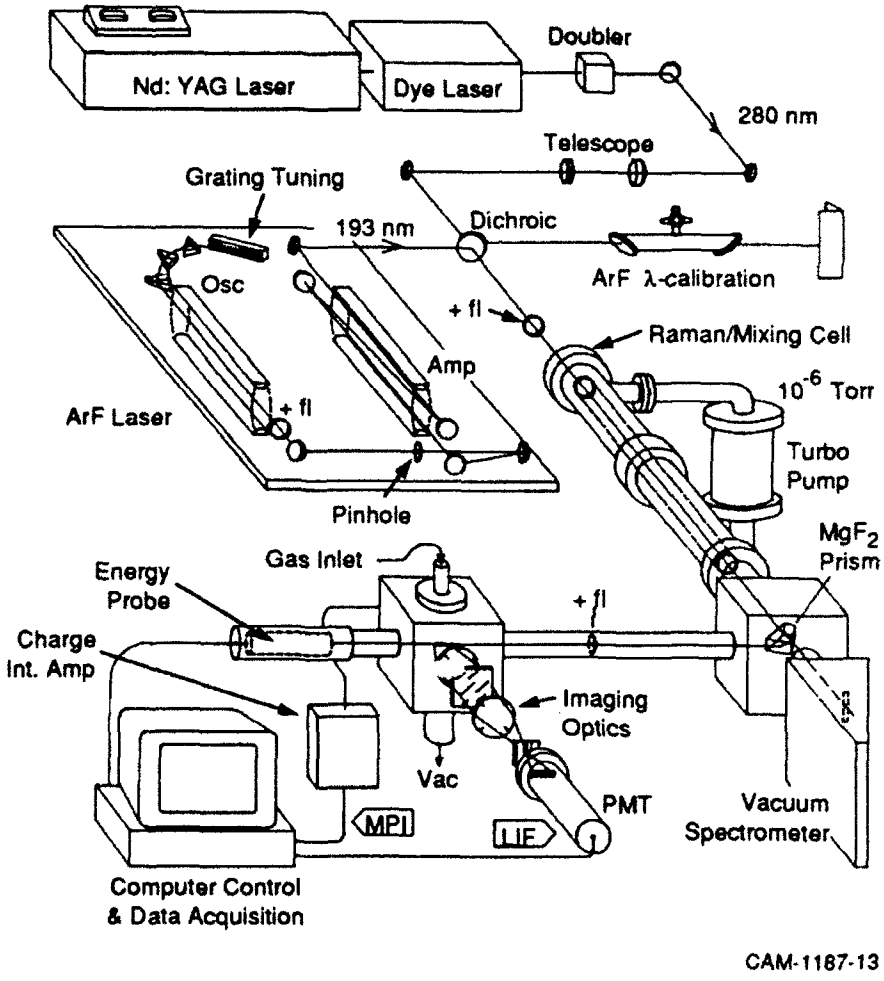

Figure 3. Experimental arrangement for two-photon resonant difference frequency generation.

have observed on these bands is shown in Figure 4. Similar ASE behavior is expected in HD, although this has not been investigated.

We have obtained up to 6 μJ at 147 nm by mixing in krypton. This power has been measured with a pyroelectric energy meter after separation of the other wavelengths with the Pellin Broca prism. The power generated in the gas cell is actually much higher (at least 50 μJ), but it is attenuated by absorption by the MgF_2 lens and prism.

The vuv generation in krypton is maximized when the ArF laser is exactly on resonance with the two-photon resonance, as is shown in Figure 5, where the vuv generated at 147 nm and the ionization signal for 2+1 REMPI in a separate krypton cell are shown as a function of detuning of the ArF laser. Examination of the dependence of the vuv intensity on the input laser powers indicates saturation for both lasers. The dependence on the frequency-doubled dye laser power is shown in Figure 6. The power increases proportionally to the first power of the laser power as expected up to about 1 mJ, where saturation begins to occur. The power dependence for the ArF laser, shown in Figure 7, is not fully understood. The power increases as a power of 1.4 over nearly an order of magnitude in laser power before further saturation. The expected power dependence is the square of the ArF laser power, so some saturation is occurring even at low powers. Noninteger laser power dependence has been seen in multiphoton spectroscopy when strong saturation makes the change in laser focal volume the dominant factor that affects the ion signal size, leading to a 3/2 power dependence.[11] Similar effects may be occurring for this vuv generation, although phase matching considerations are probably more important than volume considerations in determining power dependence.

The effects of phase matching are made very clear in the pressure dependence of the vuv power, shown in Figure 8. At low pressures, the vuv power increases as the square of the pressure, as is expected. However, at higher pressures, the power drops off because of the increased importance of phase matching at larger densities. The maximum conversion occurs at a density of about 60 Torr.

The saturation of both input lasers and the loss in conversion efficiency indicate that the vuv generation process is significantly less efficient than is ideally possible. These inefficiencies are ultimately related to phase matching. With better phase matching, we can take better advantage of the quadratic increase in efficiency at higher pressures, and looser focusing can be used, which will reduce the saturation effects that decrease the efficiency. One possible phase matching approach is noncollinear phase matching.[12] However, because of the large phase mismatch for mixing in the vuv, the crossing angles are large, leading to poor beam overlap. Partial ionization of the gas leads to electrons making a negative contribution to the refractive index. The electron

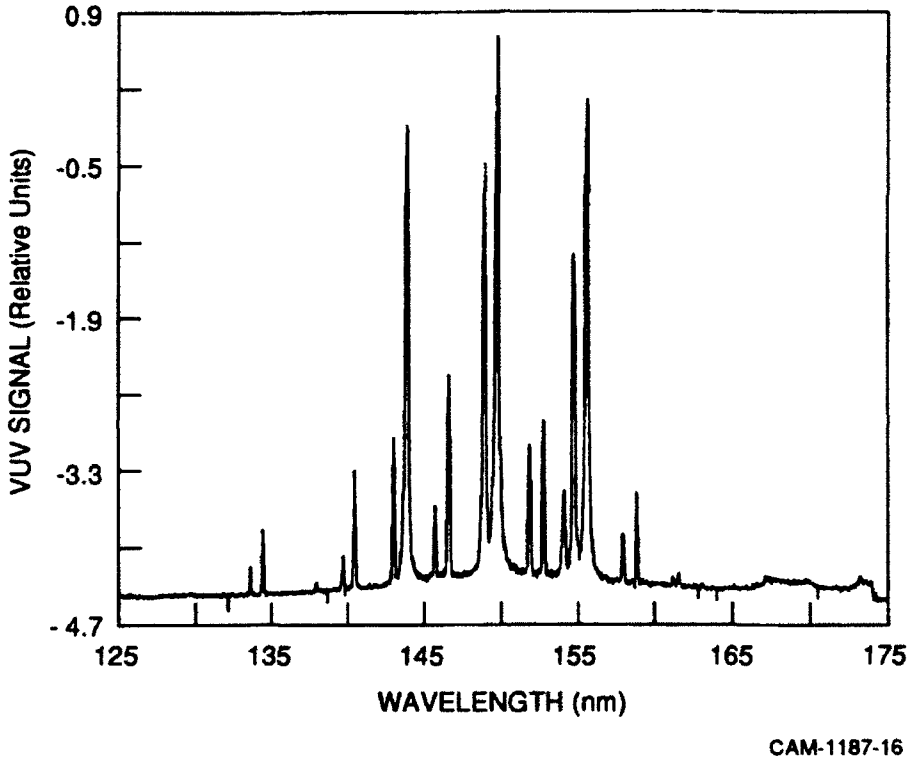

Figure 4. Vacuum ultraviolet amplified spontaneous emission generated on pumping $E,F^1\Sigma_g^+$ (v'=0) ← $X^1\Sigma_g^+$ (v"=0) Q(1) transition in H_2.

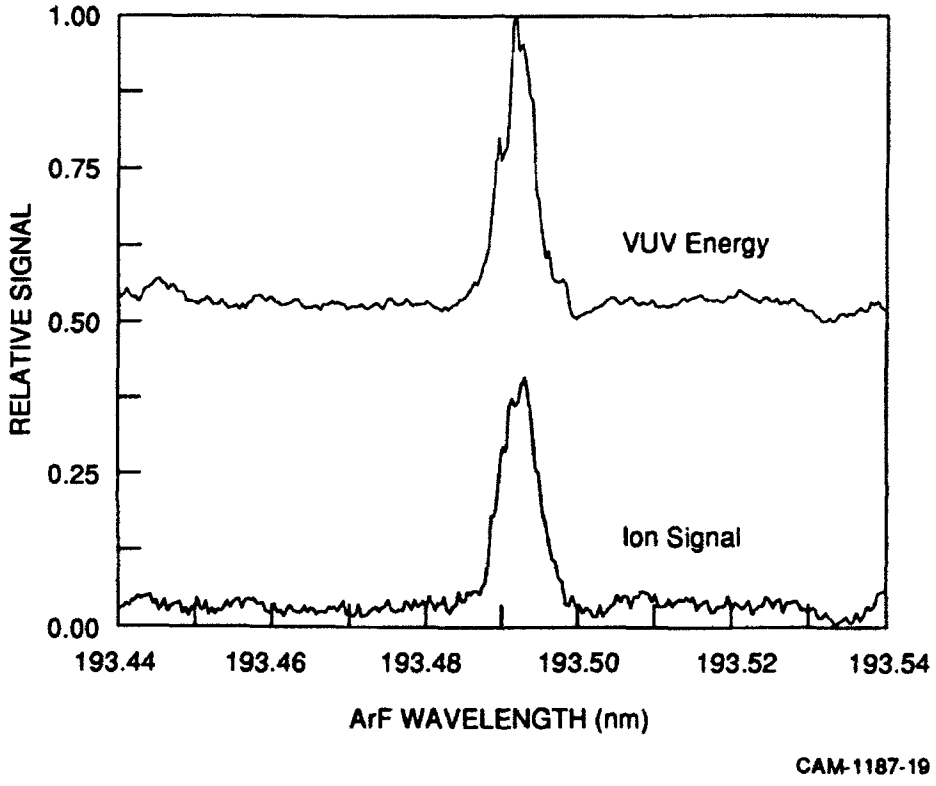

Figure 5. Vacuum ultraviolet energy and 2+1 REMPI in krypton as a function of ArF laser detuning.

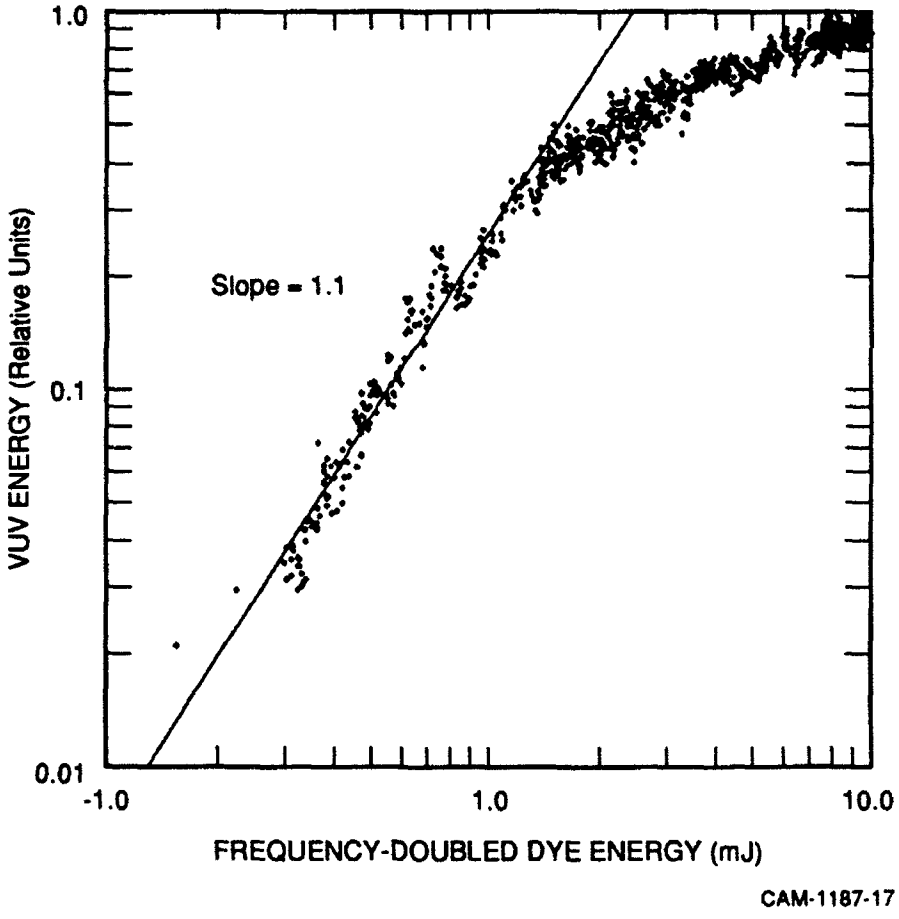

Figure 6. Dependence of vacuum ultraviolet radiation on frequency-doubled dye laser energy.

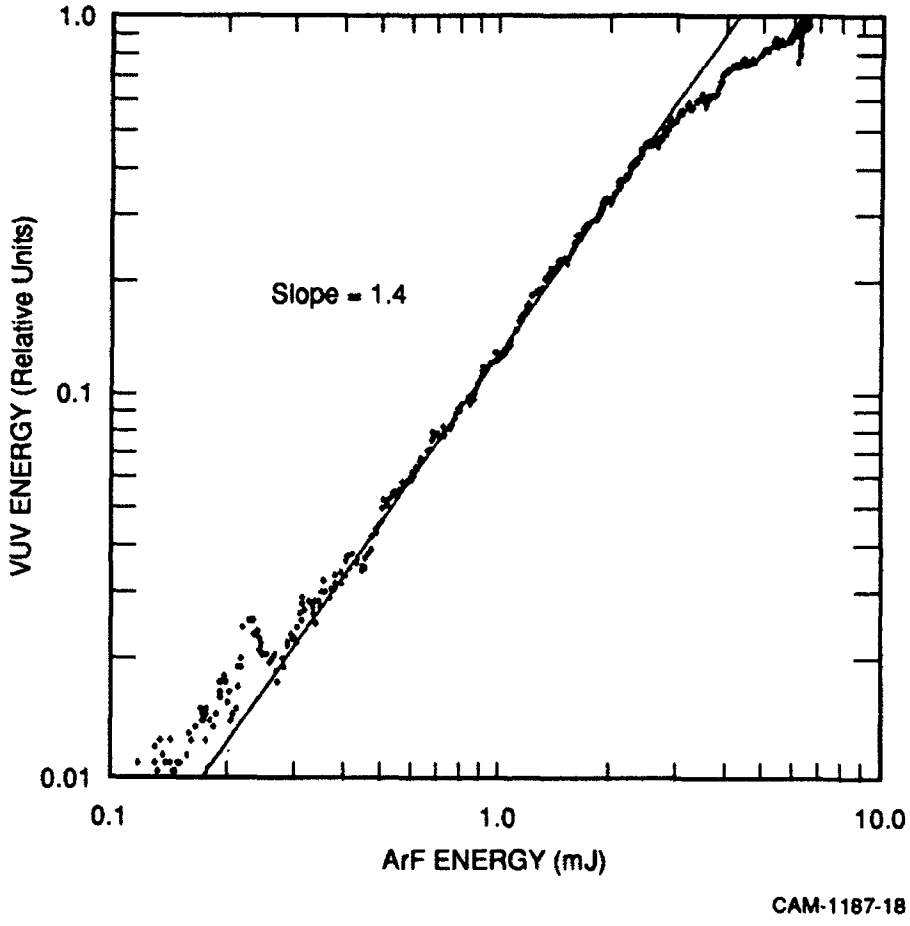

Figure 7. Dependence of vacuum ultraviolet radiation on ArF laser energy.

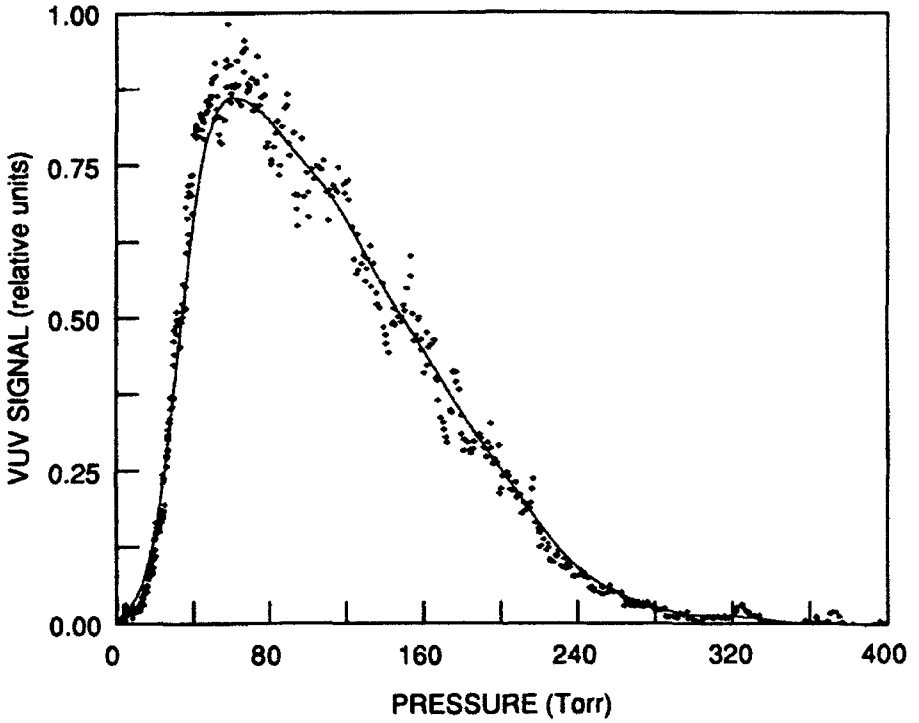

Figure 8. Dependence of vacuum ultraviolet radiation on krypton pressure.

contribution to the index of refraction becomes more positive at shorter wavelengths, though, and a negatively dispersive correction is required for phase matching. In the region near optical resonances in the vuv, certain gases exhibit negative dispersion, so a mixture of gases can provide phase matching.[13] This procedure may make higher powers possible in limited regions of the vuv.

When producing shorter wavelengths, ASE becomes less of a problem for mixing in H_2. This radiation is strongest between about 140 and 160 nm. Mixing in krypton at shorter wavelengths leads to lower efficiencies than at longer wavelengths. This is illustrated in Figure 9, which shows the pressure dependence for production of 133-nm radiation in krypton. The peak energy is only 2 μJ, significantly less than that obtained near 147 nm in krypton (6 μJ). We have performed mixing in H_2 to produce 133 nm and found that the ASE is weak enough in this region to allow use of the mixing process. Figure 10 shows pressure dependencies of the ASE at 145 nm and mixing to produce 134 nm. By operating at a lower pressure of H_2, we can further reduce the ASE. We have obtained up to 20 μJ at 134 nm by mixing in H_2. This energy is adequate for nonlinear optical diagnostic techniques such as two-photon-excited fluorescence.

We applied the vuv radiation to two experiments to examine feasibility of multiphoton techniques at short vuv wavelengths. By performing multiphoton excitation on noble gases, we can examine basic questions concerning sensitivity and technological complications without the additional experimental difficulty of the production of atomic ions. We have investigated two systems: 1+1 REMPI of atomic xenon, and two-photon excited fluorescence of atomic neon.

We used two photons at 147 nm to perform 1+1 REMPI through the $5p^5 6s[3/2,1]$ state of xenon, as shown in Figure 11. The 147-nm radiation was produced through mixing in krypton. Because vuv radiation can readily ionize many molecular species, background ion signals are a major consideration for vuv REMPI. With energies of only 3μJ, we have obtained signal-to-noise ratios of >50 for the ion signal, a good indication that this approach can give useful signals. A 1+1 REMPI spectrum and an absorption spectrum for Xe are shown in Figure 12. The strong resonance absorption in xenon leads to a dip in the REMPI signal at line center. The power dependence of the ion signal from xenon is shown in Figure 13. From the figure, it is apparent that the signal follows the expected square dependence on the vuv power.

Because the signal relies on detection of ions, 1+1 REMPI is not very well suited to detection in plasmas. However, 1+1 REMPI might be performed in plasmas in conjunction with optogalvanic detection. In addition, 1+1 REMPI with vuv radiation is useful when high sensitivity measurements are required, such as for resonant ionization mass spectroscopy of trace species, when two-photon techniques lead to photodissociation or other production or destruction

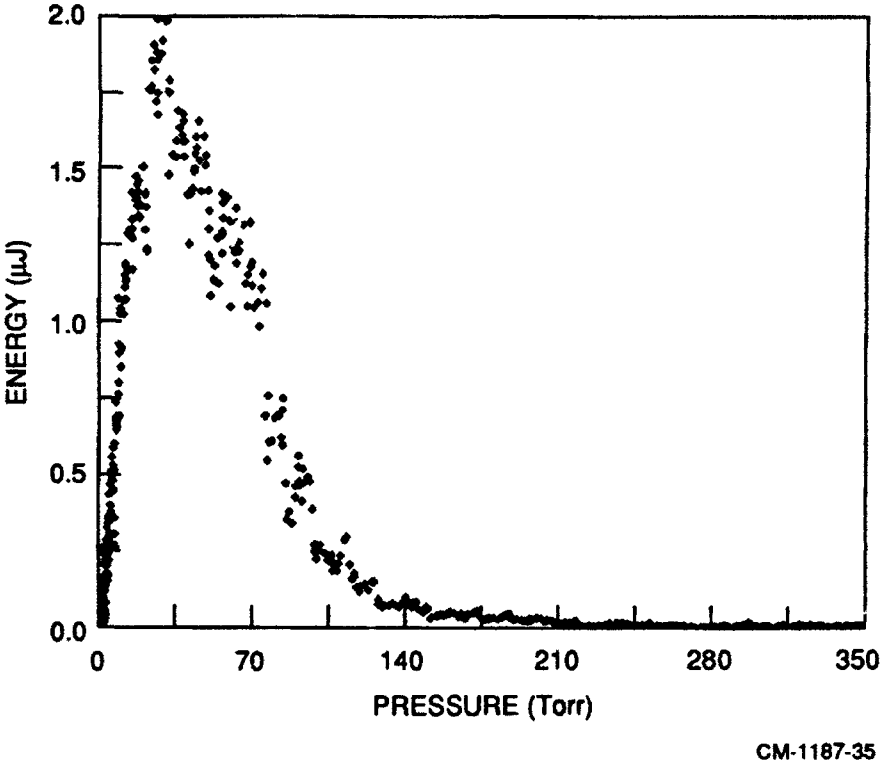

Figure 9. Pressure dependence of vacuum ultraviolet radiation at 133 nm for mixing in krypton.

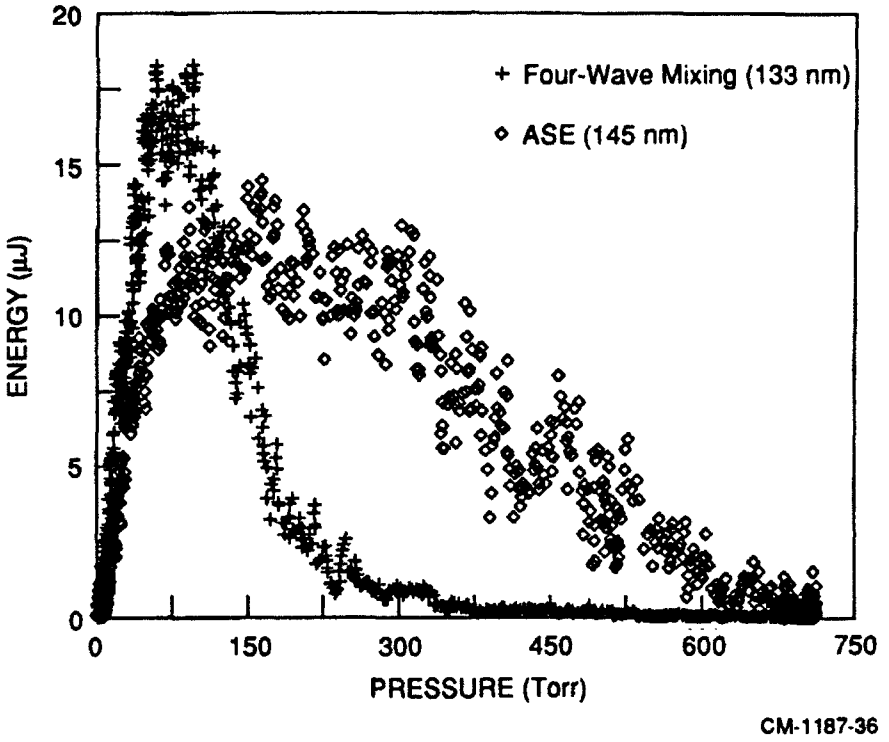

Figure 10. Pressure dependence of vacuum ultraviolet radiation for mixing and ASE in H_2.

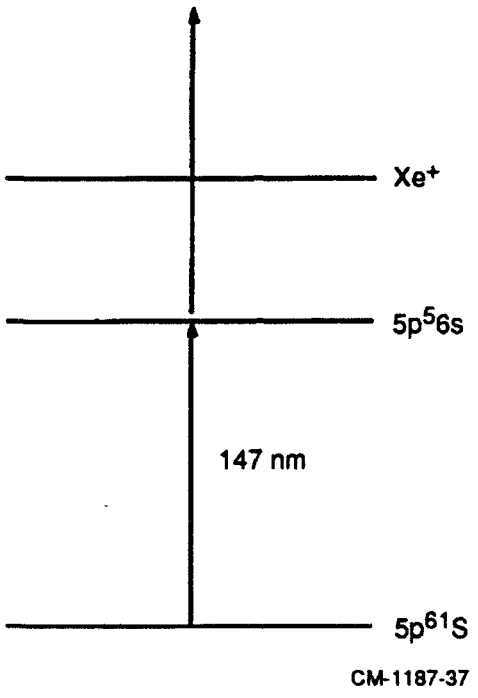

Figure 11. Energy level diagram for 1+1 REMPI in xenon at 147 nm.

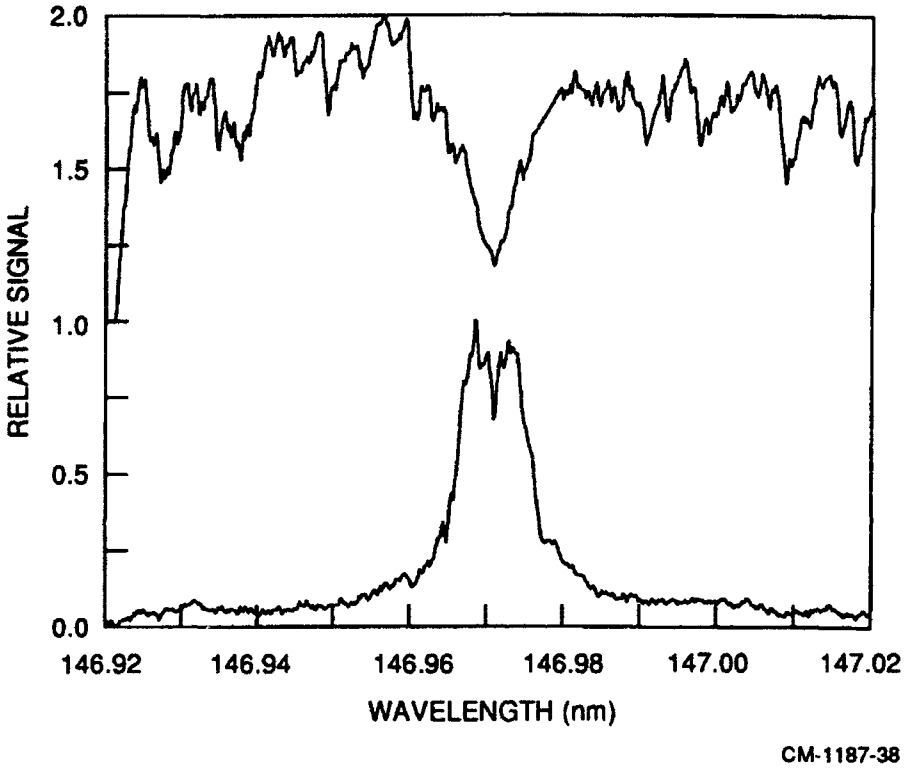

Figure 12. Absorption and 1+1 REMPI spectra for xenon with 147-nm radiation.

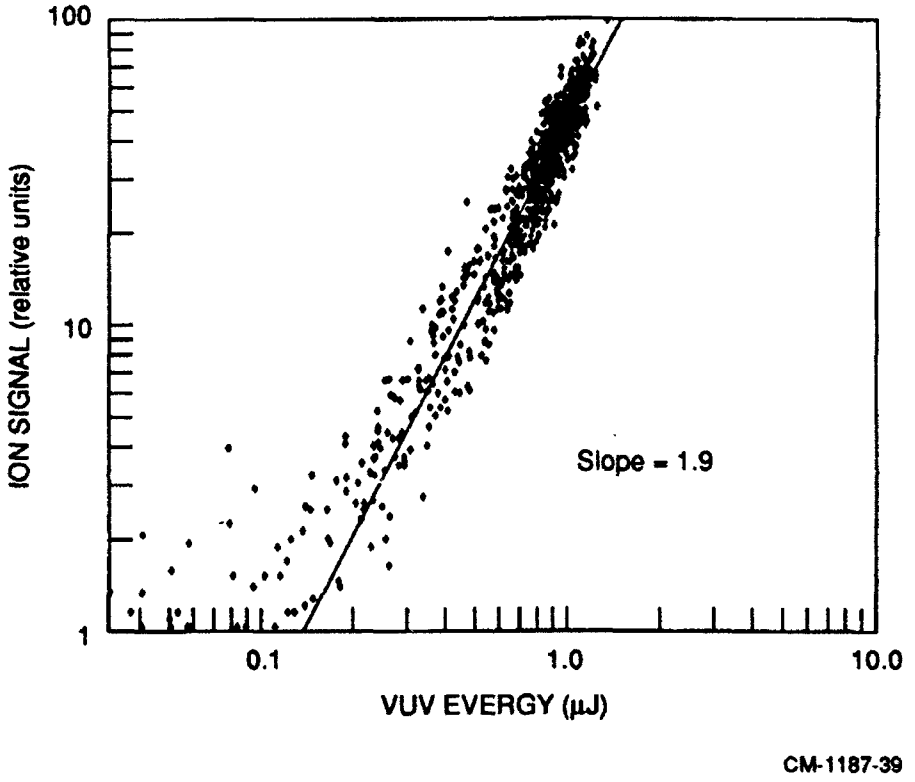

Figure 13. Power dependence of ion signal from 1+1 REMPI in xenon.

mechanisms that can cause detection errors, and as a calibration procedure for two-photon excitation.

For demonstration of two-photon excited fluorescence at shorter wavelengths in the vuv, we have chosen neon, which, with the first two-photon resonance corresponding to 133 nm, is the second most difficult neutral atom to excite (after helium). We have been able to observe fluorescence following two-photon resonant excitation of the $2p^5 3p[3/2,2]$ state of neon from the ground state using the excitation scheme shown in Figure 14.[14] Fluorescence is detected using a photomultiplier and a 700-nm short pass filter. Figure 15 shows an excitation spectrum for this transition for a pressure of 100 Torr of neon. Experimental improvements have allowed determination of the power dependence of the fluorescence signal (Figure 16), which confirmed that we were indeed performing a two-photon-resonant excitation. For these measurements, we had the luxury of being able to operate at fairly high atom densities (pressure = ~100 Torr). For detection of atomic ions, we must be able to detect significantly lower densities. To successfully perform such measurements will require significantly higher powers.

From measurements of the transmission of our optics in the vuv using a hydrogen arc light source and a vuv spectrometer, we found that much of the energy we generate is absorbed by the MgF_2 optics we use, apparently through color center formation.[14] To take better advantage of the energies that we produce, we changed our optical setup to greatly reduce the optical path through MgF_2 for the vuv. Instead of using a separate collimating lens and dispersing prism, amounting to perhaps 5 cm of optical path, we use a single lens placed off-axis to both focus the vuv and separate the vuv from the pump beams, resulting in an optical path of only a few millimeters. The apparatus for this arrangement is shown in Figure 17. With this arrangement, we have been able to increase our generated energies by over a factor of 3, from 20 μJ to over 65 μJ. These energies were measured directly using a pyroelectric energy meter in vacuum.

We are now pursuing generation of shorter wavelengths, in the region of 120 nm. There are a number of motivations for exploring this region. By using mixtures of krypton and hydrogen, we can use the negative dispersion of krypton to phase match the mixing process. Phase matching offers the potential for significantly increased vuv powers, which will be essential for the demonstration of the detection of atomic ions. In addition, a number of significant transitions occur in this region. Lyman alpha radiation at 121.6 nm is a very important wavelength for many reasons, including the potential for performing planar imaging of hydrogen atoms. Planar imaging of N atoms can be performed using 120 nm, and two-photon-excited fluorescence of N^+ can be performed using 117 nm. We have obtained vuv radiation at about 122 nm and are in the process of improving the system to allow production of calibrated energies. We should know soon the practicality of some of these diagnostic possibilities.

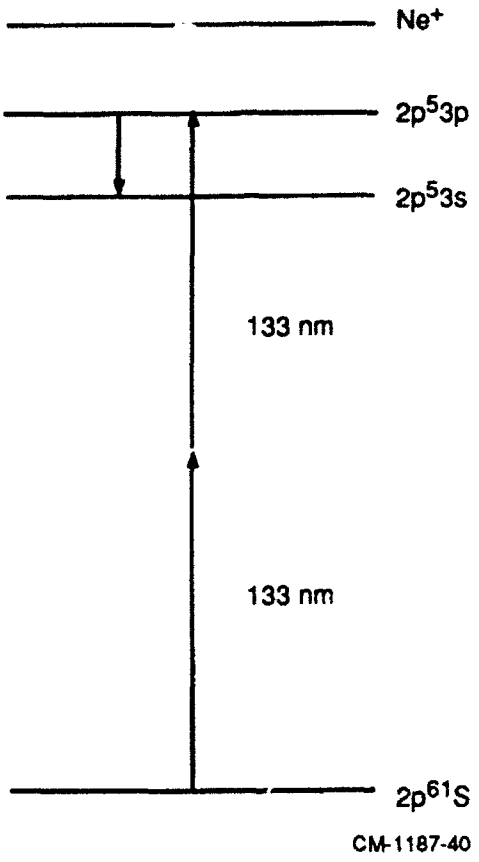

Figure 14. Energy level diagram for two-photon-excited fluorescence in neon at 133 nm.

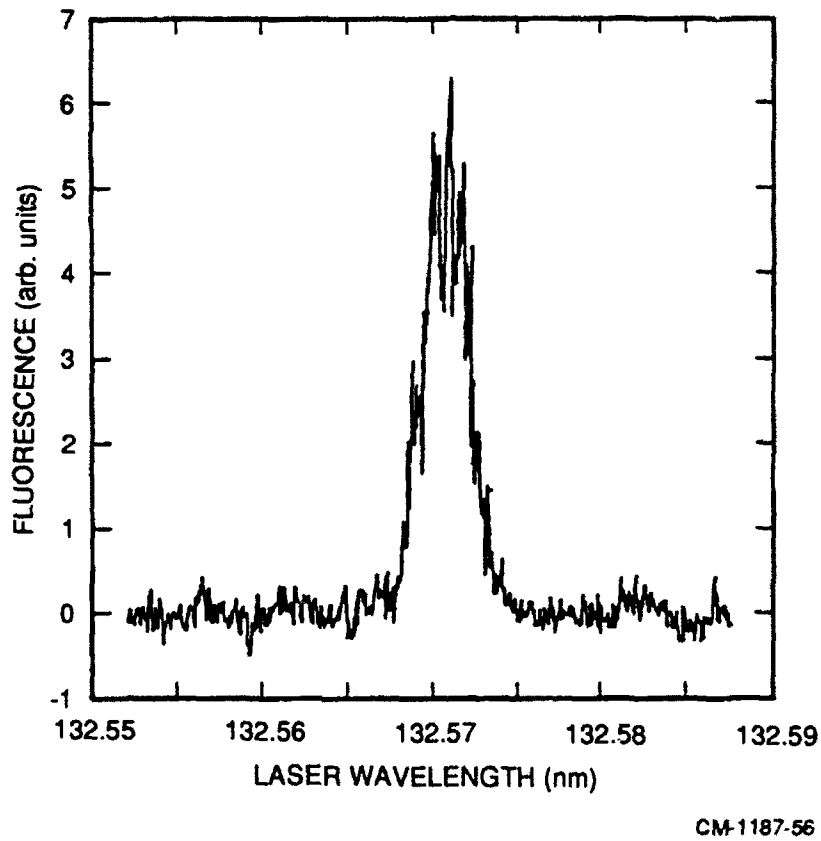

Figure 15. Two-photon-excited fluorescence signal in neon with 133-nm radiation.

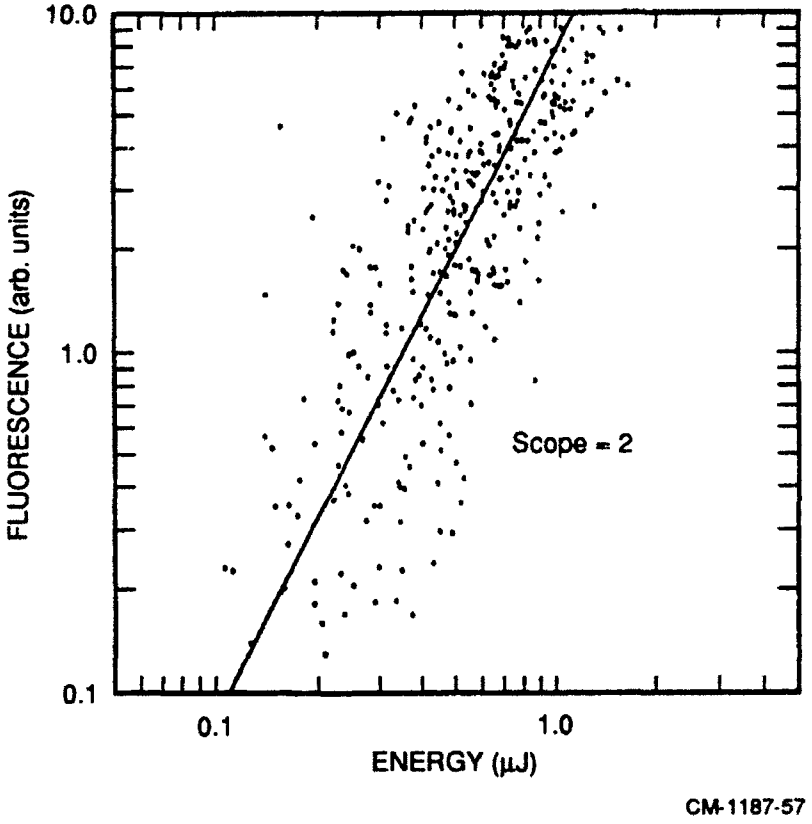

Figure 16. Power dependence for two-photon-excited fluorescence in neon.

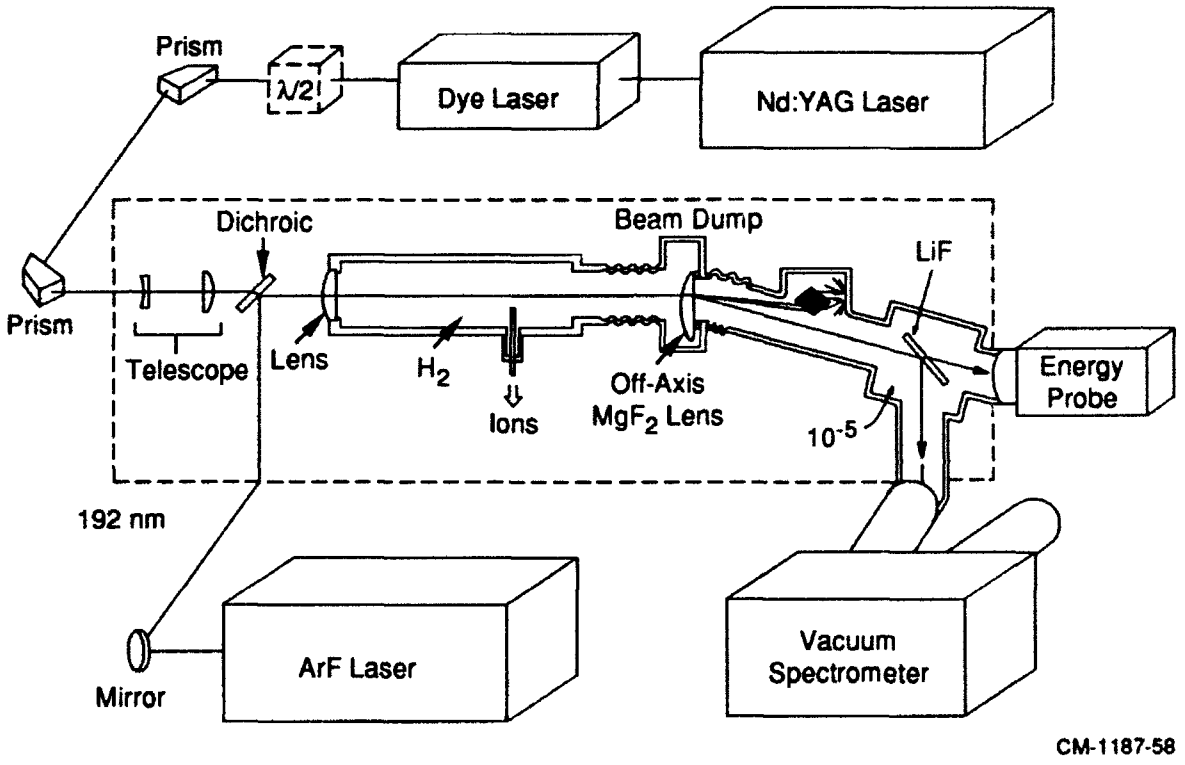

Figure 17. Off-axis lens apparatus for high power VUV generation.

Task 2: LASER-EXCITED ASE MEASUREMENTS

Two photon laser-induced fluorescence (LIF) is often used as a means of detecting light atoms in combustion environments.[15] This technique involves exciting some of the ground state population into an excited state of the same overall parity as the ground state through two-photon absorption. Some of this excited state population relaxes to intermediate states via one-photon fluorescence, which is the detected signal. It is possible that a second physical process, amplified spontaneous emission (ASE), can occur simultaneously, and ASE has been observed.[16] For light atoms, the intermediate states lie several electron volts of energy above the ground state and therefore have no appreciable thermal population even at the elevated temperatures found in combustion environments. If the excitation rate is sufficient to move a significant population via the two-photon laser excitation, this lack of a thermal population in the intermediate state produces a population inversion between the excited and intermediate states. Any spontaneous emission can then experience optical gain via stimulated emission. With enough gain, an ASE signal is generated; since excited atoms only are present along the path of the excitation laser, gain is present only along this path. The ASE signal propagates forward and backward along the pump laser beam.

The physical process of ASE is well known from studies of laser systems.[17] More recently, ASE has prompted interest as an optical diagnostic for combustion environments.[16] Atomic hydrogen,[18] oxygen,[19] carbon,[20] nitrogen,[21] and chlorine,[22] as well as carbon monoxide,[16] have all been detected by their ASE signals. The ASE signal is attractive as an optical diagnostic for several reasons: the spatial coherence of the ASE signal beam implies that a large signal to background contrast ratio is possible with only a single optical access port, and the nonlinear origin of the ASE signal makes a very large signal possible. To date, the ASE studies that have been conducted concentrated on obtaining a relative ASE signal as a function of pump laser energy and partial pressure of the test gas.

The goal of this project is to investigate the degree of quantitative information that can be obtained from ASE signals from atoms. In particular, we are studying the use of ASE as a thermometric probe of reactive flows. Since the two-photon pump laser couples a Doppler broadened ground state velocity distribution to the excited state, we anticipated that the bandwidth of the emitted ASE would include information about the temperature of the local environment. In an effort to test this idea, we made measurements and developed a model of the bandwidth of hydrogen and oxygen atoms in low-pressure flames as a function of temperature. In addition, we compared simultaneous ASE and LIF signals in a variety of flames probing both hydrogen and oxygen atoms. We found ASE signals can be large enough to deplete LIF signals, and that ASE

signals are influenced by gas collisions. With a continuous wave (cw) seed laser we directly observed gain from the two-photon excitation. Such direct gain measurements may provide a strategy for quantitative atom concentration measurements in reacting flows, and these results set an encouraging new direction for further work on two-photon-excited ASE from atoms.

Atomic hydrogen and atomic oxygen are both important reactive intermediates during hydrocarbon combustion. Both atoms may be excited by two-photon laser excitation; the selection rules allow excitation of states that do not have allowed single-photon transitions back to the ground state. We monitor atomic hydrogen by exciting of the 3S and 3D states from the 1S ground state by two photons near 205 nm and monitoring the fluorescence of Balmer α transitions to the 2P near 656 nm. Oxygen $3p^3P$ is excited from $2p^3P$ via two photons near 226 nm, and fluorescence near 845 nm is produced from the $3s^3S^o \leftarrow 3p^3P$ transition.

Low-pressure flames are supported on a 6-cm-diameter, water-cooled, McKenna burner in an evacuated housing. Computer controlled motion of the burner allows signals to be monitored as a function of height above the burner surface. For these premixed low-pressure flames, height above the burner surface relates directly to reaction time if the gas temperature is known. Using conditions identical to those in previous studies of H_2/O_2,[23] CH_4/O_2,[24-26] and CH_4/air.[27] stoichiometric flames, we obtained careful measurements of the gas temperature as a function of height above the burner and LIF measurements of radical concentrations as a function of height above the burner for a number of key radical intermediates. The majority of the data were collected from 7 Torr H_2/O_2 and CH_4/O_2 flames at a height of 4 cm above the burner. Under these conditions the local environment is known, and the temperature is 1200 K in the hydrogen flame and 1800 K in the methane flame. A detailed description of the burner, and the associated optics and data acquisition system can be found in References 23 through 27.

Figure 18 shows the experimental design for the oxygen atom experiment. The excitation pulse was produced by frequency doubling the output from a Nd:YAG pumped dye laser. Dielectric mirrors separated the 6-ns light pulse near 226 nm from the fundamental near 452 nm. Excitation light for hydrogen atoms was produced by first frequency doubling the output of the dye laser at 615 nm, then mixing the resulting doubled light near 307.5 nm with residual light from the fundamental pulse and separating the difference frequency pulse at 205 nm with dichroic mirrors. The excitation beam was focused into the burner chamber with either a 0.15-m or a 0.50-m focal length lens. The backward-moving (counterpropagating with respect to the pump pulse) ASE signal was detected using a filtered red-sensitive photomultiplier tube (PMT). The forward ASE pulse was filtered, expanded with a negative lens, and passed through an etalon. The etalon fringes were captured onto an intensified CCD camera array. Images of the etalon fringes were used to measure the bandwidth of the ASE with the excitation laser wavelength fixed at line center.

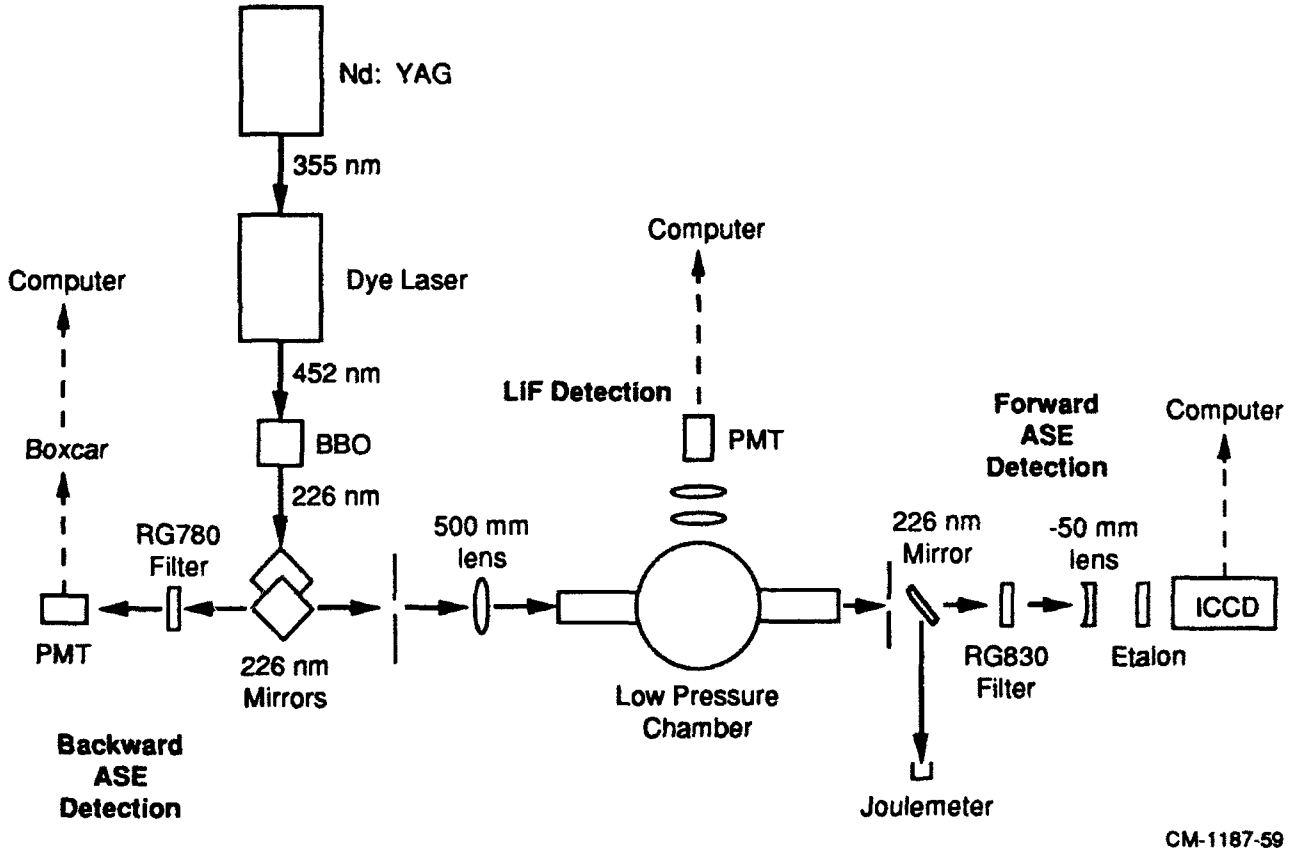

Figure 18. Schematic of the experimental arrangement for ASE excitation and detection of atomic oxygen in low pressure flames.

Excitation spectra were also collected by scanning the dye laser through the two-photon resonance and recording the ASE signal on the PMT.

Figure 19 shows the two-photon LIF signal from atomic hydrogen as a function of height above the burner for three different stoichiometric flames. The upper panel shows a 7.2 Torr H_2/O_2 flame identical to that used earlier for quantitative OH measurements.[23] The middle panel presents data for a 6 Torr CH_4/O_2 flame where OH, HCO (Reference 26), CH (Reference 24), and $^1CH_2$ (Reference 25) were previously measured. The bottom panel has data for a 30 Torr CH_4/air flame that previously was used to measure OH, CH, and NO profiles.[27] High intensity laser light at 205 nm can photodissociate vibrationally hot H_2O producing H atoms[28,29] and these product H atoms are subsequently observed by LIF in the same laser pulse.[29] To investigate possible photochemical interference in the profiles shown in Figure 19, we collected LIF profiles with different laser pulse energies. The data in Figure 19 were acquired with laser energy near 200 μJ/pulse, and the profiles are identical to those acquired with 50-90 μJ/pulse. This result indicates that with the laser pulse energy, beam divergence, and pulse length used, the three profiles for these low-pressure flames are free of significant photochemical interference.

The LIF signal presented in Figure 19 is uncorrected for collisional quenching. Quenching measurements have been reported for H atoms at room temperature[30] and for a few important colliders at temperatures between 300 and 700 K.[28] If these rate constants are applicable at flame temperatures, an H atom fluorescence lifetime near 3 ns is predicted for these flames, which is consistent with an observed lifetime that is too fast to be resolved by our 7-ns laser pulse and the photomultiplier/amplifier combination used. Goldsmith and coworkers[31] used picosecond laser pulses to obtain direct measurements of the fluorescence lifetime of the 3S and 3D hydrogen in low-pressure H_2/O_2 flames. They found the value of the fluorescence lifetime to be consistent with the quenching predicted by a model calculation of the species and the room temperature quenching rate constants from Stuttgart.[28, 30]

Using the method demonstrated by Meier et al.[28] and used by Goldsmith et al.,[32] we corrected the LIF signal by

$$[H] \alpha \frac{S\,(A + Q)}{A} = \frac{S}{A}\,(64.5\ \mu s^{-1} + \sum_i k_Q^i\, n_i)$$

where S is the signal, A the radiative decay rate, Q the first-order quenching rate, k_Q^i the quenching rate constant for the ith species, n_i the concentration of species i, and the summation over all the species in the flame. We used our chemical model of these premixed flames[27,33] to

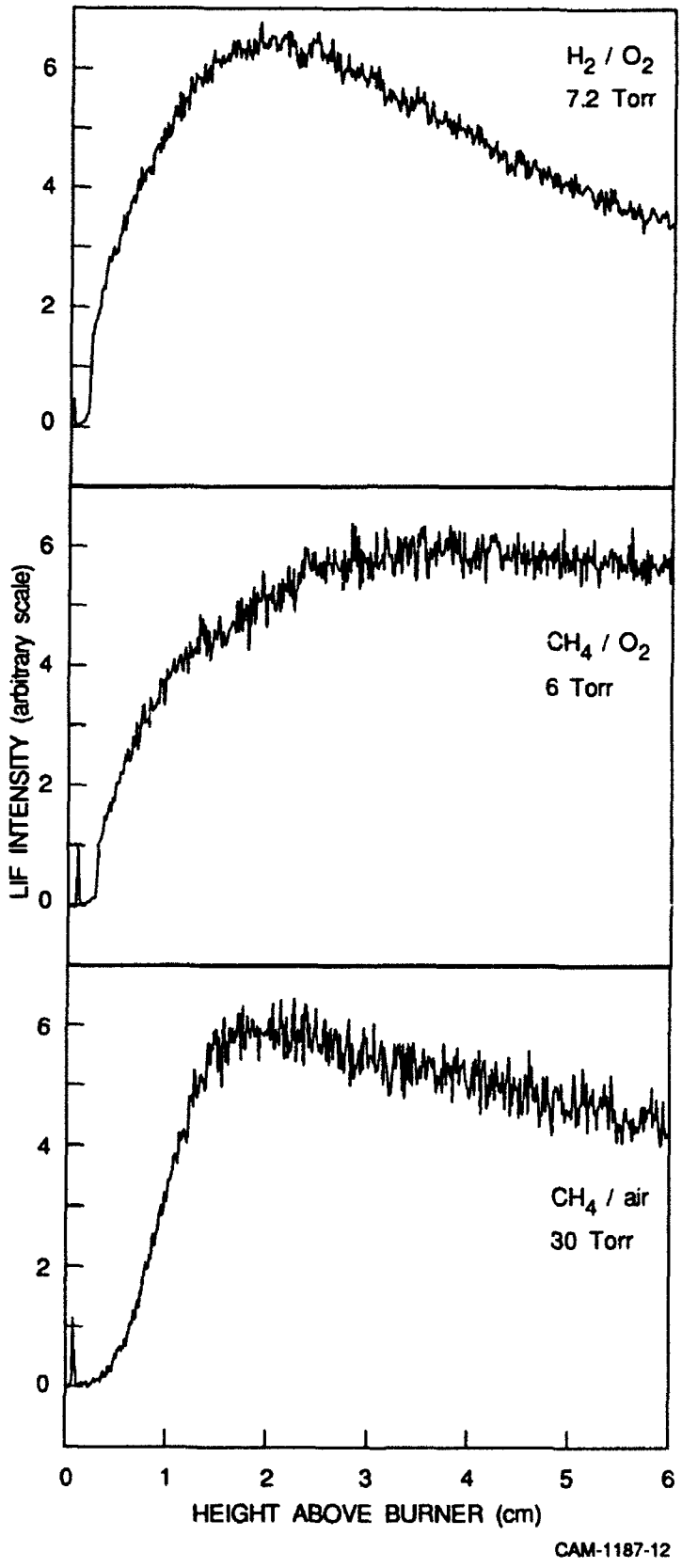

Figure 19. Two-photon-excited LIF signals from atomic hydrogen in three stoichiometric, low-pressure flames: upper panel, 7.2 Torr H2/O2; middle panel, 6 Torr CH4/O2; and lower panel, 30 Torr CH4/air.

predict the concentrations of the colliders, and we used the quenching rate constants of Bittner et al.[30] We assumed that the quenching rate constant for n = 3 H atoms by OH is the same as for H_2O. The quenching corrected relative H atom concentration for the H_2/O_2 flame is given in Figure 20.

The smooth curve in Figure 20 is the H atom mole fractions predicted by our chemical model of the premixed H_2/O_2 flame.[27,33] The LIF signal height has been arbitrarily scaled to match the peak values of the model calculation. There are clear differences between the model and the measurement; especially notable is the growing discrepancy between model and measurement moving up from the peak H atom in the burnt gases. The model predicts that the H atom mole fraction declines much more slowly than was observed by LIF. The model does not predict a significant change in the collider species over the range 3-6 cm above the burner, and the measured gas temperature is nearly constant.[25] Thus, our quenching assumption cannot explain these differences. The sensitivity analysis of the model calculation indicates that the recombination reactions H+H+M and $H+O_2$+M are the most sensitive reactions for the H atom concentration in this region.

The observations made from Figure 20 motivated a major change in our treatment of fluid flow in our model of our lowest pressure flames. With support from the Gas Research Institute (GRI), we determined that radial transport is significant in the lowest pressure flames. Radial profiles of OH were measured, the extent of flame blooming determined, and radial transport added to the model code. The corrected model agrees quite well with the atom measurements, as shown by the solid line in Figure 20. This is an example of synergism of the various projects in our laboratory. Flame modeling is not supported by this contract, but atom LIF measurements needed to compare with ASE measurements did not agree with predictions by the GRI-supported model. Model development under their contract provides us with specifications for a well characterized and well studied reactive flow environment to make ASE measurements for the Air Force.

Balmer α ASE signals were observed in all the flames studied. The ASE signal forms a collimated beam propagating forward and backward along the excitation laser beam. The largest ASE signals were observed in rich H_2/O_2 flames. In this flame, the forward and backward ASE signal intensities were approximately equal. In the forward direction, it is also possible to phase match four-wave mixing signals at 656 nm, and the equal intensity measurement indicates that ASE and not four-wave mixing is the primary source of the collimated signal, in agreement with other flame measurements on H, O, C, and N.[19-21]

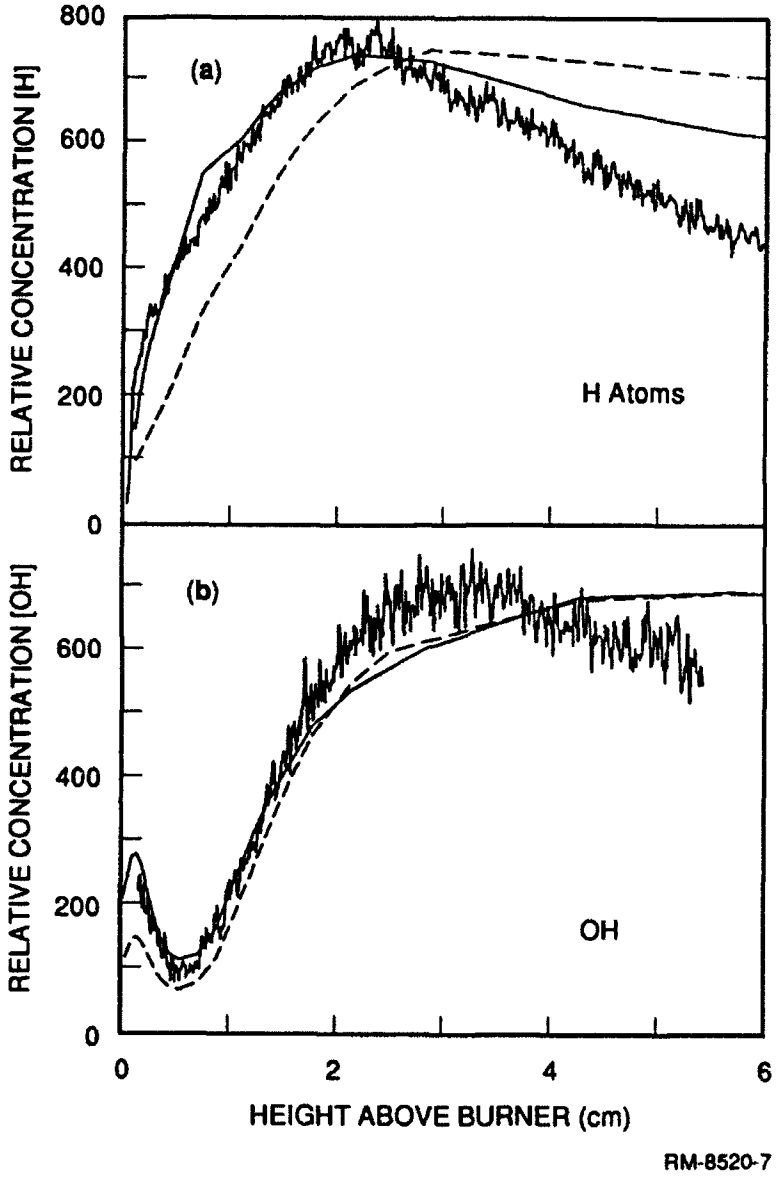

Figure 20. Quenching corrected LIF signal from OH and H atoms in a 7.2 Torr H_2/O_2 flame, dashed curve represents the model calculation of the concentrations without radial transport, and the solid curve model calculation including radial transport.

We found that the ASE signal was slightly polarized, with a ratio of 3:2 as measured with a linear polarizer. This value is in good agreement with the polarization predicted from the combination of 3S and 3D states initially excited. When linear polarized light is used to excite the 1S ground state of atomic hydrogen, the selection rule $\Delta m_J = 0$ produces an anisotopic distribution of m_J in the 3D. The 1S and 3S only have $m_J = \pm 1/2$, while the $3D_{3/2}$ has $m_J = \pm 1/2, \pm 3/2$ and the $3D_{5/2}$ has $m_J = \pm 1/2, \pm 3/2, \pm 5/2$. Thus, excitation of the 1S with linearly polarized light cannot initially populate the $m_J = \pm 3/2$ and $\pm 5/2$ sublevels of the 3D. The isotropic 3S and anisotropic 3D population distribution radiates to the $2P_{1/2}$ and $2P_{3/2}$, with the relative intensities of the two linear polarization components of the light propagating along the laser beam calculable from angular momentum algebra. The initial population ratios $3D_{3/2}$:$3D_{5/2}$ and 3S:3D (values = 18/45:27/45 and 1:7.56,[34] respectively, led us to predict a relative polarization of 0.62:0.38. This result is in excellent agreement with our measured 3:2 ratio, however, it is significantly different from the >10:1 linear polarization observed by Goldsmith.[34] At this point in our analysis we will not speculate on the origin of this difference.

In Figure 21, the variation of the ASE and LIF signals at 3.1 cm height above the burner in the 7.2 Torr H_2/O_2 flame is plotted versus laser power. The nearly linear increase in the plot of LIF versus laser power is indicative of significant losses to ionization and ASE. The ASE power dependence shows a threshold below which no ASE is observed and an exponential increase in ASE signal with laser energy. Such a region of exponential growth is predicted[35] by the theoretical treatments of ASE. Similar features were observed for all the flames studied and for both 10 and 20 cm focal length lenses for the excitation laser light. The position of the threshold in laser energy and the strength of the exponential increase is quite dependent on flame conditions. In fact, the threshold of the ASE power dependence varies quite a lot as a function of height above the burner in the same flame.

At the laser pulse energies used, we do not see the saturation of the ASE gain observed by Goldsmith,[34] whose experiment used three times more laser pulse energy and a threefold longer focal length lens. Thus, the laser fluence is comparable in the two studies but the gain lengths are quite different. The excitation rate of the two-photon transition will be largest in the beam waist of the focused laser beam, and hence the greatest gain is localized to the beam waist. The gain length can be longer if longer focal length lenses are employed; such a situation may allow the ASE to build up to an intensity that induces stimulated emission from all the atoms along the remaining path length. Indeed, we see the ASE signal increase more than 50% when we replace the 10 cm focal length lenses with 20 cm focal length lenses.

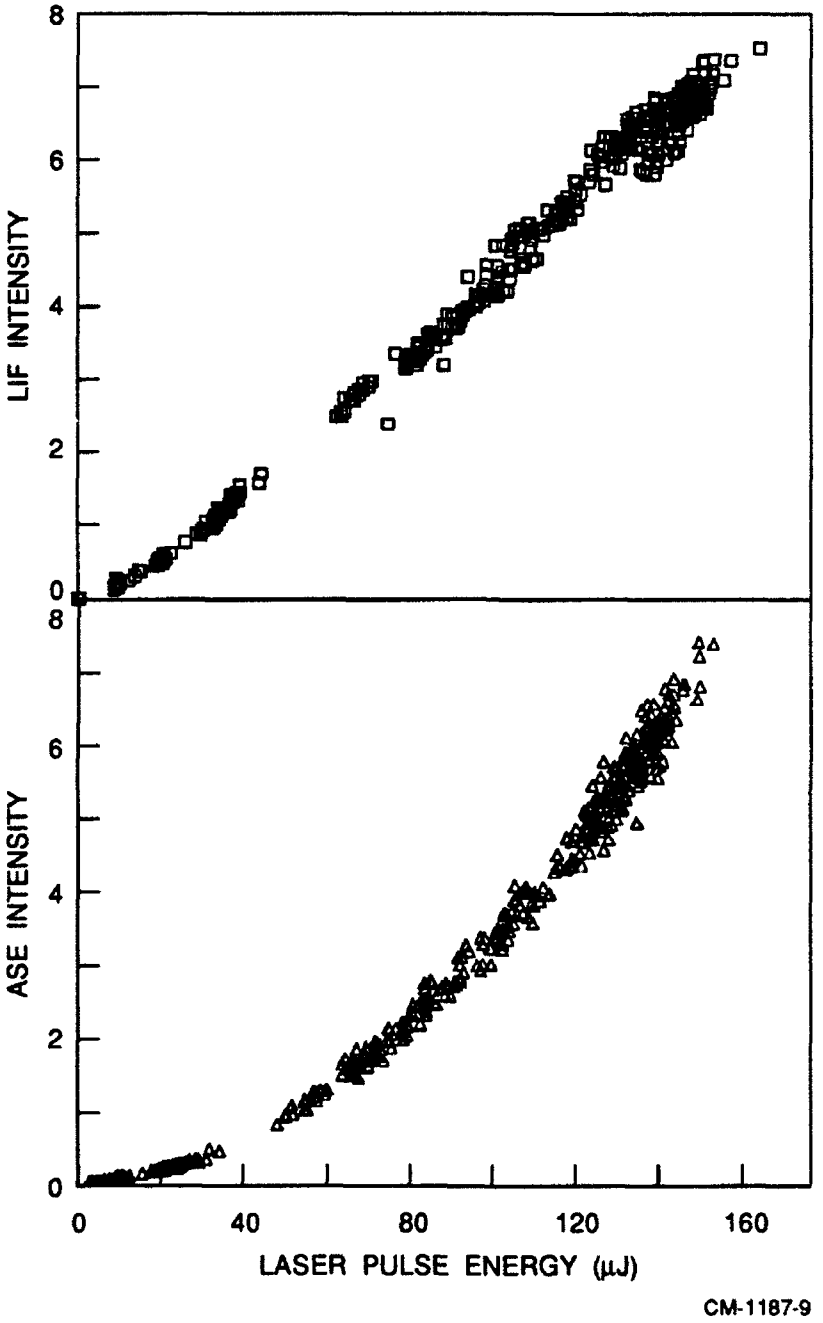

Figure 21. Laser pulse energy dependence of LIF (upper panel) and ASE (lower panel) signals 3.1 cm above the burner in a 7.2 Torr H_2/O_2 flame.

In Figure 22 the ASE signal is plotted versus height above the burner for a rich, stoichiometric, and lean H_2/O_2 flame. The simultaneously acquired LIF signals are also shown. The ASE and the LIF agree well in the rich case, but there is a significant difference in the burnt gases of the lean flame. Goldsmith and coworkers[32] measured the total quenching rate in lean and rich H_2/O_2 flames and found the total quenching rate to be nearly a factor of two faster in the lean flame. Thus, as the quenching rate increases we see a growing difference between ASE and LIF signals. The quenching causes a loss of population inversion, and in the region of exponential growth of the ASE signal the quenching can have a very large influence on the ASE intensity because it alters terms in the exponent of the model of the ASE signal.

The ASE collimation is measured by replacing the photomultiplier tube with a CCD array. The collimated ASE has a 0.35 cm full width at half maximum (FWHM) corresponding to the collection with a 10 cm lens of f28. The ASE is then expanded with a diverging lens and directed through an etalon with a 3.8 cm^{-1} free spectral range. The resulting interference pattern is observed on the face of the image intensifier of the CCD array. A single slice across the image is plotted in Figure 23. The FWHM of the interference fringes is 1.4 cm^{-1}, which is about twice the Doppler width in this 1200 K flame. The fine structure splitting of the 2P state is 0.37 cm^{-1}, however, nearly 80% of the transitions terminate on the $2P_{3/2}$ fine structure state. The contributions of Stark broadening and gain narrowing to the bandwidth are being evaluated.

To extract useful gas temperature determinations from ASE bandwidth measurements, it is necessary to know some details about the two-photon pumping and subsequent ASE emission. The ASE process is intrinsically nonlinear, and attention must be paid to pump saturation, gain narrowing, and any ac Stark shifting or broadening that may arise. To this end we conducted a series of experiments under different conditions and compared the results with theoretical calculations.

To better understand the pumping process, we recorded a number of excitation scans. Six such scans are shown in Figures 24 and 25 as a function of pump laser intensity. These spectra were recorded in a H_2/O_2 flame by using two different focal length lenses for a range of pump laser energies. Spectra taken with a short focal length lens (0.150 m) appear in Figure 24 as double-peaked. The left peak corresponds to the $3p^3P_2 \leftarrow 2p^3P_2$ transition, while the right peak corresponds to the $3p^3P_1 \leftarrow 2p^3P_2$ transition. These two transitions are separated by 0.0014 nm, which at 1200 K amounts to one quarter of the two-photon Doppler width. A calculation of the relative cross section of these two lines[36] indicates that they should have a relative signal strength of 3.6:1, with the J = 2←2 transition appearing as the stronger of the two. However, in the two upper curves of Figure 24, the transitions are present with very similar strengths, suggesting

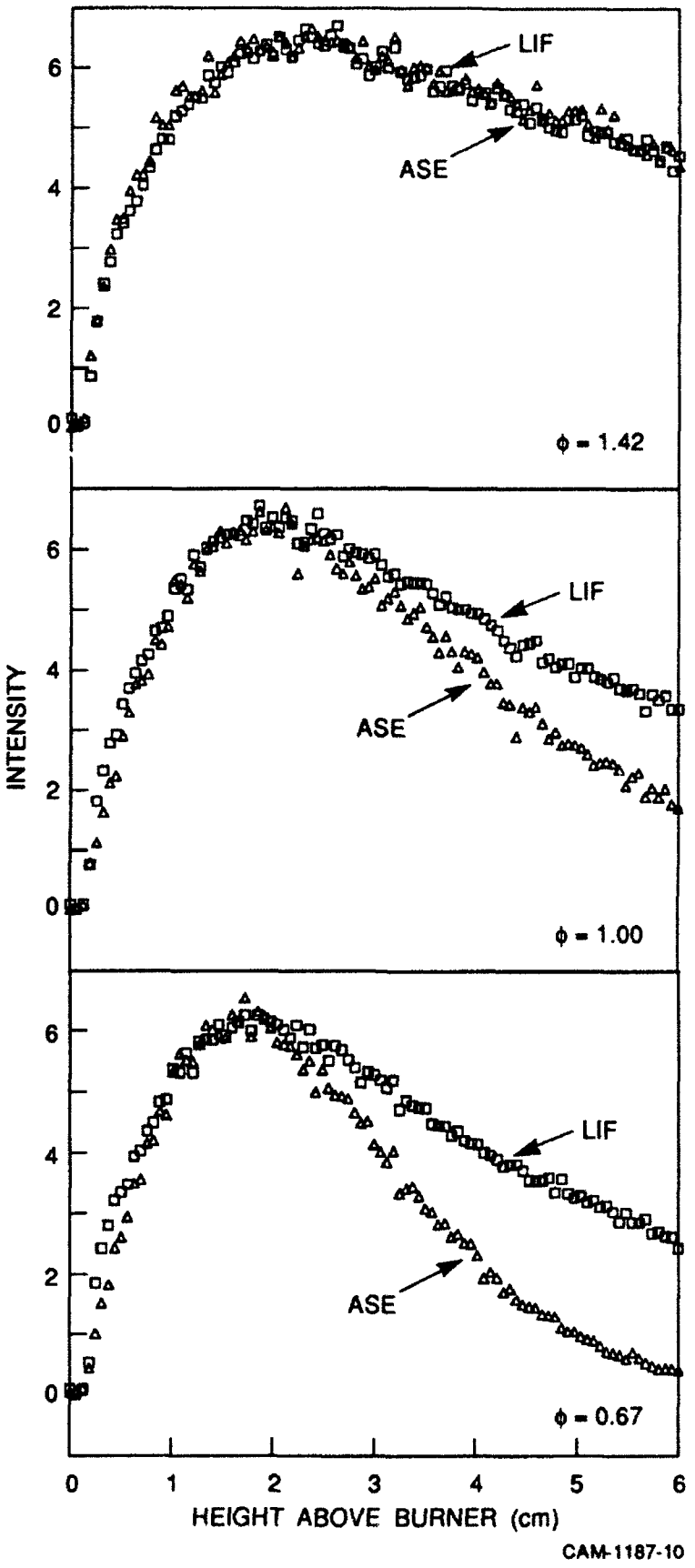

Figure 22. Simultaneously acquired ASE and LIF data plotted versus height above the burner for fuel rich (ϕ=1.42), stoichiometric (ϕ=1.00), and lean (ϕ=0.67) 7.2 Torr H_2/O_2 flames.

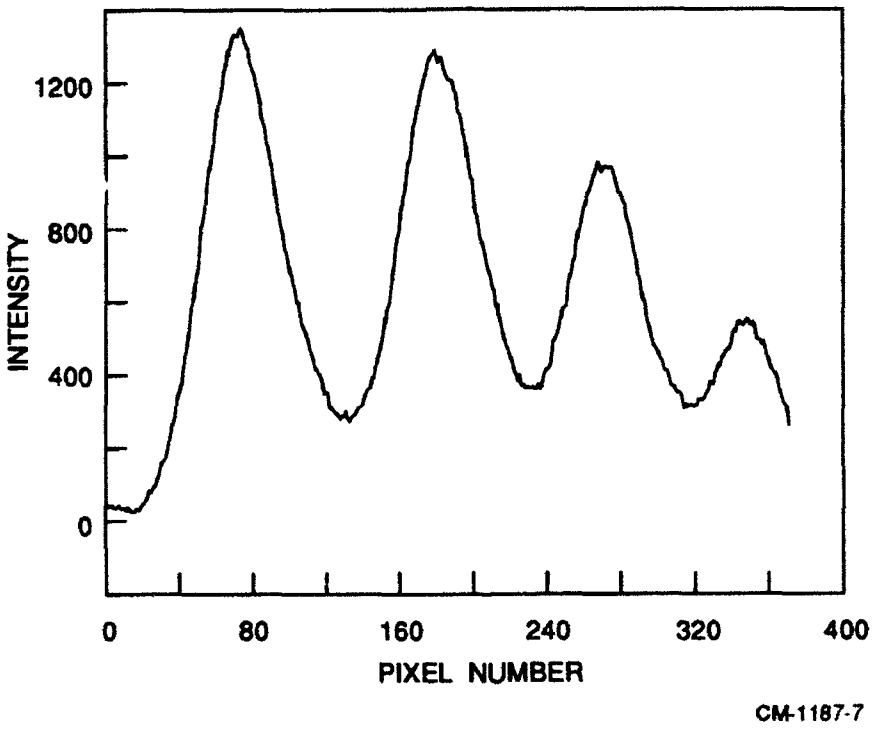

Figure 23. Slice through the etalon interference pattern of ASE in rich 7.2 Torr H_2/O_2 flame.

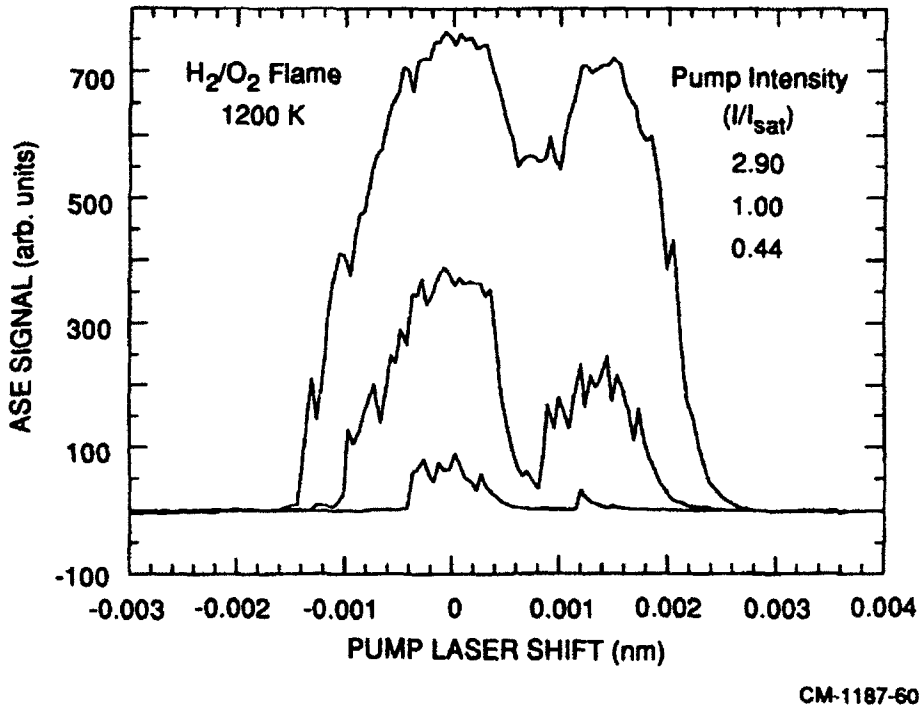

Figure 24. ASE excitation scans taken using a 0.15 m focal length lens. Saturation of the J=2←2 transition makes the J=1←2 transition appear relatively strong.

saturation of the J = 2←2 transition. An estimate of the saturation intensity can be made using the following expression,[37]

$$W^{(2)} \tau = \frac{1}{2}$$

Here, τ indicates the pulse width of the laser and $W^{(2)}$ denotes the two-photon transition rate at saturation, which is given by[38]

$$W^{(2)} = \frac{\alpha I_{sat}^2}{h \nu}$$

The two-photon absorption cross section, Planck's constant, and the frequency are denoted by α, h and ν, respectively. From the above, we estimate the saturation intensity for the J = 2←2 transition is I_{sat} = 432 MW/cm^2. The upper two curves in Figure 20 were recorded with pump intensities of ~2.9 I_{sat} and ~1.0 I_{sat}, respectively.

We used a longer focal length lens (500 mm), to record the excitation scans that appear in Figure 25. For each of these scans the pump laser intensity is well below saturation and the spectra have a different overall appearance. The J = 1←2 transition now appears relatively weak compared with the J = 2←2 transition. When making quantitative bandwidth measurements it is prudent to operate in the low pump intensity limit to simplify the data analysis.

Figure 26 displays etalon fringes of ASE emission from oxygen atoms in a H_2/O_2 flame at 1200 K. The central spot of the diffraction pattern lies just to the left of the first fringe. These fringes were recorded by summing the emission following ten pump laser shots at an intensity of 0.31 I_{sat}. The apparent noise in the fringes is due to the ASE light that passes through the etalon without any reflections. Accounting for the intrinsic bandwidth of the etalon at the emission wavelength of 845 nm, analysis of the fringes yields an ASE bandwidth of 0.08 ± 0.04 cm^{-1}. Similar fringes were recorded in a CH_4/O_2 flame at 1800 K with a pump intensity of 0.43 I_{sat}. The corresponding bandwidth amounts to 0.15 ± 0.04 cm^{-1}. These experimental values are plotted in Figures 27 and 28.

ASE Bandwidth Calculations

To interpret the bandwidth measurements discussed above, we performed calculations of the ASE signal. Previous theoretical treatment[39] of the frequency distribution of the ASE signal did not include the finite bandwidth of the exciting pump laser, which could not be neglected in our work. The calculation should be considered as a two-step process in which the frequency dependent population of the excited state after two-photon absorption is determined first, and then

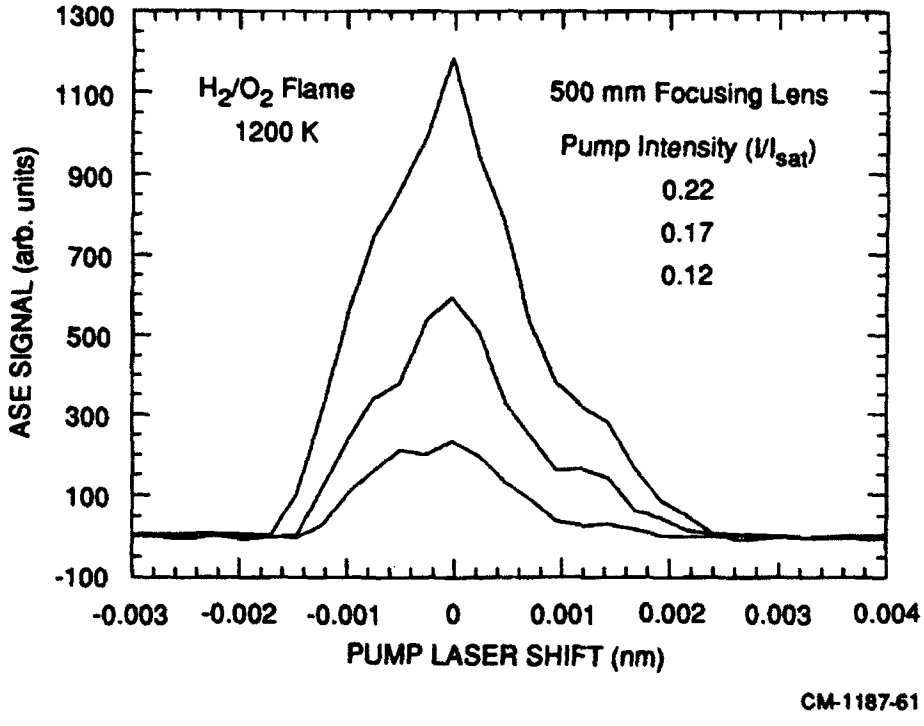

Figure 25. ASE excitation scans taken using a 0.5 m focal length lens.

The J=2←2 transition is not saturated which changes the appearance from Fig. 24.

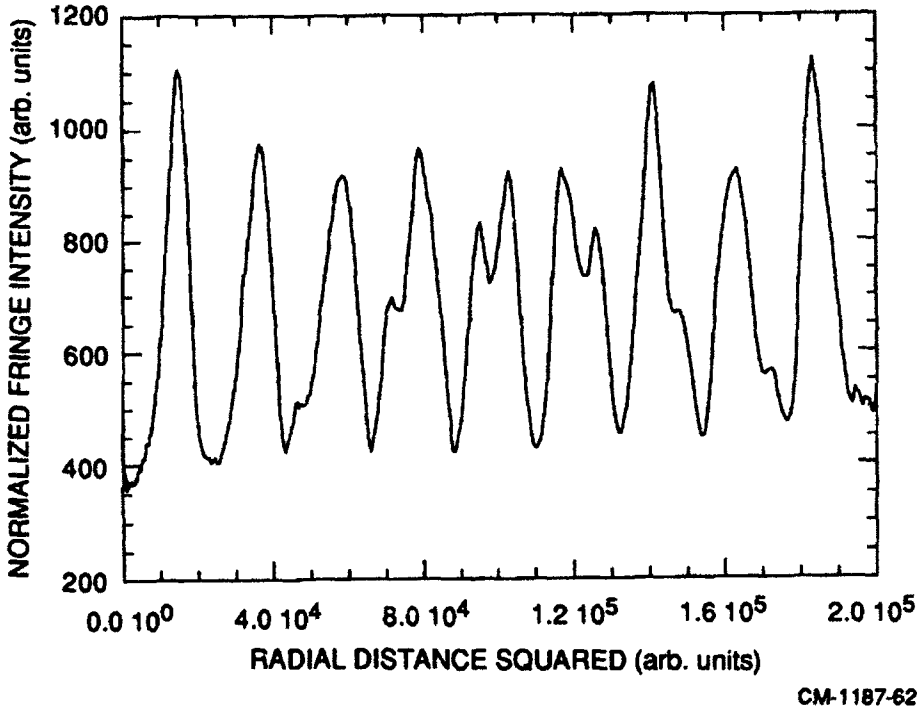

Figure 26. Etalon fringes of the ASE at 1200 K.

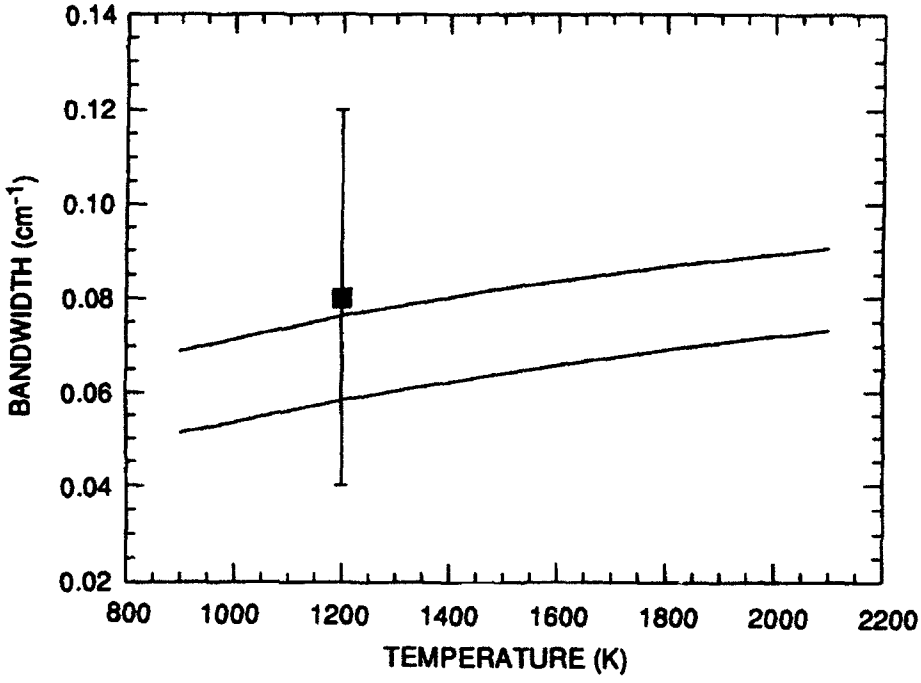

Figure 27. Comparison of the ASE bandwidth measurement and the calculated values for a H_2/O_2 flame.

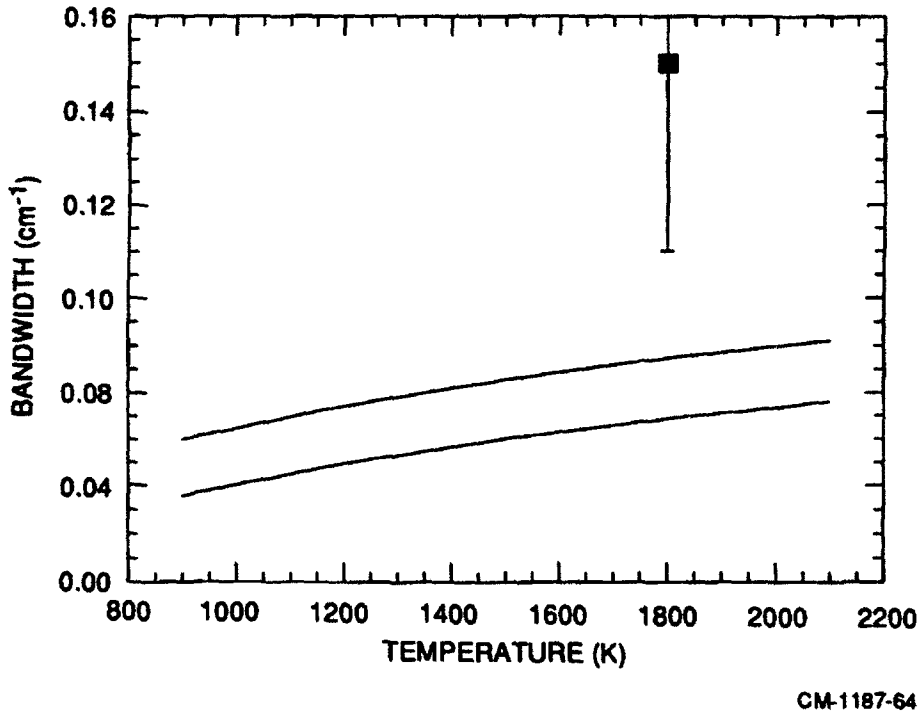

Figure 28. Comparison of the ASE bandwidth measurement and the calculated values for a CH_4/O_2 flame.

the frequency dependent gain experienced by the ASE beam as it propagates through the excited medium.

In the first step, the frequency response of the oxygen atoms is represented by the appropriate Voigt profile while the laser is represented by a Gaussian. The laser is assumed to be fixed at exact resonance and the apparent bandwidth of the pump laser during the two-photon absorption,[40] at 226 nm, is taken into account. The relative population of the excited state as a function of frequency is found from the product of the Voigt profile and the laser intensity frequency distribution. Each frequency of the excited state population corresponds to an atomic velocity that is easily determined. Then each of these velocities can be converted into an ASE frequency distributed about 845 nm (where fluorescence is produced from the $3s^3S^0 \leftarrow 3p^3P$ transition). In this way, the initial excited state population is found as a function of frequency, and then remapped as a modified function of frequency, which then experiences the gain associated with the ASE process.

In the second step, standard laser amplifier theory is used to calculate the gain coefficient for an inhomogeneously broadened system, using the excited state frequency distribution found as described above.[41] This gain coefficient is then used in the expression for the ASE signal intensity.[41] One of the input quantities required to calculate the gain coefficient is the total population inversion of the two energy levels that produce the ASE light. We estimated this population inversion by numerically integrating a system of rate equations modeling the three relevant energy levels of the oxygen atom. As noted earlier, the cross sections for two-photon absorption, ionization, quenching, and intermultiplet transfer are known for the oxygen system, so the rate equation analysis is tractable.

The results of our ASE bandwidth calculation are shown in Figure 27 for the H_2/O_2 flame and in Figure 28 for the CH_4/O_2 flame. The calculations were made using our measured pump laser bandwidth of 0.25 cm^{-1}. The two solid lines in Figure 27 indicate numerical results appropriate for the ground state oxygen atom concentration (2.48×10^{15} cm^{-3}) found in the H_2/O_2 flame[23] at 1200 K. At this temperature, the two-photon Doppler width amounts to 0.55 cm^{-1} for the 226-nm pump laser. The two lines differ only in the input value of the population difference between the excited and intermediate states. The lower line corresponds to the calculated population inversion of 1.2×10^{11} cm^{-3}, while the upper line corresponds to a population inversion that is a factor of 10 smaller. The lower line represents the ideal case suggested by the rate equations, while the upper line is probably closer to the truth, given that several factors (including fluctuations in the pump laser intensity and inhomogeneities in the flame environment) reduce the overall population inversion obtained. The two lines appearing in Figure 28 represent

similar calculations done for the oxygen atom concentration (4.96×10^{14} cm^{-3}) found in a CH_4/O_2 flame[24-26] at 1800 K. The Doppler width, at 1800 K, amounts to 0.67 cm^{-1}.

As seen in Figure 27, there is good agreement between the measured and calculated ASE bandwidths for the H_2/O_2 flame environment. However, as seen in Figure 28 there is poor agreement for the CH_4/O_2 flame environment. At present, we do not know the reason for the disagreement. We have calculated the AC Stark broadening associated with the two-photon pumping process and find it to be insignificant under the experimental conditions used. Calculations also indicate that power broadening is not significant.

The calculations do show, as expected, a dependence on the pump laser bandwidth. In Figure 29 we show the calculated results for the ASE bandwidth as a function of the dye laser bandwidth. (The bandwidth of the doubled pump beam is simply given by the product of the dye laser bandwidth and a factor of $2^{1/2}$.) This calculation was made for the conditions of the 7 Torr H_2/O_2 flame. Notice that when the dye laser bandwidth is greater than the two-photon Doppler width, the ASE bandwidth becomes independent of this quantity.

Figure 30 compares the calculated and experimental values of simultaneous LIF and ASE signals from atomic oxygen in the 7 Torr H_2/O_2 flame. The LIF signal is significantly reduced by the ASE at the largest ASE signal, yet the model fits both of the signals quite well. The success of this model is crucial to evaluate the potential of ASE as a quantitative diagnostic.

The gain from the laser excited population inversion in atomic oxygen can be directly measured by a cw probe laser. This approach overcomes the difficulty of quantitative interpretation of ASE signals in a collisional environment. For this experiment, a single-mode cw diode laser near 845 nm illuminates the focal region of the two-photon excitation beam in the low-pressure burner. The probe laser is directed through the excitation region at a small (~5°) angle to the pump beam and stimulates the $3p^3P \rightarrow 3s^3S^o$ transition. When the cw probe laser is tuned to the ASE transition, gain is observed on the intensity of the probe and loss is observed on the spontaneous ASE. Figure 31 shows the depletion of the spontaneous ASE as a function of diode laser power. Although the measurements are preliminary, they are quite encouraging; the gain on the cw probe laser intensity from the laser excited atoms ranges from 0.3%-25%. The probe laser intensity sets the stimulation rate, which can be significantly faster than the spontaneous emission or collisional quenching rates. The measured gain is proportional to the number of laser excited atoms, and we can determine the number density of ground state atoms from the excitation parameters. Thus, accurate single-shot atom concentration measurements are feasible using the stimulated emission gain of a probe laser beam.

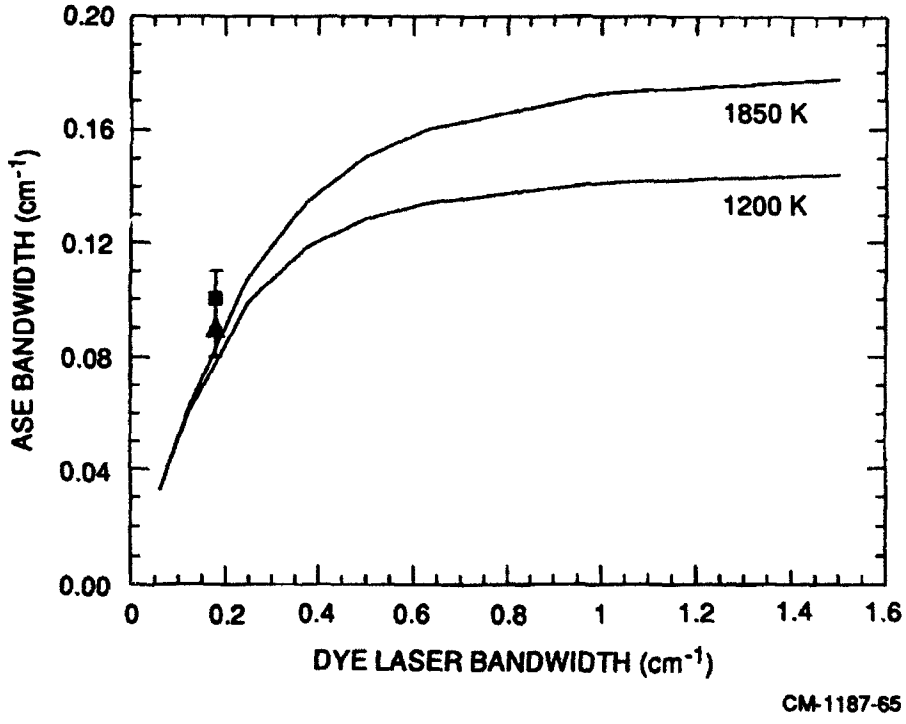

Figure 29. The dependence of the calculated ASE bandwidth on the bandwidth of the excitation dye laser for two different Doppler widths for atomic oxygen in the small gain limit.

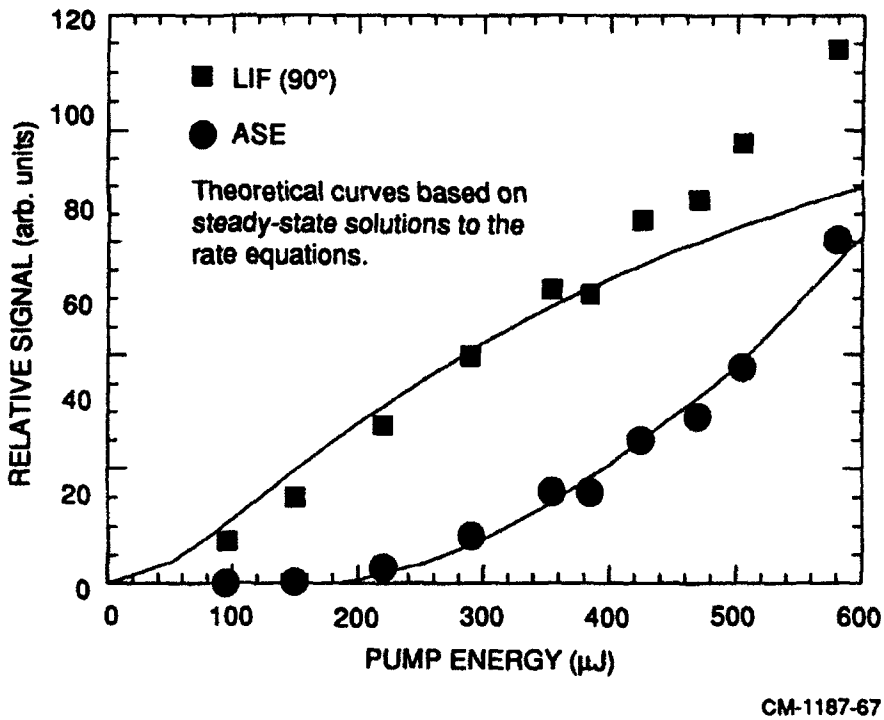

Figure 30. Measured and calculated dependence of LIF and ASE on the excitation pulse energy for oxygen atomic in a 7 Torr H_2/O_2 flame.

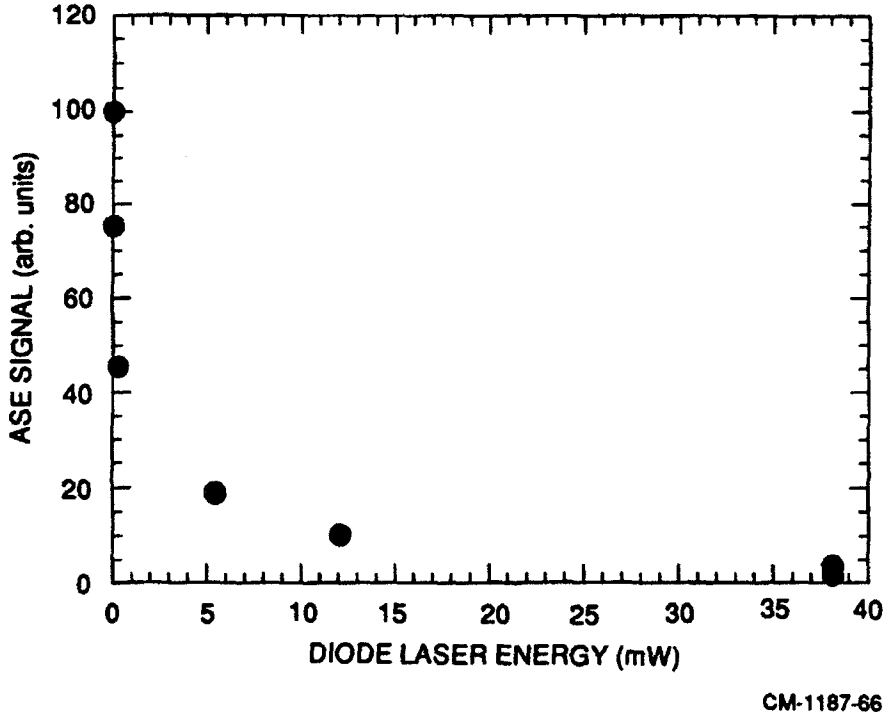

Figure 31. Depletion of the spontaneous ASE as a function diode laser power.

CONCLUSIONS

TASK 1

SRI has developed a high power vuv source that produces adequate power for multiphoton excitation in the vuv. Powers up to 65 μJ have been obtained at 133 nm. Krypton appears to be the best candidate for vuv generation in the range 140 to 160 nm, while mixing in hydrogen is more efficient at shorter wavelengths. We have used the resulting radiation to perform both 1+1 REMPI and two-photon-excited fluorescence in the vuv. Excitation of atomic ions will require higher powers than we have now. We are now using an off-axis lens apparatus to reduce losses, and we will explore the use of negatively dispersive gases for phase matching to enhance the vuv generation. With the resulting radiation, we should be able to perform two-photon-excited fluorescence from atomic ions and planar imaging of light atoms.

TASK 2

Simultaneous ASE and LIF measurements have been demonstrated for atomic hydrogen and oxygen in a variety of low-pressure flames. These measurements show that ASE can alter the LIF signal from atoms in reacting flow and that collisions influence the ASE intensity. Direct measurement of the gain from the laser excited population inversion provides a means for quantitative ASE measurements that avoids the complications of collisional quenching. The gain on a cw diode probe laser is measured coincident with the two-photon excitation of the atoms. A model of the ASE and LIF has been developed that predicts both intensity and bandwidth of the signal. The bandwidth of the ASE is influenced by gain narrowing, Stark and pressure broadening, the bandwidth of the excitation wavelength, and the Doppler width of the atoms. Thus, bandwidth measurements can be used to probe gas temperature, and by exploiting gain narrowing, the directed flow velocity can be measured. Preliminary measurements of ASE bandwidth and direct measurements of the gain have been demonstrated.

REFERENCES

1. G. W. Faris, M. J. Dyer, W. K. Bischel, and D. L. Huestis, "Multiphoton Detection Techniques for F and F_2," Final Report, AFOSR Contract No. F49620-88-K-0003, SRI International, Menlo Park, CA (November 1990).

2. G. W. Faris, M. J. Dyer, D. L. Huestis, and W. K. Bischel, "Two-Photon Spectroscopy of the $F^1\Pi_g$ and $f^3\Pi_g$ States of Molecular Fluorine," J. Chem. Phys. **97**, 5964-5969 (1992).

3. G. W. Faris and M. J. Dyer, "Multiphoton Spectroscopy Using Tunable VUV Radiation from a Raman-Shifted Excimer Laser," in *Short Wavelength Coherent Radiation: Generation and Applications*, Philip H. Buckbaum and Natale M. Ceglio, Eds. (Optical Society of America, Washington, DC, 1991) pp. 58-61.

4. G. W. Faris and M. J. Dyer, "VUV Multiphoton Spectroscopy Using a Raman-Shifted Excimer Laser," J. Opt. Soc. Am. B, in press, 1993.

5. G. Hilber, A. Lago, and R. Wallenstein, "Broadly Tunable Vacuum-Ultraviolet/Extreme-Ultraviolet Radiation Generated by Resonant Third-Order Frequency Conversion in Krypton," J. Opt. Soc. Am. B **4** , 1753-1764 (1987).

6. J. P. Marangos, N. Shen, H. Ma, M. H. R. Hutchinson, and J. P. Connerade, "Broadly Tunable Vacuum-Ultraviolet Radiation Source Employing Resonant Enhanced Sum-Difference Frequency Mixing in Krypton," J. Opt. Soc. Am. B 7, 1254-1259 (1990).

7. R. Hilbig, G. Hilber, A. Lago, B. Wolff, and R. Wallenstein, "Tunable Coherent VUV Radiation Generated by Nonlinear Optical Frequency Conversion in Gases," Comments At. Mol. Phys. **18**, 157-180 (1986).

8. T. Okada, Y Hirakawa, and M. Maeda, "Generation of Tunable XUV Radiation by Two-Photon Resonant Four-Wave Mixing in H_2, Paper CThD6 presented at the Conference on Lasers and Electro-Optics 1990, Anaheim, CA, May 21-25, 1990.

9. C.E.M. Strauss and D. J. Funk, "Broadly Tunable Difference-Frequency Generation of VUV Using Two-Photon Resonances in H_2 and Kr," Opt. Lett. **16**, 1192 (1991).

10. H. Pummer, H. Egger, T. S. Luk, T. Srinivasan, and C. K. Rhodes, "Vacuum-Ultraviolet Stimulated Emission from Two-Photon-Excited Molecular Hydrogen," Phys. Rev. A **28**, 795-801 (1983).

11. S. H. Lin, Y. Fujimura, H. J. Neusser, and E. W. Schlag, *Multiphoton Spectroscopy of Molecules* (Academic Press, Inc., New York, 1984), pp. 96-99.

12. John F. Reintjes, *Nonlinear Optical Parametric Processes in Liquids and Gases* (Academic Press, New York, 1984), pp. 56-57.

13. S. E. Harris and R. B. Miles, "Proposed Third Harmonic Generation in Phase-Matched Metal Vapors," Appl. Phys. Lett. **19**, 385-387 (1971).

14. G. W. Faris and M. J. Dyer, "Two-Photon-Excitation of Ne at 133 nm," Opt. Lett. **18**, 382-384 (1993a).

15. A. C. Eckbreth, "Laser Diagnostics for Combustion Temperature and Species," (Abacus Press, Cambridge, MA, 1988).

16. U. Westblom, S. Agrup, M. Alden, H. M. Hertz, and J. E. M. Goldsmith, Appl. Phys. B **50**, 487 (1990).

17. See, for example, A. E. Siegman, *Lasers,* (University Science Books, Mill Valley, CA 1986).

18. J.E.M. Goldsmith, J. Opt. Soc. Am. B **6**, 1979 (1989).

19. M. Alden, P-E. Bengtsson, and W. Westblom, Opt. Comm. **71**, 263 (1989).

20. M. Alden, U. Westblom, and J.E.M. Goldsmith, Opt. Lett. **14**, 305 (1989).

21. S. Agrup, U. Westblom, and M. Alden, Chem. Phys. Lett. **170**, 406 (1990).

22. A. D. Sappey and J. B. Jeffries, Appl. Phys. Lett. **55**, 1182 (1989).

23. K. Kohse-Höinghaus, J. B. Jeffries, R. A. Copeland, G. P. Smith and D. R. Crosley, in *Twenty-Second (International) Symposium on Combustion,* (The Combustion Institute, Pittsburgh, PA, 1989) p. 1857.

24. K. J. Rensberger, M. J. Dyer, and R. A. Copeland, Appl. Opt., **27**, 3679 (1988).

25. A. D. Sappey, D. R. Crosley, and R. A. Copeland, Appl. Phys. B **50**, 463 (1990).

26. J. B. Jeffries, D. R. Crosley, I. J. Wysong, and G. P. Smith, *23rd Symposium (Int) on Combustion,* (The Combustion Institute, Pittsburgh, PA, 1990) pg. 1847.

27. D. E. Heard, J. B. Jeffries, G. P. Smith, and D. R. Crosley, Combustion and Flame, **88**, 137 (1992).

28. U. Meier, K. Kohse-Höinghaus, and Th. Just, Chem. Phys. Lett. **126**, 567 (1986).

29. J.E.M. Goldsmith, Opt. Lett. **11**, 416 (1986).

30. J. Bittner, K. Kohse-Höinghaus, U. Meier, and Th. Just, Chem. Phys. Lett. **143**, 571 (1988).

31. J.E.M. Goldsmith, R.J.M. Anderson, and L. R. Williams, Opt. Lett. **15**, 78 (1990).

32. J. E. M. Goldsmith, J. A. Miller, R. J. M. Anderson, and L. R. Williams, *23rd Symposium (Int) on Combustion*, (The Combustion Institute, Pittsburgh, PA, 1990) p. 1821.

33. G. P. Smith, unpublished data, manuscript in preparation.

34. J.E.M. Goldsmith, J. Opt. Soc. Am. B **6**, 1979 (1989).

35. D. J. Bamford, L. E. Jusinski, and W. K. Bischel, Phys. Rev. A **34**, 185 (1986).

36. G. I. Peters and L. Allen, J. Phys. B **4**, 238 (1971); L. Allen and G. I. Peters, J. Phys. B**4**, 377 (1971); L. Allen and G. I. Peters, J. Phys. B**4**, 564 (1971).

37. D. C. Hanna, M. A. Yuratich, and D. Cotter, *Nonlinear Optics of Free Atoms and Molecules*, (Springer-Verlag, Berlin, 1979).

38. W. K. Bischel, B. E. Perry and D. R. Crosley, Appl. Opt. **21**, 1419 (1982).

39. L. Allen and G. I. Peters, J. Phys. A **5**, 695 (1972).

40. B. R. Marx, J. Simons and L. Allen, J. Phys. B **11**, L273 (1978).

41. J. T. Verdeyen, *Laser Electronics*, (Prentice-Hall, Inc., Englewood Cliffs, NJ 1981).

PROFESSIONAL PERSONNEL

The following professional scientists participated in the research supported by this contract:

TASK 1

Gregory W. Faris, Physicist, Co-Principal Investigator; Task Leader and lead experimentalist for Task 1.

Mark J. Dyer, Physics Associate, specialist in lasers and nonlinear optics; made many of the major technical accomplishments in Task 1.

David L. Huestis, Associate Director of the Molecular Physics Laboratory, Co-Principal Investigator, project supervisor, and Task 1 technical contributor, especially on theory and spectroscopy.

TASK 2

Jay B. Jeffries, Senior Chemical Physicist, Co-Principal Investigator; Task Leader for Task 2.

Dwayne E. Heard, Postdoctoral Fellow, Laboratory Scientist for Task 2; performed measurements on atomic hydrogen.

Michael S. Brown, Postdoctoral Fellow, Laboratory Scientist for Task 2; modeled probe laser gain in atomic oxygen with ASE.

David R. Crosley, Associate Director of the Molecular Physics Laboratory, Technical advisor on spectroscopy (angular momentum algebra) and collision dynamics.

Gregory P. Smith, Senior Chemical Physicist for Task 2. Performed chemical model calculations to obtain the partial pressures of flame species.

PUBLICATIONS

TASK 1

The following publications were published or submitted for publication on research supported by this contract:

G. W. Faris and M. J. Dyer, "Multiphoton Spectroscopy Using Tunable VUV Radiation from a Raman-Shifted Excimer Laser," in *OSA Proceedings on Short Wavelength Coherent Radiation: Generation and Applications*, Phillip H. Bucksbaum and Natale M. Ceglio, Eds. (Optical Society of America, Washington, DC, 1991), pp. 58-61.

G. W. Faris, M. J. Dyer, D. L. Huestis, and W. K. Bischel, "Two-Photon Spectroscopy of the $F^1\Pi_g$ and $f^3\Pi_g$ States of Molecular Fluorine," J. Chem. Phys. **97**, 5964-5969 (1992).

G. W. Faris and P. C. Cosby, "Observation of NO $B^2\Pi(v=3)\leftarrow X^2\Pi(v=0)$ Absorptions with 1+1 Multiphoton Ionization: Precision Line Position Measurements and Parity Assignment of the $B^2\Pi$ State," J. Chem. Phys. **97**, 7073-7086 (1992).

G. W. Faris and M. J. Dyer, "Two-Photon-Excitation of Ne at 133 nm," Opt. Lett. **18**, 382-384 (1993).

G. W. Faris and M. J. Dyer, "VUV Multiphoton Spectroscopy Using a Raman-Shifted Excimer Laser," to appear in J. Opt. Soc. Am. B, 1993.

TASK 2

J. B. Jeffries, G. P. Smith, D. E. Heard, and D. R. Crosley, "Comparing Laser-Induced Fluorescence Measurements and Computer Models of Low Pressure Flame Chemistry," Ber. Bunsenges. Phys. Chem. **96**, 1410 (1992).

J. B. Jeffries and M. S. Brown, "Amplified Spontaneous Emission Measurements of Atomic Oxygen," in *AIAA 93-0047 Technology Compendium*, J. D. Trolinger, Ed. (in press, 1993).

Manuscripts in Preparation

Although the data are collected for all three of these manuscripts, the development of a predictive model of the ASE signal allows us to significantly improve the analysis and interpretation of these data.

M. S. Brown, D. E. Heard, and J. B. Jeffries, "Bandwidth Measurements of Amplified Spontaneous Emission," to be submitted to Applied Physics B.

M. S. Brown, D. E. Heard, D. R. Crosley, G. P. Smith, and J. B. Jeffries, "Laser-Induced Fluorescence Measurement and Model Calculation of Atomic Hydrogen and Oxygen Concentrations in Low-Pressure Flames," to be submitted to Combustion and Flame.

M. S. Brown, D. E. Heard, and J. B. Jeffries, "Amplified Spontaneous Emission as a Quantitative Diagnostic," to be submitted to Applied Physics B.

PRESENTATIONS

TASK 1

The following conference papers were presented on research supported by this contract.

D. L. Huestis, G. W. Faris, and J. B. Jeffries, "Novel Nonlinear Laser Diagnostic Techniques," Contractors Meeting in Propulsion (AFOSR/ONR), Atlanta, GA, June 11-15, 1990.

G. W. Faris and M. J. Dyer, "Multiphoton Spectroscopy Using Tunable VUV Radiation from a Raman-Shifted Excimer Laser," Paper TuA10, Short Wavelength Coherent Radiation: Generation and Application, OSA Topical Meeting, Monterey, CA, April 8-10, 1991.

G. W. Faris, M. J. Dyer, D. L. Huestis, and William K. Bischel, "Two-Photon Spectroscopy in the Vacuum Ultraviolet Using a Raman-Shifted ArF Excimer Laser," Paper QTuI5, Quantum Electronics and Laser Science Conference, Baltimore, MA, May 12-17, 1991.

G. W. Faris and M. J. Dyer, "Multiphoton Spectroscopy at 147 nm Using Two-Photon-Resonant Difference Frequency Mixing," Paper QTuI30, Quantum Electronics and Laser Science Conference, Anaheim, CA, May 12-14, 1992.

D. Huestis, G. Faris, and J. Jeffries, "Novel Nonlinear Laser Diagnostic Techniques," AFOSR Contractors Meeting in Propulsion, La Jolla, CA, June 15-19, 1992.

TASK 2

J. B. Jeffries, "Amplified Spontaneous Emission Velocity Measurements," Workshop on Diagnostics for Hermes Testing Facilities, Le Fauga, France, July 1990.

D. E. Heard and J. B. Jeffries, "Measurements of Atomic Hydrogen in Low-Pressure Flames," Western States Section, Combustion Institute, Boulder, CO, March 1991.

D. E. Heard and J. B. Jeffries, "Laser Excited Amplified Spontaneous Emission of Atomic Hydrogen in Low-Pressure Flames," Gordon Conference on the Physics and Chemistry of Laser Diagnostics in Combustion, Plymouth, NH, July 1991.

D. E. Heard and J. B. Jeffries, "Amplified Spontaneous Emission Measurements of Atomic Hydrogen in Low-Pressure Flames," VII International Laser Science Conference, Monterey, CA, September 1991 [Bull. Amer. Phys. Soc. **36**, 1950 (1991)].

D. E. Heard and J. B. Jeffries, "Laser-excited Amplified Spontaneous Emission of Atomic Hydrogen in Low-Pressure Flames," Annual Meeting of the Optical Society of America, San Jose, CA, November 1991.

D. E. Heard and J. B. Jeffries, "Laser Excited Amplified Spontaneous Emission of Atoms in Low-Pressure Flames," Optical Society of America, CLEO, May 1992.

M. S. Brown and J. B. Jeffries, "Investigation of Stimulated Emission as an Optical Diagnostic of Reacting Flows," International Laser Science Conference '92, Optical Society of America, Albuquerque, NM, September 1992.

J. B. Jeffries, D. E. Heard, and M. S. Brown, "Amplified Spontaneous Emission Measurements of Atomic Oxygen and Hydrogen," 31st AIAA Aerospace Sciences Meeting, Reno, NV, January 1993.

M. S. Brown and J. B. Jeffries, "Laser-Excited Amplified Spontaneous Emission,"Laser-Diagnostics Gordon Conference, Plymouth, NH, July, 1993.

M. S. Brown and J. B. Jeffries, "Measurements of Oxygen Atoms in Low-Pressure Flames Using Amplified Spontaneous Emission," Optical Society of America, Toronto, Canada, October, 1993.

TECHNICAL INTERACTIONS

We have served as informal advisors on aspects of the work supported by this contract in the following technical interactions.

TASK 1

AFOSR/ONR Contractors Meeting on Propulsion, June 11-15, 1990, Atlanta, Georgia.

Conversations with Dr. Bish Ganguli of Wright Research and Development Center on wide-ranging development of diagnostic techniques.

Conversations with Dr. H. F. Calcote of Aerochem, Princeton, NJ, on various subjects, including soot formation.

Conversations with Dr. Arthur Fontijn of Rensselaer Polytechnic Institute, Troy, NY, on Raman shifting an ArF excimer laser for detection of BF. (These discussions were followed by telephone conversations and written correspondence on the same subject from June through August 1990.)

Professor Karl Welge of the University of Bielefeld, Germany; visit to SRI International in August 1990 to discuss vuv generation from ArF lasers.

Dr. R. N. Compton of Oak Ridge National Laboratory; telephone conversation in September 1990 to discuss detection of F_2, especially by laser production of H_2^+.

Dr. Stefan Kroll of Lund Institute of Technology, Lund, Sweden; written correspondence in October 1990 on Raman shifting an ArF laser for excitation of doubly ionized sulfur.

Dr. Michael Smith of Arnold Air Force Base, TN; telephone conversations on October 4, 1990, and March 5, 1991, on polarization optimization for excimer lasers, frequency drift of narrowband ArF lasers.

Dr. Robert J. Gordon of the Department of Chemistry (M/C 111), University of Illinois at Chicago; written correspondence in November and December 1990 on two-photon detection of F and F_2.

The Conference on Short Wavelength Coherent Radiation: Generation and Application, April 8-10, 1991, Monterey, CA.

Conversations with Dr. Ken Baldwin of Australian National University, Canberra, Australia, on liquid nitrogen cooled Raman cells, Raman shifting of excimer lasers, two-photon-resonant four-wave difference frequency mixing.

Conversations with Dr. P. B. Corkum of the National Research Council of Canada on two-photon-resonant four-wave difference frequency mixing.

Bernd Nikolaus, Lamda Physik; conversation at SRI International in April 1991 on second anti-Stokes Raman shifting of ArF lasers for clients at Aerodyne interested in imaging at 160-170 nm.

Drs. Richard Miles and Walter Lempert of Princeton University, Princeton, NJ; conversations on Raman shifting, at the Quantum Electronics and Laser Science Conference, Baltimore, MD, May 12-17, 1991.

Professor Terry Cool of Cornell University; visit to SRI International on November 4, 1991, discussed generation of high power vuv for trace analysis.

Professor Edward Eyler of the Department of Physics and Astronomy, the University of Delaware, telephone conversation on high power vuv for basic physics measurements.

Masayuki Katehara, Keio University, Japan, visit to SRI International, May 19, 1992, discussions on spectroscopy of molecular fluorine.

Michael Casassa, NIST, Gaithersburg, MD, telephone conversation on June 1, 1992 on F_2 operation using excimer laser systems.

Conference on Lasers and Electro-Optics and Quantum Electronic and Laser Science Conference, May, 1992, in Anaheim, California

Conversations with Masayuki Katehara, Keio University, Japan, on vuv lasers.

Conversations with Professor Edward Eyler of the University of Delaware on vuv generation and techniques.

Conversations with Bruce Hudson of the University of Oregon on high power vuv for electronic Raman scattering.

AFOSR Contractors Meeting in Propulsion, June, 1992, La Jolla, California

Conversation with Dr. Bish Ganguly of Wright-Patterson on AFB ion detection and interactions.

Conversation with Professor Robert Pitz of Vanderbilt University on nonlinear optical diagnostic techniques.

Conversation with Dr. H. F. Calcote of Aerochem Research Laboratories on ion interactions and soot formation.

Conversation with Professor John Daily of the University of Colorado on coherent transient diagnostic techniques.

Scott Meier, NASA Ames; visit to SRI on October 30, 1992 and several telephone conversations, discussed generation of 130 nm by Raman shifting a KrF laser with a liquid nitrogen cooled Raman cell.

Dr. Nicolo Omenetto, ISPRA, Italy; June-July 1993, written correspondence on multiphoton diagnostics.

AFOSR Contractor's Meeting, Atlantic City, NJ, (1993).

Discussions with Art Fontjin (Rensselaer) about chemical reactions

Discussions with Tim Edwards (Wright-Patterson AFB) and Doug Talley (Edwards) about superartificial combustion and mixing diagnostics

Discussions with Bob Santoro (Pennsylvania State) about H-atom detection

TASK 2

The principles of ASE were discussed with numerous visitors to SRI during the past year and with many colleagues at several conferences. The most notable interactions are summarized below.

AFOSR Contractor's Meeting, June 1990

Presentation of new ideas for laser-excited ASE diagnostics during the workshop "Turbulent Reacting Flow," chaired by Dr. Werner Dahm.

Numerous conversations with other Air Force contractors.

Workshop on Diagnostics for Hermes Testing Facilities, July 1990, Le Fauga, France.

Invited presentation discussing the use of ASE as a velocity measurement.

Because the workshop was hosted by Dr. Jean-Pierre Taran of ONERA in Chatillon, France, and was held at the F4 flow facility at Le Fauga, France, there was an opportunity to inspect a large scale test facility and gain a better understanding of the practical difficulties in making optical diagnostic measurements on hypersonic flows.

Other speakers at the workshop included researchers from DLR in Stuttgart and Göttingen, Germany; Stanford University; and Sandia National Laboratory.

Visits with Air Force Personnel

David Weaver of Phillips Laboratory, Edwards AFB; significant discussions at 1990 Air Force Contractor's Meeting, subsequent telephone conversations, and contact at both the Fall and Spring Meetings of the Western States Section of the Combustion Institute.

Allan Garscadden, Aero Propulsion and Power Laboratory, Wright Patterson AFB; thorough discussion of ASE work during his May 1991 visit to SRI International.

W. M. Roquemore and Tim Edwards, Aero Propulsion and Power Laboratory, Wright Patterson AFB; discussions at both the 1990 and 1991 Air Force Contractors Meetings.

Ingrid Wysong, Dayton Research Contractor, Phillips Laboratory, Edwards AFB; significant discussions on ASE and energy transfer work completed when Dr. Wysong was a postdoctoral fellow in the SRI group.

Numerous discussions with other Air Force contractors, including substantive discussions and/or laboratory visits with Hanson and Bowman at Stanford, Winter at UTRC, Branch at Colorado, and Long at Yale.

Laboratory visits on the subject of supersonic fluid flow with McKenzie at NASA Ames; Taran, Pealat, and Attal-Tretout at ONERA at Le Fauga and Chatillon, France; and Cattolica, Sandia National Laboratory.

Gordon Conference, July 1991

A lengthy discussion was conducted on the problems for quantitative ASE with Dr. Marcus Alden and Dr. Ulf Westblom from Lund Institute of Technology, Dr. John Goldsmith of Sandia National Laboratory, and Dr. Katharina Kohse-Höinghaus of DLR. All these scientists have ongoing research on various aspects of ASE.

International Laser Science Conference, September 1991

ASE was again the subject of lengthy discussions with Dr. Ingrid Wysong from Phillips Laboratory, Dr. Andrew Sappey from Los Alamos, Dr. Mark Crofton from Aerospace, and Dr. Robert Lucht from Sandia National Laboratory.

Annual Meeting of the Optical Society of America, November 1991

Discussions on ASE with Dr. Terry Cool of Cornell, Dr. Rosario Sausa and Dr. Andrzej Miziolek of the U.S. Army Ballistics Research Laboratory.

OSA topical meeting on laser applications to chemical analysis, January 1992

ASE was again discussed with Dr. Alan Eckbreth of UTRC, Dr. Westblom of Lund, and Dr. Miziolek of BRL.

CLEO, May 1992

New results with ASE on atomic oxygen were discussed at length with Dr. Robert Lucht and Dr. John Goldsmith of Sandia National Laboratory.

AFOSR Contractors Meeting, June 1992

Numerous conversations concerning ASE were held with fellow contractors, especially Ingrid Wysong and David Weaver of Phillips Laboratory.

Wright-Patterson AFB, October 1992, panel member for the workshop on plume signatures

Conversations about ASE were held with Dr. Bish Ganguli, Dr. Richard Miller of ONR, and Dr. David Mann of ARO.

AFOSR Contractors Meeting, June 1993

Numerous conversations on optical diagnostics were conducted with fellow contractors.

INVENTIONS

TASK 1

The following invention disclosure was prepared on an invention developed under this contract:

- Multi-gas Calibration of an ArF Laser. Inventors: G. W. Faris and M. J. Dyer

TASK 2

The following discoveries were made:

- We discovered that, even with substantial ASE signals, the ASE bandwidth is not significantly gain narrowed if a short gain length is used. This feature makes ASE gas temperature measurements feasible.

- The ASE bandwidth measurement shows that ASE Doppler shift measurements of subsonic/hypersonic gas velocities are possible.

Both these discoveries must be reduced to practice before filing for a patent. This research is a significant part of our renewal proposal.

Appendix A

MULTIPHOTON SPECTROSCOPY USING TUNABLE VUV RADIATION FROM A RAMAN-SHIFTED EXCIMER LASER

Multiphoton Spectroscopy Using Tunable VUV Radiation from a Raman-Shifted Excimer Laser

Gregory W. Faris and Mark J. Dyer

Molecular Physics Laboratory, SRI International, 333 Ravenswood Avenue, Menlo Park, California 94025

Abstract

Raman shifting an ArF excimer laser in D_2 and HD, and applications to two-photon spectroscopy in the vuv and near-vuv are described. Preliminary results on generation of vuv by two-photon-resonant difference-frequency mixing of an ArF laser and frequency-doubled dye laser are reported.

Multiphoton spectroscopy has proved to be a valuable technique at visible and uv wavelengths, allowing access to high-lying states and the excitation of transitions not allowed for one photon excitation. Using vuv radiation for multiphoton excitation allows probing even higher states, but high powers are required to obtain reasonable signals. Two-photon excitation with vuv radiation has been performed using tunable excimer laser radiation[1] and by Raman-shifting a frequency-doubled dye laser.[2]

We are using the technique of Raman-shifting a tunable ArF excimer laser for the production of high powers in the vuv. Raman-shifting can provide relatively high efficiency for frequency conversion compared to non-resonant four-wave-mixing techniques. By Raman shifting an ArF laser, which provides high energy radiation tunable around 193.4 nm, anti-Stokes orders in the vuv can be obtained with low order Raman shifts. This allows high powers and lower power fluctuations than when using higher order Raman shifting. Raman shifting an ArF laser in H_2 for production of vuv radiation has been reported previously.[3] We have investigated Raman shifting in D_2 and HD. The use of different isotopes of hydrogen for Raman shifting allows greater spectral coverage, compensating in part for the limited tuning range of the ArF laser.

The apparatus used for our experiments is shown in Figure 1. The laser is a Lambda Physik EMG 150 dual discharge laser. Because the laser mode quality is very important for multi-wave mixing, we have made a number of modifications to the laser. The laser is operated as an oscillator triple-pass amplifier instead of an injection-locked amplifier. The output from the oscillator is passed through a spatial filter, which also magnifies the beam. The beam is then passed through the amplifier discharge in a vertical zigzag path, saturating the amplifier on the last pass. Optimum energies of over 60 mJ have been obtained through pressure optimization of the oscillator and amplifier discharge timing. We have found that depolarization of the beam can be reduced by careful alignment of the excimer laser's MgF_2

Proceedings on Short-Wavelength Coherent Radiation, 58
Vol. 11, Philip H. Bucksbaum and Natale M. Ceglio (eds.)

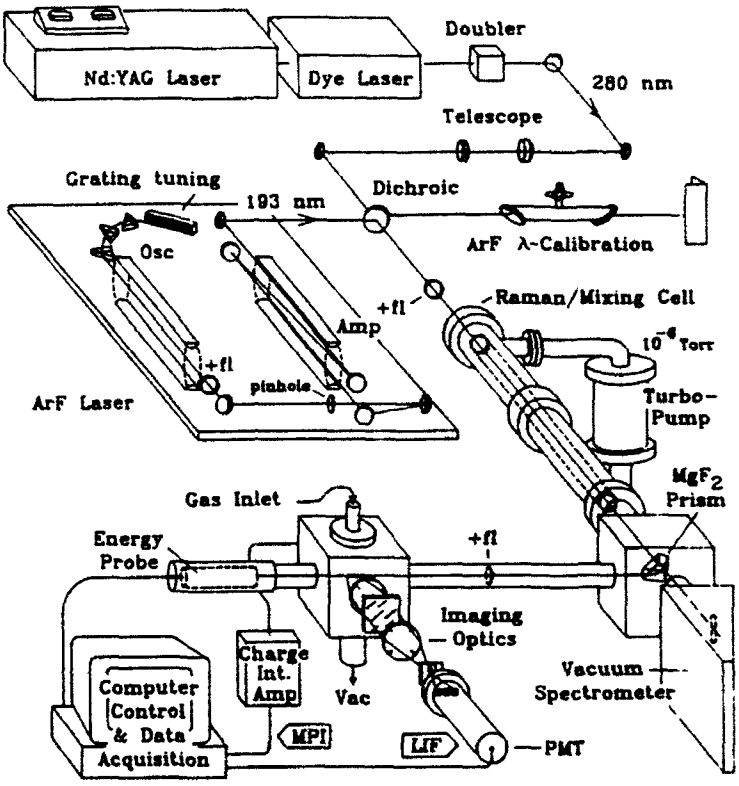

Figure 1. Experimental arrangement for multiphoton excitation using a Raman-shifted using a Raman-shifted excimer laser.

windows. This is performed by passing polarized light at 193 nm through the windows and rotating and tightening them to minimize the depolarization. Polarization of 200:1 has been obtained and the pulse-to-pulse amplitude stability is improved.

The laser is focused into a cell containing HD or D_2. To minimize absorption from the oxygen Schumann Runge bands, almost the entire beam path up to the cell is either evacuated or purged with argon. Because of the low Raman gain coefficient in HD, the Raman cell is cooled to liquid nitrogen temperature. This cooling increases the gain through redistribution of the HD ground state population, reduction of the Raman linewidth, and reduction of losses as impurities are frozen out. The Raman cell and surrounding iiquid nitrogen jacket are contained in a vacuum for insulation and to avoid condensation on the cell windows. The different Raman orders exiting the Raman cell are separated using a MgF_2 prism.

Raman shifting in D_2 at room temperature, we have observed at least eight anti-Stokes orders (to 132 nm) and five Stokes orders. Up to 60% conversion into the first Stokes has

been obtained. In HD at room temperature, 10% conversion into the first Stokes, and low order anti-Stokes were seen. At liquid nitrogen temperature, four anti-Stokes and four Stokes orders have been observed using HD. Competition from rotational Raman scattering and phase matching effects lead to a well defined maximum density for anti-Stokes conversion. By optimizing the second anti-Stokes radiation in HD, we have obtained 1 mJ at 170 nm at a density of 3 amagat.

We have applied the Raman-shifted source to two-photon-resonant excitation of a number of states. Detection is through ions produced by absorption of a third photon. Using the first Stokes radiation in D_2 at about 205 nm, we have excited the $^1\Pi_g$ (v' = 3) state of F_2 from the ground X $^1\Sigma_g^+$ state. This is the central spectrum shown in Figure 2. The band heads correspond to the O and P branches. The top profile in the figure is the power of the first Stokes radiation. The dips in the power are due to Schumann Runge absorption of the fundamental ArF beam in the small length of beam path that is not purged. The bottom trace in the figure is a calibration spectrum for the fundamental ArF beam. It is obtained in a cell containing a mixture of H_2, HD, and krypton, all of which have two-photon resonances within the ArF tuning range. The accuracy of the calibration is limited by the ac Stark effect. We have also observed single lines for two-photon excitation of F atoms and H_2. Using radiation at about 169.67 nm produced as the second anti-Stokes line of ArF in HD we have excited the $^2D^o_{3/2}$ state in atomic fluorine from the $^2P^o_{3/2}$ ground state. A single rotational level of the H,$\bar{H}$ $^1\Sigma_g^+$ has been excited using two photons at about 173.53 nm produced as second anti-Stokes radiation using D_2.

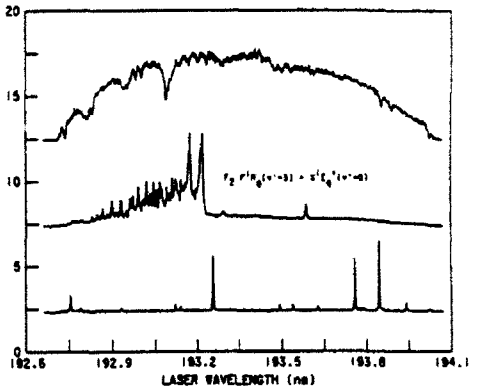

Figure 2. Two-photon resonant spectrum for excitation of the $^1\Pi_g$ (v' = 3) state of F_2. The x axis denotes the fundamental wavelength of the ArF laser.

Through understanding of the Raman process and optimization of the laser beam quality, Raman shifting an ArF excimer laser can provide large energies in the vuv even when shifting in D_2 and HD. The generated vuv power is more than adequate for two-photon spectroscopy.

To produce continuously tunable vuv radiation, we have begun to examine the capabilities of the ArF laser for two-photon-resonant difference frequency generation in krypton. By combining two ArF photons at ω_1 with a photon from a tunable laser at ω_T, vuv photons may be generated through the difference-frequency process

$$\omega_{vuv} = 2\omega_1 - \omega_T.$$

When the two photons at ω_1 lie near a resonance, this process is efficient, as has been shown for the 5p[5/2,2] $\leftarrow$ $4p^6\ ^1S_o$ (Ref 4) and 5p[1/2,0] $\leftarrow$ $4p^6\ ^1S_o$ (Ref 5) resonances. Two-photon resonances for the 6p $\leftarrow$ $4p^6\ ^1S_o$ transitions in krypton lie within the tuning

range of the ArF laser. The high peak powers and good mode quality of the ArF make vuv generation using this technique attractive.

The apparatus for these experiments is also shown in Figure 1. A Nd:YAG-pumped frequency-doubled dye laser is used as the tunable laser. The pulse timing of two lasers is synchronized and they are overlapped using a dichroic mirror. A 1 m lens focuses the two beams into a cell containing krypton. The generated vuv is filtered with a vuv monochomator and detected with a solar blind photomultiplier. Light at 147 nm has been generated. The pressure dependence of the vuv radiation is shown in Figure 3. The optimum pressure is about 60 torr. By varying the input intensities, it is determined that both beams are saturating at the input energies of 6 mJ and 20 mJ for the ArF and frequency-doubled dye lasers, respectively. Experiments to measure the linewidth and energy of the vuv are in progress.

This work was supported by the AFOSR under contracts F49620-88-K-0003 and F49620-90-C-0044.

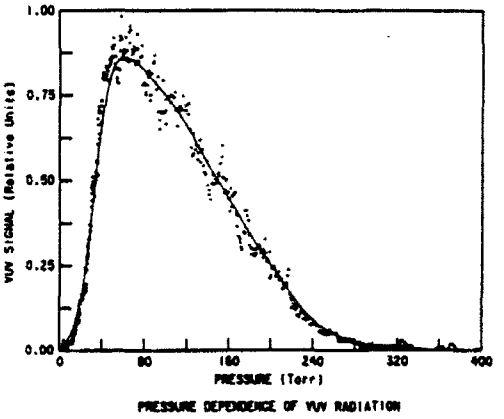

Figure 3. Pressure dependence of vuv radiation.

References

1. D. J. Kligler, J. Bokor, and C. K. Rhodes, "Collisional and Radiative Properties of the H_2 E,F $^1\Sigma_g^+$ State," Phys. Rev. A 21, 607-617 (1980).
2. G. C. Herring, M. J. Dyer, L. E. Jusinski, and W. K. Bischel, "Two-Photon-Excited Fluorescence Spectroscopy of Atomic Fluorine at 170 nm," Opt. Lett. 13, 360-362 (1988).
3. H. F. Döbele and B. Rückle, "Application of a Argon-Fluoride Laser System to the Generation of VUV Radiation by Stimulated Raman Scattering," Appl. Opt. 23, 1040-1043 (1984).
4. G. Hilber, A. Lago, and R. Wallenstein, "Broadly Tunable Vacuum-Ultraviolet/Extreme-Ultraviolet Radiation Generated by Resonant Third-Order Frequency Conversion in Krypton," J. Opt. Soc. Am. B, 4, 1753-1764 (1987).
5. J. P. Marangos, N. Shen, H. Ma, M. H. R. Hutchinson, and J. P. Connerade, "Broadly Tunable Vacuum-Ultraviolet Radiation Source Employing Resonant Enhanced Sum-Difference Frequency Mixing in Krypton," J. Opt. Soc. Am. B 7, 1254-1259 (1990).

Appendix B

TWO-PHOTON SPECTROSCOPY OF THE F $^1\Pi_g$ AND F $^3\Pi_g$ STATES OF MOLECULAR FLUORINE

Two-photon spectroscopy of the $F\ ^1\Pi_g$ and $f\ ^3\Pi_g$ states of molecular fluorine

Gregory W. Faris, Mark J. Dyer, David L. Huestis, and William K. Bischel
Molecular Physics Laboratory, SRI International, Menlo Park, California 94025

(Received 12 May 1992; accepted 21 July 1992)

We report what is to our knowledge the first two-photon excitation spectroscopy of molecular fluorine. The $F\ ^1\Pi_g$ and $f\ ^3\Pi_g$ states are excited with two photons in the range of 206–212 nm. Detection is through vacuum ultraviolet (VUV) fluorescence or ionization. Measurement of the fluorescence spectrum with a VUV spectrometer indicates that the VUV fluorescence occurs on the 157 nm F_2 laser transition frequency. Using our spectra and the data of Porter [J. Chem. Phys. 48, 2071 (1968)] we report improved spectroscopic constants for vibrational levels in the F, f, and $I\ ^1\Sigma_u^+$ states.

INTRODUCTION

The spectroscopy of molecular fluorine is not well known, partly because of the high ionization potential of this molecule. The lowest known bound state that can be reached in a spin-allowed transition from the ground state is the $F\ ^1\Pi_g$ state at $\sim 94\,000\ cm^{-1}$ above the $X\ ^1\Sigma_g^+$ ground state. Thus, much of the spectroscopy on the bound excited states of F_2 has been performed using vacuum ultraviolet (VUV) absorption spectroscopy[1–5] or emission spectroscopy.[6–9] The $F\ ^1\Pi_g$ state is not accessible in an electric-dipole-allowed transition from the ground state. This state and the nearby $f\ ^3\Pi_g$ state have been observed in emission spectroscopy from the $I\ ^1\Sigma_u^+$ state,[6–9] as well as by electron impact spectroscopy.[10–13] The $F\ ^1\Pi_g$ state can, however, be reached in a two-photon excitation from the ground state. Multiphoton excitation allows laser spectroscopy of the high-lying states in F_2, as was reported in a study of the 3+1 resonantly enhanced multiphoton ionization (REMPI) excitation of the $H\ ^1\Sigma_u$ and $h\ ^3\Sigma_{1,u}$ states of F_2.[14] In our studies of F_2, the vibrational levels $v'=0,1,2$ of the $F\ ^1\Pi_g$ state and $v'=3$ of the $f\ ^3\Pi_g$ state are excited from the ground $X\ ^1\Sigma_g^+$ state by two photons and detected by VUV fluorescence or by ionization through a third photon.

Some calculated potential energy curves for F_2 are given in Fig. 1. The ground state is taken from Colbourn,[5] the two lower excited states are taken from Cartwright and Hay,[15] and the two upper states are taken from Sakai *et al.*[16] The upper states have been lowered from the position given by Sakai *et al.* by 5000 cm^{-1} to give the proper energy spacing for the $F\ ^1\Pi_g \leftarrow X\ ^1\Sigma_g^+$ and $f\ ^3\Pi_g \leftarrow X\ ^1\Sigma_g^+$ transitions. The line approaching the f-state potential is the Coulomb attraction arising from the $F^+(^3P)+F^-(^1S)$ ion pair limit,[5] which the f state should approach for large internuclear separation.[15] The 157 nm F_2 laser transition is believed to arise from a transition from the outer well of the $f\ ^3\Pi_g$ state to a weakly bound $^3\Pi_u$ state, and some experimental evidence supports this.[13] When the potential curve of Sakai *et al.* for the $f\ ^3\Pi_g$ state is shifted down to give the proper energy spacing relative to the inner well, the outer well is still too high compared to the 157 nm transition to the lower state, shown in Fig. 1. It is not clear whether the assignment of the laser transition or the relationship between the inner and outer wells is incorrect.

EXPERIMENT

The experimental arrangement for two-photon excitation of F_2 is shown in Fig. 2. For most of the experiments, an excimer-pumped dye laser (Lambda Physik EMG102 and FL3002) is used with 2-(4-biphenyl)-6-phenylbenzoxatol-1,3 (PBBO) as the dye, producing ~6 mJ at 414 nm. This light is frequency doubled in a β-BaB_2O_4 (BBO) crystal to give ~200 μJ at 207 nm. For some of the early measurements, including excitation of $v'=0$ and 1 of the $F\ ^1\Pi_g$ state, light was produced by Raman-shifting the frequency-doubled output from a Nd:YAG-pumped dye laser in H_2 and using the third anti-Stokes radiation. The laser light is focused with a lens of focal length from 5 to 35 cm into a stainless steel cell containing a mixture of either 5% or 10% fluorine in helium. The fluorine–helium mixture is flowed slowly through the cell to maintain passivation. Ions are detected with a single electrode biased at 100 V relative to the cell. The ion signals are amplified with an Ortec model 142 PC charge-integrating preamplifier.

Fluorescence is collected with a 5 cm MgF_2 lens and focused with a 25 cm MgF_2 lens onto the slits of a vacuum monochromator (SPEX 1500SP). The fluorescence is detected with a CsI solar blind photomultiplier (EMI model 542G-08-18). The positions of the lenses are set to image the focal volume of the laser onto the slits, which enhances the contrast between the fluorescence and the scattered laser light in the cell and matches the solid angle of the fluorescence to the f/number of the spectrometer. For the measurement of excitation spectra, the vacuum monochromator was not used. One set of slits (removed from the vacuum monochromator) was placed at the image of the second lens, and the photomultiplier was placed directly behind the slits. In all cases, it was necessary to evacuate the entire fluorescence optical path to detect the fluorescence. The linewidths of the F_2 spectra are 1.5 cm^{-1} when using direct frequency doubling to the excitation wavelength and 2.5 cm^{-1} when Raman-shifting.

 0021-9606/92/B-1 4-06$006.00

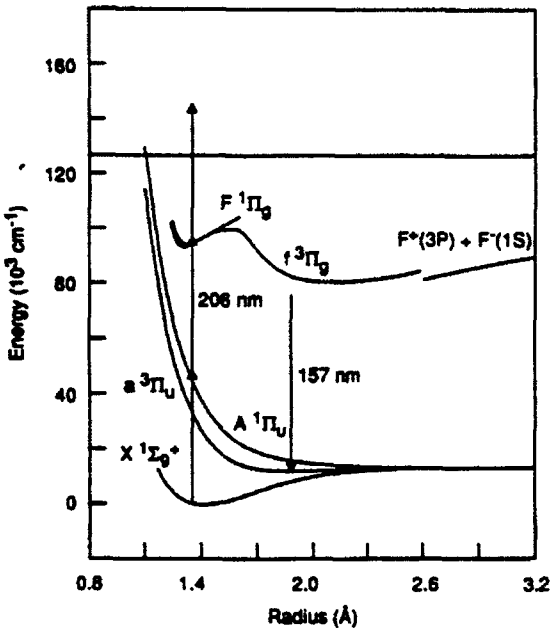

FIG. 1. Calculated potential curves of some states in F_2 [from Colbourn (Ref. 5), Cartwright and Hay (Ref. 15), and Sakai *et al.* (Ref. 16)].

The 207 nm light that passes through the cell passes either through a calibration cell containing NO or onto a pyroelectric energy meter. The 1+1 REMPI signal from the $B\ ^2\Pi \leftarrow X\ ^2\Pi$ (3,0) β band in NO is used as a wavelength calibration. The line positions of this band have been measured[17] to an accuracy of 0.05 cm^{-1} relative to known iodine line positions,[18] and provide a wavelength calibration for the present measurements over the entire range for spectra of the $F\ ^1\Pi_g(v'=2)$ and $f\ ^3\Pi_g(v'=3)$ levels.

Because of the high intensities required for two-photon spectroscopy, the ac Stark effect can perturb the level positions significantly. By comparing data on the $F\ (v'=2)$ state using a 35 and 5 cm lens, in both cases calibrated against the NO (3,0) β band, the discrepancy in line positions is found to be <0.1 cm^{-1}. Based on these measurements we can set an upper bound for the ac Stark effect for that state of ~ 1 GHz/(GW/cm^2). Our measurements of the energy spacing between the $F\ (v'=2)$ and $f\ (v'=3)$ levels agree with the previous measurements of Porter[9] to 0.01 cm^{-1} (this close agreement is happenstance; our absolute accuracy, as discussed below, is 0.2 cm^{-1}), indicating that ac Stark shifts for our measurements on the f state are not significant either.

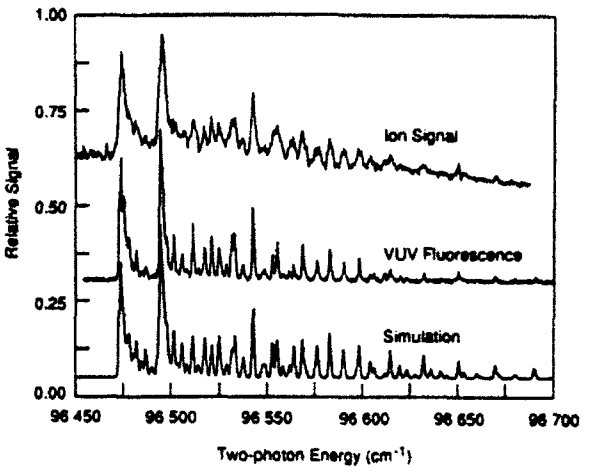

FIG. 3. $F_2\ F\ ^1\Pi_g(v'=2) - X\ ^1\Sigma_g^+(v''=0)$ two-photon spectra. Fluorescence is detected for wavelengths between ~120 and 180 nm.

Based upon the vibrational band head energies for the $F\ ^1\Pi_g$ state given by Colbourn,[5] we initially attempted two-photon excitation of the $v'=0$ level. An ion spectrum at poor signal to noise ratio resulted. It was anticipated that the Franck–Condon factor would improve for the higher vibrational levels of the $F\ ^1\Pi_g$ state. Excitation of the $v'=1$ level yielded somewhat better signal to noise ratio, but it was still not sufficient for rotational analysis. Excitation of $v'=2$ gave spectra of sufficient quality for rotational analysis. Based upon the previous demonstration of singlet to triplet multiphoton excitation in F_2 of the $h\ ^3\Sigma_{1,u}$ state,[14] we successfully attempted two-photon excitation of the $v'=3$ vibrational level of the $f\ ^3\Pi_g$ state.

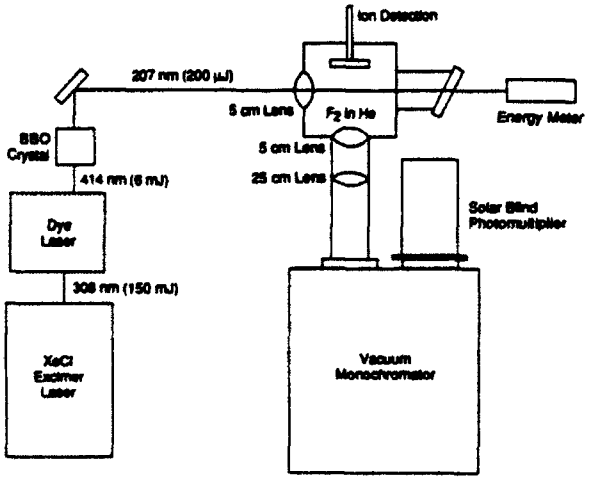

FIG. 2. Experimental arrangement for two-photon spectroscopy of F.

RESULTS AND DISCUSSION

Ionization and fluorescence excitation spectra of the $F\ ^1\Pi_g(v'=2)$ state are shown in Fig. 3. The ion spectra in Figs. 3 and 5 were taken with Raman-shifted radiation while the fluorescence spectra were taken with light generated by direct frequency doubling. This accounts for the difference in linewidth for the ion and fluorescence spectra. The bandwidth for fluorescence detection is determined by the transmission of the optics and the photomultiplier response, corresponding to between ~120–180 nm. The vibrational assignments for the $F\ ^1\Pi_g$ state used throughout this paper are those of Wang *et al.*,[11] based on electron energy loss spectroscopy. Five rotational branches ($\Delta J=0, \pm 1, \pm 2$) are expected for this two-photon transition. The

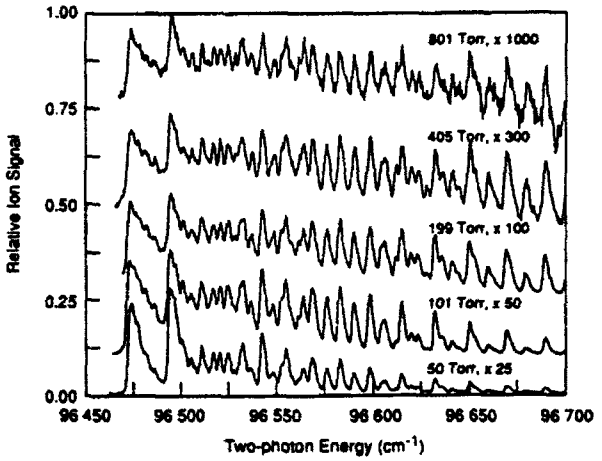

FIG. 4. F_2 $F\,^1\Pi_g(v'=2) \leftarrow X\,^1\Sigma_g^+(v''=0)$ MPI spectra as a function of pressure.

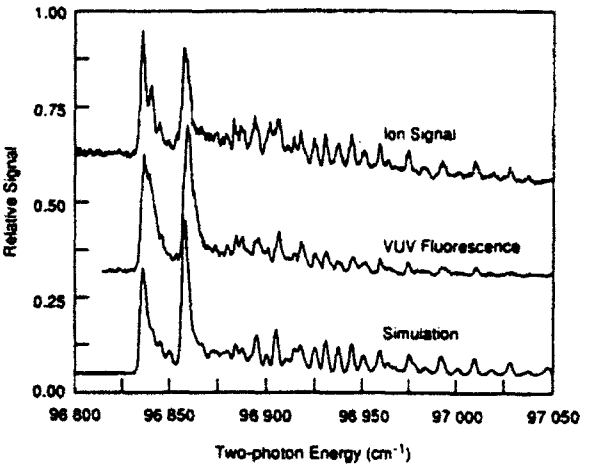

FIG. 5. F_2 $f\,^3\Pi_g(v'=3) \leftarrow X\,^1\Sigma_g^+(v''=0)$ two-photon spectra. Fluorescence is detected for wavelengths between ~120 and 180 nm.

O and *P* branches form heads, while the other three branches are degraded to the blue, indicating that the rotational constant of the upper state is greater than that of the ground state. Also shown in Fig. 3 is a spectral simulation. The line intensities are calculated from the two-photon Höni–London factors given by Halpern *et al.*,[19] while the rotational energies for the $X\,^1\Sigma_g$ ground state are calculated from the constants in Huber and Herzberg.[20] A room-temperature Boltzmann population is assumed. Line shapes are produced by convolving the line intensity spectrum with a Gaussion profile. The linewidth, vibrational band origin, and rotational constants for the upper $F\,^1\Pi_g$ state are used as fitting parameters to reproduce the observed band profile. Fitting has been performed using a nonlinear, least-squares, curve-fitting routine.[21] The agreement in structure between the theoretical and fluorescence spectra is good, but the intensities for the ion spectra do not match as well. The ion signal intensities depart dramatically from the theoretical intensities at higher pressures. This is shown in Fig. 4 where spectra are shown as a function of total pressure. The change in relative line intensities may be due to saturation of the detection efficiency due to space charge effects.

Figure 5 shows ionization and fluorescence excitation spectra for the transition $f\,^3\Pi_g(v'=3) \leftarrow X\,^1\Sigma_g^+(v''=0)$. The vibrational assignment used in this paper is that of Hoshiba *et al.*,[12] which they characterize as tentative. This assignment is supported by the energy spacing between the *F* and *f* states calculated by Sakai *et al.*[16] A simulation spectrum calculated in the same manner as for the *F* state is also shown in Fig. 5. The calculation does not take into account spin–orbit fine structure of the $f\,^3\Pi_g$ state. The agreement between the experimental and simulated spectra is not as good as for the singlet state, but the qualitative agreement suggests that the main source of transition probability is spin–orbit mixing of the $f\,^3\Pi_g(\Omega=1)$ spin component with the $F\,^1\Pi_g(\Omega=1)$ state.

The spectroscopic constants of the *F* and *f* states have been measured previously. The rotational constants *B* for vibrational levels 2–6 of the *F* state and level 3 of the *f* state have been determined by Porter[9] based on emission from the $I\,^1\Sigma_u^+$ state in 15 vibrational bands interconnecting $I(v'=0,1)$ with $F(v'=0\text{–}7)$ and $f(v''=3)$. Using the positions of the $I\,^1\Sigma_u^+$ state determined by extreme ultraviolet (XUV) absorption spectroscopy, together with band head positions given by Porter[9] and Colbourn *et al.*[5] have given approximate energies for the *F* and *f* states relative to the ground state. However, Porter does not report the centrifugal distortion constant, *D*, or vibrational band origins. For this reason, we have reexamined the spectroscopic constants for the *F* and *f* states based on our data and Porter's data.

For the determination of rotational constants, Porter's data are better than our two-photon data because of the larger number of rotational lines, narrower linewidths, and higher accuracy (0.05 cm^{-1} for the sharper band lines). We have used a line fitting program[22] to fit the line positions in each of the nine vibrational bands listed by Porter, using his assignments for the lines.[9] Porter does not give line positions for $I \rightarrow F$ emission to $v''=0$, 1, and 7 as the spectra were too broad, although he gives band head positions for $v''=0$ and $v''=1$. Note that these vibrational assignments for the *F* state differ from those of Porter due to the renumbering of Wang.[11] (Wang assigns the lowest observed vibrational level of the *F* state to $v=0$, which Porter had labeled $v=1$.) We have excluded a number of lines from the fit which appear to be perturbed. When calculated line positions differed from measured line positions by ~1 cm^{-1} or more in a manner consistent with perturbation of a single rotational level for all listed branches and bands coupling that level, lines connecting that level were excluded from the fit. The perturbed levels and the bands in which the perturbations were observed are listed in Table I. The results of the individual band fits are shown in Table II which gives values of the relative energy spacing, ν_0, rotational constants for the upper (B',D') and lower (B'',D'') levels, and the standard deviation of the residuals between the fit and the data, σ. Note that in some cases the uncer-

TABLE I. Perturbed levels for fits to data of Porter (Ref. 9).

State	v	Perturbed rotational levels	Bands where perturbations were observed
F	2	none	
F	3	none	
F	4	none	
F	5	13,14,21	$I \rightarrow F$ (0,5),(1,5)
F	6	14,20,21,25	$I \rightarrow F$ (0,6),(1,6)
f	3	4,5,8,9,39	$I \rightarrow f$ (0,3)
I	0	4,5,10,19,21,29	$I \rightarrow F$ (0,2),(0,3),(0,4),(0,5),(0,6); $I \rightarrow f$(0,3)
I	1	2,9,15	$I \rightarrow F$ (1,2),(1,5),(1,6)

tainty in the values is quite large. We do not recommend using the constants from the fits to individual bands, but rather the result from merging[23] the results from all of the bands to obtain a minimum-variance, linear, unbiased estimate of the relative energies and rotational constants in the F, f, and I states. The rotational constants B and D from the merge are listed in Table III. The merged results of the fit have an estimated variance of the residuals ($\hat{\sigma}^2_M$ in Ref. 23) of 0.914 for 22 degrees of freedom, indicating little or no systematic error[23] in Porter's band measurements. The constants B differ slightly from those Porter listed in some cases. The values for the levels $F(v'=2)$ and $f(v'=3)$ are comparable to what we find for our data determined either by least-squares fits of simulations to the experimental spectra or by measuring individual line positions and performing a conventional fit of the line positions. Note that for the I state, $B_1 > B_0$. This unusual situation and the irregular vibrational spacing in the I state are ascribed by Colbourn *et al.* to perturbation by a nearby state. To find the energies of the F, f, and I levels relative to $X\,^1\Sigma_g^+$ ($v=0, J=0$) we have fitted theoretical spectra to our experimental data with the rotational constants B and D fixed to the values given in Table III. Five fluorescence-excitation spectra and four ion-excitation spectra were fitted to data for the F ($v=2$) and f ($v=3$) states, respectively. The fluorescence excitation spectra tended to give better matches to the line intensities, but no absolute wavelength calibration of the excitation spectra was performed for the $f(v=3) \leftarrow X$ transition. The values found from these fits are given in Table III.

TABLE III. Vibrational energy levels and rotational constants for several levels of the F, F, and I states.

State	v	v_0 (cm^{-1})	B (cm^{-1})	$D \times 10^6$ (cm^{-1})
F	2	96 501.51(20)[a]	1.0102(07)	3.67(33)
F	3	97 563.11(22)	0.9981(07)	3.72(35)
F	4	98 604.84(29)	0.9858(09)	3.67(44)
F	5	99 627.67(22)	0.9734(08)	3.33(45)
F	6	100 632.70(23)	0.9605(10)	2.81(79)
f	3	96 864.58(23)	1.0029(07)	4.53(36)
I	0	113 939.64(21)	0.8010(07)	1.95(33)
I	1	115 048.94(21)	0.8117(08)	2.89(44)

[a]Single standard deviation errors in the last two digits of each value are given in parentheses. The errors in the band origins are the square root of the sum of the squared errors of the band positions relative to the $F(v=2)$ state from the merged fit and the error in the position of the $F(v=2)$ state (0.2 cm^{-1}).

We place an absolute accuracy of 0.20 cm^{-1} on our determination of the vibrational energy of the F ($v=2$) state. This is a relatively small fraction of the linewidth for the spectra, which is 1.5 cm^{-1}, but comparison of fits to different data sets and fits to each half of each spectrum give results consistent to better than the 0.2 cm^{-1} accuracy. When the theoretical simulation follows the experimental data well, fitting the entire spectrum gives significantly better accuracy than fitting a single line. As mentioned above, the energy spacing between the F ($v'=2$) and f ($v'=3$) levels from the fits to the two-photon spectra agree with Porter's data to 0.01 cm^{-1}.

Vibrational energy differences found from fitting Porter's data are used together with our determination of the absolute energy of the F ($v=2$) state to find absolute vibrational energies for the $v=0$ and 1 levels of the I state, given in Table III. These values for the vibrational band origins of the $v=0$ and 1 levels are 0.2 and 0.6 cm^{-1} lower, respectively, than those of Colbourn *et al.*[5] and 0.3 cm^{-1} lower than those of Di Lonardo and Douglas.[4] Colbourn *et al.* give an upper bound on the absolute accuracy of their measurements of 0.5 cm^{-1}. Di Lonardo and Douglas do not give estimated errors. Our measurements, with an accuracy of 0.2 cm^{-1}, are consistent with these other measurements.

The emission spectra obtained through excitation of

TABLE II. Constants from individual band fits to data of porter (Ref. 9).

State	v_0 (cm^{-1})	B' (cm^{-1})	$D' \times 10^6$ (cm^{-1})	B'' (cm^{-1})	$D'' \times 10^6$ (cm^{-1})	σ (cm^{-1})
$I \rightarrow F(0,2)$	17 438.09(06)[a]	0.8004(16)	1.81(67)	1.0096(16)	3.54(66)	0.244
$I \rightarrow F(0,3)$	16 376.53(08)	0.7995(20)	1.34(82)	0.9966(20)	3.12(82)	0.302
$I \rightarrow F(0,4)$	15 334.81(21)	0.8035(49)	2.72(207)	0.9883(49)	4.43(202)	0.445
$I \rightarrow F(0,5)$	14 312.06(14)	0.7979(47)	−0.22(290)	0.9702(47)	1.14(290)	0.434
$I \rightarrow F(0,6)$	13 307.15(26)	0.7985(107)	0.07(1460)	0.9586(116)	2.30(1715)	0.530
$I \rightarrow F(1,2)$	18 547.45(05)	0.8135(18)	4.40(141)	1.0121(18)	5.18(137)	0.172
$I \rightarrow F(1,5)$	15 421.13(14)	0.8130(56)	0.38(945)	0.9730(50)	−2.68(850)	0.262
$I \rightarrow F(1,6)$	14 416.21(12)	0.8090(44)	1.80(344)	0.9579(45)	1.81(353)	0.363
$I \rightarrow f(0,3)$	17 075.06(10)	0.8007(22)	1.74(94)	1.0026(22)	4.33(94)	0.312

[a]Single standard deviation errors in the least significant digits are given in parentheses.

B-4

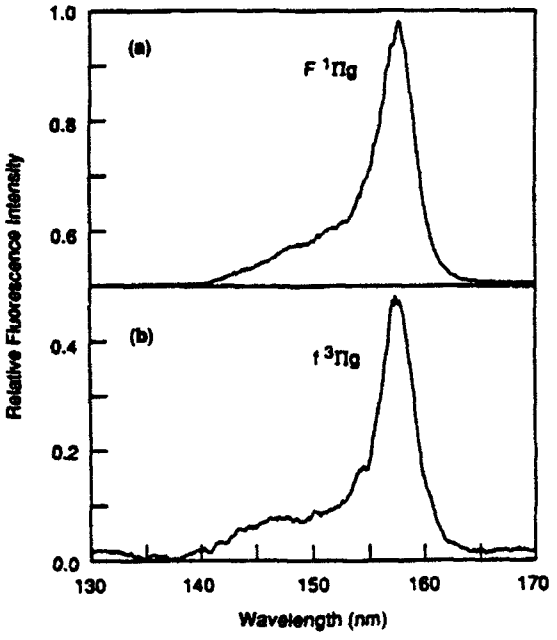

FIG. 6. VUV emission on excitation of the F_2 $F\,^1\Pi_g(v'=2)$ (a) and F_2 $f\,^3\Pi_g(v'=3)$ (b) states. Excitation is performed near the peak of the P branch; $\sim 96\,495$ cm^{-1} for (a) and $\sim 96\,858$ cm^{-1} for (b).

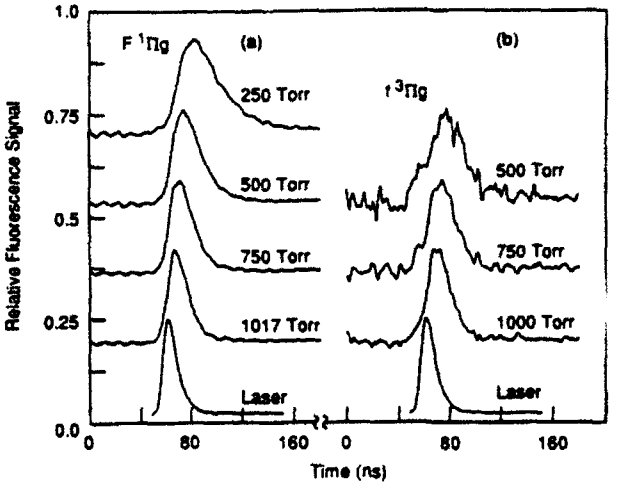

FIG. 7. Pressure dependence of the fluorescence signal from the F_2 $F\,^1\Pi_g(v'=2)$ (a) and F_2 $f\,^3\Pi_g(v'=3)$ (b) states. Excitation is at $\sim 96\,495$ cm^{-1} for (a) and $\sim 96\,858$ cm^{-1} for (b). Fluorescence is collected between ~ 120 and 180 nm.

$v'=2$ of the $F\,^1\Pi_g$ state and $v'=3$ of the $f\,^3\Pi_g$ state and detection through the vacuum spectrometer are shown in Fig. 6. These spectra agree very well with those observed in electron-excited F_2–rare gas mixtures.[24,25] The fluorescence for the $F\,^1\Pi_g$ state follows a third power of the laser power, indicating that population of the upper level for the fluorescence transition is probably occurring through ionization of F_2. This conclusion is supported by an increase in the fluorescence signal as the He partial pressure is increased, and by the time dependence of the fluorescence signal, which is shown in Fig. 7 for the $F\,^1\Pi_g(v'=2)$ and $f\,^3\Pi_g(v'=3)$ states for various total pressures. The peak fluorescence signal is always delayed with respect to the laser pulse, the delay increasing as the total pressure in the cell decreases (for a fixed F_2/He ratio). This might be interpreted as being due to slowing of the possible excitation processes

$$F_2+3h\nu \rightarrow F_2^+ + e,$$
$$e+F_2 \rightarrow F^- + F,$$
$$F^- + F_2^+ \rightarrow F_2^* + F,$$
or
$$F_2+3h\nu \rightarrow F^* + F,$$
$$F^* + F_2 \rightarrow F_2^* + F,$$
or
$$F_2+3h\nu \rightarrow F^+ + F^-,$$
$$F^+ + F^- + M \rightarrow F_2^* + M. \qquad \text{B-5}$$

We have compared relative signal strengths for the singlet F and triplet f states. When ion and fluorescence spectra for both states are normalized for the expected third-order laser power dependence for $2+1$ multiphoton ionization, the triplet excitation signal is a factor of ~ 2 smaller for fluorescence detection, and ~ 10 times smaller for ion detection. This corresponds to a surprisingly large transition probability for the singlet to triplet transition. As mentioned, the fluorescence intensity from the $F\,^1\Pi_g$ state follows the third power of the laser intensity. While we have not investigated the intensity dependence of the triplet fluorescence, the relative-intensity comparison suggests that a significant part of the $f\,^3\Pi_g$ fluorescence may come from directly excited levels (and should follow a quadratic power dependence). Because the fluorescence and ion signal comparison were measured at different total pressures (500 Torr for fluorescence and 10 Torr for ion signals), it is possible that other effects are responsible for the larger relative size of the triplet fluorescence signal. There appears to be some difference in the time dependence of the fluorescence signals for the F and f states shown in Fig. 7, particularly at 500 Torr total pressure. However, the signal to noise ratio for the f-state fluorescence is too poor to draw conclusions concerning differences between F and f-state excitation on the population of the fluorescing level. More study is required to definitively determine the mechanism for population transfer for fluorescence on excitation of the $f\,^3\Pi_g$ state.

Two-photon excitation of F_2 opens new opportunities for study of the spectroscopy and kinetics of F_2. There is still much to be learned about the F and f states. Only a single vibrational level of the f state has been observed optically ($v=3$). A frequency-tripled Nd:YAG-pumped narrow band dye laser would provide both high power and high resolution for further study of the F and f states. The two-photon excitation scheme also allows detection of

ground state F_2. We have recently performed two-photon excitation of the F ($v'=3$) state by using the first Stokes radiation produced by Raman shifting a tunable ArF excimer in D_2.[26] Tens of millijoules can be produced through this Raman-shifting process, allowing improvement in the efficiency for the production of excited F_2. Excitation with a second laser allows probing higher-lying states of F_2, making possible detailed spectroscopy as well as lifetime, quenching, and other kinetic measurements of these states. Only limited information on collisional kinetics of the excited states of F_2 is so far available,[25,27] partly because of the lack of a convenient excitation scheme. Such studies should provide valuable information about various kinetic processes in the F_2 laser at 157 nm, the spectrally brightest source in the VUV today.[28]

ACKNOWLEDGMENTS

We are grateful for helpful discussions with Dr. P. C. Cosby, especially those concerning the spectral fitting. This research was supported by the AFOSR under Contract Nos. F49620-85-K-0005, F49620-88-K-0003, and F49620-90-C-0044.

[1] R. P. Iczkowski and J. L. Margrave, J. Chem. Phys. **30**, 403 (1959).
[2] W. Stricker and L. Krauss, Z. Naturforsch. Teil A **23**, 486 (1968).
[3] J. L. Gole and J. L. Margrave, J. Mol. Spectrosc. **43**, 65 (1972).
[4] G. Di Lonardo and A. E. Douglas, J. Chem. Phys. **56**, 5185 (1972).
[5] E. A. Colbourn, M. Dagenais, A. E. Douglas, and J. W. Raymonda, Can. J. Phys. **54**, 1343 (1976).
[6] H. G. Gale and G. S. Monk, Astrophys. J. **59**, 125 (1924).
[7] H. G. Gale and G. S. Monk, Astrophys. J. **69**, 77 (1929).
[8] J. Aars, Z. Phys. **79**, 122 (1932).
[9] T. L. Porter, J. Chem. Phys. **48**, 2071 (1968).
[10] H. Nishimura, D. C. Cartwright, and S. Trajmar, J. Chem. Phys. **71**, 5039 (1979).
[11] R.-G. Wang, Z.-W. Wang, M. A. Dillon, and D. Spence, J. Chem. Phys. **80**, 3574 (1984).
[12] K. Hoshiba, Y. Fujita, S. S. Kano, H. Takuma, T. Takayanagi, K. Wakiya, and H. Suzuki, J. Phys. B **18**, L875 (1985).
[13] D. Spence, H. Tanaka, M. A. Dillon, and K. Lanik, J. Phys. B **19**, L569 (1986).
[14] W. K. Bischel and L. E. Jusinski, Chem. Phys. Lett. **120**, 337 (1985).
[15] D. C. Cartwright and P. J. Hay, J. Chem. Phys. **70**, 3191 (1979).
[16] T. Sakai, K. Tanaka, A. Murakami, H. Iwaki, H. Terashima, and T. Shoda, J. Phys. B **21**, 229 (1988).
[17] G. W. Faris and P. C. Cosby (to appear in J. Chem. Phys.).
[18] S. Gerstenkorn and P. Luc, *Atlas du Spectre d'Absorption de la Molécule de l'Iode entre 14800–20000* cm^{-1} (Editions du C.N.R.S., Paris, 1978); Rev. Phys. Appl. (Paris) **14**, 791 (1979).
[19] J. B. Halpern, H. Zacharias, and R. Wallenstein, J. Mol. Spectrosc. **79**, 1 (1980).
[20] K. P. Huber and G. Herzberg, *Molecular Spectra and Molecular Structure IV. Constants of Diatomic Molecules* (Van Nostrand Reinhold, New York, 1979).
[21] QUASIL, Quasilinear Least-Squares Fitting Program, D. L. Huestis, SRI International (unpublished).
[22] R. N. Zare, A. L. Schmeltekopf, W. J. Harrop, and D. L. Albritton, J. Mol. Spectrosc. **46**, 37 (1973) (program LINFIT).
[23] D. L. Albritton, A. L. Schmeltekopf, and R. N. Zare, J. Mol. Spectrosc. **67**, 132 (1977).
[24] J. K. Rice, A. K. Hays, and J. R. Woodworth, Appl. Phys. Lett. **31**, 31 (1977); J. R. Woodworth and J. K. Rice, J. Chem. Phys. **69**, 2500 (1978).
[25] M. Diegelmann, K. Hohla, F. Rebentrost, and K. L. Kompa, J. Chem. Phys. **76**, 1233 (1982).
[26] G. W. Faris and M. J. Dyer, in OSA Proceedings on Short-Wavelength Coherent Radiation, edited by Philip H. Buckbaum and Natale M. Ceglio (Optical Society of America, Washington, D.C., 1991), Vol. 11, pp. 58–61.
[27] D. L. Huestis, R. M. Hill, H. H. Nakano, and D. C. Lorents, J. Chem. Phys. **69**, 5133 (1978).
[28] K. Yamada, K. Miyazaki, T. Hasama, and T. Sato, Appl. Phys. Lett. **54**, 597 (1989).

Appendix C

OBSERVATION OF NO B $^2\Pi(v=3)\leftarrow X\ ^2\Pi(v=0)$ ABSORPTIONS WITH 1+1 MULTIPHOTON IONIZATION: PRECISION LINE POSITION MEASUREMENTS AND PARITY ASSIGNMENT OF THE B $^2\Pi$ STATE

Observation of NO $B\,^2\Pi(v=3)\leftarrow X\,^2\Pi(v=0)$ absorptions with 1+1 multiphoton ionization: Precision line position measurements and parity assignment of the $B\,^2\Pi$ state

G. W. Faris and P. C. Cosby
Molecular Physics Laboratory, SRI International, Menlo Park, California 94025

(Received 25 June 1992; accepted 6 August 1992)

Absorptions are observed in the $\beta(3,0)$ band of NO, $B\,^2\Pi(v=3)\leftarrow X\,^2\Pi(v=0)$ using 1+1 multiphoton ionization at photon energies in the range 47 801–48 542 cm^{-1}. Line positions are reported in 10 of the 12 possible branches with an accuracy of 0.05 cm^{-1}, directly traceable to the visible I_2 absorption spectrum. Λ doubling in the $\beta(3,0)$ band is explicitly resolved, allowing a definitive parity assignment of the $B\,^2\Pi(v=3)$ rotational levels. Accurate term energies and molecular constants are presented for $B\,^2\Pi(v=3)$. Comparison with previous measurements reveals significant discrepancies. Line positions are also reported in the $\gamma(2,0)$ band, $A\,^2\Sigma^+(v=2)\leftarrow X\,^2\Pi(v=0)$, of the $^{14}N^{18}O$ and $^{15}N^{16}O$ isotopes.

I. INTRODUCTION

The β bands of NO, transitions between the $B\,^2\Pi$ and $X\,^2\Pi$ states, are prominent in the emission spectrum of air,[1] in chemiluminescence,[2,3] and in discharges explicitly containing the NO molecule.[4] The upper state in these bands, $B\,^2\Pi$, is the lowest excited valence $^2\Pi$ state of the molecule and has received considerable experimental[5–9] and theoretical[10–16] attention due to the profound perturbation of its levels $v>7$ by the valence $L\,^2\Pi$ and the $n\pi$ Rydberg $(C,K,Q,W)\,^2\Pi$ states. Information on the lower vibrational levels of the B state is relatively sparse, yet it is these lower levels that are populated in $N(^4S)+O(^3P)$ recombination through the intermediary of the $a\,^4\Pi$ state.[3,17] This information is based largely on the 1927 emission band measurements of Jenkins, Barton, and Mulliken[1] which terminate in high vibrational levels of the $X\,^2\Pi$ ground electronic state. More recent observations have been made in absorption at moderate resolution from $X\,^2\Pi(v=0)$ by Callear and Smith[18] and by absorption at high resolution from $X(v>5)$ by Engleman and Rouse.[19] The latter work estimated a rather high line position accuracy of ± 0.01 cm^{-1}, but the X state vibrational energies derived in it deviate well beyond this range from those accurately known[20] from infrared measurements, thus rendering it of questionable value. In all of this work, observations have been restricted only to five or fewer of the twelve branches expected for a $^2\Pi$–$^2\Pi$ transition.

We report here the observation of the $B\,^2\Pi(v=3)\leftarrow X\,^2\Pi(v=0)$ $\beta(3,0)$ band using 1+1 multiphoton ionization (MPI) of room temperature NO gas. The motivation for the present work was the lack of practical wavelength standards required for observations on other molecules (viz. F_2) at wavelengths near 207 nm. Consequently, considerable attention has been given to wavelength calibration of the present observations. As a by-product of the very wide dynamic range of absorption that can be viewed with the MPI technique, the present observations include extended ranges of rotational lines in 10 of the 12 rotational branches and explicit observation of the Λ-doublet splittings in many of these branches. This has allowed a unique determination of the rotational level parity of the $B\,^2\Pi$ state from that which has recently been established[21] for $X\,^2\Pi(v=0)$. Absolute term energies for $B(3)$, $0.5<J<32.5$ are derived from these measurements together with molecular constants for $B(3)$. These, in combination with the well defined rotational energies of the ground state, permit evaluation of the accuracy in past β-band measurements.

In addition to the $\beta(3,0)$, the present observations include lines in the $\gamma(2,0)$ band $(A\,^2\Sigma^+(v=2)\leftarrow X\,^2\Pi(v=0))$ of $^{14}N^{18}O$ and $^{15}N^{16}O$ as well as lines associated with the $b\,^4\Sigma^-$ $(v=2)\leftarrow X\,^2\Pi(v=0)$ intercombination band in the normal isotope. The latter is reported in a separate work.[22]

II. EXPERIMENT

A. Apparatus and measurements

The experimental arrangement for the measurements is shown in Fig. 1. A Lambda Physik EMG 102 excimer laser operating on XeCl is used to pump a Lambda Physik FL3002 dye laser with etalon using Rhodamine B dye. The excimer laser is run at a 50 Hz repetition rate. The dye radiation is frequency doubled in a KDP (potassium dihydrogen phosphate) crystal, and the doubled and fundamental frequencies are sum frequency mixed in a β-BaB_2O_4 (BBO) crystal to produce the third harmonic of the dye laser frequency. To provide the proper polarizations for the sum frequency mixing, the polarization of the dye beam is rotated 90° with a half wave plate before the KDP crystal. In addition, between the frequency doubling and sum frequency mixing crystals, the fundamental and second harmonic beams are separated using a dichroic mirror, the polarization of the fundamental dye beam is rotated 90° with a Fresnel rhomb, and the beams are combined again on another dichroic mirror. Servo-tracking units (Inrad Autotracker I and Autotracker II for the doubling and sum frequency mixing, respectively) were used to maintain frequency conversion while scanning the dye laser frequency. Approximately 5 μJ is obtained in the third har-

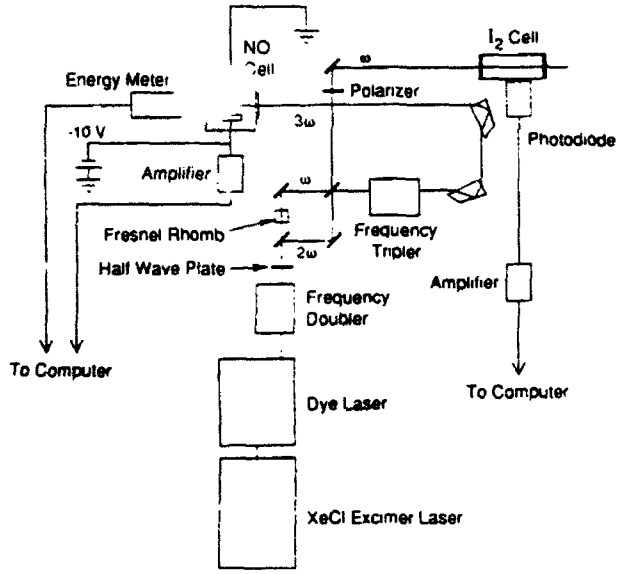

FIG. 1. Schematic diagram of the experimental apparatus used for 1+1 multiphoton ionization of NO.

monic near 208 nm. The third harmonic radiation is separated from the other frequencies with a Pellin–Broca prism, and passed unfocused into an aluminum cell containing 99% pure NO. The gas mixture is flowed slowly through the cell to maintain passivation. Ion signals from 1+1 MPI are detected by an electrode biased at −10 V relative to ground. A second electrode opposite the signal electrode is grounded. If the signal electrode is not biased relative to the cell, space charge effects lead to irreproducible and unstable ion signals. The ion signal is amplified with an EG&G Ortec 142PC charge integrating amplifier. The energy of the 208 nm radiation that passes through the cell is measured with a Laser Precision Rj-7200 pyroelectric energy meter.

A portion of the fundamental dye beam near 625 nm that passes through the second dichroic mirror is attenuated with a polarizer and by reflection off a glass window and passed through a cell containing iodine vapor at room temperature. Fluorescence in the cell is detected by a photodiode through a Schott RG 645 long pass filter and amplified using a second EG&G Ortec 142PC amplifier. Signals from the ion cell amplifier, energy meter, and photodiode amplifier are accumulated using Stanford Research Systems SR250 boxcar averagers with ten shot averaging. The outputs from the boxcars are digitized at 10 Hz (about 0.0018 cm^{-1} per point at the fundamental wavelength, 0.0054 cm^{-1} per point at the third harmonic) with a 12 bit Data Translation DT2814 asynchronous digitizer in an AST 286 PC-compatible computer. A single spectrum covered typically about 40 cm^{-1}. The experimental linewidths are $\sim 0.06\ cm^{-1}$ for the iodine lines and $\sim 0.2\ cm^{-1}$ for the NO lines. The room temperature Doppler width of the NO at 48 000 cm^{-1} is 0.11 cm^{-1}.

B. Peak fitting

Performing at least two complete scans of the entire (3,0) β band produced a large amount of data, about megabytes when stored as binary. The data was transferred to a VAX 750 computer for peak fitting and calibration. Because of the large number of lines in the iodine and NO spectra, we have written a routine to find accurate line positions and heights for isolated lines. The routine performs analytical least squares quadratic fits to that portion of a line with negative second derivative. When the fits are limited to the region with negative second derivative, quadratic curves fit most line shapes quite well. To find the regions of negative second derivative for fitting a line, a spectrum is differentiated two times. This accentuates the high frequencies in the spectrum, causing noise spikes to appear quite large. To reduce the noise, the second derivative spectrum is filtered by performing a fast Fourier transform (FFT), multiplying the Fourier transform by a Gaussian with width chosen to limit frequencies above those expected from a typical linewidth in the original spectrum, and then performing an inverse FFT. This is equivalent to convolving the second derivative data with a Gaussian profile. For the iodine data the Gaussian profile has a full width at half maximum (FWHM) of 12.5 data points ($\sim 0.02\ cm^{-1}$), the FWHM is 30 for the NO data ($\sim 0.16\ cm^{-1}$). The differentiation and filtering could also be performed in a single step by use of the appropriate filter in frequency space. Regions for line fitting are found by finding the most negative point in the filtered second derivative spectrum (ideally, for identical line shapes, this would be the strongest line) and determining the first zero crossings on either side of this line. A quadratic fit is then performed on the data points in the original spectrum within this range defined by the zero crossings and the line position and height are placed in a list of lines. This fitting region is removed from the filtered second derivative spectrum by setting the points between the zero crossings to zero. The next most negative point in the second derivative spectrum is found, and the same procedure is used to find what is approximately the next strongest line. The search and fitting procedure is repeated until a desired number of lines is found or until no second derivative points lie below a given threshold. We typically chose to find a number of lines that was greater than the number of lines apparent in the original spectrum to ensure finding all lines. Extraneous lines appeared in the line list due to noise in the spectrum. The noise lines were found by overlaying the fitted lines and the original spectrum, and visually inspecting each line. Lines that are clearly extraneous are removed from the list and lines that were clearly blended were noted.

This technique was applied to both the I_2 and NO spectra. The fitting approach as we have implemented does not accurately determine line positions for partially overlapping lines. The iodine lines are used as calibration, and it is not necessary to use all of them. For this reason, and because the iodine lines are typically fairly dense (~ 4 lines per cm^{-1} over the region that we have investigated: 47 800–48 620 cm^{-1}), it was not necessary to use blended I_2 lines in the calibration.

For the NO spectra, positions of overlapping lines were determined using a nonlinear fit to a Gaussian line profile,

a form which was appropriate for the features except far into their absorption wings. Nonzero and sloping base lines were incorporated into the Gaussian fits when necessary. The full width at half maximum of the Gaussians lay in the range of 0.16–0.20 cm^{-1}. Blended features with apparent widths in excess of 0.20 cm^{-1} were fit to two equal width Gaussians. Line positions are taken as the centroid of the Gaussian in the fit.

C. Calibration

Calibration of the iodine spectra is performed against the data of Gerstenkorn and Luc for iodine positions.[23] Diskettes containing data on their line positions were obtained from the Laboratoire Aime' Cotton, Centre Nationale de la Recherche Scientifique (CNRS). This data were corrected by -0.0056 cm^{-1} as recommended.[24] The same calibration found for the iodine spectra is applied to the NO spectra, although the wave numbers are multiplied by three because of the frequency tripling.

Calibration of the iodine spectrum requires pairing the relative iodine line positions (vs data point number) to the known iodine line frequencies. As this involves matching a large number of lines, we partially automated the matching procedure. Approximate line positions for the iodine lines are determined by scaling our measured spectra (converting from data point number to approximate frequency in cm^{-1} such that our line positions align with those of Gerstenkorn and Luc when both are plotted on an absolute frequency scale). A single file is created containing pairs of points from the two iodine spectra: for our data the pairs consist of data point number and approximate frequency position for each line, and for the Gerstenkorn and Luc data the pairs consist of two identical points giving the absolute line position in cm^{-1}. The file is sorted by the second column to create a file which has adjacent points from our data and the measured values. This file is edited to remove the second column and produce a file containing pairs of measured data point number and absolute frequency. In this process, we refer to a graphic overlay of the two spectra to check that the proper pairing is being made.

On fitting a straight line to the frequency calibration between our line positions and the absolute positions, we find that the iodine line positions deviate on average by ~ 0.02 cm^{-1}, root mean square, from the straight line. We believe this is due to slight variation of the dye laser scan from a true linear scan in frequency. To incorporate this variation into the frequency calibration, we filtered the data points using a Gaussian filter in frequency space as was performed for the second derivative in the line finding routine. However, as the FFT forces periodic boundary conditions at the ends of the data, the large difference in ordinate values for the end points leads to perturbations on the filtered data. A simple correction of subtracting the linear fit from the points prior to the FFT filtering was not sufficient to avoid perturbations. Instead, we added points to the ends of the calibration to produce a boundary that is sufficiently far from the true end points to avoid the boundary effects. These extra points are removed after the filtering. The form of the added points is obtained by extrapolating the data through inversion about the end points. Ordinate values to serve as the origins for this inversion were determined by performing linear least square fits to a few points near each end point. This procedure was found to give very good smoothed fits to the calibration points as judged by visual inspection. The Gaussian used to smooth the calibration curves has a 3.2 cm^{-1} FWHM. One calibration curve is produced for each spectrum. The average of the root mean squared deviation between the resulting smoothly varying calibration curve and the calibration points for all of the spectra is 0.005 cm^{-1}.

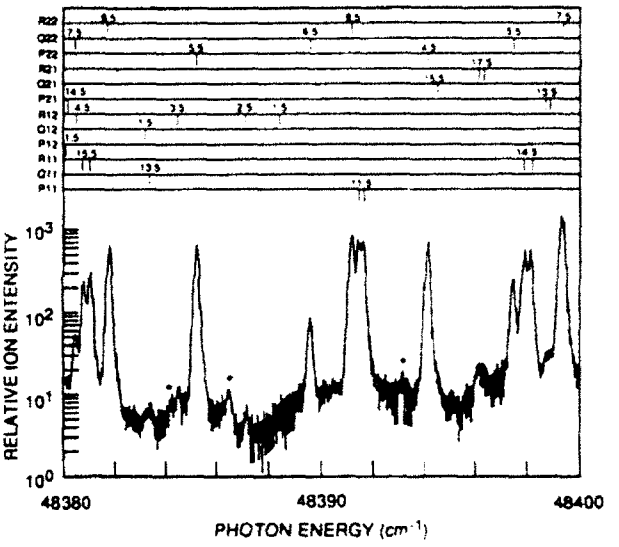

FIG. 2. The 1+1 multiphoton ionization spectrum of NO observed between 47 380–47 400 cm^{-1}. Note that the intensity scale is logarithmic to show the wide dynamic range of the absorptions. Transitions in all branches of the $\beta(3,0)$ band are labeled; some were not of sufficient intensity to measure accurate line positions. The three peaks denoted by asterisks are not assigned to $\beta(3,0)$ absorptions.

The NO MPI spectral scans, determined as a function of data point numbers are converted to absolute frequencies through interpolation using the smoothed I_2 calibration curves for each spectra. Each region of the $\beta(3,0)$ absorption spectrum was covered in at least two, and typically, three or more independent, calibrated spectral scans. Multiple determinations of a line position from the various spectral scans were averaged to obtain the line positions reported here. The average of the standard deviation of these mean line positions for all of the lines is 0.04 cm^{-1}. A conservative estimate for the absolute line position accuracy is 0.05 cm^{-1}.

D. NO absorption spectrum

The great advantage of MPI detection is the sensitive detection of weak absorptions with a wide dynamic range, approaching 10^3 in the present study. This dynamic range is illustrated in Fig. 2 which shows one spectral scan of the region 48 380–48 400 cm^{-1}. Sensitivity is important here because of the very small absorption coefficient[25] of the $B(3)$–$X(0)$ transition. The observed intensities of the strongest lines of the $\beta(3,0)$ system are comparable to lines

in the $\gamma(2,0)$ band of $^{15}N^{16}O$ or $^{14}N^{18}O$ isotopomers, present in the NO gas at natural abundance (0.37% and 0.20%, respectively). The MPI dynamic range further allowed line position measurements over a wide range of rotational levels ($0.5<J<31.5$) and in (previously unobserved) weak branches of the $\beta(3,0)$ system, which permit definitive assignment of all relevant quantum numbers in the transitions. As the price for this sensitivity, however, extreme care must be taken to avoid impurities in the gas sample. In the present work, this was achieved by repeated passivation of the ionization cell and the continuous flow of NO gas in the cell during the measurements. However, even with these precautions, broad features, presumably due to ionization of diffusion pump oil or other trace impurities, underlie portions of the spectral region examined in the present work. These were of particular concern in the reddest portion of the spectrum where the $\beta(3,0)$ absorptions, though appreciably sharper than those of the impurities, probe high rotational levels of the X state and are quite weak. A second disadvantage of the $1+1$ MPI detection scheme is that the ionization signal depends on the square of the laser intensity, although this is a vast improvement over higher order absorption schemes. Because power normalization is made on the basis of a ten shot average power, the effect of shot to shot fluctuations cannot always be quantitatively corrected, but its effect is random in the different scans of a given spectral region. Furthermore, the photoionization cross section is not necessarily independent of wavelength due to the possibility of autoionization, producing a systematic distortion of the apparent absorption intensities. This effect was presumably responsible for the two components in some of the Λ doublets persistently appearing in different scans with unequal relative intensities, as much as a factor of 2 in some cases.

III. RESULTS

The $^2\Pi$–$^2\Pi$ structure of the β bands has been described in detail by a number of authors.[1,4,26] The $\beta(3,0)$ band is red degraded with weak heads involving only the first several rotational quanta forming in each of the branches. Twelve branches are possible for electric dipole transitions between $^2\Pi$ states with angular momentum coupling intermediate between Hund's case (a) and (b), as is appropriate for both the NO X and B states. We adopt here the usual branch notation $\Delta J_{F'F''}(J'')$, where $\Delta J=-1,0,1=P,Q,R$ denotes the change in total rotational angular momentum J, excluding spin, and J'' denotes the absorbing X state rotational level, when such specificity is appropriate. The first and second subscripts label the spin–orbit component $F=F_1,F_2=1,2$ of the upper (B) and lower (X) states, respectively. Both the X and B states are regular, with F_1 denoting levels in the $^2\Pi_{\Omega=1/2}$ substate, which lies energetically below the $^2\Pi_{\Omega=3/2}$ substate, whose levels are labeled F_2. Only four of these branches are intense, $P_{11},R_{11},P_{22},R_{22}$, with absorption maxima near $J''=7.5$ for a 300 K rotational distribution. Previous observations of the β bands[1,18,19] have almost exclusively been restricted to the observation of transitions in these branches. Transitions in the Q_{11} and Q_{22} branches are roughly a factor of 5 weaker, with absorption intensity maximizing at the very lowest J''. Four satellite branches, $P_{12},R_{12},P_{21},R_{21}$, are observed in the present work for the first time. These have expected intensities of order 2% that in the intense main branches, with absorptions maximizing near $J''=11.5$. The remaining two satellite branches, Q_{12} and Q_{21}, are predicted to be extremely weak, with intensities of 1×10^{-3} and 6×10^{-5}, respectively, relative to that in the R_{11} branch. These are too weak to be observed, either here or in previous work. The rotational levels in both the B and X states have two nearly degenerate parity components; absorption lines in each of the 12 branches are doublets (Λ doublets) whose separation is dependent on F, J, and ΔJ.

A. Transition energies

Initial identification of the NO $\beta(3,0)$ absorption lines in the main branches was easily made from the positions and intensities calculated by diagonalization of the $^2\Pi$ Hamiltonians[27] using the $B(v=3)$ constants of Hallin *et al.*[28] and the $X(v=0)$ constants of Amiot *et al.*[29]. Transitions in the main branches ($P_{11},R_{11},P_{22},R_{22}$) were within 1 cm^{-1} of the calculated positions. With small, iterative adjustments of these initial constants, transitions in 10 of the 12 possible rotational branches could be tentatively identified. Due to Λ doubling in the $^2\Pi$ states, each transition should consist of two closely spaced lines connecting the appropriate parity levels in the upper and lower states. Where the separation of these doublets roughly equaled or exceeded the mean experimental linewidth (~0.18 cm^{-1}), the peaks appear as two distinct features in the absorption spectrum. This occurs for $J''>13.5$ in the $P_{11},R_{11},P_{21},R_{21}$ branches and at $J>20.5$ in the P_{12},R_{12} branches. At lower J, and throughout the P_{22},R_{22} branches, the doublets are manifested only by a broadening of the absorption lines beyond the nominal range of 0.16–0.20 cm^{-1}. Depending on the proximity of the individual transitions to others, the broadened peaks could be fit by two equal width Gaussians to recover doublet splittings below this range. In the Q_{11} and Q_{22} branches, no definitive evidence of doublets could be detected from the linewidths.

In all, 119 pairs of Λ doublets could be measured and an additional 97 lines, where the splittings are too small for confident measurement, are reported as single lines. The measured line positions are listed in Table I. Assignment of the specific parity for the doubled transitions is discussed in the following section. Confirmation of the appropriate assignment for the lines in Table I was made by term value analysis[30,31] (combination differences) of the line positions using the accurate term values for the X state given by Amiot *et al.*[29] as constants in the fit. For this analysis, the line positions of the doubled lines are used directly as listed. For those lines where explicit doubling could not be measured, the reported position was assigned to each of the two parity components of the Λ doublet. Because the magnitude of an undetected splitting is quite large in comparison to both the accuracy and precision of the line center measurements, and the fact that some line positions by virtue of their intensity or proximity to other features

TABLE I. Observed lines of the NO $B\,^2\Pi - X\,^2\Pi$ (3,0) band as a function of X state rotational quantum number (J'') and parity ($+/-$). All units are cm^{-1}. When an entry is given for only a single parity component, the entry refers to the centroid of the transition with the Λ doubling unresolved. Where a transition is obscured by a stronger line, the identification of the overlapping line is given.

J''	P_{11}	Q_{11}	R_{11}	P_{12}	R_{12}	P_{21}	R_{21}	P_{22}	Q_{22}	R_{22}
0.5+	...	$R_{11}(3.5)$	48 508.115	...	...	...	$R_{21}(2.5)$	...	...	...
0.5−										
1.5+	48 499.953[a,d]	48 503.066[a]	48 508.319				48 542.320[a]	...	48 416.875	48 422.448
1.5−										
2.5+	48 494.726	$P_{11}(1.5)$	48 507.276[a]				48 541.774[a]	48 408.280	$R_{11}(13.5)$	48 421.650
2.5−										
3.5+	48 488.241	48 495.565	48 504.984[a]				48 540.107	48 401.826	48 409.636	48 419.635
3.5−										
4.5+	48 480.513[a]	48 489.905[a]	48 501.468[a]				48 537.288[a]	48 394.145	48 404.150	48 416.404
4.5−			48 501.406[a]							
5.5+	48 471.486	$R_{11}(7.5)$	48 496.598[a]	48 350.172[b]			48 533.347[a]	48 385.229	48 397.476	48 411.909
5.5−	48 471.570		48 496.666[a]							
6.5+	48 461.388	$R_{11}(8.5)$	48 490.675	$P_{21}(16.5)$	48 368.571[a]		48 528.258[b]	48 375.106	48 389.580	48 406.253
6.5−	48 461.240		48 490.541							
7.5+	48 449.732	$R_{11}(9.5)$	48 483.272	48 327.108[b]	48 360.584[a]	48 486.509[b]	48 522.051[b]	48 363.779	48 380.458	48 399.329
7.5−	48 449.886		48 483.412							
8.5+	48 437.175	48 454.895[b]	48 474.909	$P_{11}(5.5)$	$P_{22}(8.5)$	$R_{11}(8.5)$	48 514.789[b]	48 351.234	48 370.099	48 391.180
8.5−	48 437.012		48 474.758				48 514.596[b]			
9.5+	48 423.069	48 442.978[c]	48 464.996	48 298.765[b]	48 340.658[a]	48 461.870[b]	48 506.119[a]	48 337.461	48 358.503	48 381.775
9.5−	48 423.235		48 465.160				48 506.215[a]			
10.5+	48 408.042		48 454.197	48 282.553[a]	48 328.733[b]	48 447.889[a]	$R_{11}(5.5)$	48 322.476	48 345.709	48 371.138
10.5−	48 407.871		48 454.008			48 447.757[a]				
11.5+	48 391.440		48 441.842	48 265.082[a]	48 315.505[b]	48 432.507[a]	48 485.640	48 306.201	$R_{22}(13.5)$	48 359.264
11.5−	48 391.626		48 442.018			48 432.735[a]	48 485.797			
12.5+	48 373.962		48 428.628	48 246.333[b]	48 300.940[b]	$R_{22}(4.5)$	48 473.831	48 288.710	$R_{22}(14.5)$	48 346.155
12.5−	48 373.759		48 428.414				48 473.680			
13.5+	48 354.897		48 413.795	48 226.202[a]	48 285.077[a]	$R_{22}(7.5)$	$P_{11}(6.5)$	48 270.007	48 299.812	48 331.796
13.5−	48 355.078		48 413.974	48 226.262[a]	48 285.119[a]					
14.5+	48 335.013		48 398.133	48 204.895[a]	48 267.984[a]	$Q_{22}(7.5)$	48 446.297[a]	48 250.053	48 282.023	48 316.175
14.5−	48 334.790		48 397.883	48 204.835[a]	48 267.926[a]		48 446.140[a]			
15.5+	48 313.453		48 380.799	48 182.128[a]	48 249.472[a]	48 360.199	48 430.612[a]	48 228.866	48 263.007	48 299.316
15.5−	48 313.696		48 381.049	48 182.168[a]	48 249.536[a]	48 360.393	48 430.816[a]			
16.5+	48 291.175		48 362.776	$P_{22}(18.5)$	48 229.826[a]	48 339.367	$R_{11}(13.5)$	48 206.416	$P_{11}(18.5)$	48 281.180
16.5−	48 290.931		48 362.482		48 229.730[a]	48 339.196				
17.5+	48 267.142		48 342.952	48 132.901[a]	48 208.738[a]	48 317.041[b]	48 396.128	48 182.720	48 221.215	48 261.838
17.5−	48 267.420		48 343.242	48 132.949[a]	48 208.830[a]	48 317.246[b]	48 396.385[b]			
18.5+	48 242.466		$P_{22}(10.5)$	48 106.429[b]	48 186.507	48 293.856	48 377.287[b]	48 157.812[a]	48 198.453	48 241.212
18.5−	48 242.149			48 106.363[b]	48 186.343	48 293.614	48 377.079			
19.5+	48 215.949		48 300.251	48 078.461	48 162.750	48 269.064[a]	48 356.791	48 131.622[a]	48 174.405[a]	48 219.332
19.5−	48 216.270		48 300.568	48 078.593	48 162.905	48 269.330	48 357.085[b]			
20.5+	48 188.852		48 277.398	48 049.491	48 138.048	48 243.599	48 335.590	48 104.187[a]	48 149.164[a]	48 196.207
20.5−	48 188.522		48 277.056	48 049.351	48 137.885	48 243.384	48 335.380			
21.5+	48 159.926		48 252.678	48 018.967	48 111.736	$P_{11}(19.5)$	$P_{11}(15.5)$	48 075.570[a]	48 122.615[a]	48 171.804[b]
21.5−	48 160.240		48 253.019	48 019.140	48 111.910					
22.5+	48 130.410		48 227.413	47 987.473	48 084.509	$P_{11}(20.5)$	$P_{22}(12.5)$	48 045.647[a]	48 094.845[a]	48 146.186[a]
22.5−	48 130.066		48 227.051	47 987.308	48 084.317					
23.5+	48 098.994		48 200.216	47 954.439[a]	48 055.601	48 159.080	48 263.899	48 014.426[a]	48 065.817[a]	48 119.340[a]
23.5−	48 099.357		48 200.558	47 954.608[a]	48 055.794	48 159.331	48 264.157	48 014.533[a]		
24.5+	48 067.095		48 172.541	47 920.408	e	48 128.835	48 237.918	47 982.130[a]		48 091.219
24.5−	48 066.716		48 172.158	47 920.199		48 128.569	48 237.666	47 982.008[a]		48 091.112
25.5+	48 033.231		48 142.874		47 994.405	48 096.915	48 210.254	47 948.381[a]		48 061.723[a]
25.5−	48 033.606		48 143.272		47 994.638	48 097.177	48 210.515	47 948.510[a]		48 061.817[a]
26.5+	47 998.922		48 112.813			48 064.307		47 913.624		48 031.240
26.5−	47 998.530		48 112.406			48 063.995	48 181.594[f]	47 913.511		48 031.112
27.5+	47 962.606		48 080.680			48 029.965	48 151.794	47 877.384		47 999.210
27.5−	47 963.013		48 081.112			48 030.234	48 152.057	47 877.514		47 999.340
28.5+	47 925.908		48 048.200					47 840.132		47 966.244[b,d]
28.5−	47 925.483		48 047.764					47 840.022		47 966.072[b,d]
29.5+	47 887.130		48 013.604					47 801.398		47 931.665[d]
29.5−	47 887.531		48 014.069					47 801.557		47 931.812[d]
30.5+	47 848.028		47 978.704[c]							47 896.142[d]
30.5−	47 847.585		47 978.262[c]							47 896.051[d]
31.5+	47 806.801									47 859.185[b,d]
31.5−	47 807.235									47 859.295[b,d]

[a]Line weighted by the reciprocal square of two standard errors in the fits.
[b]Line weighted by the reciprocal square of three standard errors in the fits.
[c]Line weighted by the reciprocal square of four standard errors in the fits.
[d]Line is not part of the multiply connected set.
[e]Line obscured by a broad impurity band in the high power spectrum.
[f]Second parity component not observed; line not used in the fits.

C-5

TABLE II. Term energies and relative uncertainties of the $B\,^2\Pi$ ($v=3$) levels. Units are cm^{-1}. The zero of energy is the $X\,^2\Pi_{1/2}(v=0, J=0.5(e))$ level. The absolute accuracy of the energies is 0.05 cm^{-1}.

J	$^2\Pi_{1/2}$ (e)		$^2\Pi_{1/2}$ (f)		$^2\Pi_{3/2}$ (e)		$^2\Pi_{3/2}$ (f)	
0.5	48 504.963	0.031[a]	48 504.990	0.031[a]	...	...	...	...
1.5	48 508.102	0.017	48 508.121	0.017	48 541.792	0.017	48 541.792	0.017
2.5	48 513.316	0.017	48 513.351	0.017	48 547.366	0.017	48 547.369	0.017
3.5	48 520.659	0.018	48 520.643	0.018	48 555.174	0.016	48 555.177	0.016
4.5	48 530.062	0.018	48 530.052	0.018	48 565.179	0.015	48 565.191	0.015
5.5	48 541.603	0.017	48 541.542	0.017	48 577.419	0.016	48 577.424	0.016
6.5	48 555.180	0.017	48 555.125	0.017	48 591.862	0.016	48 591.871	0.016
7.5	48 570.889	0.016	48 570.835	0.016	48 608.541	0.016	48 608.545	0.016
8.5	48 588.702	0.016	48 588.655	0.016	48 627.405	0.016	48 627.413	0.016
9.5	48 608.612	0.016	48 608.566	0.016	48 648.480	0.016	48 648.478	0.016
10.5	48 630.635	0.016	48 630.588	0.016	48 671.730	0.016	48 671.726	0.016
11.5	48 654.771	0.016	48 654.712	0.016	48 697.164	0.017	48 697.172	0.017
12.5	48 681.031	0.016	48 680.995	0.016	48 724.809	0.016	48 724.799	0.016
13.5	48 709.430	0.016	48 709.369	0.016	48 754.622	0.015	48 754.621	0.015
14.5	48 739.920	0.016	48 739.864	0.016	48 786.607	0.015	48 786.598	0.015
15.5	48 772.545	0.016	48 772.474	0.016	48 820.743	0.015	48 820.750	0.015
16.5	48 807.281	0.016	48 807.199	0.016	48 857.060	0.016	48 857.053	0.016
17.5	48 844.157	0.016	48 844.043	0.016	48 895.545	0.015	48 895.520	0.015
18.5	48 883.120	0.015	48 883.016	0.015	48 936.187	0.016	48 936.172	0.016
19.5	48 924.216	0.015	48 924.099	0.015	48 978.952	0.016	48 978.953	0.015
20.5	48 967.434	0.015	48 967.319	0.015	49 023.872	0.018	49 023.876	0.016
21.5	49 012.763	0.015	49 012.640	0.015	49 070.942	0.016	49 070.952	0.016
22.5	49 060.219	0.015	49 060.093	0.015	49 120.182	0.017	49 120.159	0.017
23.5	49 109.786	0.015	49 109.643	0.015	49 171.515	0.016	49 171.487	0.016
24.5	49 161.437	0.015	49 161.309	0.015	49 225.023	0.016	49 224.991	0.016
25.5	49 215.240	0.016	49 215.093	0.016	49 280.614	0.015	49 280.572	0.015
26.5	49 271.131	0.015	49 270.972	0.015	49 338.355	0.015	49 338.327	0.015
27.5	49 329.145	0.016	49 328.980	0.016	49 398.209	0.016	49 398.172	0.016
28.5	49 389.225	0.016	49 389.063	0.016	49 460.185	0.015	49 460.144	0.015
29.5	49 451.452	0.016	49 451.272	0.016	49 524.303	0.087[a]	49 524.220	0.087[a]
30.5	49 515.739	0.016	49 515.553	0.016	49 590.445	0.018[a]	49 590.395	0.018[a]
31.5	49 582.136	0.018[a]	49 581.957	0.018[a]	49 658.702	0.039[a]	49 658.716	0.039[a]
32.5					49 729.129	0.087[a]	49 729.133	0.087[a]

[a]Term energies based on nonmultiply connected transitions.

could be measured less accurately than others, the lines were weighted in the fit. This weighting is explicitly defined in Table I. The 430 nominal transition frequencies were fit to 128 term values in $B(v=3)$ with a standard deviation of 0.0138 cm^{-1}. With the exception of the eleven lines denoted in Table I, each of these transitions accesses a multiply connected B state level; hence its transition assignment is confirmed independent of any model of electronic structure in the B state. A minimum variance, linear unbiased estimate of the term energies of $B(v=3)$ is a byproduct of this fit. These term energies, together with their (random) statistical uncertainties are given in Table II. These energies are relative to the energy of $X(v=0, J=0.5+(e), \Omega=0.5)$. The energy of any arbitrary transition for the $\beta(3,0)$ band can be generated from the combination of these term energies and the X state term energies of Amiot *et al.*[29]

The line positions in Table I can be compared directly to those reported by Callear and Smith.[18] These workers observed the $\beta(3,0)$ band in absorption with a 3 m spectrograph and report line positions in the range $1.5<J''<26.5$, but only in the four strong branches, $P_{11},R_{11},P_{22},R_{22}$, and with no evidence of Λ doubling. No indication is given as to the probable accuracy of their measurements; line positions are listed with a least significant digit of 0.1 cm^{-1}. Comparing the P_{11},R_{11} lines with the mean line positions of the Λ doublets when appropriate, the Callear and Smith lines in these branches generally lie to lower energy with a mean deviation of 0.39 cm^{-1} and a range of $+0.9$--0.2 cm^{-1} on specific lines. In the P_{22},R_{22} branches, the mean deviation is 0.52 cm^{-1} with a range of $+1.0$--$+0.1$ cm^{-1}.

Comparison can also be made between the term values of Table II and the energies reported for these levels in the literature. Barrow and Miescher[32,33] quote values for the $Q_{11}(0.5)$ lines for most of the vibrational levels in the $B\,^2\Pi$ state, thus specifying their energy relative to $X\,^2\Pi(v=0, J=0.5)$. For $B(v=3)$, their line position (48 509.6 cm^{-1}) should correspond to the average energy of the e and f components in F_1, $J=0.5$ of Table II, 48 504.977 cm^{-1}, but actually lies 4.623 cm^{-1} too high in energy. Callear and Smith[18] noted this large discrepancy, but the use of the Barrow and Miescher values has continued to propagate into current literature. Both Gallusser and Dressler[12] and Raoult[13] unfortunately use the Barrow and Miescher values for the term energies of $B(0<v<4)$[34] in their analysis of $^2\Pi$ Rydberg-valence interactions.

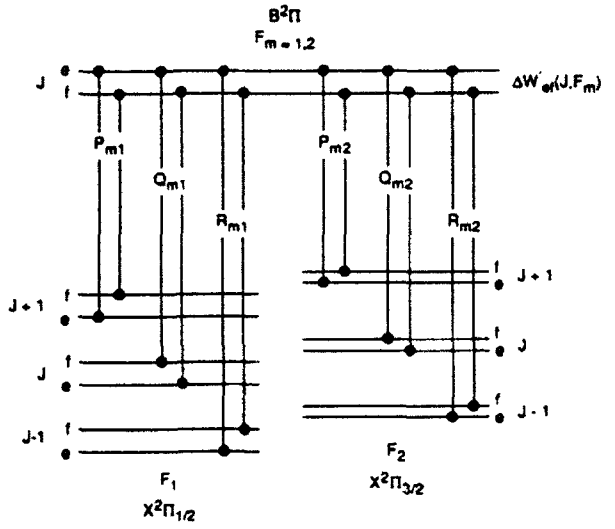

FIG. 3. Schematic diagram of the Λ doubling in the $X\,^2\Pi$ and $B\,^2\Pi$ states of NO. All electric dipole-allowed absorptions into one rotational level in one of the two spin–orbit substates ($F_{m=\Omega+1/2}$) of the $B\,^2\Pi$ are shown.

B. Parity identification

The doublet structure of the rotational levels in the $B\,^2\Pi$ and $X\,^2\Pi$ states is shown schematically in Fig. 3. Each $^2\Pi$ state is split by spin–orbit coupling into two components $\Omega=1/2$ and $\Omega=3/2$ which are labeled F_1 and F_2, respectively. In addition to this splitting, each rotational level J of the $^2\Pi$ consists of two parity components labeled $+$ and $-$, denoting their inversion symmetry. Since the symmetry of the rotational wave function alternates with J, the overall inversion symmetry of the parity wave function is labeled e or f, defined by the convention[35] that e levels transform as parity $(-1)^{J-0.5}$ while f levels transform as $(-1)^{J+0.5}$. For electric dipole transitions, the selection rules are $e\leftrightarrow e$ and $f\leftrightarrow f$ for $\Delta J=\pm 1$ (R,P branches) and $e\leftrightarrow f$ for $\Delta J=0$ (Q branches). In an isolated $^2\Pi$ state, these two components are degenerate. However, spin–orbit and Coriolis couplings in the molecule[36] produce a rotationally dependent mixing of $^2\Pi$ and $^2\Sigma$ states that is manifested in a perturbation of the e terms relative to the f terms in the $^2\Pi$, which removes the degeneracy (Λ doubling).

The Λ doubling in the lowest vibrational levels of the $X\,^2\Pi$ state is now well understood. High resolution Fourier-transform infrared (FTIR) measurements of Amiot *et al.*[29] have established the term energies of the e and f levels to high accuracy in $v=0$ over the range $0.5<J<39.5$. The recent experimental investigation of Geuzebroek *et al.*[30] has uniquely assigned the parity of these levels $W_f>W_e$ in the F_1 substate. Their assignment, which extends also to the F_2 substate following the work of Amiot *et al.* is predicated only on the assumption that the lowest excited Σ state in NO (the A state) is $^2\Sigma^+$, which is unequivocal in view of the high quality *ab initio* molecular structure calculations[14,37] that have been made for NO. This parity assignment for the Λ doublets is further supported by the quantitative *ab initio* calculations of de Vivie and Peyerimhoff,[38] which match not only the assigned order of the levels, but also the magnitude of the observed splittings.

The Λ doubling in the $B\,^2\Pi$ state is less well founded. Huber[39] observed a J-dependent splitting of the rotational transitions in the $B'\,^2\Delta$–$B\,^2\Pi$ $\beta'(1,0)$ band, where the entirety of the line doubling could reasonably be attributed to Λ doubling in the $B(v=1)$. By comparing the magnitude of this splitting with the magnitude of the line doubling observed by Jenkins, Barton, and Mulliken[1] reported for the $\beta(0,10)$ and $\beta(0,11)$ bands, he concluded that the parity order in the B state is opposite to that in the X state, viz. $W_e>W_f$. This is predicated on the assumption that the Λ doubling in both the B and X states does not change appreciably with vibration, and the Λ doubling in the $^2\Delta$ state is negligibly small. Engleman and Rouse[19] observed splittings in the $F',F''=1$ components in a variety of emission bands in the β system. Their assignments are consistent with an opposite parity order in the B and X states, though they offer little explanation as to how this parity order was established.

The splittings observed in an electronic absorption or emission spectrum reflect the energetic difference of the Λ doublets in the upper and lower electronic states. If we acknowledge these energy differences and the dipole selection rules explicitly, the transition splittings in the six branches of the $^2\Pi$–$^2\Pi$ transition that access a single rotational level J,F'_m of the upper state (B) can be written as

$$\begin{aligned}\Delta\nu_{ij}^{Qmn}(J)&=\nu_{ij}^{Qmn}(J)-\nu_{ji}^{Qmn}(J)\\&=W'_i(J,F'_m)-W''_j(J,F''_n)-[W'_j(J,F'_m)\\&\quad-W''_i(J,F''_n)]\\&=\Delta W'_{ij}(J,F'_m)+\Delta W''_{ij}(J,F''_n),\end{aligned}\tag{1}$$

$$\begin{aligned}\Delta\nu_{ij}^{Pmn}(J+1)&=\nu_{ii}^{Pmn}(J+1)-\nu_{jj}^{Pmn}(J+1)\\&=\Delta W'_{ij}(J,F'_m)-\Delta W''_{ij}(J+1,F''_n),\end{aligned}\tag{2}$$

$$\begin{aligned}\Delta\nu_{ij}^{Rmn}(J-1)&=\nu_{ii}^{Rmn}(J-1)-\nu_{jj}^{Rmn}(J-1)\\&=\Delta W'_{ij}(J,F'_m)-\Delta W''_{ij}(J-1,F''_n),\end{aligned}\tag{3}$$

where m and n denote the label (1 or 2) for the spin–orbit component in the B and X states, respectively, and i and j denote a mutually exclusive ($i\neq j$) level parity (e or f). From Eqs. (1)–(3), if the order of parity is the same in both the B and X states, then the splitting in the Q-branch transitions, reflecting the sum of each state's contributions, will equal or exceed that in the P and R branches, which reflect the difference. Conversely, an opposite parity order in the two states will produce the larger splitting in the P and R branches. This opposite parity order is clearly consistent with the lack of Q-branch splitting observed here. However, this does not lead to a confident assignment of parity order since it is not known *a priori* that the two parity components in the Q branch produce comparable photoionization signals, for example.

Since the energy separation of the Λ doublets in the X state, $\Delta W''_{ij}$, are known explicitly, Eqs. (1)–(3) can then be written as

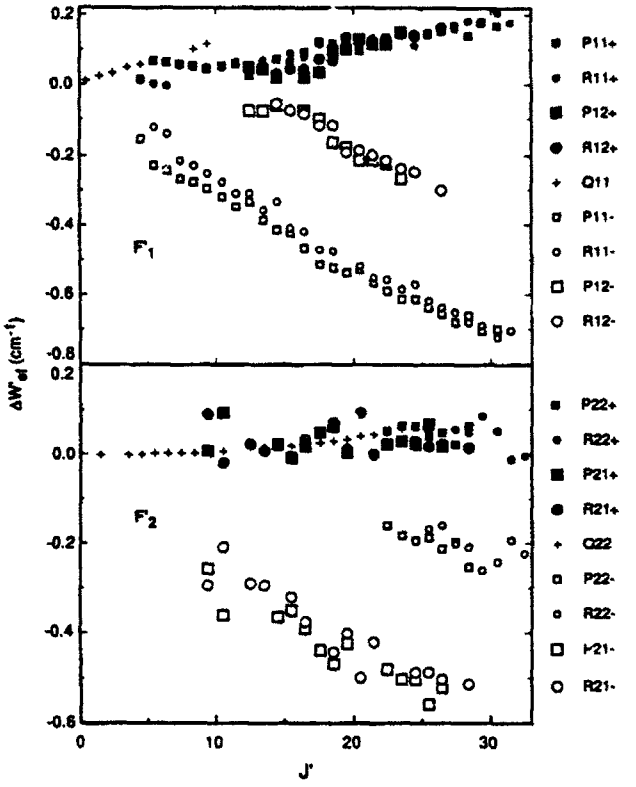

FIG. 4. $B\,^2\Pi(v=3)$ Λ-doublet splittings ($\Delta W'_{ef}$) as a function of rotational level as given by the observed lines in the various rotational branches. The closed and open symbols denote the choice of sign in Eq. (4) as + and −, respectively. The Q-branch transitions, with no observed splitting, yield the same result regardless of sign and are shown by crosses. The grouping of splittings into a single, continuous variation with J occurs only if the parity e levels lie energetically above the parity f levels in both the F'_1 and F'_2 components of $B\,^2\Pi(v=3)$. Upper figure: transitions terminating in F'_1. Lower figure: transitions terminating in F'_2.

$$\Delta W'_{ef}(J,F'_m) = \Delta W''_{fe}(J,F''_n) \pm |\Delta\nu_{ij}^{Qmn}(J)| \tag{4a}$$

$$= \Delta W''_{ef}(J+1,F''_n) \pm |\Delta\nu_{ij}^{Pmn}(J+1)| \tag{4b}$$

$$= \Delta W''_{ef}(J-1,F''_n) \pm |\Delta\nu_{ij}^{Rmn}(J-1)|, \tag{4c}$$

where the upper (+) sign denotes $i,j=e,f$ and the lower (−) sign denotes $i,j=f,e$. The results of these equations for the transitions in each of the five observed branches accessing F'_1 and F'_2 are shown by the upper and lower plots in Fig. 4, respectively, where the closed symbols denote the sign taken positive and the open symbols denote the sign taken negative. For clarity, points are shown only for the P- and R-branch lines where an explicit splitting is measured. In the Q branches, points are shown for all observed lines, with the line splittings taken to be zero. It is clear from Fig. 4 that an unique solution to the upper state Λ-doublet splittings, as evidenced by the grouping of the closed symbols along a monotonic dependence of the splittings on J in each substate, is possible for all of the branches only when the sign in Eq. (4) is taken to be positive. This conclusion is made particularly compelling

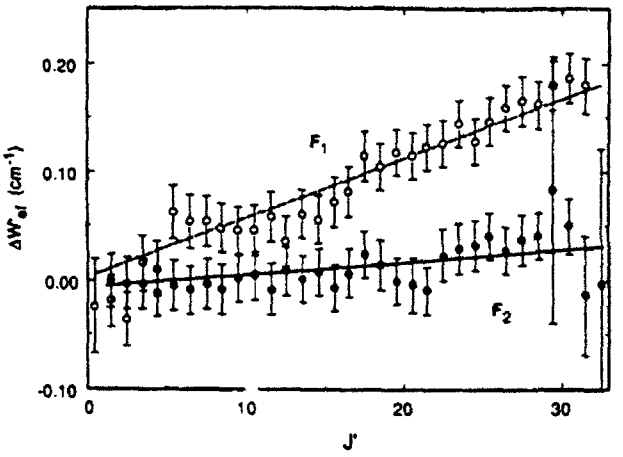

FIG. 5. The circles show the Λ-doublet splitting ($\Delta W'_{ef}$) of $B\,^2\Pi(v=3)$ as a function of rotational level J given by the term values of Table II. The solid and dashed lines give this splitting calculated from the molecular constants of Table III.

by the satellite P- and R-branch lines, which produce deviations in the Λ-doublet splittings in excess of 0.3 cm^{-1} from those predicted from the main branch lines when i,j is taken as f,e. In contrast, the deviations are reduced to only the statistical scatter in the energy differences (~0.03 cm^{-1}) when i,j is taken as e,f.[40] Thus, the order of parity levels is uniquely determined to be $W'_e > W'_f$ in both substates of $B(v=3)$ for all but the very lowest rotational levels, where the order is indeterminate with the accuracy of the present transition energies. This conclusion is opposite to that reached by both Huber[39] for $B(v=1)$, and by Engleman and Rouse[19] for $B(v=0$–$5)$, due to their assumed parity order in the $X\,^2\Pi$ state, which was opposite to that presently[21] accepted.

The Λ-doublet splittings determined from the $B(v=3)$ term values given in Table II are plotted in Fig. 5 as a function of B state rotational quantum number in both the F_1 and F_2 substates. The error bars in this figure reflect the relative errors of the term value differences. The discontinuities that appear in the F_1 splittings near $J=5.5$ and in the F_2 splittings near $J=22.5$ reflect the transition between unobserved (presumed zero) and explicitly measured doublet separations in the lines accessing these two substates. While the weighting of the unsplit lines (Table I) was chosen to minimize these effects, the weighting in itself cannot eliminate them.

C. Molecular constants of $B(v=3)$

The term energies of $B\,^2\Pi(v=3)$, given in Table II were fitted[41] to the effective $^2\Pi$ Hamiltonian of Zare *et al.*[27] This Hamiltonian has the advantage of separating the vibrational and rotational properties of the molecule and has been used to describe $^2\Pi$ states in O_2^+,[42] HCl,[+43] and HF.[+31] Applied to the NO $X\,^2\Pi$ ($v=0$–2), this Hamiltonian successfully reproduces the term values of Amiot *et al.*[29] to within 3×10^{-4} cm^{-1}. Brown *et al.*[44] have discussed in some detail the properties of this Hamiltonian for

TABLE III. Molecular constants of NO $B\,^2\Pi$ ($v=3$). Constants for the $X\,^2\Pi(v=0)$ state are included for reference. All units are cm^{-1}.

	ν_0	A	$A_D(10^{-4})$	B	$D(10^{-6})$	$q(10^{-5})$	$p(10^{-1})$	$o(10^{-2})^a$
Present	48 461.7680(20)[b]	35.6764(38)	10.33(13)	1.079 436(12)	5.347(12)	−2.74(13)	6.48(12)	2.678 85
Hallin *et al.*[c]	48 462.073(22)	35.583(17)	26.83(70)	1.079 477(78)	5.760(70)	...	...	...
Transformed[d]	48 462.073	35.610	24.73	1.079 491	5.760	...	...	...
E&R $\beta(3,7)$[e]	35 918.90	35.76	102	1.079 50	5.0	9.0	−5.5	...
Transformed	48 461.69	35.78	102	1.079 51	5.0	−9.0	5.5	2.28
E&R $\beta(3,8)$[e]	34 238.84	35.82	24	1.079 55	4.4	34	−2.9	
Transformed	48 461.78	35.85	24	1.079 56	4.4	−34	2.9	1.20
$X\,^2\Pi(v=0)$[f]	0.0	123.028 35	3.4386	1.696 1438 5	5.467 30	−9.469[g]	−11.669[h]	−10.5802[i]

[a]Calculated $o=(A/B)p/8$.
[b]Number in parentheses is one standard deviation expressed in units of the least-significant digits.
[c]Reference 28.
[d]Expressed in a form consistent with the present measurement.
[e]Reference 19.
[f]Constants of the $^2\Pi$ Hamiltonian reproducing the $X\,^2\Pi(v=0)$ term values of Ref. 29.
[g]$q_D=-3.4\times10^{-10}$ cm^{-1}.
[h]$p_D=-2.463\times10^{-8}$ cm^{-1}.
[i]$o_D=-2.2334\times10^{-7}$ cm^{-1}.

$^2\Pi$ states and its relationship to other representations. Apart from the vibrational origin ν_0, this Hamiltonian includes terms A and A_D for spin–orbit coupling and its centrifugal correction, B and D for rotation and its centrifugal correction, and q, p, and o for the Λ doubling. The value of the spin–rotation constant γ is not separable from the equivalent effect of A_D on the $^2\Pi$ energy levels. Hence γ is constrained to a value of zero in the fit,[27,43,44] with its effects incorporated in the value of A_D obtained from the fit. Λ doubling is treated in the unique perturber approximation,[27] i.e., it is attributed to perturbation by a single, effective $^2\Sigma^{\pm}$ state, and the parameter o is constrained in the fit to the value $o=1/8(A/B)p$. The assigned parity of the levels in $B(v=3)$ can be attributed to either a $^2\Sigma^-$ state lying energetically above the B state or to a $^2\Sigma^+$ lying below the B state. (The signs of the two constants q and p are opposite in the two cases.) The case of a $^2\Sigma^-$ was empirically chosen here because its choice produced smaller (0.5%) residuals in the fit. It is also the more reasonable choice, since the $3s\sigma$ $A\,^2\Sigma^+$ state is the only $^2\Sigma^+$ state lying energetically below the B state, and the B–A interaction is very weak, as evidenced by the very small contribution of the B state to the spin–rotation constant of the A state.[45] The $^2\Sigma^-$ perturber[29,46] is also chosen for Λ doubling in the $X\,^2\Pi$, a choice well supported by the calculations of de Vivie and Peyerimhoff.[38]

The molecular constants obtained for $B(v=3)$ are given in Table III, where the stated uncertainties represent one standard error of statistical uncertainty. Also given for reference are the constants for $X(v=0)$ in this same representation. The calculated values of the constant o are included for each of these states. The vibrational origin is the energetic difference between the origin of $B(v=3)$ and the origin of $X(v=0)$. These respective origins lie 16.7325 cm^{-1} above $B\,^2\Pi_{1/2}(v=3,\ J=0.5f)$ and 59.9359 cm^{-1} above $X\,^2\Pi_{1/2}(v=0,\ J=0.5e)$, the lowest energy levels in each of these states. The estimated absolute error of the present line measurements (0.05 cm^{-1}) is not explicitly included in the statistical uncertainty of the origins given in the table. The standard deviation of the fit was 0.0175 cm^{-1}, slightly higher than that obtained in the model-free term value fit. This probably reflects the effect of the latent line doublings in the Hamiltonian fit rather than an obvious deficiency in the $^2\Pi$ Hamiltonian itself.

The splitting of the e/f levels calculated from the model Hamiltonian using the molecular constants of Table III is shown by the dashed and solid lines in Fig. 5. Essentially identical splittings and constants, viz. $q=-3.15(86)\times10^{-5}$ cm^{-1} and $p=6.37(29)\times10^{-3}$ cm^{-1}, are obtained from a direct fit of the splittings alone to the Mulliken and Christy[47] formula, following the association of level parity[48] with label c and d specified by Mulliken.[49] Comparison can be made with the Λ doublings observed by Huber[39] in the $B'\,^2\Delta(1)\rightarrow B\,^2\Pi(0)$ band. Following a parity assignment opposite to that determined here, Huber determined a value of $p=-6.4\times10^{-3}$ cm^{-1} from a linear fit to the $J+1/2$ dependence of the F_1 splittings. Applying the full Mulliken and Christy formula to Huber's measurements and the revised parity assignment yields $q=-6.63(75)\times10^{-5}$ cm^{-1} and $p=6.74(30)\times10^{-3}$ cm^{-1}. This value of p is very close to that determined for $v=3$, suggesting little, if any, vibrational dependence in the $B\,^2\Pi$ Λ doubling over the range $0\leq v\leq3$. The value of q determined from Huber's data is significantly different from that in $v=3$, but since its magnitude is greatly influenced by the splittings in the F_2 component of the $^2\Pi$ state, which are completely latent in Huber's measurements, a true vibrational dependence of q is not necessarily indicated by this difference. De Vivie-Riedle *et al.*[15] have recently calculated the Λ doubling in the Rydberg $C\,^2\Pi$ state, which adiabatically correlates to the valence $B\,^2\Pi$ at larger internuclear separations. Unfortunately their calculations did not extend to sufficiently large internuclear separations to be of use in identifying the

contributions to the Λ doubling observed here in the lower vibrational levels of the B state.

Molecular constants for $B(v=3)$ have been reported by Hallin *et al.*[28] and by Engleman and Rouse.[19] Each of these studies derives the constants from β bands that terminate in relatively high vibrational levels of the X state. Hallin *et al.* refit the emission lines reported by Jenkins, Barton, and Mulliken[1] and merged these results with their infrared measurements to obtain the molecular constants given in Table III. Λ-doublet splittings were available only in the (0,10) and (0,11) bands of Jenkins *et al.* and were not resolved in the infrared bands; hence the constants of Hallin *et al.* do not include the constants associated with this effect. Transformation[44] must be made to the constants B, A, and A_D of Hallin *et al.* for comparison with the present values, viz. $A_{\text{trans}} \sim A_{\text{Hallin}} - o$, $B_{\text{trans}} \sim B_{\text{Hallin}} - 0.5q$, and $A_{D_{\text{trans}}} \sim A_{D_{\text{Hallin}}} - p[B/(A-2B)]$, where the unsubscripted constants are those values given in the present work. Hallin *et al.* do not report vibrational origins for the B state, but give origins for each of the β bands and infrared bands used in their analysis. Only two bands, $\beta(3,8)$ and $\beta(3,16)$ access $B(3)$ and the energy of $B(3)$ derives only from the $\beta(3,8)$. We can calculate the vibrational origin of $B(3)$ from the band origin combination $\beta(3,8) - \beta(0,8) + \beta(0,5) + (5,3) + (3,0)$, where the result and the sum of the individual uncertainties in this combination is given in the Table. It can be seen in Table III that there is good agreement between the two determinations of A and B, but significant discrepancies exist for the centrifugal distortion corrections A_D and D, and in the band origin. The band origin discrepancy was to be expected; Hallin *et al.* noted the impossibility of merging the band origins obtained from the β bands into consistent set of energy levels and attributed this to systematic wavelength calibration errors in the Jenkins *et al.* data. Judging from the magnitude of the discrepancy here, these wavelength calibration errors are quite large in comparison with the accuracy of ~ 0.05 cm^{-1} estimated by Jenkins *et al.* Comparison of the Hallin *et al.* constants for $X(v=8)$ with those of Amiot and Verges,[20] which are based on a more extensive set of infrared measurements, reveals discrepancies in the values of A_D'' and D'' of 15.78×10^{-4} cm^{-1} and -0.29×10^{-6} cm^{-1}, respectively, which are comparable to the discrepancies in the $B(3)$ constants. As noted by Amiot and Verges,[20] the Hallin *et al.* values for A_D change sign for those vibrational levels ($v'' > 6$) where all information derives from the β-band data.

Bands in the β system have been observed at high resolution by Engleman and Rouse[19] in the absorption spectrum of the photolysis products of NOCl. Two of their eleven bands access $B(3)$: $\beta(3,7)$ and $\beta(3,8)$. The constants for $B(3)$ they obtained by fitting these bands to the $^2\Pi$ energy expressions of Almy and Horsfall[50] are given in Table III. Note that they have adopted a parity convention for Λ doubling in the X state ($q'' > 0$, $p'' > 0$) which is opposite to that of Amiot *et al.*[29] and to that used in the present work. For comparison with the present results, the following transformations must be applied to the Engleman and Rouse constants: $T^{\Pi}_{\text{trans}} \sim T^{\Pi}_{er} + B_{er} + o_{er}/2$, $B_{\text{trans}} \sim B_{er} + q_{er}/2$, $A_{\text{trans}} \sim A_{er} - o_{er}$, $q_{\text{trans}} \sim -q_{er}$, $p_{\text{trans}} \sim -p_{er}$, and $A_{D_{\text{trans}}} \sim C_{er}$, where $o = (A/B)p/8$ and T^{Π} specifies the vibrational origin of the Π state. To transform the band origin to a useful difference of upper and lower state vibrational energies (Ref. 51), T^{Π}_{trans} must be evaluated for both the B state and the X state levels: $\nu_{\text{trans}} \sim \nu_{er} + (B'_{er} - B''_{er}) + 0.5(o'_{er} - o''_{er})$. To reference the band origin to the vibrational origin of $X(0)$ for comparison with the present measurements, the vibrational energy of the relevant ground state vibrational level [relative to that of $X(0)$] given by Amiot and Verges[20] is added to the transformed origin. These transformed values are reported in Table III. The band origins compare quite favorably with that determined in the present measurement, with deviations of $-.08$ and $+0.01$ cm^{-1} for $\beta(3,7)$ and $\beta(3,8)$, respectively. Nevertheless, the deviation associated with the $\beta(3,0)$ origin is quite large compared to the estimated accuracy of 0.01 cm^{-1} attributed by Engleman and Rouse to the positions of strong unblended lines. Amiot and Verges[52] have estimated that the actual line position accuracy of Engleman and Rouse is 0.05 cm^{-1}, which appears to also be supported here (see below). In most of the constants, the fluctuation in values for the various vibrational bands are comparable to their difference from the constants in the present determination. An exception is the spin–orbit coupling constant A, which is consistently larger than that of the present measurement. It appears that the magnitude of A has been affected by the very large, but poorly defined, centrifugal correction to this constant in the work of Engleman and Rouse. This is supported by a direct comparison of the Engleman and Rouse line positions for $\beta(3,8)$ with those computed from the present set of constants for $B(3)$ and the $X(8)$ constants (transformed, with the exception of the vibrational origin) of Amiot and Verges, assuming $q_8'' = -9 \times 10^{-5}$ and $p_8'' = -1.162 \times 10^{-2}$cm^{-1}. Excluding five lines in their data with deviations in excess of 0.1 cm^{-1}, the calculated and measured line positions agreed with a mean deviation of -0.018 cm^{-1} and a standard deviation about this mean of 0.037 cm^{-1}. The average deviation (calc–obs) of the F_1 lines was -0.019 cm^{-1} while that for F_2 was -0.018 cm^{-1}. A similar comparison of the $\beta(3,7)$ line positions produces an average deviation of -0.039 cm^{-1} and a standard deviation of 0.0365 cm^{-1}. The average deviation in the spin–orbit component branches is -0.0370 cm^{-1} in F_1 and -0.0412 cm^{-1} in F_2. Certainly no systematic error exists in the Engleman and Rouse data that would affect the spin–orbit coupling constant for the B state.

Since a reasonable degree of accuracy is demonstrated by the Engleman and Rouse[19] measurements, it is interesting to compare their $\beta(3,8)$ line positions with those reported by Jenkins, Barton, and Mulliken,[1] in view of the large band origin error noted in the Hallin *et al.*[28] fit. Excluding the five lines noted above and all marked blends, the deviations [Engleman and Rouse-Jenkins *et al.*] observed in the P_{11} branch ranged from -0.189–0.013 cm^{-1} with a mean deviation of -0.094 cm^{-1}. In the R_{11} branch, the deviations ranged from -0.156–$+0.100$ cm^{-1} with an average of -0.062 cm^{-1}. In P_{22}, range $= -0.299/-0.118$

cm^{-1}, average $=-0.175$ cm^{-1} and in R_{22}, range $=-0.920/-0.077$ cm^{-1}, average $=-0.204$ cm^{-1}, excluding the large deviation in the $R_{22}(19.5)$ line. Apart from the large scatter in the line positions, far in excess of the combined estimated accuracies ($0.01+0.05$ cm^{-1}) of the measurements, it should be noted that mean deviation in the F_1 branches is -0.078 cm^{-1} while that in the F_2 branches is -0.190 cm^{-1}. This systematic error is quite large (0.112 cm^{-1}) but is not reflected in the spin–orbit coupling constant of Hallin *et al.*, presumably because of contributions from $\beta(3,16)$ to this constant.

D. Perturbations

There is no indication in the fit to molecular constants of any localized perturbations in $B(3)$ at the level of >0.03 cm^{-1} over the complete range of rotational levels probed here. This is significant in that the levels of $a\,^4\Pi(v=12)$ state intersect $B(3)$ within the observed levels.[4] Using the term energies of the $a\,^4\Pi$ state[17] and the present term energies for $B(3)$, we find that $B\,^2\Pi_{3/2}(v=3, J=17.5)$ lies 7.7 cm^{-1} below and $(v=3, J=18.5)$ lies 0.96 cm^{-1} above the same rotational levels in $a\,^4\Pi_{3/2}(v=12)$. A similar intersection between the $\Omega=1/2$ components should also occur near $J>31.5$, but this high J represents a significant extrapolation with the $a\,^4\Pi$ rotational constants.[53] Field, Gottscho, and Miescher[54] have presented explicit matrix elements for the B–a perturbation in a Hunds case (a) basis

$$\langle v,a\,^4\Pi^{\pm}_{3/2}|H_{so}|B\,^2\Pi^{\pm}_{3/2},v'\rangle = -(0.322a_1+0.149a_2)\langle v|v'\rangle$$
$$= 53\ cm^{-1}\langle v|v'\rangle, \qquad (5)$$

using their estimates ($a_1=107$ cm^{-1}, $a_2=124$ cm^{-1}) for the one electron orbital integrals. The identical matrix element describes the interaction of the $\Omega=1/2$ components. As seen in Eq. (5), the matrix element of the a–B interaction is potentially quite large, but is modified by a vibrational overlap integral $\langle v|v'\rangle$, which is quite small for the vibrational levels considered here: $\langle 12|3\rangle=-1.61\times10^{-4}$, evaluated from the (rotationless) Rydberg–Klein–Rees (RKR) potential energy curves for the two states. This suggests that the level shift to be expected at either the $\Omega=1/2$ ($J\sim17.5$) or $\Omega=3/2$ ($J\sim31.5$) crossings is $<9\times10^{-3}$ cm^{-1}, which is just below the precision of the present measurements.

Much larger spin–orbit matrix elements (~3 cm^{-1}) are estimated for the $B\,^2\Pi(v=3)$–$b\,^4\Sigma^-$ perturbation due to the better vibrational overlap of these two states. However, the origin[53] of the nearest b state level ($v=2$) lies 87 cm^{-1} above that of $B(3)$. Since $b(2)$ has the larger rotational constant, the intersection of its levels with either component of $B(3)$ is not possible. Nevertheless, Huber and Vervloet[53] have observed large perturbations in the rotational structure associated with the $b(2)\sim a(0)$ band. The lack of any significant perturbation in the $B(3)$ rotational levels supports their suggestion that the $b(2)$ perturbation is due to $a(12)$.

The only other state in the region of $B(3)$ is $A\,^2\Sigma^+(v=1)$, with an origin 1981 cm^{-1} below that of $B(3)$. Intersection of these levels would occur at $J\sim48.5$, but as noted above (Sec. III C), the B–A interaction is expected to be weak.[45]

Despite the lack of local perturbations in the $B(3)$ levels, a strong vibronic perturbation[10] of the B state by other NO valence ($L\,^2\Pi$) and $n\rho\pi$ Rydberg ($C,K,Q,W\,^2\Pi$) states is known to occur. This have been treated in detail by Gallusser and Dressler[12] and more recently by Raoult.[13] Profound perturbations occur in levels $B(v>7)$, where the perturbing states are near degenerate, but lower vibrational levels of the B state are also affected by the couplings. Gallusser and Dressler[12] estimate energy shifts ranging from -3 cm^{-1} for $B(0)$ to -23 cm^{-1} in $B(3)$ as a result of this perturbation, which will certainly affect the interpretation of the molecular constants given in Table III. An additional effect of the perturbation may arise in the relative branch intensities of the $B(3)\leftarrow X(0)$ absorption spectrum observed here. For the reasons discussed above (Sec. II D), quantitative intensity measurements are difficult with the technique employed here. Nevertheless, qualitative comparison can be made between the present observations and the branch intensities predicted by the Hönl–London factors[26,55] or equivalently, by the eigenvectors of the B and $X\,^2\Pi$ Hamiltonians.[27] By summing the observed intensities over ranges of unblended lines at both low J and high J, two observations are clear (1) the observed intensities in the Q branches relative to the P and R branches are approximately a factor of 2 higher than predicted for unperturbed states and (2) the lines in branches terminating in F_2' are approximately a factor of 2 stronger than predicted when compared with the intensity of branches terminating in F_1'.

E. Other transitions

An intense series of violet degraded lines appear ~57 cm^{-1} to the blue of the red shaded $\beta(3,0)$ band. These are shown in Fig. 6, which presents the MPI spectrum between the $\beta(3,0)$ R_{11} bandhead and the termination of the present investigation near $48\,619$ cm^{-1}. The lines in this series could be assigned by inspection to the $\gamma(2,0)$ band of the $^{14}N^{18}O$ isotope, present in the NO gas at natural abundance. The assigned lines, listed in Table IV, are confirmed using the $X(0)$ term values of Amiot *et al.*[29] for this isotope. A fit to the line positions in Table IV using fixed ground state term energies[29] yields a band origin of $48\,664.135(13)$ cm^{-1} and a rotational constant for the $A\,^2\Sigma^+(v=2)$ of $B=1.848\,39(9)$ cm^{-1}, presuming values for the spin rotation constant and the centrifugal correction to the rotational constant are well approximated by the values $\gamma=-2.6\times10^{-3}$ cm^{-1} and $D=5.1131\times10^{-6}$ cm^{-1}, respectively. At photon energies >48614.5 cm^{-1}, the $\gamma(2,0)$ lines are overlapped by the lines at and near the P_{12} bandhead of the even more intense $\gamma(2,0)$ band in the $^{15}N^{16}O$ isotopomer, as indicated in Fig. 6. The positions of several lines in the P_{12} branch could be measured. These are also listed in Table IV. A fit of these lines to the $^2\Sigma$ Hamiltonian with $\gamma=-2.6\times10^{-3}$ cm^{-1} and $D=5.2938\times10^{-6}$ cm^{-1} and the $X(0)$ term energies of Amiot *et al.*[29]

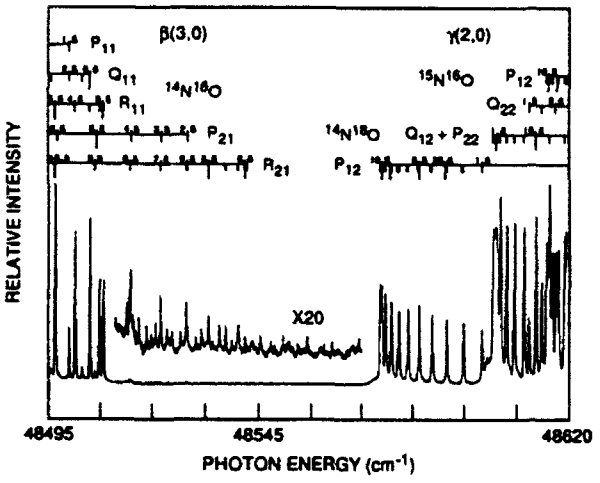

FIG. 6. The 1+1 multiphoton ionization spectrum of NO in the region 48 495–48 620 cm^{-1}. The $\beta(3,0)$ band of $^{14}N^{16}O$ occurs at photon energies $<48\,543$ cm^{-1} with the R_{21} branch, barely visible on the scale of the figure, also shown on a magnified scale. Weak features interspersed with this branch also appear at higher photon energies and are not associated with $\beta(3,0)$. The $\gamma(2,0)$ band occurs as the series of strong lines at photon energies $>48\,574$ cm^{-1} for $^{14}N^{18}O$ and $>48\,614$ cm^{-1} for $^{15}N^{16}O$.

TABLE IV. Line positions in the $A\,^2\Sigma^+(v=2)\leftarrow X\,^2\Pi_{1/2}(v=0)$ $\gamma(2,0)$ band of $^{14}N^{18}O$ and $^{15}N^{16}O$ in units of cm^{-1}. Column headings denote branch and lower state parity label. The absolute accuracy of the line positions is ± 0.05 cm^{-1}.

	$^{14}N^{18}O$			$^{15}N^{16}O$
J''	$P_{12}(e)$	$Q_{12},P_{22}(f)$[a]	$Q_{22}(e)$	$P_{12}(e)$
1.5	48 599.337		48 610.415	
2.5	48 594.893		48 613.366	
3.5	48 590.871		48 616.731	
4.5	48 587.295			
5.5	48 584.182			
6.5	48 581.494	48 603.618		
7.5	48 579.221	48 605.102		48 619.211
8.5	48 577.398	48 606.956		48 617.374
9.5	48 575.991	48 609.263		48 615.976
10.5	48 575.060[c]	48 612.028		48 614.916[c]
11.5	48 574.611[c]	48 615.208[c]		48 614.501[c]
12.5	48 574.611[d]	48 618.832[c]		48 614.501[c]
13.5	$P_{12}(10.5)$[b]			48 614.916[d]
14.5	$P_{12}(9.5)$			48 615.681
15.5	$P_{12}(8.5)$			48 617.032
16.5	48 579.891[c]			$^{14,18}Q_{12}(12.5)$
17.5	48 581.081[c]			
18.5	48 583.747[c]			
19.5	48 586.851[c]			
20.5	48 590.382[c]			
21.5	48 594.459[c]			

[a]Lines in these branches are persistently blended with a separation <0.03 cm^{-1} over the observed range of J''.

[b]Where a line is overlapped by a stronger transition, identification of the stronger transition is given.

[c]Line weighted by the reciprocal square of two standard deviations in the fits.

[d]Line weighted by the reciprocal square of three standard deviations in the fits.

yields a band origin of $\nu_0=48\,704.588(41)$ cm^{-1} and a rotational constant $B=1.880\,42(31)$ cm^{-1}. Although these constants are poorly determined due to the paucity of lines, they nevertheless allow for verification in the calculation of isotope shifts. The ratio of the observed intensities of $^{15}N^{16}O$ lines to $^{14}N^{18}O$ lines is in accord with the natural abundance ratio of the ^{15}N and ^{18}O isotopes (1.8).

It should also be noted that the line profiles of the γ-band transitions are observed to be appreciably wider (FWHM $=0.32$ cm^{-1}) than those of the β bands and more poorly described by a Gaussian peak shape, having rather broad Lorentzian-like bases. This probably reflects the effects of saturation arising from the ~ 150 times larger absorption coefficient[25] of the $\gamma(2,0)$ band relative to that of $\beta(3,0)$. A substantial difference also in photoionization rates is reflected by the intensities of the bands observed here. The ratio of the relative MPI intensity in the $\beta(3,0)$ R_{11} branch (observed peak area divided by calculated line strength) to that in the $\gamma(2,0)$ P_{12} branch of $^{14}N^{18}O$ is 0.19. In contrast, the ratio of the integrated absorption coefficients[25] $\beta(3,0)/\gamma(2,0)$ of the normal isotope is 6.8×10^{-3}. Considering the fractional abundance of ^{18}O (0.002 04) applied to the $\gamma(2,0)$ band, the expected absorption ratio would be $\beta(3,0)/\gamma(2,0)\sim 3.4$. This implies that the photoionization cross section of $A\,^2\Sigma^+(v=2)$ is ≥ 18 times larger than that of $B\,^2\Pi(v=3)$. This is commensurate with the relative ease for photoionization of the $3s\sigma$ Rydberg electron of $A\,^2\Sigma^+$ $(...3\sigma^2\,1\pi^4\,3s\sigma^1)$ to produce NO^+ $X\,^1\Sigma^+(...3\sigma^2\,1\pi^4)$, in comparison with the two electron process required from the $B\,^2\Pi$ $(...3\sigma^2\,1\pi^3\,1\pi^{*2})$ valence configuration.[14]

Apart from lines associated with the $\gamma(2,0)$ bands of the isotopes, an additional 80 features were detected using the criteria discussed in Sec. II B within the covered wavelength region. Most of these features were extremely weak; only 25 of the features could be detected in more than one spectral scan with the remainder appearing only in those scans offering the widest dynamic range in intensity. Three of these features appear in Fig. 2, where they are indicated by asterisks, and others appear interspersed with the $\beta(3,0)$ R_{21} branch lines in Fig. 6, where they are unmarked. A plot of the positions and intensities of these lines is given in Fig. 7. Note that the strongest lines in this figure are only 5% the intensity of the strong lines in the $\beta(3,0)$ band; hence many other lines are likely obscured by $\beta(3,0)$ features. The strong lines in the region of 48 460–48 490 cm^{-1} are almost certainly associated with $b\,^4\Sigma^-(v=2)\leftarrow X\,^2\Pi_{3/2}(v=0)$ transitions, comparing the line positions and intensities recently observed for this band using laser-induced fluorescence.[22] However, as mentioned above, $b(2)$ is strongly perturbed[53] [by $a\,^4\Pi(v=12)$] and a specific rotational assignment of the lines observed here is not yet possible.

IV. CONCLUSIONS

Using the technique of 1+1 MPI, lines in ten of the branches of the $B\,^2\Pi(v=3)\leftarrow X\,^2\Pi(v=0)$ system have been observed with an absolute accuracy of 0.05 cm^{-1} and a relative accuracy of 0.036 cm^{-1}. These measurements

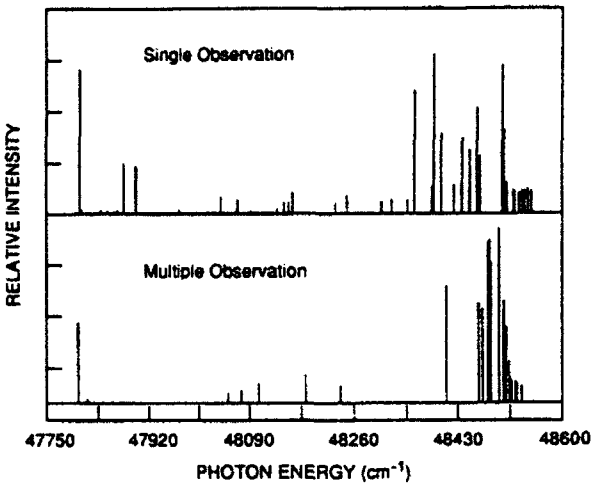

FIG. 7. Positions and relative intensities of the unassigned lines observed in the region 47 750–48 600 cm^{-1}. Note that many associated lines may be obscured by $\beta(3,0)$ transitions, which have a relative intensity <250 on the scale of this figure. Lines in the lower figure denote those transitions that were observed in at least two scans. Lines detected in only a single scan within this region are shown in the upper spectrum. These single-observation lines should be considered less reliable.

have allowed for the first time a definitive specification of rotational level parity in the $B(v=3)$ state and provide accurate level energies in $B(3)$ over the range $0.5<J<32.5$. A rather large error (4.6 cm^{-1}) in the presumed energy of the lowest rotational levels of $B(3)$ is found to be propagated in the literature from ca. 1927 to the present time, despite the fact that most of this error was identified by Callear and Smith[18] in 1965. It is anticipated that similar errors apply for all $B(v<4)$ levels. Molecular constants for $B(3)$ are determined utilizing the unique perturber approximation. It appears that interaction with the $G\,^2\Sigma^-$ accounts for much of the observed Λ doubling in $B(3)$. It would be useful if *ab initio* calculations of this doubling, which have thus far been performed for the $X\,^2\Pi$ and $C\,^2\Pi$ states,[15,38] were also extended to the B state. The line positions of $\beta(3,7)$ and $\beta(3,8)$ bands of Engleman and Rouse[19] have been verified to be free of systematic errors >0.05 cm^{-1} by comparison to those calculated from the present $B(3)$ molecular constants and the $X(8)$ constants of Amiot and Verges,[20] with the implication that line positions in their other nine β bands exhibit a similar degree of accuracy. Unfortunately, the rotational development in the Engleman and Rouse bands is not extensive ($J_{max}<22.5$), which limits their utility in establishing the Λ doubling in the $X\,^2\Pi$ state, the experimental knowledge[29,30] of which is limited to $0<v<2$ at the present time. In this regard, extension of the ground state Λ-doubling calculations[38] to $v>2$ would be quite useful.

It should be noted that there have been a great many observations of the NO band systems, in particular the $A\,^2\Sigma^+$–$X\,^2\Pi$ γ system, some[56] with sub-Doppler resolution. Yet only two of these measurements,[57,58] excluding the present, have reported calibrated line positions. As a result, the absolute energies for most of the levels in the $^2\Sigma$ and $^2\Pi$ states, while in some cases known with high relative precision, remain uncertain by >0.1 cm^{-1}.

ACKNOWLEDGMENT

This work was supported in part by the U.S. Air Force Office of Scientific Research under Contract Nos. F49620-88-0003 and F49620-90-C-0044.

[1] F. A. Jenkins, H. A. Barton, and R. S. Mulliken, Phys. Rev. **30**, 150 (1927).
[2] L. A. Gundel, D. W. Setser, M. A. Clyne, J. A. Coxon, and W. Nip, J. Chem. Phys. **64**, 4390 (1976).
[3] Ph. Caubet, S. J. Dearden, and G. Dorthe, Chem. Phys. Lett. **108**, 217 (1984).
[4] E. Miescher, J. Chem. Phys. **73**, 3088 (1980).
[5] A. Lagerqvist and E. Miescher, Helv. Phys. Acta **31**, 221 (1958).
[6] A. Lagerqvist and E. Miescher, Can. J. Phys. **44**, 1525 (1966).
[7] E. Miescher, Can. J. Phys. **54**, 2074 (1976).
[8] W. Y. Cheung, W. A. Chupka, S. D. Colson, D. Gauyacq, P. Avouris, and J. J. Wynne, J. Phys. Chem. **90**, 1086 (1986).
[9] J. Kimman, M. Lavollee, and M. J. Van der Wiel, Chem. Phys. **97**, 137 (1985).
[10] K. Dressler and E. Miescher, Astrophys. J. **141**, 1266 (1965).
[11] P. Felenbok and H. Lefebvre-Brion, Can. J. Phys. **44**, 1677 (1966).
[12] R. Gallusser and K. Dressler, J. Chem. Phys. **76**, 4311 (1982).
[13] M. Raoult, J. Chem. Phys. **87**, 4736 (1987).
[14] R. de Vivie and S. D. Peyerimhoff, J. Chem. Phys. **89**, 3028 (1988).
[15] R. de Vivie-Riedle, M. C. van Hemert, and S. D. Peyerimhoff, J. Chem. Phys. **92**, 3613 (1990).
[16] S. R. Langhoff, H. Partridge, and C. W. Bauschlicher, J. Chem. Phys. **94**, 6638 (1991).
[17] P. C. Cosby and T. G. Slanger, J. Chem. Phys. **95**, 2203 (1991).
[18] A. B. Callear and I. W. M. Smith, Trans. Faraday Soc. **61**, 1303 (1965).
[19] (a) R. Engleman and P. E. Rouse, J. Mol. Spectrosc. **37**, 240 (1971); (b) R. Engleman, P. E. Rouse, H. M. Peek, and V. D. Baiamonte, *The Beta and Gamma Band Systems of Nitric Oxide* (Los Alamos Scientific Laboratory Report LA-4364, 1970).
[20] C. Amiot and J. Verges, J. Mol. Spectrosc. **81**, 424 (1980).
[21] F. H. Geuzebroek, M. G. Tenner, A. W. Kleyn, H. Zacharias, and S. Stolte, Chem. Phys. Lett. **187**, 520 (1991).
[22] M. J. Dyer, G. W. Faris, P. C. Cosby, D. L. Huestis, and T. G. Slanger (submitted for publication).
[23] S. Gerstenkorn and P. Luc, *Atlas du Spectre d'Absorption de la Mole'cule de l'Iode entre 14800–20000 cm^{-1}* (Editions du CNRS, Paris, 1978).
[24] S. Gerstenkorn and P. Luc, *Absolute Iodine Standards Measured by Means of Fourier Transform Spectroscopy* [Rev. Phys. Appl. **14**, 791 (1979)].
[25] H. A. Barton, F. A. Jenkins, and R. S. Mulliken, Phys. Rev. **30**, 175 (1927).
[26] G. W. Bethke, J. Chem. Phys. **31**, 662 (1959).
[27] R. N. Zare, A. L. Schmeltekopf, W. J. Harrop, and D. L. Albritton, J. Mol. Spectrosc. **46**, 37 (1973); copies of the programs RLS for calculation of transition line strengths and LINFIT for nonlinear least squares fitting of line positions to molecular constants were kindly provided by these authors.
[28] K-E. J. Hallin, J. W. C. Johns, D. W. Lepard, A. W. Mantz, D. L. Wall, and K. N. Rao, J. Mol. Spectrosc. **74**, 26 (1979).
[29] C. Amiot, R. Bacis, and G. Guelachvili, Can. J. Phys. **56**, 251 (1978).
[30] D. L. Albritton, W. J. Harrop, A. L. Schmeltekopf, R. N. Zare, and E. L. Crow, J. Mol. Spectrosc. **46**, 67 (1973).
[31] P. C. Cosby, H. Helm, and M. Larzilliere, J. Chem. Phys. **94**, 92 (1991).
[32] R. F. Barrow and E. Miescher, Proc. Phys. Soc. London A **70**, 219 (1957).
[33] Barrow and Miescher do not specify the source of the energies for many of the B state levels that they list. Callear and Smith (Ref. 18) attribute this source to the formulae of Jenkins, Barton, and Mulliken (Ref. 1), which were derived from emission band measurements terminating in $X(v>4)$.
[34] Energies for $v>5$ are based on the direct absorption measurements of Miescher and co-workers (Ref. 5), which appear to be of high quality.

See G. E. Gadd and T. G. Slanger, Chem. Phys. Lett. **169**, 581 (1990).
[35] J. M. Brown, J. T. Hougen, K.-P. Huber, J. W. C. Johns, I. Kopp, H. Lefebvre-Brion, A. J. Merer, D. A. Ramsay, J. Rostas, and R. N. Zare, J. Mol. Spectrosc. **55**, 500 (1975).
[36] H. Lefebvre-Brion and R. W. Field, *Perturbations in the Spectra of Diatomic Molecules* (Academic, Orlando, 1986).
[37] H. Lefebvre-Brion and C. M. Moser, J. Mol. Spectrosc. **15**, 211 (1965).
[38] R. de Vivie and S. D. Peyerimhoff, J. Chem. Phys. **90**, 3660 (1989).
[39] M. Huber, Helv. Phys. Acta **37**, 329 (1964).
[40] The numerical equivalent of this result is manifested by an eightfold increase in the standard deviation of the term value fit when the parity labels are reversed.
[41] Equivalent results are obtained by fitting the $\beta(3,0)$ transitions in Table I, using the relative line weighting given in that table and holding the values of the $X\,^2\Pi(v=0)$ constants fixed to those values that reproduce the X state term energies given by Ref. 29.
[42] D. L. Albritton, W. J. Harrop, and A. L. Schmeltekopf, J. Mol. Spectrosc. **46**, 89 (1973).
[43] K. L. Saenger, R. N. Zare, and C. W. Mathews, J. Mol. Spectrosc. **61**, 216 (1976).
[44] J. M. Brown, E. A. Colbourn, J. K. G. Watson, and F. D. Wayne, J. Mol. Spectrosc. **74**, 294 (1979).
[45] T. Bergeman and R. N. Zare, J. Chem. Phys. **61**, 4500 (1974).
[46] A. Lofthus and E. Miescher, Can. J. Phys. **42**, 848 (1964).
[47] R. S. Mulliken and A. Christy, Phys. Rev. **38**, 87 (1931).
[48] The transformation between the labels *e,f* and *c,d* defined by Brown *et al.* (Ref. 35) for $S=1/2$, $\Lambda=1$ appears to be opposite to that specified by Mulliken (Ref. 49) for a regular $^2\Pi$ state.
[49] R. S. Mulliken, Rev. Mod. Phys. **3**, 89 (1931).
[50] G. M. Almy and R. B. Horsfall, Phys. Rev. **51**, 491 (1937).
[51] Removing the implicit rotational and magnetic contributions to the $^2\Pi$ origin is particularly crucial when interpreting the band origins of the γ system of Engleman and Rouse (Ref. 19), where the correction is large and varies by 0.15 cm^{-1} over the range of $X\,^2\Pi$ levels probed in their measurements. For the β system, the correction varies by only 0.022 cm^{-1}.
[52] C. Amiot and J. Verges, Phys. Scr. **26**, 422 (1982).
[53] K. P. Huber and M. Vervloet, J. Mol. Spectrosc. **129**, 1 (1988).
[54] R. W. Field, R. A. Gottscho, and E. Miescher, J. Mol. Spectrosc. **58**, 394 (1975).
[55] I. Kovacs, *Rotational Structure in the Spectra of Diatomic Molecules* (American Elsevier, New York, 1969), Chap. 3.
[56] A. Timmermann and R. Wallenstein, Opt. Commun. **39**, 239 (1981).
[57] D. T. Biernacki, S. D. Colson, and E. E. Eyler, J. Chem. Phys. **89**, 2599 (1988).
[58] M. Versluis, M. Ebben, M. Drabbels, and J. J. ter Meulen, Appl. Opt. **30**, 5229 (1991).

Appendix D

TWO-PHOTON EXCITATION OF NEON AT 133 nm

Two-photon excitation of neon at 133 nm

Gregory W. Faris and Mark J. Dyer

Molecular Physics Laboratory, SRI International, Menlo Park, California 94025

Received October 9, 1992

High VUV powers, up to 2.5 kW at 133 nm, are obtained from two-photon-resonant, difference-frequency generation in hydrogen by using an ArF excimer laser and a frequency-doubled Nd:YAG-pumped dye laser. This radiation is used to perform two-photon excitation of neon at greater than 150 000 cm^{-1}, the shortest two-photon transition yet accessed to our knowledge.

Two-photon spectroscopy using VUV radiation allows access of very-high-lying states, in the range of 100 000 to 200 000 cm^{-1}. By using a relatively simple two-laser system, we have demonstrated two-photon-excited fluorescence using radiation at 133 nm, the shortest two-photon spectroscopy yet demonstrated to our knowledge. The excitation scheme is shown in Fig. 1.

The ability to perform two-photon spectroscopy with VUV radiation opens several new opportunities for spectroscopy and optical diagnostics, including the excitation of transitions in the extreme-ultraviolet (XUV) range that are not single-photon-allowed transitions and the possibility of performing spatially resolved diagnostic measurements through windows at XUV energies. Thus, for example, light atomic ions may be detected for diagnostics of plasma processing, fusion reactors, or plasma propulsion.

There have been numerous demonstrations of two-photon spectroscopy at two-photon energies of less than 118 000 cm^{-1} by the use of various techniques. Raman shifting has been used to produce VUV for two-photon spectroscopy in atomic fluorine and H_2 at energies of ~115 000 to 118 000 cm^{-1} by use of a frequency-doubled dye laser[1] or an ArF excimer laser as primary sources.[2] With light at 193 nm from an ArF excimer laser, two-photon experiments at ~103 000 cm^{-1} have been performed in H_2 and Kr.[3-6] By the use of different wavelengths for the two photons (i.e., mixing one photon in the visible or near-infrared region with another from synchrotron radiation[7] or the ninth harmonic of a Nd:YAG laser[8]), excitation of two-photon transitions in the range of 70 000 to 109 000 cm^{-1} has been achieved. Further progress toward shorter wavelengths by using these approaches is limited by low conversion efficiencies and large intensity fluctuations for Raman shifting to wavelengths below ~170 nm and by the extremely short wavelengths required for the shorter wavelength in two-color mixing techniques.

To perform short VUV wavelength two-photon spectroscopy, we have adopted the two-photon-resonant, difference-frequency generation technique.[9] This technique has been used for two-photon excitation of Ar at 187 nm.[10] In this four-wave-mixing approach, one laser at frequency ν_1 is tuned to a two-photon resonance and mixed with a second laser at ν_2. Tuning the second laser provides tunable radiation at frequency $2\nu_1 - \nu_2$. We use a dual-discharge tunable ArF excimer laser (Lambda Physik EMG150) as the two-photon-resonant laser and a frequency-doubled dye laser as the second laser. A tunable ArF excimer laser can reach two-photon resonances in H_2, HD, and Kr. The ArF laser has been used for two-photon-resonant sum-frequency mixing for some time,[11,12] but two-photon-resonant difference-frequency mixing by using the ArF laser was not demonstrated until last year by the authors[2] and by Strauss and Funk.[13] Previous research using two-photon-resonant difference-frequency mixing has applied a frequency-doubled dye laser as the two-photon-resonant laser.[10,14,15] The use of an ArF excimer laser instead of a dye laser offers the advantages of higher laser powers, the production of shorter wavelengths (tuning from 110 to 180 nm is possible), and smaller phase mismatch.

Our experimental apparatus is shown in Fig. 2. A dual-discharge excimer laser (Lambda Physik Model 150) has been modified to improve the beam quality.[2] The laser is operated as an oscillator/triple-pass amplifier. A lens, pinhole, and concave mirror between the oscillator and the amplifier are used to filter the beam spatially. The normal-incidence mirrors at either end of the amplifier are masked with apertures

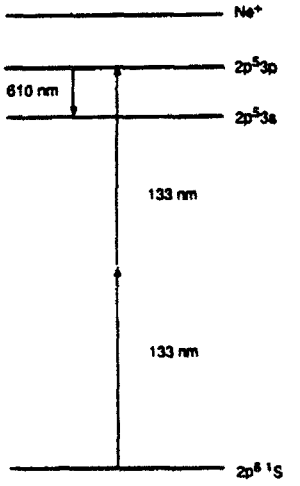

Fig. 1. Two-photon-excited fluorescence scheme for atomic neon.

0146-9592/93/050382-03$5.00/

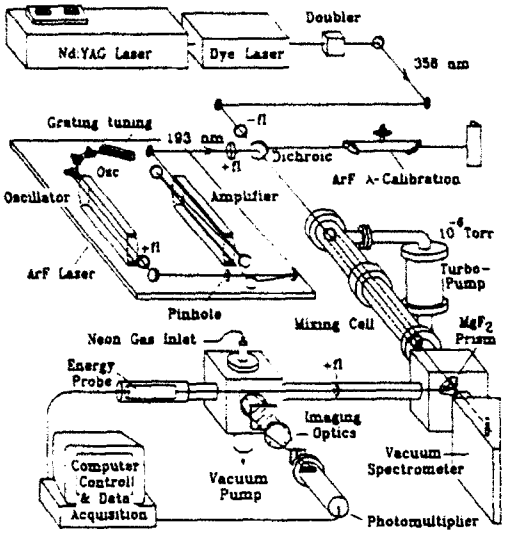

Fig. 2. Experimental arrangement for VUV generation and two-photon excitation of atomic neon.

to minimize parasitic oscillations. The output is as much as 60 mJ per pulse in a beam five times the diffraction limit. The beam path of the ArF beam is purged with argon to minimize absorption caused by the oxygen Schumann–Runge bands. The second laser is a Nd:YAG-pumped tunable dye laser (Quanta-Ray DCR II and PDL). Both lasers are focused through the mixing cell with fused silica lenses 1 m in focal length and combined on a dielectric ArF 45-deg mirror, which serves as a dichroic mirror. The timing of the two laser pulses is synchronized to ~1 ns. A feedback circuit corrects for drift in the timing of the excimer laser pulse. After passing through the mixing cell, the VUV radiation is collimated with a 50-cm MgF_2 lens and separated from the input beams with a MgF_2 Pellin–Broca prism. The VUV radiation is focused into a cell containing ~100 Torr of neon with a 5-cm focal-length MgF_2 lens. Fluorescence is collected at a right angle to the VUV beam with an $f/1.5$ lens, filtered with a 610-nm interference filter, and focused through slits onto an RCA 31034 photomultiplier tube; VUV energies are measured after the neon cell by use of a pyroelectric energy probe.

We have used both Kr and H_2 as nonlinear media for mixing. At 133 nm, H_2 is more efficient than Kr. However, mixing in H_2 is complicated by the presence of strong VUV-amplified spontaneous emission (ASE) caused by two-photon excitation of the E, F state.[4,5] The pressure dependencies of the energies from the four-wave mixing (two-photon-resonant difference-frequency mixing) at 133 nm and ASE near 145 nm with the ArF laser tuned to the E, $F\ ^1\Sigma_g^+$ $(v' = 6) \leftarrow X\ ^1\Sigma_g^+$ $(v' = 0)$ $Q(1)$ transition in H_2 are shown in Fig. 3. While the two processes have their peak energies at different pressures, it is not possible to obtain useful four-wave-mixing energies without simultaneously generating significant energy through the ASE. The MgF_2 prism provides enough dispersion to separate the 133-nm VUV from the ASE. We have measured up to 20 μJ at 1

nm from the four-wave-mixing process. Because the VUV beam has passed through ~5 cm of MgF_2 in the lenses and prism, energy generated in the mixing cell is actually significantly higher—perhaps well over 100 μJ—on the basis of measurements of the VUV transmission of our optics. The VUV energy decreases exponentially over approximately 15 min because of what appears to be color-center formation or other optical damage processes in the MgF_2 optics. The transmission of the optics is recovered by heating them in a vacuum[16] and polishing the surfaces.[17]

Neon, with the first two-photon resonance corresponding to ~133 nm, is the second most difficult neutral atom to excite optically after helium. We have succeeded in obtaining two-photon-excited fluorescence of the $2p^5 3p[3/2, 2]$ state of neon, which lies 150 858.5 cm^{-1} above the ground state.[18] Fluorescence at 610 nm to the $2p^5 3s[3/2, 1]$ state is detected. An excitation spectrum for this transition is shown in Fig. 4. The VUV linewidth at 133 nm is 1.8 cm^{-1}. This width is due almost entirely to the linewidths of the lasers, approximately 1 and 1.5 cm^{-1} for the ArF laser and the frequency doubled dye radiation, respectively. The Doppler width is 0.2 cm^{-1} at 133 nm.

The transition energy agrees with the expected excitation energy to within 2 cm^{-1} at the VUV wavelength (132.6 nm). The estimated VUV wavelength is calculated assuming that the ArF wavelength coincides exactly with the H_2 two-photon energy. The

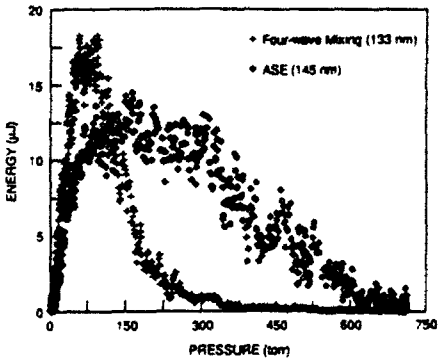

Fig. 3. Pressure dependence of two-photon-resonant difference-frequency mixing and ASE in H_2.

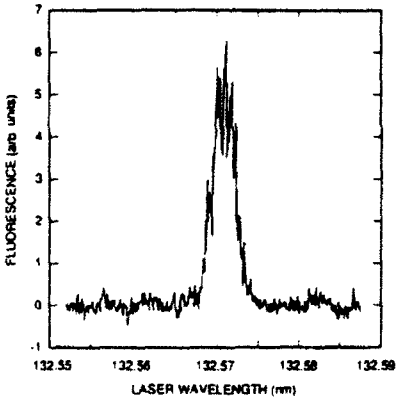

Fig. 4. Excitation spectrum for two-photon-excited fluorescence in atomic neon at 133 nm.

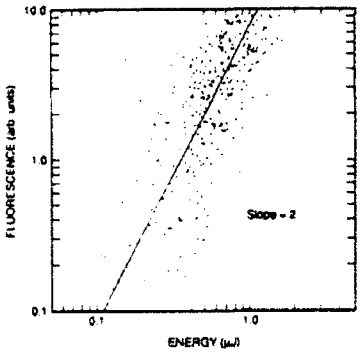

Fig. 5. Power dependence for two-photon-excited fluorescence signal in atomic neon.

2-cm^{-1} energy discrepancy may be due to the ArF's not being exactly on resonance. With careful control of both the ArF and the dye laser wavelengths, the four-wave-mixing technique could be used for accurate measurements of XUV transition energies. The two-photon resonance cannot be used as an accurate absolute reference for the ArF wavelength because of ac Stark shifts.[4] Calibration could be performed in a separate cell using low laser intensity. Currently, the frequency stability of the ArF laser is not sufficient to perform accurate calibrations with this approach.

The power dependence of the two-photon-excited fluorescence is shown in Fig. 5. The VUV intensity was varied by detuning the ArF laser from the H_2 resonance. A line with a slope of 2 fits the data fairly well, as shown in the figure.

Several other two-photon-allowed transitions can be found at nearly the same energy in neon. To date, we have observed only a single transition. The measurements have been somewhat hampered by the current short operating times. With some improvement in VUV energy and signal-to-noise ratio, we expect to be able to observe the other two-photon-allowed transitions in neon as well.

The two-photon excitation of neon offers a few applications such as the remote detection of neon and the production of highly excited states for excitation with a second laser for spectroscopy and lifetime measurements of higher-lying states. This experiment demonstrates the ability to perform tunable nonlinear-optics experiments with primary radiation well below 150 nm. While much of the research with laser-produced VUV to date has been on single-photon absorption experiments, we expect many interesting experiments in nonlinear optics, laser-based diagnostics, trace element detection, and other fields to be possible through the use of high-power VUV radiation.

We acknowledge helpful conversations with David L. Huestis. This research was supported by the U.S. Air Force Office of Scientific Research under contract F49620-90-C-0044.

References

1. G. C. Herring, M. J. Dyer, L. E. Jusinski, and W. K. Bischel, Opt. Lett. **13,** 360 (1988).
2. G. W. Faris and M. J. Dyer, in *Proceedings on Short Wavelength Coherent Radiation,* P. H. Bucksbaum and N. M. Ceglio, eds. (Optical Society of America, Washington, D.C., 1991), pp. 58–61.
3. W. K. Bischel, J. Bokor, D. J. Kligler, and C. K. Rhodes, IEEE J. Quantum Electron. **QE-15,** 380 (1979).
4. H. Pummer, H. Egger, T. S. Luk, T. Srinivasan, and C. K. Rhodes, Phys. Rev. A **28,** 795 (1983).
5. U. Czarnetzki and H. F. Döbele, Phys. Rev. A **44,** 7530 (1991).
6. W. Lempert, G. Diskin, V. Kumar, I. Glesk, and R. Miles, Opt. Lett. **16,** 660 (1991).
7. R. Pizzoferrato and M. Casalboni, J. Phys. E **20,** 896 (1987).
8. M. P. McCann, C. H. Chen, and M. G. Payne, J. Chem. Phys. **89,** 5429 (1988).
9. R. Hilbig, G. Hilber, A. Lago, B. Wolff, and R. Wallenstein, Comments At. Mol. Phys. **18,** 157 (1986).
10. R. Hilbig and R. Wallenstein, IEEE J. Quantum Electron. **QE-19,** 1759 (1983).
11. H. Egger, T. Srinivasan, K. Boyer, H. Pummer, and C. K. Rhodes, in *Laser Techniques for Extreme Ultraviolet Spectroscopy,* Vol. 90 of AIP Conference Proceedings, T. J. McIlrath and R. R. Freeman, eds. (American Institute of Physics, New York, 1982), pp. 445–453.
12. Y. Hirakawa, T. Okada, M. Maeda, and K. Muraoka, Opt. Commun. **84,** 365 (1991).
13. C. E. M. Strauss and D. J. Funk, Opt. Lett. **16,** 1192 (1991).
14. G. Hilber, A. Lago, and R. Wallenstein, J. Opt. Soc. Am. B **4,** 1753 (1987).
15. J. P. Marangos, N. Shen, H. Ma, M. H. R. Hutchinson, and J. P. Connerade, J. Opt. Soc. Am. B **7,** 1254 (1990).
16. A. Apinov, N. E. Budina, V. M. Reiterov, and L. P. Shishatskaya, Sov. J. Opt. Technol. **50,** 483 (1983).
17. L. P. Shishatskaya, P. A. Tsiryul'nik, V. M. Reyterov, and L. N. Safonova, Sov. J. Opt. Technol. **39,** 651 (1972).
18. V. Kaufman and L. Minnhagen, J. Opt. Soc. Am. **62,** 92 (1972).

Appendix E

RAMAN SHIFTING ArF EXCIMER LASER RADIATION FOR MULTIPHOTON SPECTROSCOPY

RAMAN SHIFTING ArF EXCIMER LASER RADIATION FOR VUV MULTIPHOTON SPECTROSCOPY

Gregory W. Faris and Mark J. Dyer
Molecular Physics Laboratory
SRI International, Menlo Park, CA 94025

ABSTRACT

We present the results of Raman-shifting the radiation from an ArF laser in HD and D_2 to produce tunable high power vacuum ultraviolet (vuv) radiation. Calculations of the Raman gain for H_2, D_2, and HD at 193 nm are presented. Modifications to the ArF laser to improve beam quality are described. Wavelengths as short as 132 nm are achieved by Raman shifting in D_2. The gas must be cooled below room temperature to Raman shift efficiently in HD. We obtain up to 1 mJ at 170 nm by Raman shifting in HD at liquid nitrogen temperature. The Raman-shifted radiation is used to perform two-photon spectroscopy in atomic and molecular fluorine and molecular hydrogen.

MP 92-276
July 14, 1993

I. INTRODUCTION

Nonlinear optical techniques in the vuv wavelength region are useful both for extending laser techniques to shorter wavelengths through nonlinear frequency conversion and for exciting very high-lying electronic states of atoms and molecules through multiphoton excitation. If the generated VUV is intense enough, multiphoton spectroscopy can be used with this radiation to probe states well over 100,000 cm^{-1} above the ground state. For two-photon excitation, transitions may be excited that are not allowed for single-photon excitation. VUV two-photon spectroscopy also allows detection of species with transitions in the extreme ultraviolet (xuv) such as atomic ions while using window materials transparent to VUV radiation.

Tunable VUV generation is possible through four-wave-mixing processes such as frequency tripling or Raman shifting. The most effective frequency conversion m(thod for VUV production depends on the particular application. Frequency tripling in gases can be performed with only a single laser, but the generated powers are low. To produce adequate powers for multiphoton spectroscopy, resonant four-wave mixing processes are required, such as multi-order Raman shifting or two-photon-resonant four-wave mixing.

The Raman-shifting process is simpler to implement and requires only a single laser, while two lasers are required for the resonant mixing schemes. By Raman-shifting of a dye laser or a frequency-doubled dye laser, higher order anti-Stokes lines are produced that may be tuned continuously over the VUV region down to 120-130 nm.[1-9] However, for the high order anti-Stokes Raman orders required to reach the VUV, the powers produced are low, and the intensity fluctuations are large. These problems can be reduced by Raman-shifting an excimer laser. Excimer lasers provide high powers at short wavelengths. A high pump power allows generation of higher powers in the Raman orders. A shorter starting wavelength allows reaching VUV

wavelengths through a smaller number of anti-Stokes shifts, yielding better conversion efficiency and smaller intensity fluctuations.

Numerous studies have been reported of high power VUV generation through Raman shifting excimer lasers in H_2,[10-19] particularly the ArF laser.[10,11,13,15-19] The tuning range of the excimer lasers is small however, typically ~ 1 nm, such that the probability of accessing a particular VUV transition using a Raman-shifted excimer laser is relatively small. The portion of the VUV region covered by Raman shifting an excimer laser can be increased by using different hydrogen isotopes with different Raman shifts.[19] Previous work on Raman shifting excimer lasers has focused almost entirely on H_2. Raman shifting an ArF laser in D_2 has been reported, but this work was performed with a broadband ArF laser, and only a single anti-Stokes order was observed.[11]

We report on Raman shifting of the ArF excimer laser in D_2 and HD. H_2 is omitted in this study because of the large amount of research reported on this isotope.

The Raman gain at room temperature for HD is small, ~ 30 times smaller than for H_2. For this reason, Raman-shifting in HD has only recently been reported.[19-24] However, cooling the HD gas to liquid nitrogen temperatures increases the Raman gain coefficient for HD by a factor of ~ 8, due to changes in the population distribution in the rotational levels of the lowest vibrational level, and a large reduction in the pressure broadening coefficient.[23,24] We use liquid nitrogen cooling for the Raman shifting in HD and for some of the D_2 Raman shifting as well.

Two-photon spectroscopy in the VUV has been reported previously using ArF radiation directly,[25-29] Raman-shifting a frequency-doubled dye laser,[8] by two-color techniques using the ninth harmonic of a Nd:YAG laser,[30] or synchrotron radiation[31] and using radiation from two-photon-resonant difference-frequency mixing.[32,33] We apply the Raman-shifted ArF excimer radiation to two-photon spectroscopy in F, F_2 and H_2.

This paper is organized as follows. To provide a basis for comparison of Raman shifting in H_2, D_2, and HD, we present calculations of the vibrational and pure rotational Raman gain

coefficients at 193 nm for these three isotopes at room temperature and at liquid nitrogen temperature. We describe our experimental apparatus, including modifications to the ArF excimer laser to improve the mode quality, and the liquid nitrogen-cooled Raman cell. A method for wavelength calibration and investigations of the Raman shifting in D_2 and HD are reported. VUV multiphoton spectra are presented using two-photon-resonant excitation followed by ionization by a third photon.

II. THEORY

For a Gaussian beam, the steady-state integrated gain G for stimulated Raman scattering with a focused beam is[34]

$$G = \int_{-\frac{\ell}{2}}^{\frac{\ell}{2}} I_p \, g \, dL = \frac{4 \, g \, P_p \tan^{-1} \frac{\ell}{b}}{\frac{\lambda_p}{n_p} + \frac{\lambda_s}{n_s}} \tag{1}$$

where I_p and P_p are the intensity and power of the pump laser, respectively, g is the steady state Raman gain coefficient for a plane wave, ℓ is the length of the gain medium, λ_p, λ_s and n_p, n_s are the vacuum wavelengths and indices of refraction for the pump and Stokes waves, respectively, and b is the confocal parameter of the pump beam. The threshold condition for stimulated Raman scattering for our experiments is G ~ 25 (based on Eq. 4 of reference 35 using reasonable values of the parameters in that equation). The minimum laser power required to reach threshold is then approximately

$$P_{th} = \frac{25 \, \lambda_p}{\pi \, g} \tag{2}$$

This is the minimum threshold power for a gain medium of infinite length (much greater than the confocal parameter) and a diffraction-limited Gaussian beam. The power required for non-ideal Raman conversion will be typically greater than this value.

The peak plane-wave steady-state Raman gain coefficient may be written as[36-38]

$$g = \frac{2\,\lambda_s^2\,\Delta N}{h\,\nu_s\,n_s^2\,\pi\Delta\nu}\;\frac{d\sigma}{d\Omega} \tag{3}$$

where ν_s is the frequency of the Stokes wave, $\Delta\nu$ is the Raman full width half maximum (FWHM) linewidth, $d\sigma/d\Omega$ is the differential Raman cross section in units of power scattered per unit solid angle per molecule for the desired Raman transition and proper polarization and scattering directions, and $\Delta N = N(v,J) - [(2J + 1)/(2J' + 1)]N(v',J')$ is the population difference between the initial (v,J) and final (v',J') levels. The number density in a given rotational level J is[39]

$$N(J) = \frac{(2J + 1)\,g_J \exp\{-E(J)/kT\}}{\sum_J (2J + 1)\,g_J \exp\{-E(J)/kT\}}\;.\;N_o \tag{4}$$

where N_o is the total number of molecules per unit volume, E(J) is the energy of rotational level J, and g_J is the nuclear spin degeneracy. The ratio of the nuclear spin degeneracy for odd J to even J is 3:1 for H_2, 1:2 for D_2, and 1:1 for HD.

The wavelength dependence of the Raman gain coefficient is primarily through variation in the cross section, while the temperature dependence and pressure dependence are due mainly to variation in the population and linewidth. For vibrational Raman scattering from a diatomic molecule with parallel k vectors (copropagating) and linear and parallel polarizations for the incident and scattered waves, the cross section is given by[38,40]

$$\frac{d\sigma}{d\Omega} = \left(\frac{2\pi \nu_s}{c}\right)^4 \left\{ \alpha^2_{v,J,v+1,J} + \frac{4}{45} \frac{J\,(J+1)}{(2J-1)\,(2J+3)} \gamma^2_{v,J,v+1,J} \right\} \qquad (5)$$

where $\alpha_{vJv'J'}$ and $\gamma_{vJv'J'}$ are the off-diagonal matrix elements of the isotropic and anisotropic polarizability between states v,J and v',J'. For pure rotational Raman scattering from a diatomic molecule with parallel k vectors (copropagating) and linear and parallel polarization for the incident and scattered waves, the cross section is[40,41]

$$\frac{d\sigma}{d\Omega} = \frac{2}{15} \left(\frac{2\pi \nu_s}{c}\right)^4 \frac{(J+1)\,(J+2)}{(2J+1)\,(2J+3)} \gamma^2_{v,J,v,J+2} \qquad (6)$$

Several authors have reported calculations of the off-diagonal matrix elements of the isotropic polarizability $\alpha_{vJv'J'}$ and polarizability anisotropy $\gamma_{vJv'J'}$ for isotopes of hydrogen. Rychlewski has provided the off-diagonal matrix elements necessary for calculating the Q(0) vibrational Raman cross section and the S(0), S(1), and S(2) rotational Raman cross sections in H_2[42] and the Q(0) vibrational cross sections in D_2 and HD[43] at many wavelengths, including 193.6 nm. Wavelength-dependent off-diagonal matrix elements for vibrational Raman scattering in H_2 have also been reported by others.[44-46] Schwartz and LeRoy give all the off-diagonal polarizabilites required for calculating pure vibrational and rotational Raman scattering at a single wavelength (488 nm) for H_2, D_2, and HD for many initial J levels.[47]

Unfortunately, no values for the off-diagonal matrix elements of γ for pure rotational Raman scattering in D_2 and HD are available at 193 nm. To obtain approximate values for these parameters, we have extrapolated the values of Schwartz and LeRoy to 193 nm using a single resonance variation[48-49] [α or γ proportional to $1/(\nu_0^2 - \nu_p^2)$, where ν_0 is a resonance frequency and ν_p is the pump frequency]. We find that a single resonance model describes quite well the wavelength dependence of the off-diagonal matrix elements of the polarizability anisotropy γ_{0J0J+2} for H_2.[42] In addition, the diagonal matrix elements of for H_2[50] also fit a single resonance model with almost the same resonance energy.

We have found single resonance fits to the diagonal matrix elements of γ for D_2 and HD[42] and used this wavelength dependence to extrapolate the off-diagonal values for γ of Schwartz and LeRoy to 193 nm. The values we find are given in Table I, along with the cross sections calculated from them. All the vibrational cross sections are calculated from polarizabilities for J = 0 regardless of what the actual initial rotational level is. The Raman cross sections for vibrational Raman scattering in H_2 and D_2 from the experimental measurements of Bischel and Black[49] agree with these results to less than 15%.

Values for the density-dependent line broadening coefficients, $\Delta\nu/N_0$, for the vibrational and pure rotational Raman lines in H_2, D_2, and HD are known at room temperature and near liquid nitrogen temperature. These values are given in Table I for specific initial rotational levels. In the high pressure regime, the linewidth is entirely determined by the collisional broadening and is proportional to the density. Because the population difference ΔN is also proportional to the density, Eq. (3) shows that the Raman gain is independent of density in the high pressure regime.

Density-normalized population differences, $\Delta N/N_0$, calculated from Eq. (4) are also shown in Table I. The energy levels for these calculations are determined from literature values of spectroscopic constants for H_2,[51] D_2,[52] and HD.[53]

Using these values for the various parameters, we can use Eq. (3) to calculate the high density Raman gain coefficient for vibrational and rotational Raman scattering at room temperature and liquid nitrogen temperature. These gain coefficients are listed in Table I. The Raman gain at each temperature is given for the strongest Raman line as determined by the rotational population in the lowest vibrational level. Thus, the Raman shift listed is different at liquid nitrogen temperature than at room temperature. For H_2 at liquid nitrogen temperature, the populations in J = 0 and 1 are virtually the same, and both levels are listed in Table I. The gain values for vibrational Raman scattering in H_2 differ by 15% from those based on experimentally measured cross sections.[38,54]

At room temperature, the difference in vibrational Raman gain coefficient between H_2 and HD is a factor of ~30. The small Raman gain coefficient for HD relative to H_2 and D_2 is primarily

due to the large collisional line broadening, which results from the higher probability of rotationally inelastic collisions for the heteronuclear molecule HD.[55] At liquid nitrogen temperature, reduction in the Raman linewidth $\Delta\nu$ and an increase in the population factor ΔN lead to an increase in the Raman gain by a factor of 8.5. For D_2 and H_2, the change in the collisional line broadening is smaller, and the Raman gain increases by factors of 4.9 and 1.4, respectively. The increase in Raman gain coefficient for pure rotational Raman scattering between room temperature and liquid nitrogen temperature is about the same as the increase for vibrational Raman scattering for each isotope.

III. EXPERIMENT

A. ArF LASER

For nonlinear processes, particularly higher order frequency conversion such as multi-order anti-Stokes Raman shifting, the laser transverse mode quality is very important. For this reason, we modified the excimer laser we use for these experiments (Lambda Physik model 150 MSC dual discharge excimer laser). A prism beam expander and grating on the oscillator discharge provide wavelength tuning over the excimer gain profile of nominally 1 nm, with an energy of ~1.3 mJ and a linewidth of ~1 cm^{-1}.

Ordinarily, unstable resonator optics are used on the amplifier cavity, and the oscillator output radiation is fed into the amplifier cavity to "injection-lock" the amplifier output, providing tunable radiation of relatively low divergence. We have found that a better compromise between power and divergence is obtained by operating the amplifier in a triple-pass configuration as shown in Figure 1. Before amplification, the oscillator output was filtered spatially by focusing with a fused silica lens (~46-cm focal length at 193 nm) through a 50- or 75-μm pinhole. The light was recollimated with a 25-cm focal length dielectric mirror. The beam then passes through the

amplifier three times in a vertical zigzag pattern, since the discharge is longer vertically than horizontally.

The total gas pressure for the amplifier was adjusted to provide maximum gain at a later time to compensate for the longer path length in this configuration. We obtain up to 100 mJ with the triple pass configuration, which is roughly the same as obtained with the standard configuration. However, the beam quality is improved considerably. When the output of the new configuration was focused with a 50-cm lens, the intensity was sufficient to break down air on every pulse, while the "injection-locked" configuration resulted in intermittent air break down using the same lens. Operation as a triple-pass amplifier also results in less broadband emission and a wider tuning range than with the "injection-locked" unstable resonator.

We measured the spot size of the triple-pass-amplified beam by scanning a razor blade through the beam while monitoring the transmitted energy and found that the focused spot is five times over the diffraction limit (assuming a Gaussian beam profile).

We measured the beam profile for the ArF laser with a ccd camera. The window on the ccd was removed to allow sensitivity to the ArF radiation. The results are shown in Figures 2(a) and 2(b) for the beams exiting the oscillator and amplifier, respectively. The size of the amplified beam has been reduced optically by a factor of two so that it will fit on the ccd camera. Note that there is significant loss of spatial mode quality when the beam passes through the amplifier.

Because the Raman-shifting process is polarization-sensitive we prefer to have all the laser energy in a single polarization. Although the prism beam expander acts as a polarizing element, the windows on the laser discharge cavities are made of MgF_2, which is a birefringent material. This can lead to depolarization of the beams if the windows are not formed of a single crystal or are under stress. In the oscillator, depolarization leads to lower output power and high shot-to-shot instabilities by elevating the threshold for oscillation.

To minimize this depolarization, we carefully mounted the windows while monitoring the depolarization. Polarized light at 193 nm was produced by Raman-shifting a frequency-doubled

To minimize this depolarization, we carefully mounted the windows while monitoring the depolarization. Polarized light at 193 nm was produced by Raman-shifting a frequency-doubled Nd:YAG-pumped dye laser. This light was passed through each discharge in turn as the windows were aligned. The amount of depolarization was observed by passing the light through a birefringent crystalline quartz prism after passing through the discharge cavity. By rotating the windows in their mounts, we oriented the windows to produce the minimum depolarization. Then the mounts holding the windows were gradually tightened while we monitored the depolarization to maintain a low amount of depolarization. After this alignment, the depolarized (vertically polarized) component of the triple-pass-amplified beam was less than 1/200th of the horizontally polarized component.

This alignment might also be performed by using light from the second discharge for alignment, using a birefringent prism to produce a well-polarized beam.

B. RAMAN CELL

Because D_2 and HD have lower Raman gain coefficients than H_2, we use a liquid-nitrogen-cooled Raman cell t· enhance the Raman conversion efficiency. Liquid nitrogen cooling has been applied previously to shifting in H_2.[2,5,7] and HD.[23,24] The efficiency enhancement is due to the increase in gain coefficient described in section II and to removal of impurities. At 77 K, many vapor impurities that may be present in the Raman cell will condense, leading to lower losses.

The liquid nitrogen temperature Raman cell is shown in Figure 3. HD or D_2 is contained in the central gas cell, with a fused silica window on the input and a MgF_2 window on the output. Both windows are sealed with indium seals to allow operation at liquid nitrogen temperatures. The gas cell is surrounded along its length with a jacket for liquid nitrogen. The entire cell and liquid nitrogen jacket are enclosed in vacuum which serves several functions: provides insulation for the liquid nitrogen, eliminates condensation on the end windows of the inner cell, avoids convection due to temperature gradients from uneven cooling over the length of the cell, and provides direct coupling to the evacuated downstream beam path for the generated vuv light. To minimize

conduction between the liquid nitrogen jacket and the outer cell, the inner cell and jacket are supported only by the two tubes used to introduce liquid nitrogen into the center of the cell.

IV. RESULTS AND DISCUSSION

A. TWO-PHOTON CALIBRATION

Although the excimer laser provides tunability through tilting the grating, there is no provision for wavelength determination. Wavelength can be determined using 1+1 resonantly enhanced multiphoton ionization (REMPI) or laser-induced fluorescence in NO, as described by Robie et al.[69] and Versluis et al.,[70] respectively. Versluis et al. provide accurate line positions for the NO lines within the tuning range of the ArF excimer laser, which they have calibrated against known iodine positions.

However, the NO spectrum is dense and is not very convenient for rapidly determining the ArF wavelength. For this purpose, we use two-photon resonances in H_2, HD, and krypton. By focusing the light transmitted through one of the dielectric turning mirrors into a small cell with electrodes, we easily obtain strong ion signals from these gases through 2+1 REMPI. By mixing the three gases at partial pressures of about 2 parts H_2, 2.5 parts HD, and 1.5 parts krypton, we obtain ~15 lines of comparable intensity covering the laser energy range from 51538 cm^{-1} to 51881 cm^{-1}. The distribution and intensities of these lines are shown in Figure 4. Line positions of the two-photon resonances are given in Table II. The two-photon krypton energies are from Moore.[71] The two-photon energies in H_2 are determined from energy levels for the ground X $^1\Sigma_g^+$ state and the EF $^1\Sigma_g^+$ state given by Dabrowski,[72] and by Senn and Dressler,[73] respectively. The energies for the two-photon transitions to v' = 7 in the EF state in HD are based on observed energies for the P and R branches for EF ← X together with energies of the rotational levels in the ground state, both from Dabrowski and Herzberg.[74] The energies for two-photon transitions to v' = 6 in the EF state are calculated from energies for B ← X transitions given by Dabrowski and Herzberg

and EF $\rightarrow$ B transition energies of Dieke.[75] The line positions in Table II are given to two decimal places as in the original references. However, the absolute accuracy is typically only a single decimal place.

The small number of lines and irregular pattern of the two-photon resonances allows straightforward determination of the approximate wavelength of the ArF laser. Because the high intensities required to produce the 2+1 REMPI signal can cause ac Stark shifts,[27] this calibration is best suited for rough wavelength calibration, and the NO spectrum should be used when high accuracy is required.

Also shown in Figure 4 are two curves showing the relative ArF laser power as a function of wavelength; the lower curve shows the laser power for a new gas fill and with a sufficient purge to remove much of the oxygen absorptions due to the Schumann Runge bands. The upper curve shows the power for a gas fill after many laser shots and after passing through several meters of air. The aging of a laser fill results in a reduced tuning range of the laser. At the top of Figure 4, the positions of the (4,0) and (7,1) Schumann Runge bands are shown, based on the positions given by Yoshino et al .[76-78] With a high purge flow, the Schumann Runge absorptions may be eliminated almost entirely (see tuning curve in Fig. 14).

Several absorptions do not correspond to the (4,0) and (7,1) Schumann Runge bands. A single strong and narrow absorption marked with a "C" in Figure 4 occurs at ~ 51789 cm^{-1}. This absorption has recently been attributed to C atom absorption on the $3^1P \leftarrow 2^1D$ transition, possibly due to dissociation of carbon-containing impurities in the laser cavity.[79] Unlike the measurements reported in reference 79, our laser is not completely extinguished at the peak of the C atom absorption. This difference may be due to a smaller quantity of impurities in the gases used in our laser.

Several pairs of absorption lines also do not correspond to the (4,0) or (7,1) Schumann Runge bands. They are marked with asterisks in Figure 4. Note that the relative strengths of the lines do not correlate well with the strengths of the (7,1) and (4,0) Schumann Runge bands when

comparing the upper and lower tuning curves in Figure 4. This lack of correlation may indicate that these lines are due to absorption within the laser cavity rather than the air path. The positions do not correspond to previous measurements of line positions in CO[80] and NO.[70]

It was thought that the lines might be due to Schumann Runge bands from vibrationally excited levels, which become the dominant absorptions at higher temperatures.[81,82] To examine this possibility, line positions and intensities for Schumann Runge bands in this wavelength region, the (5,0), (6,1), (10,2), (11,2), (14,3), (15,3), and (16,3) bands, were obtained from a direct diagonalization of the effective Hamiltonians of the $X^3\Sigma_g^-$ and $B^3\Sigma_g^-$ states.[83] Literature values for the molecular constants for the B state[84] and v = 0[85] and v = 1[86] of the X state are used. Only approximate values are known for the constants of the next higher vibrational levels in the X state, i.e., for v = 2, 3, 4. The basic rotational structure in these levels was determined in the work of Creek and Nichols.[87] Using their values and the more accurate measurements in lower[86,87] and higher[88] vibrational levels, we constructed an RKR potential energy curve[89] that defined the vibrational energies and the rotational constants B and D for the intermediate levels.[90] Effective values for the fine structure constants Λ and γ describing the spin-spin and spin-rotational splittings of the ground state were interpolated for these levels using the empirical formula of Cosby et al.[88] When we compared these calculated line positions with the unidentified lines, we found no matches. The band that most resembles the unidentified lines is the (10,2) band, but the discrepancy is too large for the expected accuracy of the wavelength calibration (~1 cm^{-1}) and the line position calculation ($\pm$0.2 cm^{-1}). We have not identified these lines to date.

B. RAMAN MEASUREMENTS

We have studied the Raman conversion of the ArF laser in D_2 and HD using the apparatus shown in Figure 1. The ArF laser is focused into the Raman cell with a fused silica lens. For the anti-Stokes measurements, we used a 38-cm focal length lens, and for optimization of the first Stokes, we used a 50-cm focal length lens. Both focal lengths are for 250-nm light. Absolute energy measurements were performed by separating a desired Raman order from the pump laser

and other orders with a MgF_2 Pellin Broca prism. MgF_2 is less susceptible to color center formation than LiF or CaF_2. The energy is measured with a Laser Precision model RJP-735 pyroelectric energy meter under vacuum. The calibration of this energy meter has been verified through comparison with a Scientech model 365 calorimeter energy meter. The two were found to agree to within 10% accuracy. Relative Raman intensities are measured with a vacuum monochromator (SPEX model 1500SP) and a photomultiplier tube with CsI photocathode (EMR model 542G-08-18). A MgF_2 scattering plate is placed in front of the monochromator to reduce the directional dependence of the high order Raman intensities.

The spectral response of the vuv spectrometer and photomultiplier tube must be calibrated to determine the relative strengths of the different Raman lines. We have measured the spectral response for longer wavelengths directly using a fused silica envelop deuterium lamp in air. The absolute intensity of this lamp has been calibrated for wavelengths longer than 200 nm.[91] Using published values for the vuv relative spectral response of a D_2 lamp,[92] we have extrapolated an approximate spectral response of our D_2 lamp to 190 nm. If the absorption of the fused silica envelop of our lamp is small over this region, then this is a fairly good extrapolation because there is no line structure for D_2 lamps above 165 nm, and the relative spectral responses for the two lamps are very similar above 200 nm. By correcting for oxygen absorption in the air,[93] we have determined the spectral response down to ~ 190 nm. For shorter wavelengths of 140 nm $< \lambda <$ 195 nm, we use the typical spectral response of the photomultiplier tube,[94] and assume that the spectral response of the spectrometer is flat.

The relative spectral response determined by the two techniques agrees fairly well between 190 and 195 nm, but they diverge for $\lambda > 195$ nm where the typical photomultiplier response drops rapidly. We have made a single spectral response curve for $140 < \lambda < 260$ nm by joining the two curves at 195 nm. We believe that this calibration curve is accurate to better than a factor of 2.

In optimizing the Raman intensity, we discovered an interesting effect due to the orientation of the focusing lens. As the focusing lens is tilted around a vertical axis, the maximum intensity of the first Stokes order does not occur with the lens normal to the laser beam, but instead at a small tilt relative to normal. This behavior is illustrated in Figure 5. The cause for this behavior is not fully understood. The lens is more than 2 meters from the ArF amplifier, so the round trip time for reflections from the lens into the laser is at least 12 ns, or close to the pulse length. Thus the effects are not due to feedback into the laser. Tilting the lens causes additional aberration and different focal lengths for rays in the horizontal and vertical planes, conditions one might expect to lead to lower conversion efficiency. The low value for the normal incidence lens position may be due to a reduction in gain suppression,[95,96] changes in phase matching, or reduced AC stark broadening for the distorted wave fronts when the lens is tilted. For optimal conditions, we have obtained up to 60% energy conversion from the pump laser to the first Stokes order in D_2.

Although many Stokes and anti-Stokes orders are obtained readily for Raman-shifting the ArF laser in D_2 at room temperature, we were not able to produce even the first Stokes order when Raman shifting in HD at room temperature. By monitoring the first Stokes wavelength with the monochromator as the Raman cell was cooled, we found that the threshold for first Stokes production in HD is about 220 K at a pressure of 4200 Torr. Note that the power of our laser is ~1 MW, while the threshold for Raman scattering in HD at room temperature in Table I is only 200 kW. The numbers in Table I are for diffraction-limited Gaussian beams in an infinite medium in the high density and steady state limits. The primary cause for the higher threshold is believed to be the mode quality of the laser beam. All the Raman shifting measurements presented here for HD are performed at liquid nitrogen temperature (~77 K), while the measurements in D_2 have been performed at room temperature, except as noted.

We have observed eight anti-Stokes orders (to 132 nm) and five Stokes orders for Raman shifting in D_2. Four anti-Stokes and four Stokes orders were observed for shifting in HD. The higher order anti-Stokes orders were observed only without the scattering plate in front of the monochromator. The anti-Stokes and Stokes orders observed with the scattering plate in place are

shown in Figures 6 and 7. Figure 6 shows lines generated in D_2 at room temperature and a density of 5.4 amagat. (One amagat is the density of an ideal gas at standard temperature and pressure, 0° C and 1 atm). Figure 7 shows Raman orders generated in HD at 77 K and a density of 6 amagat. The intensities in Figures 6 through 8 have been corrected for the approximate wavelength response of the photomultiplier and spectrometer as described above. The baseline between the Raman orders does not represent a true light intensity level, but is rather the sensitivity limit for the dynamic range of the measurements. This level varies due to the varying sensitivity of the photomultiplier and spectrometer.

A few rotational lines appear on the lines generated in HD. These become accentuated at lower densities as shown in Figure 8, which shows the Raman orders in HD for a density of 3 amagat at liquid nitrogen temperature. The tendency toward more rotational lines at low temperatures is also evident in Figure 9, which shows the Raman orders in D_2 at 77 K. The intensities in Figure 9 have not been corrected for the wavelength response of the photomultiplier and spectrometer. The uncorrected intensities allow the pressure dependence of the intensities to be seen more readily.

The increase in rotational Raman scattering at liquid nitrogen temperatures is believed to be due primarily to the increase in the absolute Raman gain, allowing threshold to be reached for rotational Raman scattering. Increased circular polarization of the laser due to stress-induced birefringence of the fused silica window with the liquid nitrogen cooling may also play a role. Once the first rotational Stokes order is generated, then the other rotational lines shown in Figure 9 may be produced through mixing with the pump and primary vibrational Raman orders. The magnitude of the various Raman orders is determined by competition between the various orders for gain and population.

The density dependence of the Raman orders in Figure 9 is due to departure from the high density limit and phase matching considerations. As the density drops to zero, the Raman line-width does not drop to zero, but is ultimately limited by the Doppler width [subject to the effects of

Dicke (collisional) narrowing[97]]. Thus the Raman gain drops to zero as the density goes to zero [see Eq. (3)]. This behavior is shown in Figure 10 for vibrational and rotational Raman scattering in D_2 at room temperature [Q(2) and S(2)] and near liquid nitrogen temperature [Q(0) and S(0)]. The variations of the Raman linewidths are determined using the density dependence relation and self-diffusion coefficient at room temperature given by Smyth et al.[58] Estimates for the diffusion constant at liquid nitrogen temperature were based on values for H_2[56,98] using the scaling for the self-diffusion coefficient $D_0 \propto m^{-1/2}$.

The range of values for the self-diffusion constant from these estimates results in the range of Raman gain values for liquid nitrogen temperatures shown in Figure 10. Note that the Raman gain for rotational Raman scattering remains constant to lower densities than the gain for vibrational Raman scattering because the narrower Doppler width for rotational Raman scattering allows the linewidth to be proportional to the density at lower densities than for vibrational Raman scattering. The increased rotational Raman scattering at low densities is quite evident in Figure 9.

The contribution of rotational-vibrational Raman scattering to the rotational lines observed here has not been considered. The cross section for rotational-vibrational Raman scattering is significantly smaller than for pure rotational Raman scattering.[99] In addition, because of the large Doppler broadening of vibrational-rotational scattering compared with pure rotational scattering, there is no basis for vibrational-rotational scattering to increase relative to pure vibrational scattering at lower pressures.

At higher densities, the phase matching process necessary for generating higher order Raman lines is hampered by the increase in the index of refraction and the increasing importance of dispersion. The combined effects of decreased gain and competition with rotational scattering at lower densities and phase matching at higher densities lead to an optimal density for Raman conversion for a given Raman order. Using the pyroelectric energy meter, we measured the absolute power generated in the second anti-Stokes order in HD at liquid nitrogen temperature as a function of density. The result is shown in Figure 11. The energy peaks at a density of about

3 amagat, where an energy of about 1 mJ is produced. One difficulty was encountered with this measurement. The birefringence of MgF_2 causes the second anti-Stokes order in HD to be refracted at the same angle as the depolarized fundamental ArF wavelength. The effect of the depolarized ArF radiation was eliminated through the careful control of the polarization of the ArF laser, as described above, and the use of Brewster-angle fused silica plates in the ArF beam before the Raman cell to reject depolarized light.

We also measured the relative Raman intensity produced for different Raman orders in D_2 at room temperature. These results are shown in Figures 12 and 13. The anti-Stokes Raman orders follow the general pattern of optimizing at successively lower densities up to the sixth order. The optimal densities for the seventh and eighth orders, however, are higher than that for the sixth order. This may be due to resonant enhancements of the Raman scattering, to better phase matching below resonant transitions, or to some peculiarity with phase matching for the high order anti-Stokes processes.

Note that the depletion of the pump radiation in Figure 12 corresponds to significantly less than the 60% or more we achieved for the optimized first Stokes conversion described above. We attribute this discrepancy to the different focal length lens used for the two measurements, the fact that the lens is not tilted for the anti-Stokes measurements, and that spatial sampling bias of the laser beam on the scattering plate may make the depletion of the pump beam appear less than that experienced by the entire beam. We expect the first Stokes measurement, which is based on absolute energy measurement on the entire beam, to be more accurate than the results using the scattering plate.

C. MULTIPHOTON EXCITATION IN THE VUV

We have applied the vuv radiation produced by Raman shifting in D_2 and HD to two-photon spectroscopy of F, F_2, and H_2. The desired Raman order for each measurement was separated from the laser and other Raman orders using a MgF_2 Pellin Broca prism. The light is focused into a stainless steel cell. Ions are collected with a position-sensitive electrode. This

electrode consists of seven segments at 5-mm spacing in a line parallel to the vuv beam. The cell is grounded, and a negative voltage is applied to all segments, producing a potential of 2 to 15 V/cm between the electrodes and a facing ground plane. Under these conditions, the multi-photon ion (MPI) signal from the laser focus is directed to a single electrode segment. Collecting the signal from the electrode closest to the focus provides good discrimination against background signals from single photon ionization of contaminants.

For measurements on F and F_2, a mixture of 5% F_2 in He is used. The F atoms are prepared by flowing the gas mixture through a microwave discharge. For the measurements on F_2, the fluorine is flowed to maintain passivation. All measurements were performed at between 5 and 10 Torr total pressure. Wavelength calibrations are based on the 2+1 REMPI lines of Figure 4 together with known values for the Raman shifts. This calibration is found to be accurate to ~1.5 cm^{-1} at the photon frequency. It is difficult to know the accurate value of the Raman shift due to density and temperature dependent line shifts[56] and the ac Stark effect.[100,101] For accurate wavelength measurements, calibration of the Raman-shifted radiation is required.

The first Stokes radiation from Raman shifting the ArF laser in D_2 may be used to perform two-photon-resonant excitation of F_2 followed by ionization by a third photon (2+1 REMPI). Excitation is from (v = 0) in the ground X $^1\Sigma_g^+$ to (v = 3) in the F $^1\Pi_g$ state. The excitation spectrum for this transition is shown as the lower curve in Figure 14. The upper curve shows the Raman-shifted energy. The excitation spectrum has not been normalized to the laser power. The appearance of the band is quite similar to that previously observed for two-photon excitation of lower vibrational levels in the F state.[102] The band has two heads and is blue degraded. However, there are additional lines at energies below the lower energy band head that are not part of this transition. The peak 97500 cm^{-1}, which is shown magnified by a factor of 3 in an inset in Figure 14, is seen to consist of several lines (with reproducible shape), while the other peak, at ~97340 cm^{-1}, appears to be a single line. These peaks appear only with the introduction of fluorine into the cell. We have not identified these lines but believe that they correspond to two-photon resonances in F_2.

Using the second anti-Stokes radiation from Raman shifting the ArF laser in D_2, we performed 2+1 REMPI on a single rotational line in the $H\bar{H}$ state in H_2. The excitation spectrum for this measurement is shown in Figure 15(a). The strong peak that lies well off scale in Figure 15 is the ion signal due to 2+1 REMPI on the E,F ($v' = 7, ' = 3$) ← X ($v'' = 0, J'' = 3$) transition excited by scattered light from the ArF excimer laser fundamental at 103289.7 cm^{-1}. The smaller peak that lies at ~115248.4 cm^{-1} is due to the second anti-Stokes and corresponds to the $H\bar{H}$ $^1\Sigma_g^+$ ($v' = 1, J' = 0$) ← X ($v'' = 0, J'' = 0$) transition in H_2. This transition is expected to lie at 115251.52 cm^{-1}.[103]

Using the second anti-Stokes radiation from Raman-shifting the ArF excimer laser in HD at liquid nitrogen temperature, we excited a single fine structure line in atomic fluorine through 2+1 REMPI. The two-photon-excited fluorescence of atomic fluorine has been reported previously using ~10 μJ generated as the sixth anti-Stokes order from a frequency-doubled dye laser.[8] With ~1 mJ in the second anti-Stokes line of the ArF excimer laser, we can obtain good signal to noise as is shown in the 2+1 REMPI excitation spectrum of the $^2D^o_{3/2}$ ← $^2P^o_{3/2}$ transition shown in Figure 15b. The expected peak frequency is 117872.9 cm^{-1}.[104] The ripple in the baseline is due to the microwave discharge.

The Raman-shifted excimer laser may be used for two-photon-resonant ionization or fluorescence detection of atomic or molecular fluorine. For these applications, purging the beam path between the laser and the Raman cell will not be necessary because the wavelengths for excitation of the strongest features (the two bands heads for Figure 14 and the line in Figure 15b) lie in a region free of strong Schumann Runge absorption.

V. SUMMARY AND CONCLUSIONS

We have described Raman shifting an ArF excimer laser in D_2 and HD to produce high order anti-Stokes orders in the vuv. The mode quality of the excimer laser has been improved to enhance the Raman shifting. However, actual threshold powers are well above those required under ideal conditions, and liquid nitrogen cooling is required for Raman shifting in HD. At liquid nitrogen temperatures, there is increased rotational Raman scattering, especially at lower densities. Ample energies for multi-photon spectroscopy are obtained. One mJ is achieved for second anti-Stokes Raman shifting in HD. The Raman shifted radiation is used for 2+1 REMPI in F, F_2, and H_2.

The ability to Raman shift an ArF laser in isotopes of hydrogen other than H_2 significantly increases the portion of the vuv region for which high power vuv can be obtained from a single laser system. When feasible, this is an attractive approach for high power vuv generation for experiments such as multiphoton spectroscopy and for other nonlinear optical experiments.

ACKNOWLEDGMENTS

We are grateful for helpful discussions with Dr. William K. Bischel, Dr. Richard A. Copeland, Dr. David L. Huestis, and Dr. Tom G. Slanger and the assistance of Dr. Philip C. Cosby in performing calculations of the line positions for bands in the Schumann Runge system. This research was supported by the AFOSR under contracts F49620-88-K-0003 and F49620-90-C-0044.

REFERENCES

1. V. Wilke and W. Schmidt, "Tunable Coherent Radiation Source Covering a Spectral Range from 185 nm to 880 nm," Appl. Phys. **18**, 177-181 (1979); V. Wilke and W. Schmidt, "Tunable UV-Radiation by Stimulated Raman Scattering in Hydrogen," Appl. Phys. **16**, 151-154 (1978).

2. D. J. Brink and D. Proch, "Efficient Tunable Ultraviolet Source Based on Stimulated Raman Scattering of an Excimer-Pumped Dye Laser," Opt. Lett. **7**, 494-496 (1982).

3. H. Schomburg, H. F. Döbele, and B. Rückle, "Generation of Tunable Narrow-Bandwidth VUV Radiation by Anti-Stokes SRS in H_2," Appl. Phys. B **30**, 131-134 (1983).

4. K.G.H. Baldwin, J. P. Marangos, D. D. Burgess, and M. C. Gower, "Generation of Tunable Coherent VUV Radiation by Anti-Stokes Raman Scattering of Excimer-Pumped Dye Laser Radiation," Opt. Commun. **52**, 351-354 (1985).

5. H. Wallmeier and H. Zacharias, "Continuously Tunable VUV Radiation (129-210 nm) by Anti-Stokes Raman Scattering in Cooled H_2," Appl. Phys. B **45** 263-272 (1988).

6. B. R. Lewis, S. T. Gibson, K.G.H. Baldwin, and J. H. Carver, "Vacuum-Ultraviolet Absorption Linewidth Measurement using High-Order Anti-Stokes Raman-Shifted Radiation," J. Opt. Soc. Am. B **6**, 1200-1208 (1989).

7. V. Schulz-von der Gathen, T. Bornemann, V. Kornas, and H. F. Döbele, "VUV Generation by High-Order CARS," IEEE J. Quantum Electron. **26**, 739-743 (1990).

8. G. C. Herring, M. J. Dyer, L. E. Jusinski, and W. K. Bischel, "Two-Photon-Excited Fluorescence Spectroscopy of Atomic Fluorine at 170 nm," Opt. Lett. **13**, 360-362 (1988).

9. P. Bogen, Ph. Mertens, E. Pasch, and H. F. Döbele, "Detection of Atomic Oxygen and Hydrogen in the Vacuum UV Using a Frequency-Doubled, Raman-Shifted Dye Laser," J. Opt. Soc. Am. B **9**, 2137-2141 (1992).

10. T. R. Loree, R. C. Sze, and D. L. Barker, "Efficient Raman Shifting of ArF and KrF Laser Wavelengths," Appl. Phys. Lett. **31**, 37-39 (1977).

11. T. R. Loree, R. C. Sze, D. L. Barker, and P. B. Scott, "New Lines in the UV: SRS of Excimer Laser Wavelengths," IEEE J. Quantum Electron. **QE-15**, 337-342 (1979).

12. A. Takahashi, O. Matsumoto, M. Maeda, and Y. Miyazoe, "Tunable VUV Generation by Anti-Stokes Stimulated Raman Conversion of XeCl Laser Radiation," Jpn J. Appl. Phys. **26**, L954-L956 (1987).

13. H. F. Döbele, M. Hörl, and M. Röwekamp, "Tuning Ranges of KrF and ArF Excimer Laser Amplifiers and of Associated Vacuum Ultraviolet Anti-Stokes Raman Lines," Appl. Phys. B **42**, 67-72 (1987).

14. S. Wada, A. Kasai, and H. Tashiro, "Efficient Generation of Higher-Order Anti-Stokes VUV Radiation by Steep-Rise Pumping," Opt. Lett. **17**, 97-99 (1992).

15. R. S. Hargrove and J. A. Paisner, "Tunable, Efficient VUV Generation Using ArF-Pumped, Stimulated Raman Scattering in H_2, in *Digest of Topical Meeting on Excimer Lasers* (Optical Society of America, Washington, DC, 1979), Paper ThA6.

16. H. Schomburg, H. F. Döbele, and B. Rückle, "Tunable Narrow Line Amplification in ArF^* and Anti Stokes Production Around 179 nm," Appl. Phys. B **28**, 201 (1982).

17. H. F. Döbele and B. Rückle, "Application of an Argon-Fluoride Laser System to the Generation of VUV Radiation by Stimulated Raman Scattering," Appl. Opt. **23**, 1040-1043 (1984).

18. H. F. Döbele, M. Röwekamp, and B. Rückle, "Amplification of 193 nm Radiation in Argon-Fluoride and Generation of Tunable VUV Radiation by High-Order Anti-Stokes Raman Scattering," IEEE J. Quantum Electron. **QE-20**, 1284-1287 (1984).

19. G. W. Faris and M. J. Dyer, "Multiphoton Spectroscopy Using Tunable VUV Radiation from a Raman-Shifted Excimer Laser," in *Proceedings on Short-Wavelength Coherent Radiation*, Philip H. Bucksbaum and Natale M. Ceglio, Eds. (Optical Society of America, Washington, DC, 1991), Vol. 11, pp. 58-61.

20. H. Komine, "Stimulated Vibrational Raman Scattering in HD," IEEE J. Quantum Electron. **QE-22**, 520-521 (1986).

21. Y. Shimoji and N. Djeu, "Overtone Pumped Superfluorescent HCl Laser Frequency Converter," Appl. Phys. Lett. **49**, 1-3 (1986).

22. D. A. Haner and I. S. McDermid, "Stimulated Raman Shifting of the Nd:YAG Fourth Harmonic (266 nm) in H_2, HD, and D_2," IEEE J. Quantum Electron. **26**, 1292-1298 (1990).

23. B. P. Scott and N. Djeu, "Efficient Raman Energy Extraction in HD," Appl. Opt. **29**, 2217-2218 (1990).

24. G. W. Faris, M. J. Dyer, W. K. Bischel, and D. L. Huestis, "VUV Stimulated Raman Scattering of an ArF Laser in D_2 and HD," *Conference on Lasers and Electro-Optics, 1990 Technical Digest Series*, Vol. 7 (Optical Society of America, Washington, DC, 1990), pp. 266-268.

25. D. J. Kligler and C. K. Rhodes, "Observation of Two-Photon Excitation of the H_2 E,F $^1\Sigma_g^+$ State," Phys. Rev. Lett. **40**, 309-313 (1978).

26. W. K. Bischel, J. Bokor, D. J. Kligler, and C. K. Rhodes, "Nonlinear Optical Processes in Atoms and Molecules Using Rare-Gas Halide Lasers," IEEE J. Quantum Electron. **QE-15**, 380-392 (1979).

27. H. Pummer, H. Egger, T. S. Luk, T. Srinivasan, and C. K. Rhodes, "Vacuum-Ultraviolet Stimulated Emission from Two-Photon-Excited Molecular Hydrogen," Phys. Rev. A **28**, 795-801 (1983).

28. U. Czarnetzki and H. F. Döbele, "Generation of Vacuum-Ultraviolet Radiation in H_2 by Nonlinear Optical Processes Near the EF- and B-State Resonances," Phys. Rev. A **44**, 7530-7546 (1991).

29. J. D. Buck, D. C. Robie, A. P. Hickman, D. J. Bamford, and W. K. Bischel, "Two-Photon Excitation and Excited-State Absorption Cross Sections for H_2 E,F $^1\Sigma_g^+$ (v = 6): Measurement and Calculations," Phys. Rev. A **39**, 3932-3941 (1989).

30. M. P. McCann, C. H. Chen, and M. G. Payne, "Two-Photon (Vacuum Ultraviolet + Visible) Spectroscopy of Argon, Krypton, Xenon, and Molecular Hydrogen," J. Chem. Phys. **89**, 5429-5441 (1988).

31. R. Pizzoferrato and M. Casalboni, "Extension of Two-Photon Spectroscopy to the Vacuum Ultraviolet Using Synchrotron Radiation," J. Phys. E: Sci. Instrum. **20**, 896-899 (1987).

32. R. Hilbig and R. Wallenstein, "Resonant Sum and Difference Frequency Mixing in Hg," IEEE J. Quantum Electron. **QE-19**, 1759-1770 (1983).

33. G. W. Faris and M. J. Dyer, "Two-Photon-Excitation of Ne at 133 nm," Opt. Lett. **18**, 382-284 (1993).

34. G. D. Boyd, W. D. Johnston, Jr., and I. P. Kaminow, "Optimization of the Stimulated Raman Scattering Threshold," IEEE J. Quantum Electron. **QE-5**, 203-206 (1969).

35. M. A. Henesian, C. D. Swift, and J. R. Murray, "Stimulated Rotational Raman Scattering in Nitrogen in Long Air Paths," Opt. Lett. **10**, 565-567 (1985).

36. J. R. Murray, J. Goldhar, D. Eimerl, and A. Szöke, "Raman Pulse Compression of Excimer Lasers for Application to Laser Fusion," IEEE J. Quantum Electron. **QE-15**, 342-368 (1979).

37. J. L. Carlsten and R. G. Wenzel, "Stimulated Rotational Raman Scattering in CO_2-Pumped Para-H_2," IEEE J. Quantum Electron. **QE-19**, 1407-1413 (1983).

38. W. K. Bischel and M. J. Dyer, "Wavelength Dependence of the Absolute Raman Gain Coefficient for the Q(1) Transition in H_2," J. Opt. Soc. Am. B **3**, 677-682 (1986).

39. G. Herzberg, *Molecular Spectra and Molecular Structure, Vol. I. Spectra of Diatomic Molecules* (Van Nostrand Reinhold Company, New York, 1950), pp. 124-125, 133-135.

40. D. A. Long, *Raman Spectroscopy* (McGraw-Hill, New York, 1977), Tables I and J.

41. G. C. Herring, M. J. Dyer, and W. K. Bischel, "Temperature and Wavelength Dependence of the Rotational Raman Gain Coefficient in N_2," Opt. Lett. **11**, 348-350 (1986).

42. J. Rychlewski, "Frequency Dependent Polarizabilities for the Ground State of H_2, HD, and D_2," J. Chem. Phys. **78**, 7252-7259 (1983).

43. J. Rychlewski, personal communication (1992).

44. A. L. Ford and J. C. Browne, "Direct-Resolvent-Operator Computations on the Hydrogen-Molecule Dynamic Polarizability, Rayleigh, and Raman Scattering," Phys. Rev. A **7**, 418-426 (1973).

45. W. M. Huo and R. L. Jaffe, "*Ab Initio* Calculation of the Third-Order Susceptibility of H_2," Phys. Rev. Lett. **47**, 30-34 (1981).

46. D. M. Bishop and J. Pipin, "Calculated Raman Overtone Intensities for H_2 and D_2," J. Chem. Phys. **94**, 6073-6080 (1991).

47. C. Schwartz and R. J. LeRoy, "Nonadiabatic Eigenvalues and Adiabatic Matrix Elements for all Isotopes of Diatomic Hydrogen," J. Mol. Spectrosc. **121**, 420-439 (1987).

48. A. C. Albrecht and M. C. Hutley, "On the Dependence of Vibrational Raman Intensity on the Wavelength of Incident Light," J. Chem. Phys. **55**, 4438-4443 (1971).

49. W. K. Bischel and G. Black, "Wavelength Dependence of Raman Scattering Cross Sections from 200-600 nm," in *Excimer Lasers-1983*, C. K. Rhodes, H. Egger and H. Pummer, Eds. (American Institute of Physics, New York, 1983), pp. 181-187.

50. D. M. Bishop and L. M. Cheung, "Dynamic Dipole Polarizability of H_2 and HeH^+," J. Chem. Phys. **72**, 5125-5132 (1980).

51. S. L. Bragg, J. W. Brault, and W. H. Smith, "Line Positions and Strengths in the H_2 Quadrupole Spectrum," Astrophys. J. **263**, 999-1004 (1982).

52. A.R.W. McKellar and T. Oka, "A Study of the Electric Quadrupole Fundamental Band of D_2 Using an Infrared Difference Frequency Laser System," Can. J. Phys. **56**, 1315-1320 (1978).

53. N. H. Rich, J.W.C. Johns, and A.R.W. McKellar, "Frequency and Intensity Measurements in the Fundamental Infrared Band of HD," J. Mol. Spectrosc. **95**, 432-438 (1982).

54. K. Sentrayan, L. Major, H. Bryant, A. Michael, and V. Kushawaha, "Laser Wavelength, Pressure and Temperature Dependence on the Stimulated Raman Scattering Gain in H_2," Spectroscopy Lett. **25**, 627-637 (1992).

55. T. Witkowicz and A. D. May, "Collisional Effects in Compressed HD," Can. J. Phys. **54**, 575-583 (1976).

56. W. K. Bischel and M. J. Dyer, "Temperature Dependence of the Raman Linewidth and Line Shift for the Q(1) and Q(0) Transitions in Normal and para-H_2," Phys. Rev. A **33**, 3113-3123 (1986).

57. D. E. Jennings, A. Weber, and J. W. Brault, "Raman Spectroscopy of Gases with a Fourier Transform Spectrometer: the Spectrum of D_2," Appl. Opt. **25**, 284-290 (1986).

58. K. C. Smyth, G. J. Rosasco, and W. S. Hurst, "Measurement and Rate Law Analysis of D_2 Q-Branch Line Broadening Coefficients for Collisions with D_2, He, Ar, H_2 and CH_4," J. Chem. Phys. **87**, 1001-1011 (1987).

59. P. J. Brannon, C. H. Church, and C. W. Peters, "Electric Field Induced Spectra of Molecular Hydrogen, Deuterium and Deuterium Hydride," J. Mol. Spectrosc. **27**, 44-54 (1968).

60. G. J. Rosasco, A. D. May, W. S. Hurst, L. B. Petway, and K. C. Smyth, "Broadening and Shifting of the Raman Q Branch of HD," J. Chem. Phys. **90**, 2215-2124 (1989).

61. A. D. May, personal communication (1992).

62. R. W. Minck, E. E. Hagenlocker, and W. G. Rado, "Stimulated Pure Rotational Raman Scattering in Deuterium," Phys. Rev. Lett. **17**, 229-231 (1966).

63. D. E. Jennings and J. W. Brault, "The Ground State of Molecular Hydrogen," J. Mol. Spectrosc. **102**, 265-272 (1983).

64. G. C. Herring, M. J. Dyer, and W. K. Bischel, "Temperature and Density Dependence of the Linewidths and Line Shifts of the Rotational Raman Lines in N_2 and H_2," Phys. Rev. A **34**, 1944-1951 (1986).

65. R.A.J. Keijser, J. R. Lombardi, K. D. van den Hout, B. C. Sanctuary, and H.F.P. Knaap, "The Pressure Broadening of the Rotational Raman Lines of Hydrogen Isotopes," Physica **76**, 585-608 (1974).

66. B. P. Stoicheff, "High Resolution Raman Spectroscopy of Gases," IX. Spectra of H_2, HD, and D_2," Can. J. Phys. **35**, 730-741 (1957).

67. F. Mausault-Herail, M. Echargui, G. Levi, J. P. Marsault, and J. Bonamy, "Collisional Effects on the Rotational and Rotation-Vibration Raman Spectra of HD Compressed by Argon," J. Chem. Phys. **77**, 2715-2727 (1982).

68. K. D. van den Hout, P. W. Hermans, E. Mazur, and H.F.P. Knaap, "The Broadening and Shift of the Rotational Raman Lines for Hydrogen Isotopes at Low Pressures," Physica **104A**, 509-547 (1980).

69. D. C. Robie, J. D. Buck, and W. K. Bischel, "Bandwidth and Tuning Range of an ArF Laser Measured by 1+1 Resonantly Enhanced Multiphoton Ionization of NO," Appl. Opt. **29**, 3961-3965 (1990).

70. M. Versluis, M. Ebben, M. Drabbels, and J. J. ter Meulen, "Frequency Calibration in the ArF Excimer Laser-Tuning Range Using Laser-Induced Fluorescence of NO," Appl. Opt. **30**, 5229-5234 (1991).

71. C. E. Moore, *Atomic Energy Levels*, Vol. II, National Standard Reference Data Series, National Bureau of Standards 35 (U.S. Government Printing Office, Washington, DC, 1971), pp. 169-173.

72. I. Dabrowski, "The Lyman and Werner Bands of H_2," Can. J. Phys. **62**, 1639-1664 (1984).

73. P. Senn and K. Dressler, "Spectroscopic Identification of Rovibronic Levels Lying Above the Potential Barrier of the EF $^1\Sigma_g^+$ Double-Minimum State of the H_2 Molecule," J. Chem. Phys. **87**, 6908-6914 (1987).

74. I. Dabrowski and G. Herzberg, "The Absorption and Emission Spectra of HD in the Vacuum Ultraviolet," Can. J. Phys. **54**, 525-567 (1976).

75. G. H. Dieke, "The 2s $^1\Sigma \rightarrow 2p\ ^1\Sigma$ Bands of the Hydrogen Molecule," Phys. Rev. **50**, 797-805 (1936).

76. K. Yoshino, D. E. Freeman, and W. H. Parkinson, "Atlas of the Schumann-Runge Absorption Bands of O_2 in the Wavelength Region 175-205 nm," J. Phys. Chem. Ref. Data **13**, 207-227 (1984).

77. Note error in position of R(25) line in (7,1) band in reference 76. Correct value is probably 51665.27.

78. Positions for lines in the 7,1 band not appearing in reference 76 may be calculated from the 7,0 band line positions using the 1,0 Q Raman band given in reference 86.

79. M. Versluis and G. Meijer, "Intracavity C Atom Absorption in the Tuning Range of the ArF Excimer Laser," J. Chem. Phys. **96**, 3350-3351 (1992).

80. G. Meijer, A. M. Wodtke, H. Voges, H. Schlüter, and P. Andresen, "State-Selective Detection of CO Using a Tunable ArF Excimer Laser," J. Chem. Phys. **89**, 2588-2589 (1988).

81. X. Yang, A. M. Wodtke, and L. Hüwel, "Direct Observation of Orbit Rotation Predissociation in the O_2 Schumann-Runge System," J. Chem. Phys. **94**, 2469-2474 (1991).

82. M. P. Lee and R. K. Hanson, "Calculations of O_2 Absorption and Fluorescence at Elevated Temperatures for a Broadband Argon-Fluoride Laser Source at 193 nm," J. Quant. Spectrosc. Radiat. Transfer, **36**, 425-440 (1986).

83. R. N. Zare, A. L. Schmeltekopf, W. J. Harrop, and D. L. Albritton, "A Direct Approach for the Reduction of Diatomic Spectra to Molecular Constants for the Construction of RKR Potentials," J. Mol. Spectrosc. **46**, 37-66 (1973); a copy of the program RLS for calculating transition line strengths and positions was kindly provided by these authors.

84. A. S.-C. Cheung, K. Yoshino, W. H. Parkinson, and D. E. Freeman, "Molecular Spectroscopic Constants of O_2 ($B^3\Sigma_u^-$): The Upper State of the Schumann Runge Bands," J. Mol. Spectrosc. **119**, 1-10 (1986).

85. C. Amiot and J. Verges, "The Magnetic Dipole $a^1\Delta_g \rightarrow X^3\Sigma_g^-$ Transition in the Oxygen Afterglow," Can. J. Phys. **59**, 1391-1398 (1981).

86. M. Loëte and H. Berger, "High Resolution Raman Spectroscopy of the Fundamental Vibrational Band of $^{16}O_2$," J. Mol. Spectrosc. **68**, 317-325 (1977).

87. D. M. Creek and R. W. Nicholls, "A Comprehensive Re-Analysis of the $O_2(B\ ^3\Sigma_u^- - X\ ^3\Sigma_g^-$ Schumann-Runge Band System," Proc. R. Soc. London A **341**, 517-536 (1975).

88. P. C. Cosby, R. A. Copeland, H. Park, and T. G. Slanger, "Line Positions and Molecular Constants for O_2 Schumann-Runge Bands," in preparation, 1993.

89. R. N. Zare, "Calculation of Intensity Distribution in the Vibrational Structure of Electronic Transitions: The $B\ ^3\Pi_{0^+\ u} - X\ ^1\Sigma_{0^+\ g}$ Resonance Series of Molecular Iodine," J. Chem. Phys. **40**, 1934 -1944 (1964); E. W. Kaiser, "Dipole Moment Hyperfine Parameters of $H^{35}Cl$ and $D^{35}Cl$," J. Chem. Phys. **53**, 1686-1703 (1970).

90. J. M. Hutson, "Centrifugal Distortion Constants for Diatomic Molecules: An Improved Computational Method," J. Phys. B: At. Mol. Phys. **14**, 851-857 (1981); a copy of the program CDIST for calculating rotational constants and their centrifugal corrections was kindly provided by this author.

91. Optronics laboratories, Inc., deuterium arc calibration lamp.

92. R. D. Saunders, W. R. Ott, and J. M. Bridges, "Spectral Irradiance Standard for the Ultraviolet: the Deuterium Lamp," Appl. Opt. **17**, 593-600 (1978).

93. H. Okabe, *Photochemistry of Small Molecules* (John Wiley and Sons, New York, 1978), pp. 177-181.

94. Data sheet for model 542G-08-18 from EMR Photoelectric, Princeton, New Jersey.

95. Y. R. Shen and N. Bloembergen, "Theory of Stimulated Brillouin and Raman Scattering," Phys. Rev. **137**, A1787-A1805 (1965).

96. M. D. Duncan, R. Mahon, J. Reintjes, and L. L. Tankersley, "Parametric Raman Gain Suppression in D_2 and H_2," Opt. Lett. **11**, 803-805 (1986).

97. J. R. Murray and A. Javan, "Effects of Collisions on Raman Line Profiles of Hydrogen and Deuterium Gas," J. Mol. Spectrosc. **42**, 1-26 (1972).

98. J. O. Hirschfelder, C. F. Curtiss, and R. B. Bird, *Molecular Theory of Gases and Liquids* (John Wiley & Sons, New York, 1954), Chapter 8.

99. See expressions for rotational-vibrational Raman scattering in reference 40, and the relevant off-diagonal matrix elements for the polarizability anisotropy given in reference 47.

100. W. L. Glab and J. P. Hessler, "Frequency Shift and Asymmetric Line Shape of the Fourth Anti-Stokes Component from a Hydrogen Raman Shifter," Appl. Opt. **27**, 5123-5126 (1988).

101. M. J. Dyer and W. K. Bischel, "Optical Stark Shift Spectroscopy: Measurement of the v = 1 Polarizability in H_2," Phys. Rev. A **44**, 3138-3143 (1991).

102. G. W. Faris, M. J. Dyer, D. L. Huestis, and W. K. Bischel, "Two-Photon Spectroscopy of the F $^1\Pi_g$ and f $^3\Pi_g$ States of Molecular Fluorine," J. Chem. Phys. **97**, 5964-5969 (1992).

103. K. Dressler and L. Wolniewicz, "The $H\bar{H}$ $^1\Sigma_g^+$ State of Hydrogen: Adiabatic Calculation of Vibronic States in H_2, HD, and D_2," J. Mol. Spectrosc. **86**, 534-543 (1981).

104. S. Bashkin and J. O. Stoner, Jr., *Atomic Energy Levels and Grotrian Diagrams* (North-Holland Publishing Co., Amsterdam, 1975), p. 213.

Table 1

Vibrational Raman Gain

Room temperature (296 K)

	ν_R (cm^{-1})	J	$\Delta\nu/N_o$ (MHz/amagat)	$\Delta N/N_o$	α (a.u.)	γ (a.u.)	$d\sigma/d\Omega$ ($10^{-28} cm^2$/ster)	g (cm/GW)	P_{th} (kW)
H_2	4155.3[a]	1	52[b]	0.660	1.179	1.096	2.51	25.4	6
D_2	2987.3[c]	2	124[d]	0.385	0.968	0.877	1.85	4.28	40
HD	3628.3[e]	1	816[f]	0.390	1.085	0.997	2.22	0.82	200

Liquid nitrogen temperature (77 K)

H_2	4161.2[a]	0	29[b]	0.502	1.179	1.096	2.43	33.7	5
H_2	4155.3[a]	1	42[b]	0.494	1.179	1.096	2.51	23.9	6
D_2	2993.6[c]	0	39[g]	0.598	0.968	0.877	1.81	20.5	8
HD	3632.2[e]	0	153[h]	0.625	1.085	0.997	2.15	6.81	20

Rotational Raman Gain (Linear Polarization)[l]

Room temperature (296 K)

H_2	587.0[j]	1	114[k]	0.622	3.01	1.13	3.98	40
D_2	414.6[c]	2	124[l]	0.333	2.85	0.88	1.51	100
HD	443.1[m]	1	780[n]	0.345	2.91	1.07	0.30	500

Liquid Nitrogen Temperature (77 K)

H_2	354.4[j]	0	67[k]	0.502	2.99	1.89	8.99	20
H_2	587.0[j]	1	110[k]	0.494	3.01	1.13	3.28	50
D_2	179.1[c]	0	112[o]	0.577	2.82	1.71	5.55	30
HD	267.1[m]	0	270[o]	0.620	2.90	1.78	2.59	60

The peak plane-wave steady-state high density Raman gain coefficient, g, and the (approximate) minimum laser power to reach threshold for stimulated Raman scattering, P_{th}, are given for the strongest Raman lines for both vibrational and rotational Raman scattering in different isotopes of hydrogen at room temperature and liquid nitrogen temperature. Also given are the parameters used in calculation of g and P_{th}: the Raman shift, ν_R, the initial rotational level, J, the density-dependent line broadening coefficient, $\Delta\nu/N_o$, the density-normalized population differences, $\Delta N/N_o$, the off-diagonal matrix elements of the isotropic and anisotropic polarizabilities, α and γ, and the differential Raman cross section, $d\sigma/d\Omega$. Note that 1 a.u. = 1.481845×10^{-25} cm^3.

[a] ref. 51
[b] ref. 56 — 298 K, 81 K
[c] ref. 57
[d] ref. 58 — 297 K
[e] ref. 59
[f] ref. 60 — 298 K
[g] ref. 61 — 110 K
[h] ref. 55 — 85 K
[i] The gain coefficient for rotational Raman scattering is a factor of 1.5 larger for circular polarization (Ref. 62).
[j] ref. 63
[k] ref. 64 — 295 K, 80 K
[l] ref. 65 — 293 K
[m] ref. 66
[n] ref. 67 — 300 K
[o] ref. 68 — 77.8 K, 78.5 K

Table 2
LINE POSITIONS OF THE TWO-PHOTON RESONANCES

Krypton Lines

Energy (cm-1)	Transition
103121.95	$4p^5 6p[5/2,2] \leftarrow 4p^6\ ^1S$
103363.43	$4p^5 6p[3/2,2) \leftarrow 4p^6\ ^1S$
103762.45	$4p^5 6p[1/2,0] \leftarrow 4p^6\ ^1S$

H_2 Lines

103084.43	E,F (v'=6,J'=3)	← X (v"=0,J"=3)
103289.67	E,F (v'=7,J'=3)	← X (v"=0,J"=3)
103335.78	E,F (v'=6,J'=2)	← X (v"=0,J"=2)
103487.08	E,F (v'=6,J'=1)	← X (v"=0,J"=1)
103548.65	E,F (v'=7,J'=2)	← X (v"=0,J"=2)
103559.59	E,F (v'=6,J'=0)	← X (v"=0,J"=0)
103739.33	E,F (v'=7,J'=1)	← X (v"=0,J"=1)

HD Lines

103075.92	E,F (v'=6,J'=2)	← X (v"=0,J"=2)
103172.59	E,F (v'=6,J'=1)	← X (v"=0,J"=1)
103221.02	E,F (v'=6,J'=0)	← X (v"=0,J"=0)
103256.60	E,F (v'=7,J'=2)	← X (v"=0,J"=2)
103414.38	E,F (v'=7,J'=1)	← X (v"=0,J"=1)
103493.72	E,F (v'=7,J'=0)	← X (v"=0,J"=0)

FIGURE CAPTIONS

Fig. 1. Experimental apparatus for Raman-shifting an ArF excimer laser for multiphoton spectroscopy.

Fig. 2. Beam profiles for beams exiting oscillator (a) and amplifier (b). Amplifier beam is reduced in size by a factor of 2.

Fig. 3. Schematic of liquid-nitrogen-cooled Raman cell (output side). The input side of cell is symmetric to the output side and is not shown.

Fig. 4. (a) ArF laser intensity for old gas fill and several meters of air absorption path; (b) intensity for a new gas fill and good purge; and (c) two-photon calibration lines as a function of two-photon energy and wavelength. Tick marks at top indicate O_2 Schumann Runge lines; those at the bottom are for two-photon resonances.

Fig. 5. Dependence of first Stokes energy for Raman-shifting in D_2 on tilt of focusing lens.

Fig. 6. Stokes and anti-Stokes orders generated in D_2 at room temperature and a density of 5.4 amagat.

Fig. 7. Stokes and anti-Stokes orders generated in HD at 77 K and a density of 6 amagat.

Fig. 8. Stokes and anti-Stokes orders generated in HD at 77 K and a density of 3 amagat.

Fig. 9. Stokes and anti-Stokes orders in D_2 as a function of density at 77 K, not calibrated for wavelength-dependent detection response.

Fig. 10. Density dependence of stimulated Raman gain for vibrational and pure rotational scattering in D_2 at room temperature (Q(2) and S(2)) and near liquid nitrogen

temperature (Q(0) and S(0)). Shaded regions indicate range of uncertainty in Raman gain due to imprecise values for the self-diffusion coefficient.

Fig. 11. Density dependence of the second anti-Stokes order in HD at 77 K.

Fig. 12. Relative intensity as a function of density for ArF excimer laser (pump), first Stokes, and first through third anti-Stokes orders for Raman shifting in D_2 at room temperature, 16-mJ pump energy.

Fig. 13. Relative intensity as a function of density for first Stokes and fourth through eighth anti-Stokes orders for Raman shifting in D_2 at room temperature, 30-mJ pump energy.

Fig. 14. (a) The second anti-Stokes intensity for Raman shifting in HD and (b) the two-photon-resonant REMPI excitation spectrum for F $^1\Pi_g$ (v' = 3) ← X $^1\Sigma_g^+$ (v" = 0) transition in F_2 excited with this radiation, as a function of two-photon energy. The ion signal is not corrected for the varying excitation intensity.

Fig. 15. (a) Two-photon-resonant REMPI excitation spectrum for the $H\bar{H}$ $^1\Sigma_g^+$ (v' = 1, J' = 0) ← X (v" = 0, J" = 0) transition in H_2 (peak indicated by arrow). (b) Two-photon-resonant REMPI excitation spectrum for the $^2D^03/2$ ← $^2P^03/2$ transition in atomic fluorine.

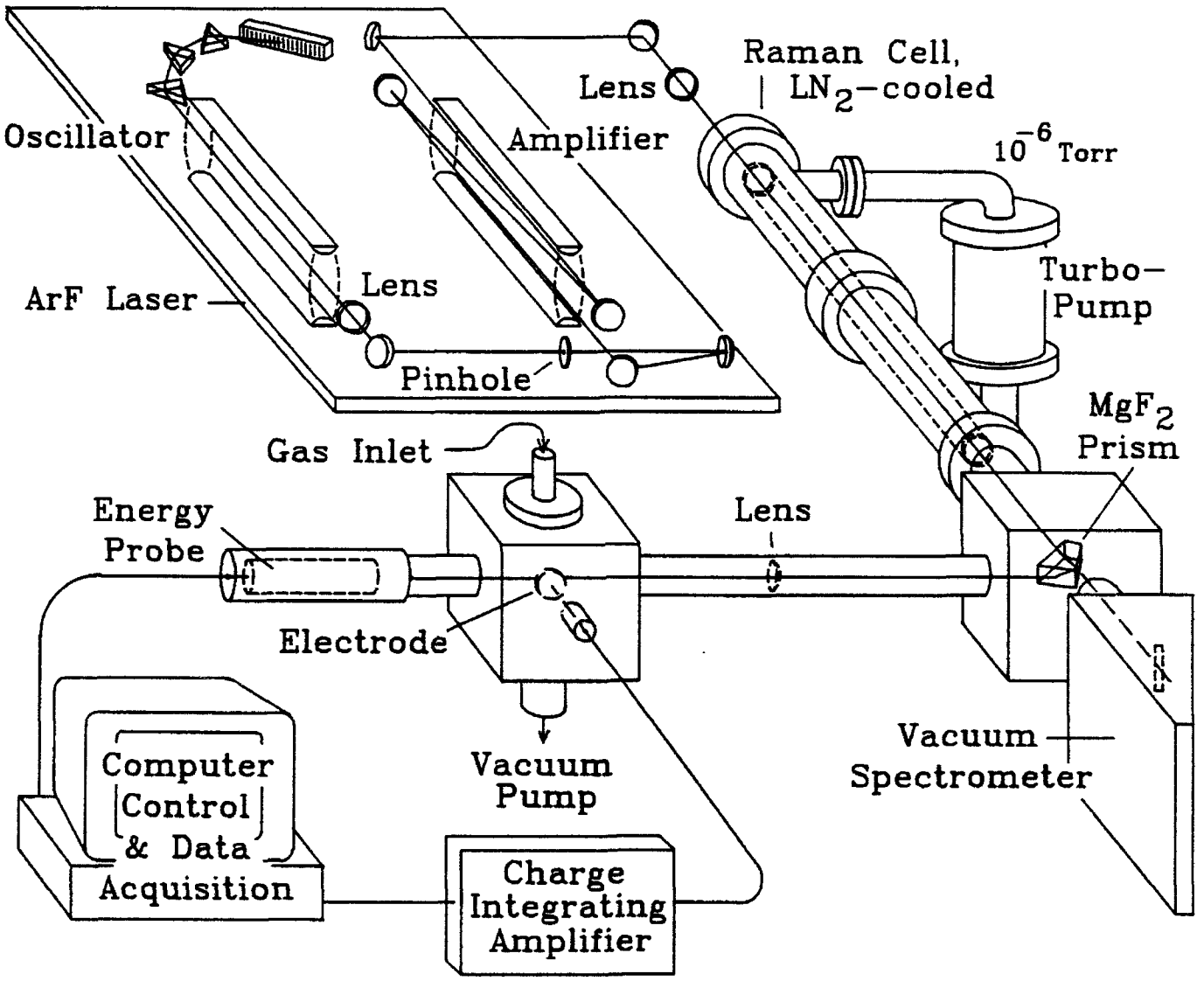
Oscillator
Amplifier
Lens
Raman Cell,
LN2-cooled
10-6 Torr
Turbo-
Pump
ArF Laser
Lens
Pinhole
MgF2
Prism
Gas Inlet
Energy
Probe
Lens
Electrode
Vacuum
Pump
Vacuum
Spectrometer
Computer
Control
& Data
Acquisition
Charge
Integrating
Amplifier

Fig . 1

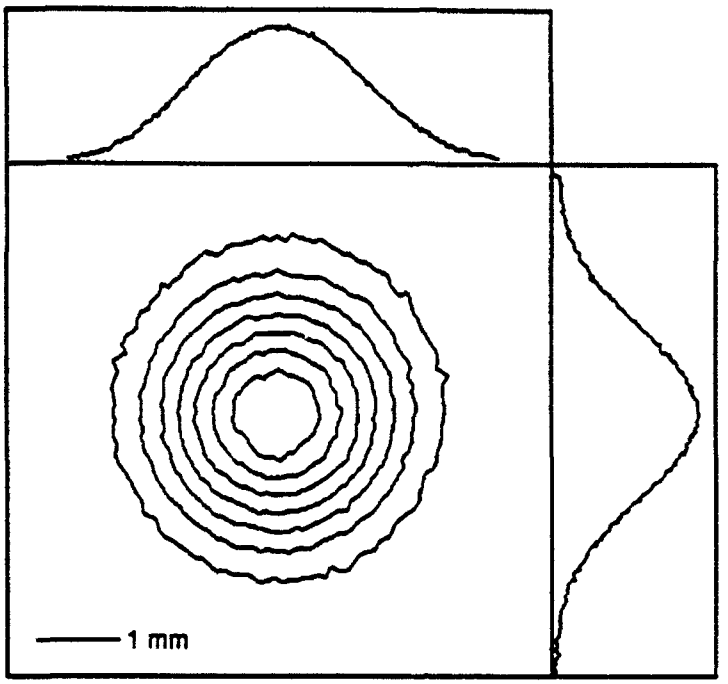

(a)

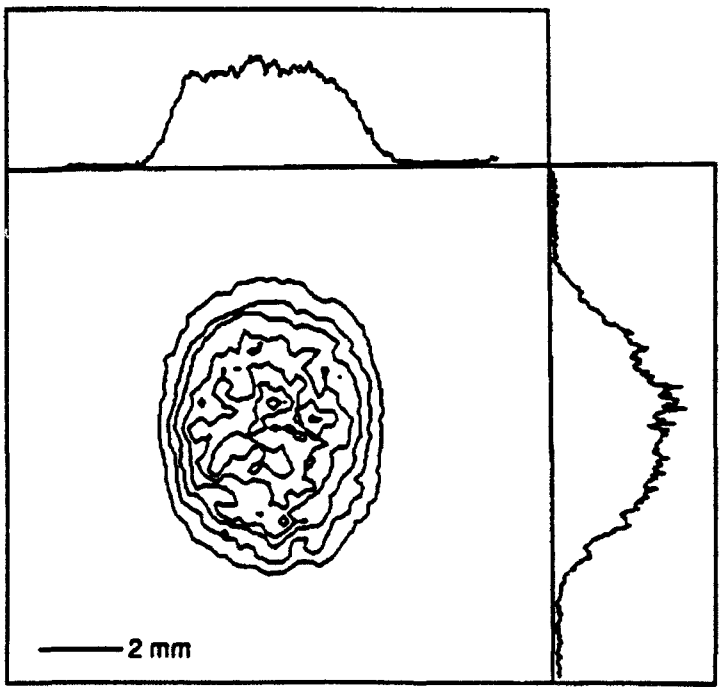

(b)

CM-1187-55

Fig. 2

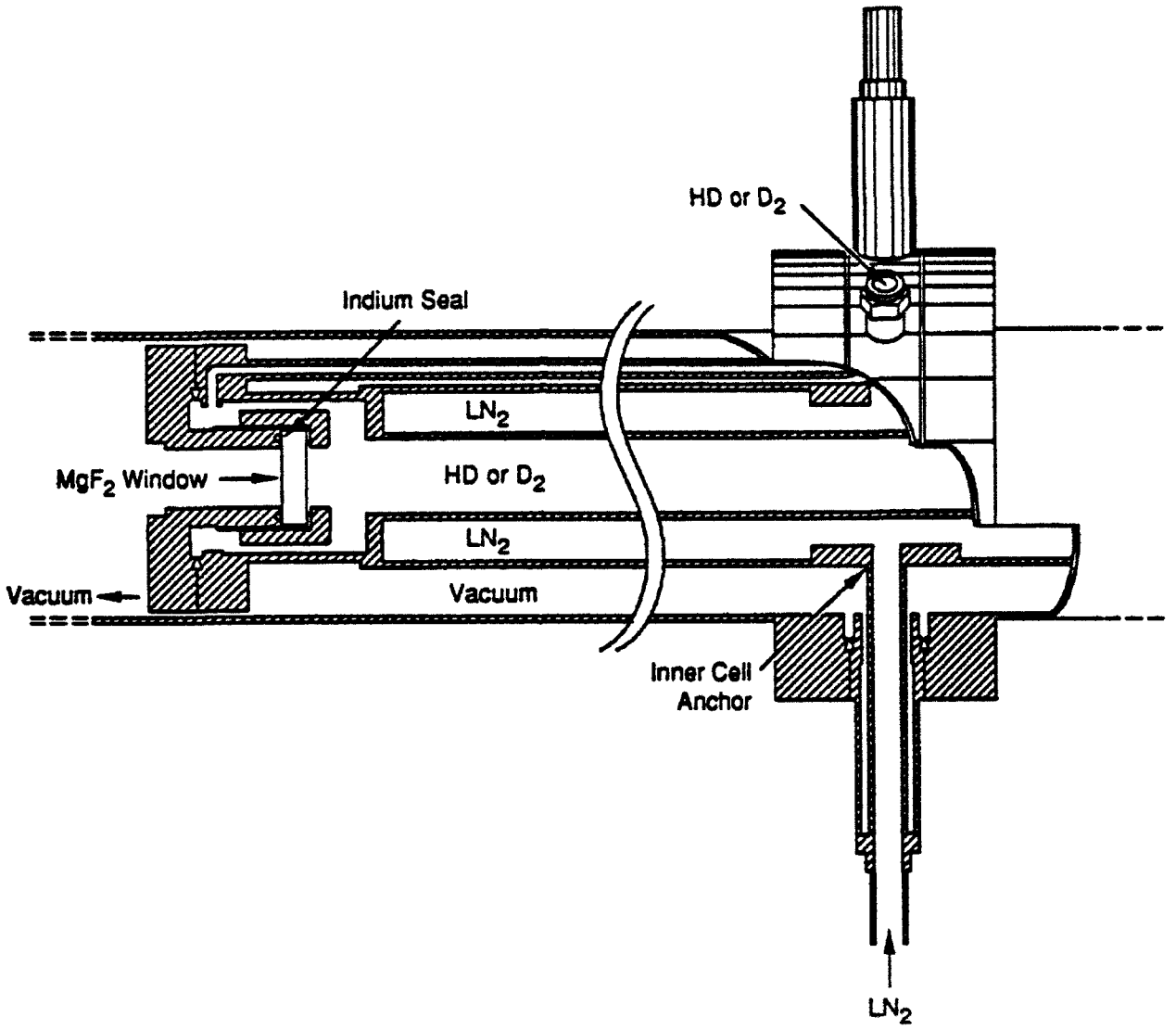
HD or D_2
Indium Seal
LN_2
MgF_2 Window
HD or D_2
LN_2
Vacuum
Vacuum
Inner Cell Anchor
LN_2
CAM-1187-44

Fig. 3

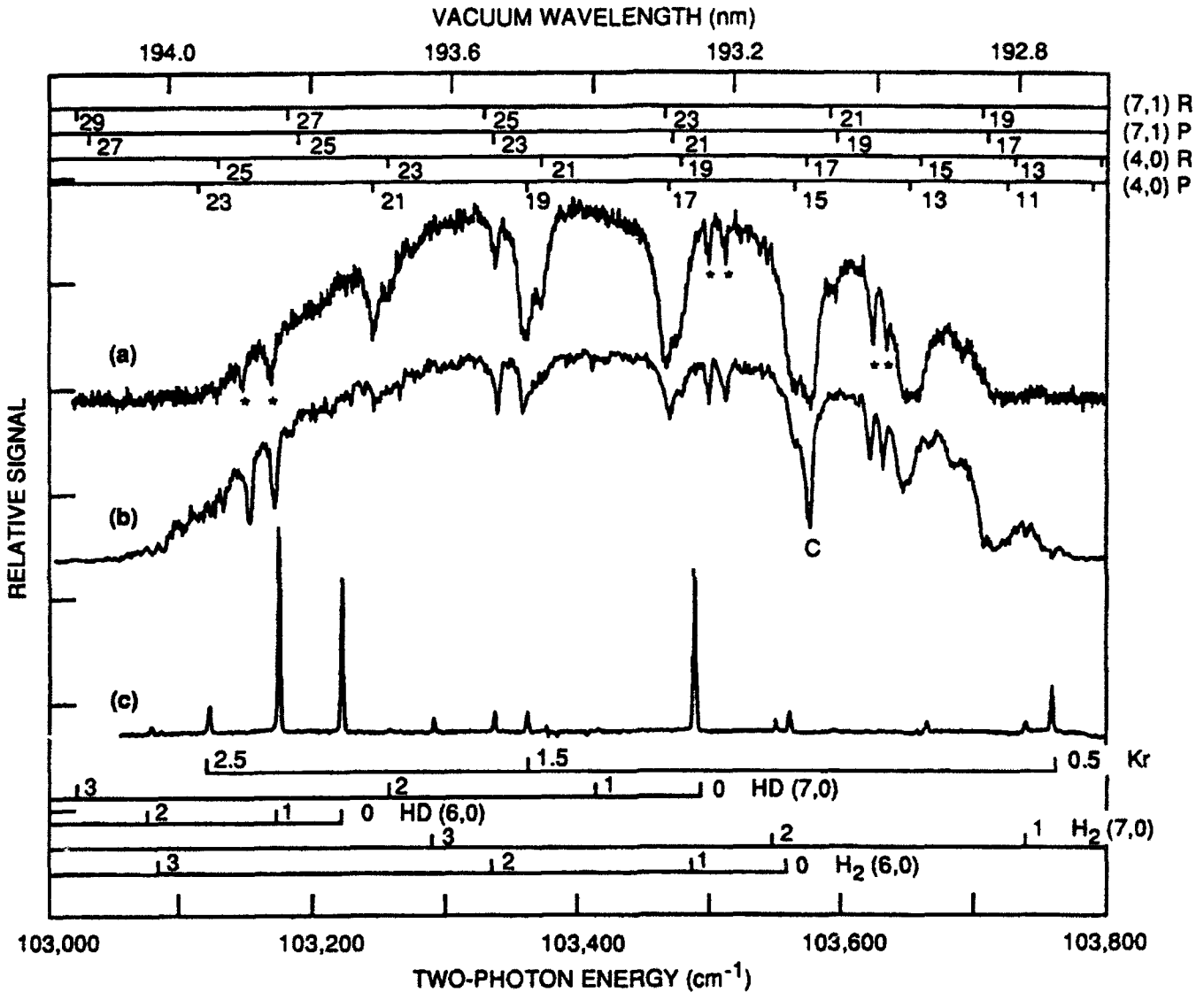

CAM-1187-53

Fig. 4

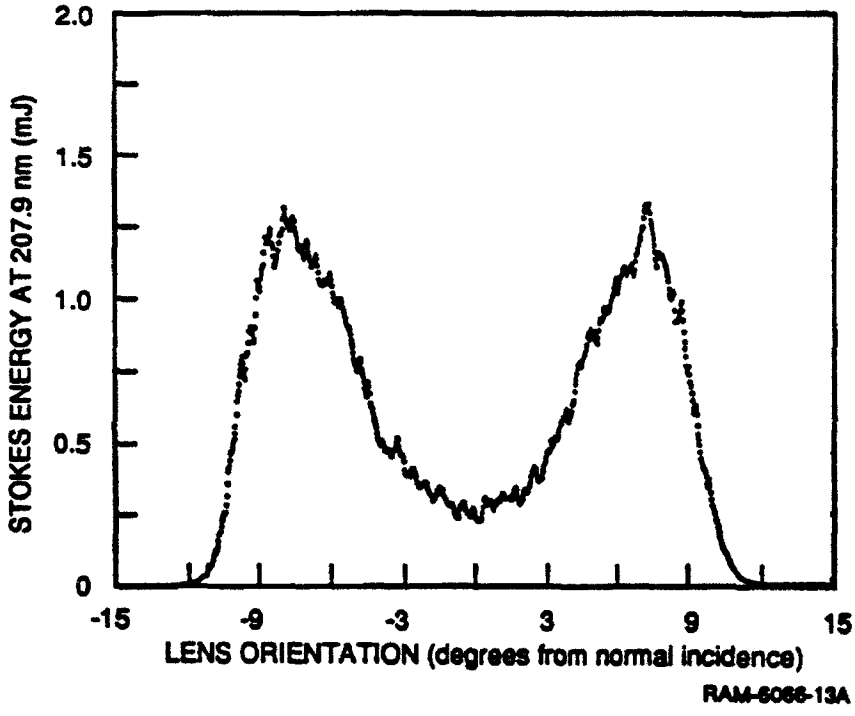
2.0
1.5
1.0
0.5
0
STOKES ENERGY AT 207.9 nm (mJ)
-15
-9
-3
3
9
15
LENS ORIENTATION (degrees from normal incidence)
RAM-6066-13A

Fig. 5

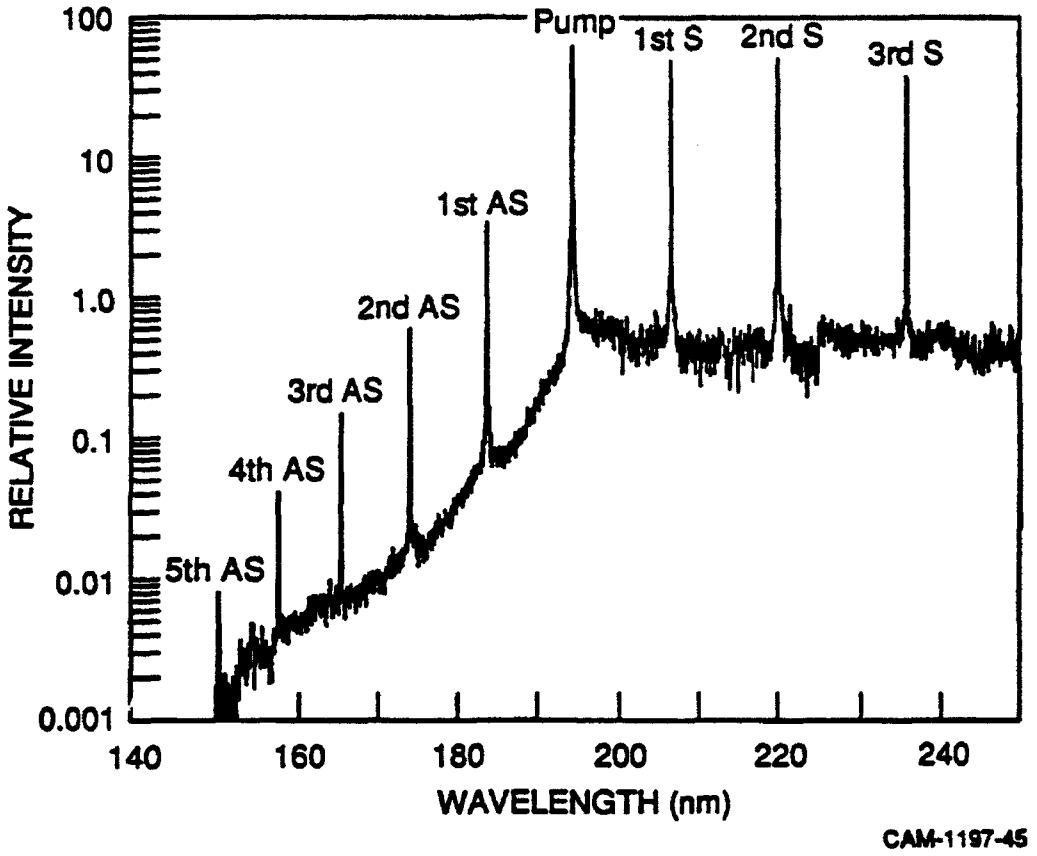
100
10
1.0
0.1
0.01
0.001
RELATIVE INTENSITY
Pump
1st S
2nd S
3rd S
1st AS
2nd AS
3rd AS
4th AS
5th AS
140
160
180
200
220
240
WAVELENGTH (nm)
CAM-1197-45

Fig. 6

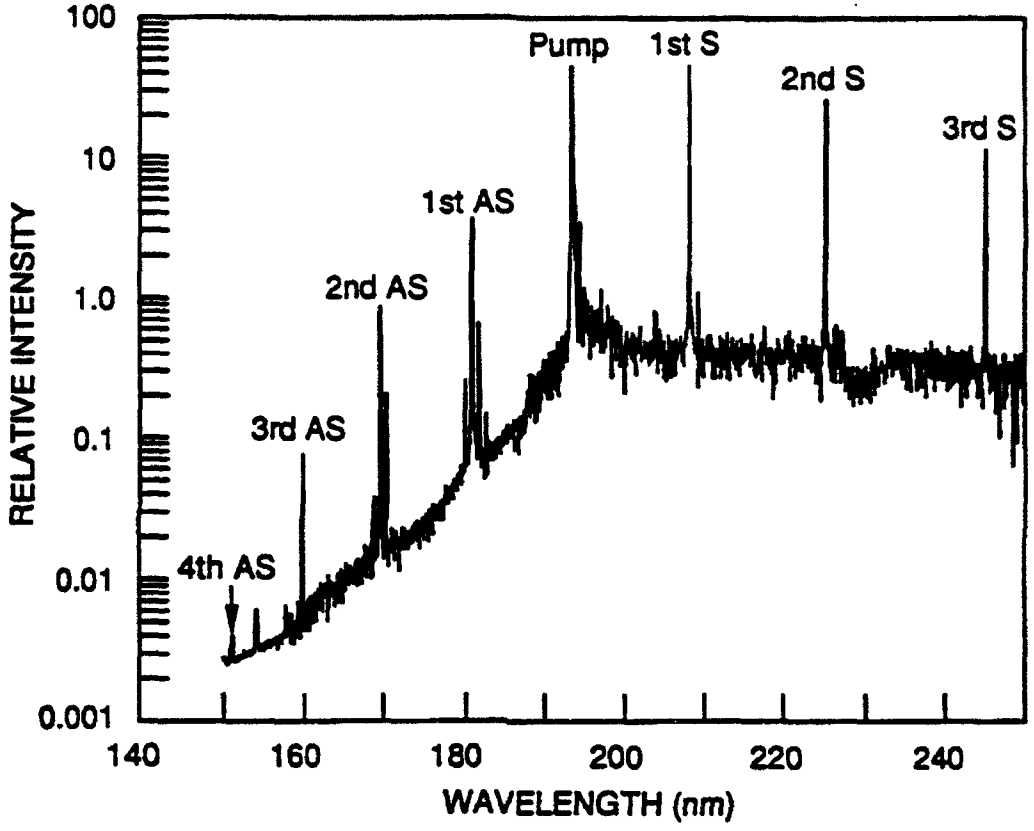
100
10
1.0
0.1
0.01
0.001
RELATIVE INTENSITY
Pump
1st S
2nd S
3rd S
1st AS
2nd AS
3rd AS
4th AS
140
160
180
200
220
240
WAVELENGTH (nm)
CAM-1197-46

Fig. 7

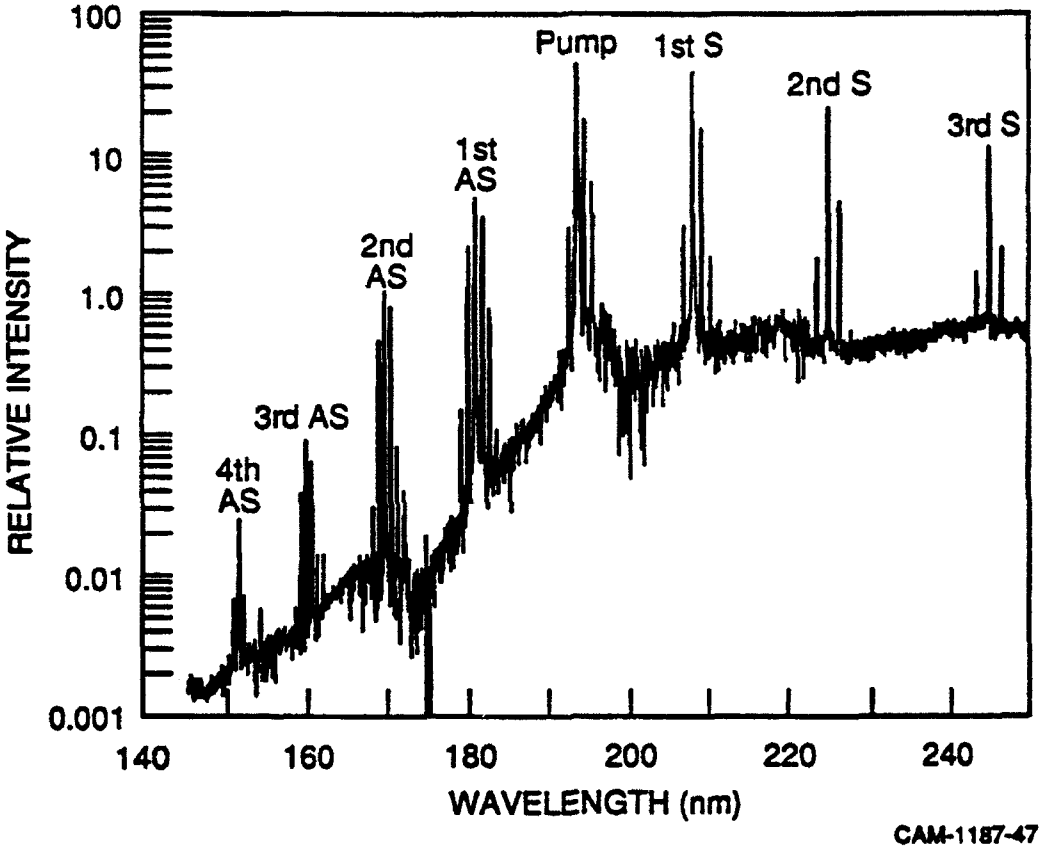
100
10
1.0
0.1
0.01
0.001
RELATIVE INTENSITY
4th AS
3rd AS
2nd AS
1st AS
Pump
1st S
2nd S
3rd S
140
160
180
200
220
240
WAVELENGTH (nm)
CAM-1187-47

Fig. 8

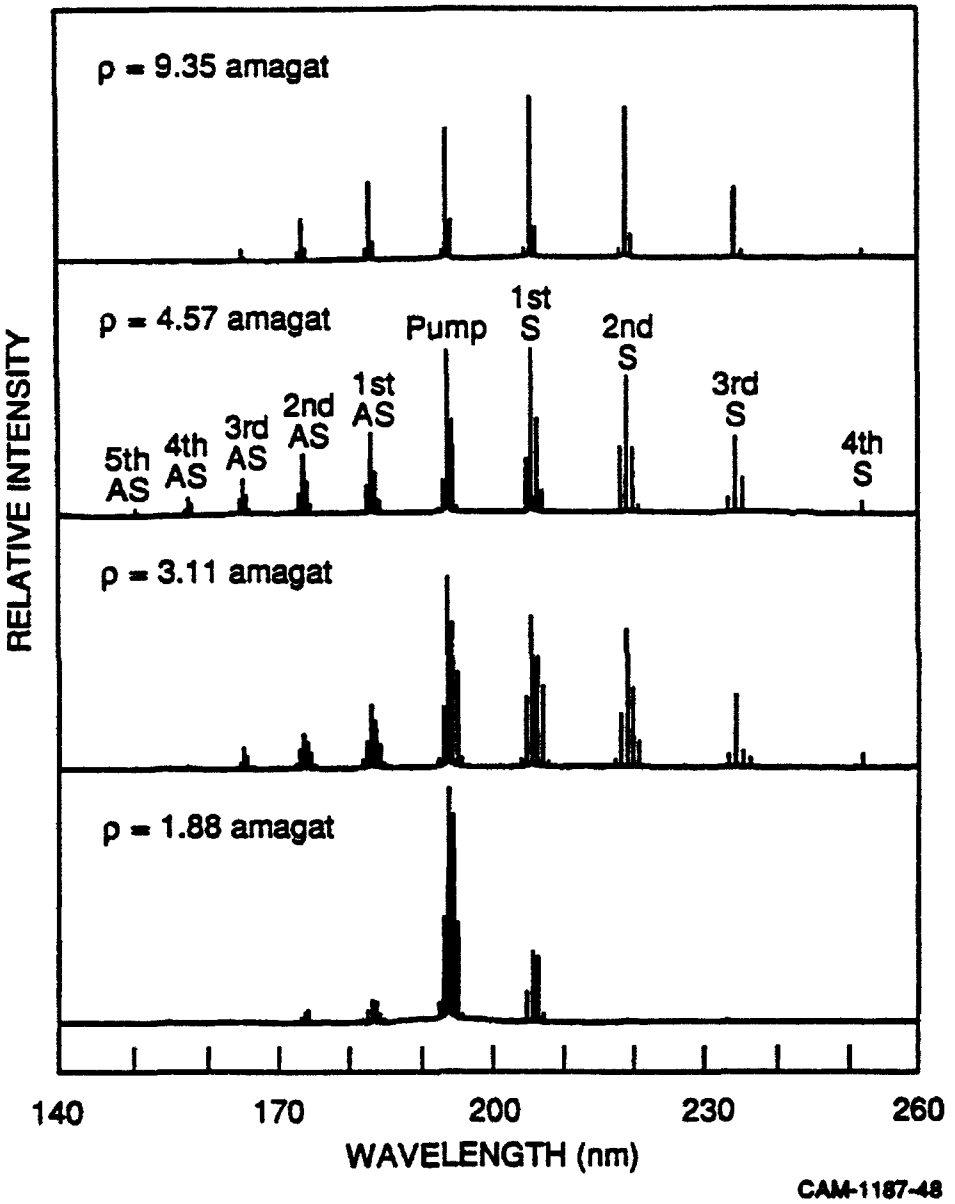
ρ = 9.35 amagat
ρ = 4.57 amagat
ρ = 3.11 amagat
ρ = 1.88 amagat
5th AS
4th AS
3rd AS
2nd AS
1st AS
Pump
1st S
2nd S
3rd S
4th S
RELATIVE INTENSITY
140
170
200
230
260
WAVELENGTH (nm)
CAM-1187-48

Fig. 9

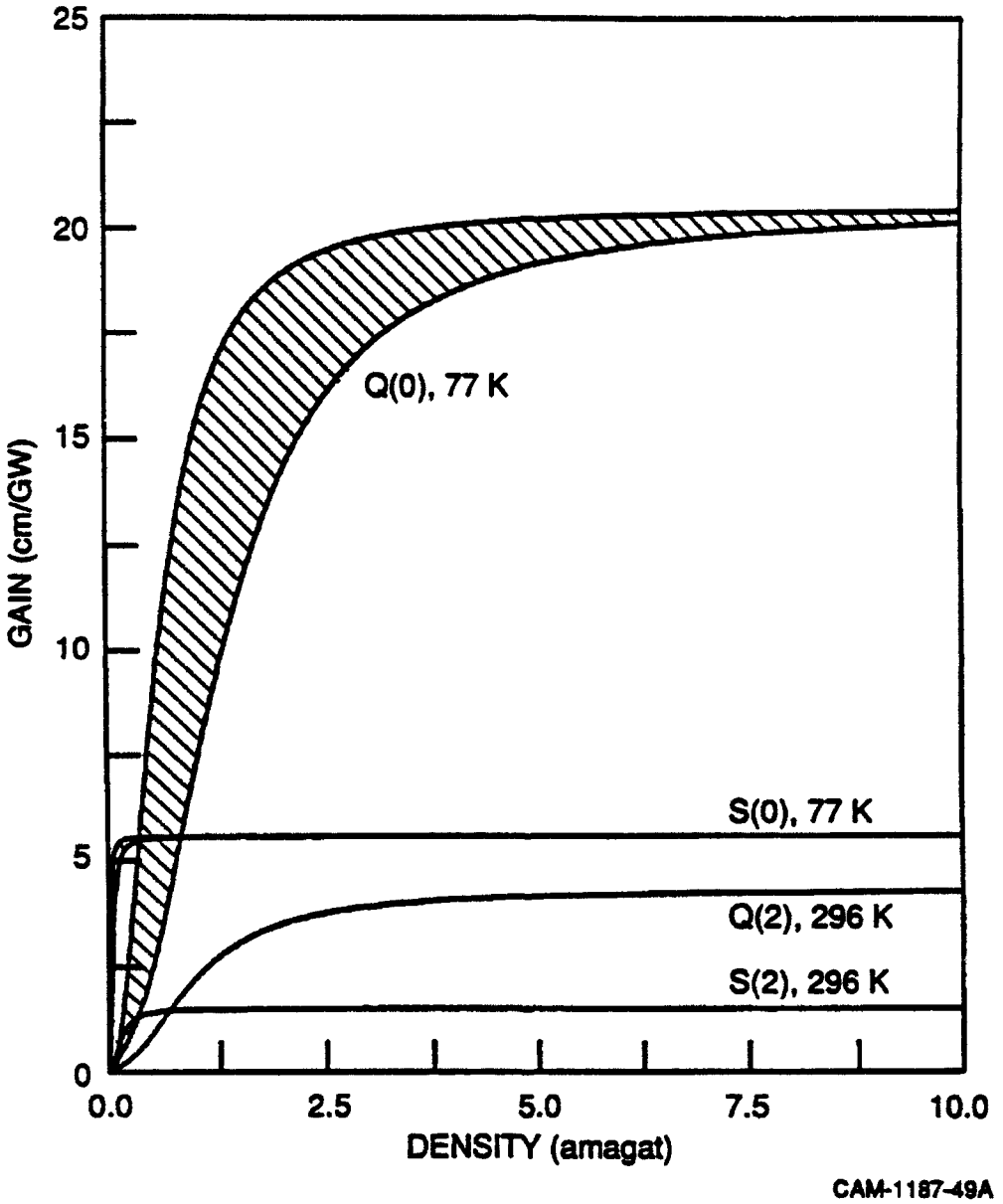
25
20
15
10
5
0
GAIN (cm/GW)
Q(0), 77 K
S(0), 77 K
Q(2), 296 K
S(2), 296 K
0.0
2.5
5.0
7.5
10.0
DENSITY (amagat)
CAM-1187-49A

Fig. 10

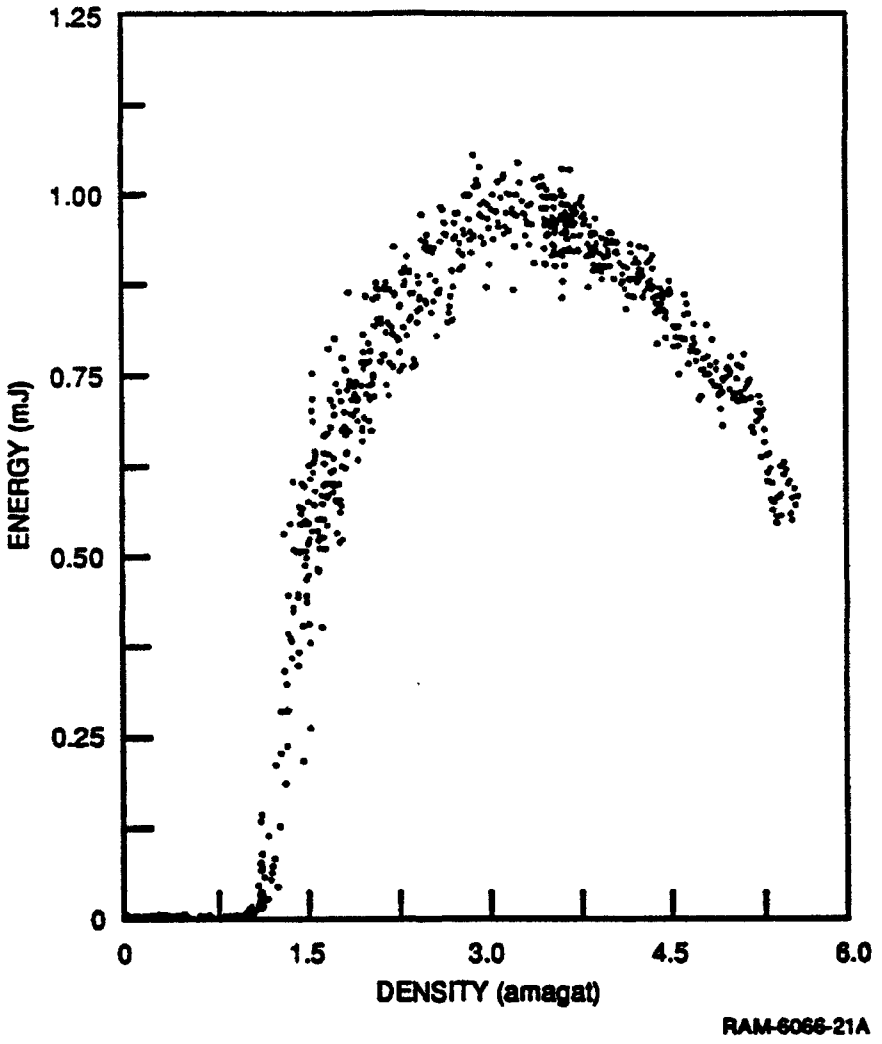
1.25
1.00
0.75
0.50
0.25
0
ENERGY (mJ)
0
1.5
3.0
4.5
6.0
DENSITY (amagat)
RAM-6066-21A

Fig. 11

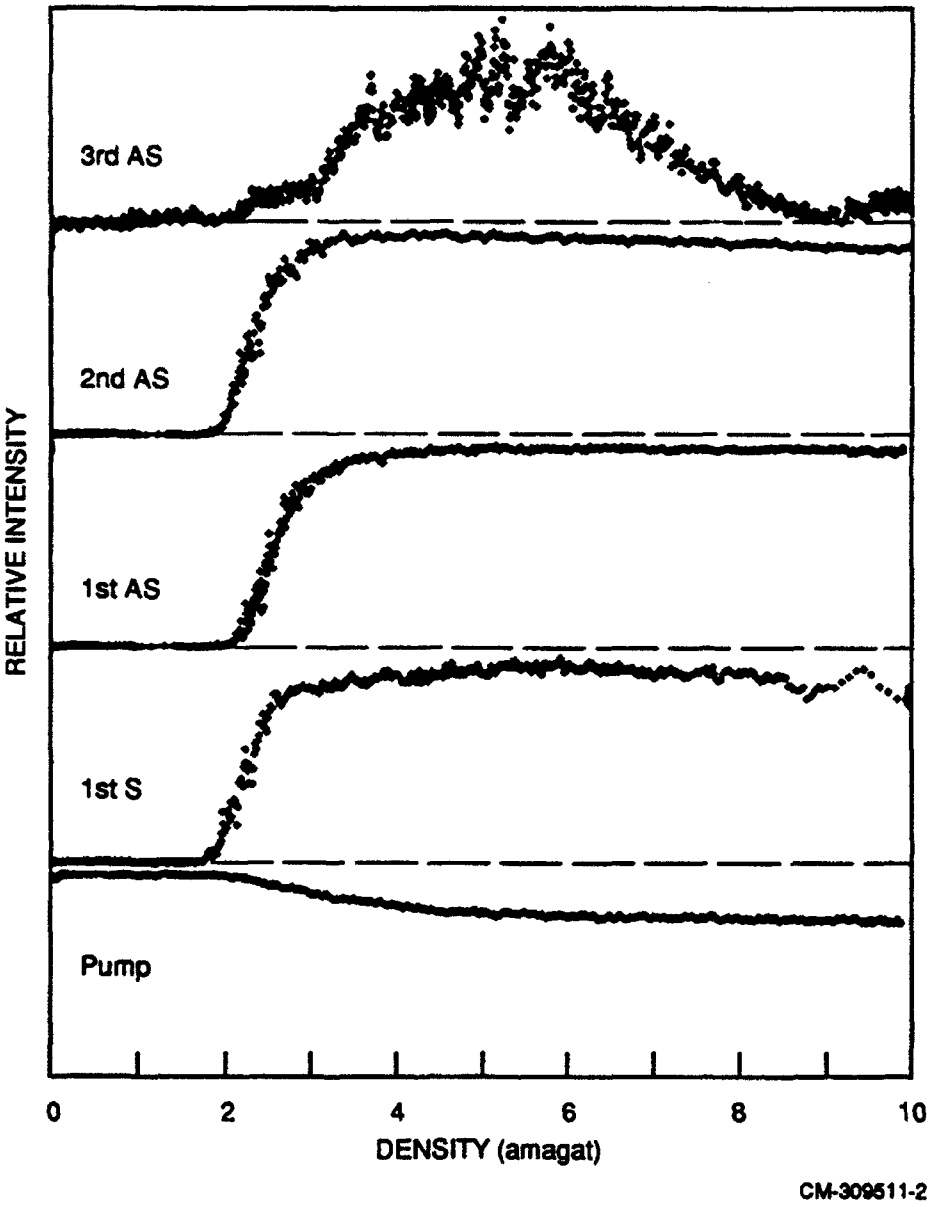
3rd AS
2nd AS
1st AS
1st S
Pump
RELATIVE INTENSITY
0
2
4
6
8
10
DENSITY (amagat)
CM-309511-2

Fig. 12

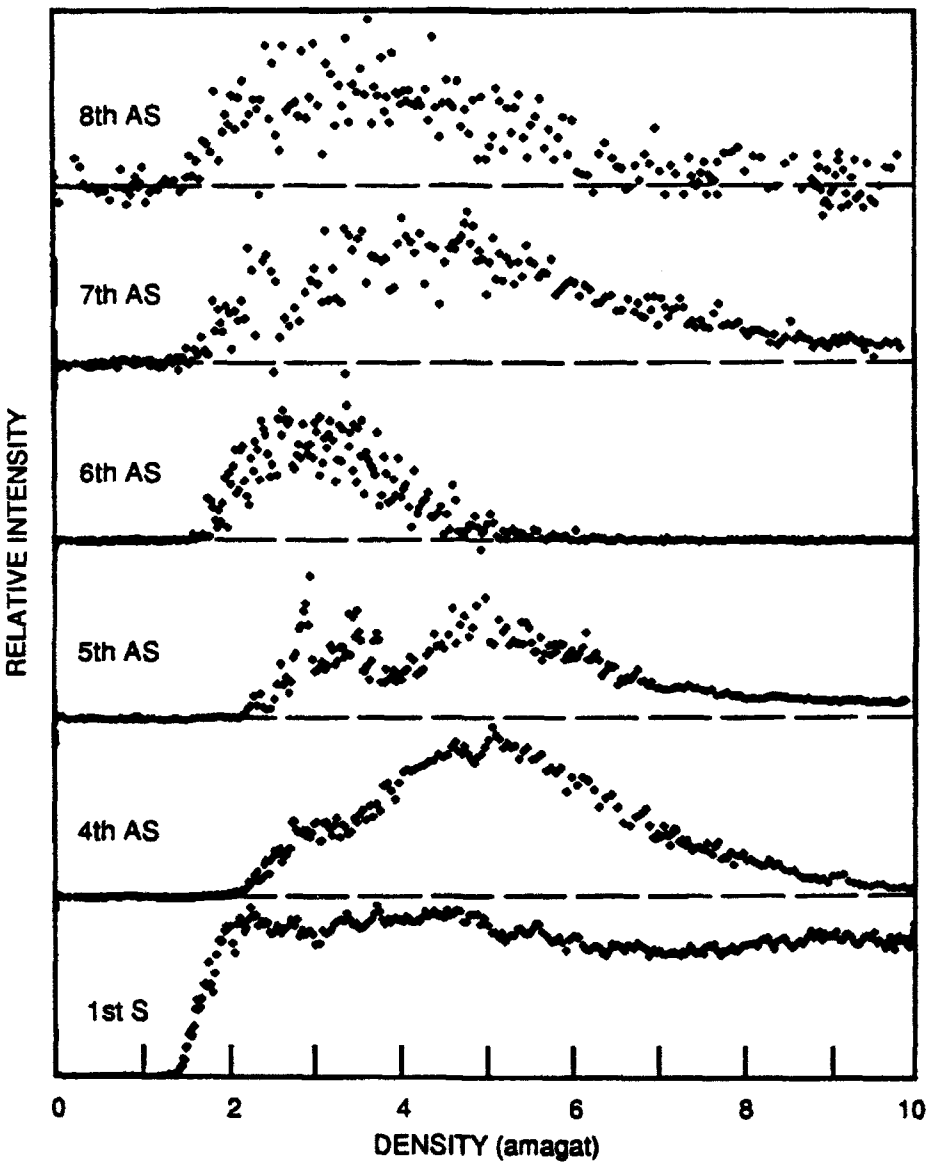
8th AS
7th AS
6th AS
5th AS
4th AS
1st S
RELATIVE INTENSITY
0
2
4
6
8
10
DENSITY (amagat)
CM-309511-1

Fig. 13

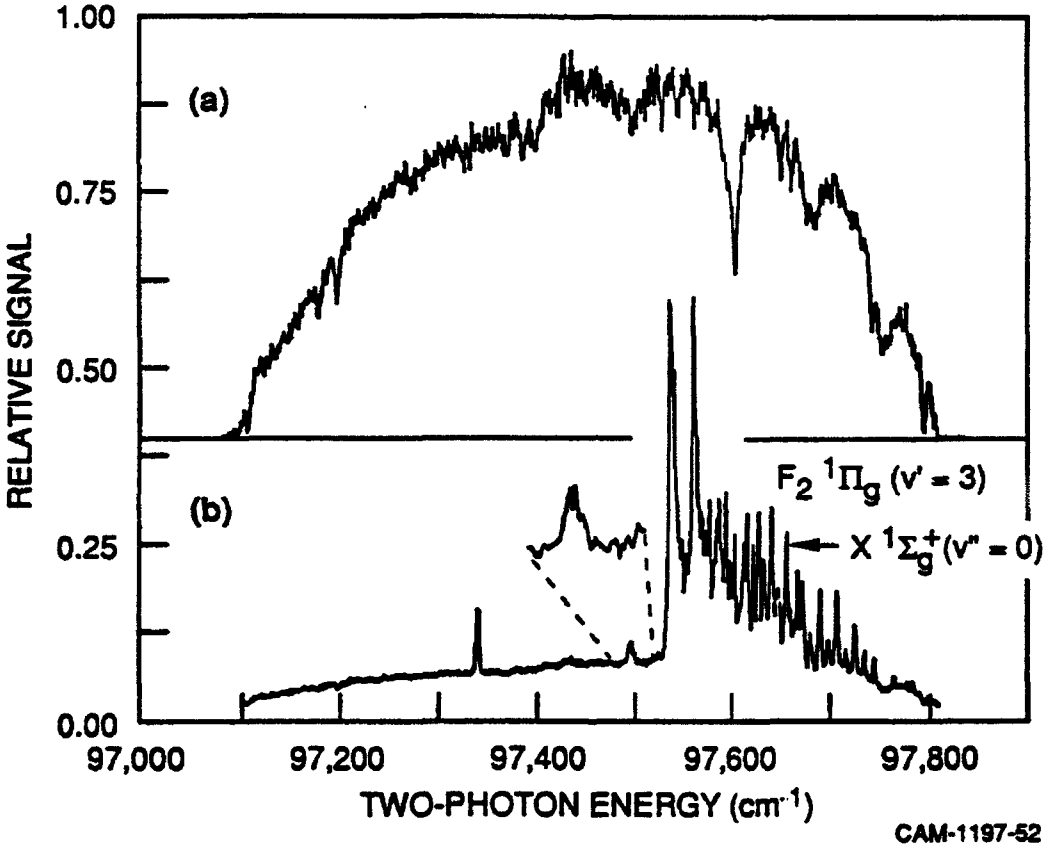
1.00
0.75
0.50
0.25
0.00
RELATIVE SIGNAL
(a)
(b)
F2 1Πg (v' = 3)
X 1Σg+(v" = 0)
97,000
97,200
97,400
97,600
97,800
TWO-PHOTON ENERGY (cm-1)
CAM-1197-52

Fig. 14

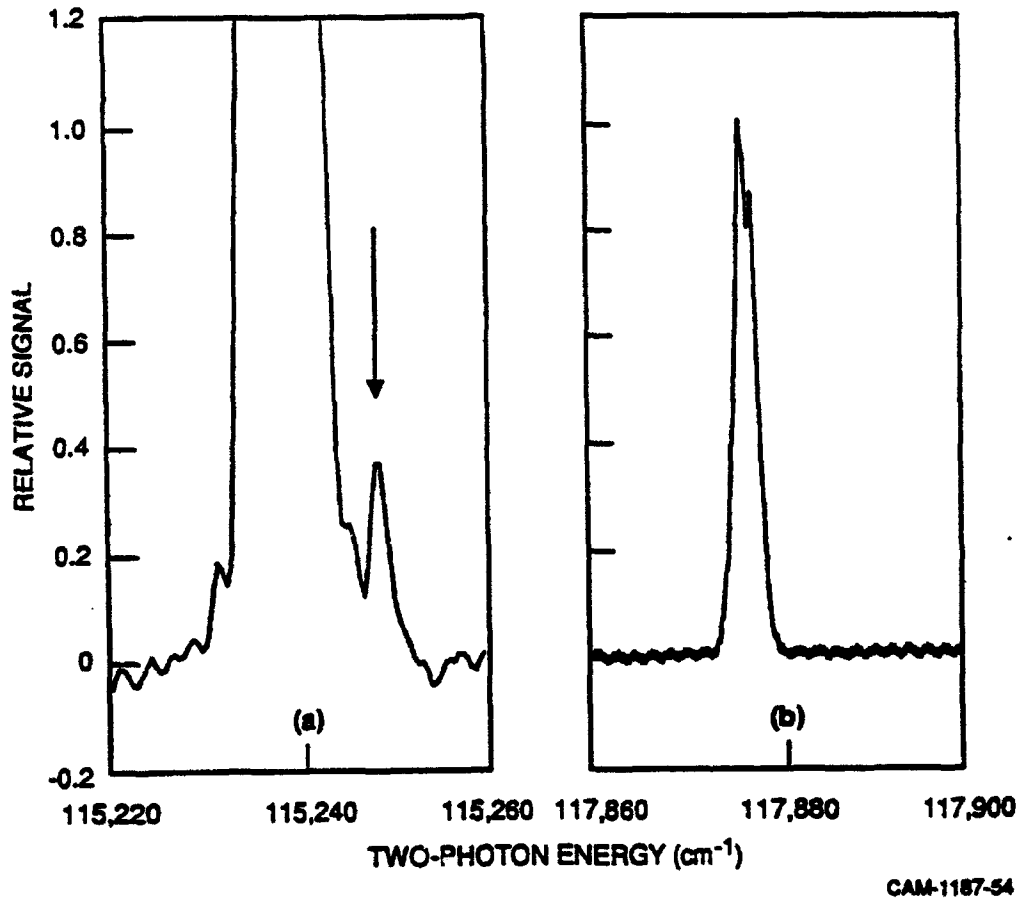
1.2
1.0
0.8
0.6
0.4
0.2
0
-0.2
RELATIVE SIGNAL
(a)
(b)
115,220
115,240
115,260
117,860
117,880
117,900
TWO-PHOTON ENERGY (cm-1)
CAM-1187-54

Fig. 15

Appendix F

COMPARING LASER-INDUCED FLUORESCENCE MEASUREMENTS AND COMPUTER MODELS OF LOW-PRESSURE FLAME CHEMISTRY

Comparing Laser-Induced Fluorescence Measurements and Computer Models of Low Pressure Flame Chemistry

Jay B. Jeffries, Gregory P. Smith, Dwayne E. Heard*), and David R. Crosley

Molecular Physics Laboratory, SRI International, Menlo Park, California 94025

Chemical Kinetics / Flames / Fluorescence

Laser-induced fluorescence measurements in low pressure flames, including hydrogen atom profiles, are examined as crucial tests of models of combustion chemistry. Both absolute and relative spatial profiles of reactive intermediate concentrations are useful for comparison. Careful temperature measurements for use as model input are emphasized. Radial OH LIF profiles in flames below 10 torr show an expanding flame which must be properly treated in model calculations. Diluted flames at pressures above 30 torr provide a preferred one-dimensional fluid flow.

Introduction

The complex chemistry of combustion processes, involving free radical intermediates present at trace concentrations, controls many processes of considerable interest; examples are the formation of pollutants (NO_x), ignition and inhibition phenomena, and the emission of visible and ultraviolet light. This chemistry is described by a large-scale computer model including fluid dynamic phenomena and independently determined elementary rate constants. Appropriate examples of such kinetics data are the high temperature shock tube kinetics measurements of key reactions involving H atoms, using atomic resonance absorption spectroscopy performed by Just and coworkers [1]. An understanding of this chemistry is essential to the development of a predictive model, useful outside the ranges of direct experimental tests. Validations of such a model are best made by comparison of its predictions with measurements of the reactive intermediates (such as H atoms) which control the chemistry, made under carefully controlled conditions.

A particularly useful test system is a low pressure, one-dimensional laminar flame. This system furnishes the spatial resolution necessary for careful and detailed comparison of the appearance of one species with another, tied to a spatially well-determined temperature profile. The method of laser-induced fluorescence (LIF), which provides sensitive, nonintrusive detection of radical species with high spatial resolution, is increasingly used for measurements. Correct accounting for the pressure dependence of the chemical reactions permits a model, tested at low pressure, to be used at higher pressure.

Over the past several years we have made measurements of radical species in several low-pressure flames, for the purpose of comparison with predictions from such a computer model. The flames have been burnt at pressures ranging from 5.6 to 150 Torr, providing an extremely high degree of spatial resolution, especially when below 10 Torr. Under these conditions we have found discrepancies with model

*) Present address: Chemistry Department, Macquane University, Sydney, Australia.

predictions which, we believe, would not be apparent in flame measurements at higher pressures. In this manuscript we summarize and discuss these findings, and present new measurements of the hydrogen profiles and the two-dimensionality of the flames, providing insights into the structure of these very low pressure flames.

Experimental and Computational Details

All measurements described were made in low-pressure flames supported on a 6 cm diameter porous plug McKenna burner inside an evacuable chamber suitable for laser probing. A 5 mm thick shroud of Ar surrounded the flame, with its linear flow velocity matched at the burner surface. Rapid flows were employed to lift the flame front 1 to 2 cm above the burner, providing spatial resolution in the cool gases below the flame front, where much interesting and important chemistry occurs. On the other hand, in these rapid flows at low pressure the cross-sectional area of the flame varies with height, as described below. The measurements were made using LIF; the laser beam was directed across the burner and the fluorescence collected at right angles, using a system comprising three lenses and a slit designed to limit the depth of field and hence the flame emission background [2]. Spatial profiles of concentrations and temperature were obtained as a function of height above the burner surface, by maintaining a fixed optical configuration while the burner was translated vertically. The radial profiles of OH were made by translating the burner horizontally perpendicular to the laser beam, in an arrangement providing optimal radial spatial resolution.

We have studied several species in four different flames at low pressure; operating parameters and spectroscopic details can be found in earlier papers and Tab. 1. Studies of H_2/O_2 and H_2/N_2O flames are described in Ref. [3]. Measurements have also been made in a 5.6 Torr CH_4/O_2 flame [4, 5] and a study of prompt NO formation in CH_4/air flames is given in Ref. [6]. Hydrogen atom profiles in these flames are reported in Ref. [7].

Table 1
Low pressure flame studies

Fuel	Oxidizer	Φ	P (Torr)	Flow (g/cm^2/s)	T_{max} (K)	LIF Species	Ref.
H_2	O_2	1.00	7.2	.00180	1220	OH,H	3,7
H_2	N_2O	1.00	7.2	.00240	2450	OH,NH	3
CH_4	O_2	1.03	5.6	.00088	1850	OH,CH,HCO, $^1CH_2$,H	4,5,7
CH_4	AIR	1.13	30.	.00190	1675	OH,CH,NO,H	6,7

The computer model of the flame chemistry is a mechanism containing rate constants of our choice based largely on recommendations by Warnatz [8] for hydrogen oxidation and Miller and Bowman [9] for the NO formation submechanism. It includes 38 species and 148 reactions. The thermodynamic input is taken from the Sandia database [10] with slight modifications of our own [11]. Model calculations are performed with the Sandia flame code [12], including thermal diffusion, bimolecular and unimolecular kinetics using our formulation of the pressure dependence of reaction rates [13], sensitivity analysis, and a provision for varying the flow cross-sectional area as a function of distance above the burner. Hydrogen atom recombination at the burner surface is also included. Gas flows at the burner surface are a necessary input. Temperature can be dealt with in two ways: an experimentally measured temperature profile imposed as input, or with the code configured to calculate the profile as a predicted variable. The former is highly preferable, as described in the next section. Further details of the hydrocarbon oxidation are found in Ref. [11], and those for prompt NO formation in Ref. [6].

Temperature Determinations

Accurate, spatially resolved temperature determinations are essential to meaningfully compare LIF measurements with predictions of chemical models. This owes to the highly nonlinear dependence of reaction rates on temperature together with the complex interplay of sequential and branching reactions. A systematic deviation of 100 K between true and apparent temperature at any given point in the flame can seriously compromise quantitative measurements/model comparison; an error of 200 K is likely to be fatal to this endeavor. In addition, spatial temperature profiles are needed to reduce LIF signals to concentrations, to account for the fraction of total molecules in the absorbing level: accuracy for this purpose is particularly important when measuring concentrations at the cooler temperatures found near the burner surface.

We have chosen to use a measured temperature profile as an imposed input to the flame model. Although the model can regard temperature as a predicted output, computed through local heat release and heat capacity with thermal transport, the accuracy demanded requires precise knowledge of heat loss mechanisms throughout the flame. Our test calculations of temperature in an H_2/O_2 flame with our flow rates and pressures show significant differences, several hundred Kelvin, from the measured profiles, which cannot be accurately accounted for a priori. We conclude that the use of a detailed model to understand the chemistry of low pressure, laminar flames demands measured, not calculated, temperature profiles.

LIF of the OH radical is excellent for determining the required accurate, spatially precise temperatures. In laminar flames signal averaging is possible with an LIF sensitivity sufficient for measurements even at low temperature where OH is present in only trace quantities. Temperature is measured by a rotational excitation scan, with data reduced to a temperature in two ways. Commonly, line intensities furnish rotational level populations $N_{J''}$ used in a plot of the Boltzmann distribution, $N_{J''} = g_{J''} \exp[-E_{J''}/kT]$ to determine T. We have adopted an alternative method [14], namely, direct spectral fitting with T as the parameter, which makes full use of all the data. Line positions and absorption coefficients are fixed input data to a spectral simulation program, and T is a parameter varied until the best match between simulation and experiment is obtained. Results from CH_4/air flames [6] show good agreement between the two methods, with typical random errors of 20–40 K.

To obtain accurate temperatures from LIF measurements in OH, one must be careful in both the data acquisition and analysis procedures. Several types of systematic errors are possible, whose presence cannot be detected by measures of the goodness of fit to either the spectrum simulations or Boltzmann plots. These vital points are discussed in detail in Refs. [14, 15]; we simply list here those problems which must be avoided. Several are accounted for by proper experimental design. These include polarization of LIF signals

and spectral bias in fluorescence detection, due to lack of rotational thermalization in the fluorescing state; both may be avoided by using a sufficiently wide, trapezoidally shaped detection bandpass. Operation in a low laser power, linear excitation regime is preferable to partial optical saturation of the transition. Optical depth considerations for both laser absorption and fluorescence must be accounted for even in low pressure flames, in regions where OH is present at concentrations >0.1%. Low pressure flames, where fluorescence decay times are ~100 ns. offer a special advantage for avoiding rotational-level-dependent quenching of excited OH by using a short electronic detection gate timed promptly after the laser pulse. The J' dependence of transition probabilities can be handled computationally. Temperature measurements using the predissociated $v' = 3$ level to avoid quenching complications must however still consider the J' dependence of the predissociation rate [16, 17].

With proper care, temperatures can be determined with the same spatial resolution as the radical concentrations, and with statistical errors of 2–3%. Even this is close to maximum tolerable uncertainty for comparison with flame models. One can calculate a temperature sensitivity [6] of predicted species concentrations, using the reaction sensitivity calculations that are part of the code output [12] together with the temperature dependence of each reaction [10]. As an example, the temperature sensitivity of predicted NO (about 4 ppm) produced via the prompt NO mechanism in a 30 Torr CH_4/air flame was computed. We find a 2% or 30 K error in temperature would produce a 20% error in predicted NO. Most of this is due to the sharp temperature dependence of the two reactions $CH + N_2 \rightarrow HCN + N$ and $H + CH_2 \rightarrow H_2 + CH$. Thus NO cannot be predicted (or controlled) to better than a factor of two unless the temperature distribution is known within 150 K.

Species Concentrations

Temperature and gas flows are the inputs to the model and species concentrations are the outputs for comparison with and interpretation of experimental profiles. The gradient of reactant concentration and the sequential appearance of reactive intermediates as a function of height above the burner surface test the chemical mechanism as shown in Fig. 1 for a 30 Torr CH_4/air flame. Absolute concentration measurements provide an even more stringent test of the model, beyond position and shape information.

For any flame containing hydrogen and oxygen, the OH radical is present at large concentrations from just below the flame front into the burnt gases and is readily measured using LIF. A comprehensive spectroscopic and collisional quantum yield data base is available for quantitative analysis of the LIF signals. Hydrogen atoms are also often present at relatively high concentrations, and are the key to

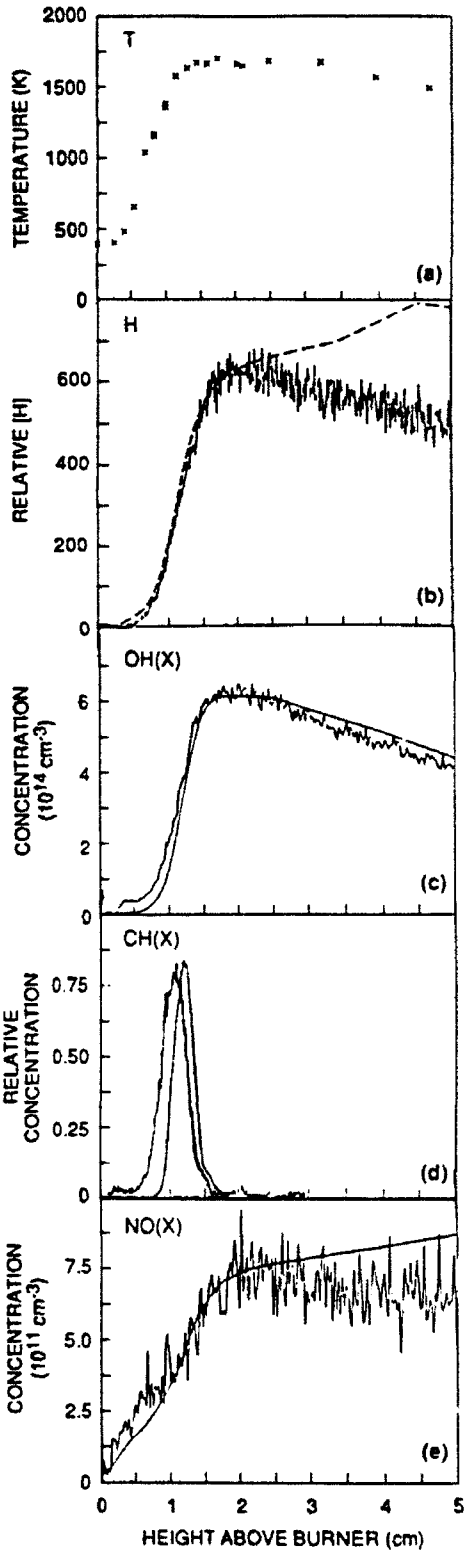

Fig. 1
Study of a 30 Torr, $\Phi = 1.13$, methane/air flame. a) Temperature measurements deduced from OH LIF and used for input for computational model. Model predictions for radical concentrations are given by smooth lines. b) Quenching corrected H atom relative concentration from two photon excitation of 3S and 3D and subsequent Balmer α LIF. c) OH concentration from LIF with an absolute scale from absorption in the burnt gases; the model OH prediction has been scaled by 0.67 to match the peak measured value. (This factor lies within experimental uncertainty). d) CH relative concentration measurement; scattered laser light is observed near the burner surface. e) NO LIF concentration measurement with absolute scale determined by calibration with known NO flow without a flame.

flame propagation. Hydrogen atoms are somewhat more difficult to measure than OH via LIF because multiphoton excitation is needed, but can easily be detected in laminar flames [18]. The H atom signal decays too rapidly to resolve in time with a short gate, and therefore quenching corrections, described below, must be applied.

No flame measurement/model comparison would be complete without a determination of at least one of these important species. The concentration of hydrogen atoms basically determines the flame speed, a key quantity for characterizing any flame. Further, diffusion of hydrogen atoms into the early pyrolysis zone of the flame forms much of the initiation chemistry in the precombustion gases near the burner surface. Both H and OH are intimately tied to the temperature profile, rising sharply through the flame front and declining slowly, as seen in Fig. 1.

However, despite the chemical importance of H and OH and the spatial regions of the flame defined by their distributions (together with temperature), their chemical information content is limited. For example, an understanding of hydrocarbon ignition also requires knowledge of species such as CH_3 and HCO, while CH is the key radical responsible for prompt NO formation. Therefore, besides OH or H, measurements of other intermediate species are vital to a real test of the reaction model. It is multiple species profiles that provide sensitive tests of flame chemistry mechanisms.

Relative concentration profiles of radical species are much easier to determine with LIF than absolute values, but nonetheless impart considerable information about chemistry. In CH_4/O_2 flames [4, 5], HCO appears before $^1CH_2$, which in turn precedes CH radicals. This ordering agrees with the flame model [11], although failure to predict early flame concentrations suggests inadequate knowledge of certain high temperature reaction rates involving these species.

Another important example is that of prompt NO formation in CH_4/air flames [6]. Experimental measurements and model predictions are shown, together with temperature, in Fig. 1. The relative NO profile is predicted well, and the absolute value of 3.7 ppm agrees excellently with the experimental result of 4.0 ppm. Were this the only measured variable, one might conclude that the pertinent chemistry is well understood. However, a close examination shows predicted CH rises and decays later in the flame than measured. The sensitivity analysis for NO shows CH production and loss kinetics are the key steps. Thus, if CH is not predicted correctly, the model cannot correctly predict NO, and the closeness of the agreement is fortuitous. The conclusion is that we understand prompt NO chemistry quite well in this flame, but at the 30% error level there still remain uncertainties, due largely to ignorance of high temperature reaction rates of CH. The CH profile discrepancy also suggests the desirability of obtaining an absolute concentration measurement to isolate this apparent kinetics problem. This trace radical will be much more difficult to calibrate than NO and OH. The predictability of prompt NO for different stoichiometries remains to be examined.

Relative values for differing conditions also provide very useful information. For example, the good agreement between the maximum relative CH concentrations at 30 and 70 Torr with those predicted by the model indicates that the pressure dependence of important reactions is properly accounted for [6].

Absolute concentrations of radical species are determined either by calibration or estimation from LIF signal sizes. The scale for NO in Fig. 1 is calibrated by LIF signals in quantitative gas flow through the burner chamber at room temperature with proper compensation for the differences in quenching and temperature between calibration and flame. At low pressure, this can be done by measurement of fluorescence decay times, as performed for NO [19]. Calibration may also be made using signal level in a spatial region where the species of interest is present at chemical equilibrium [18], provided temperature and other concentrations can be measured or calculated. Finally, if present at sufficiently high concentration, laser absorption can be used, as performed for OH in Fig. 1. Care must be taken to define the correct path length across the flame, particularly for flows which spread from the burner with increasing height. For molecules present at lower concentration, this option is not usually possible.

Semiquantitative radical concentration can be determined by estimation from absolute LIF signal level, and yet be of considerable utility to a picture of flame chemistry [20]. One needs to know obvious experimental parameters such as laser power, optical collection efficiency, and laser probe volume (often the most difficult to obtain). Spectroscopic information is usually available from independent sources, and collisional quenching may often be estimated if it has not been measured. An example is LIF detection of the NS radical in simulated coal flames. The concentration was estimated at a few ppm, within a factor of three [21], sufficient to demonstrate the chemical importance of this previously unobserved species in flames containing both fuel-bound sulfur and nitrogen.

Model and experiment can often play a highly interactive role in this regard. Semiquantitative detection of some species (e.g., $^1CH_2$) can suggest its significance in some process of flame chemistry; a subsequent model run can verify the degree of that importance and the important reaction rate paths. If warranted through model considerations, effort can be spent upon development of quantitative detection means. The model can even be used to indicate topics of study or measurements, e.g., those majority species responsible for quenching, or those key elementary reaction steps.

Hydrogen Atom Profiles

Hydrogen atoms play a key role in flame propagation and a worthy model must reproduce their concentration well in the flame front region. At low pressures, both chemical production/loss rates and diffusion are important.

We report here hydrogen atom LIF profile measurements obtained by two-photon excitation to the 3s and 3d states at 205 nm, observing the Balmer α transitions at 656 nm. The short radiative lifetime and rapid quenching necessitate correction for a collision-determined quantum yield. This is

chemistry, but comparison between measurement and model must be done with care. Temperature is best determined empirically and used as an input to the model; both relative spatial profiles and absolute concentrations constitute useful output. Flames at extremely low pressure, <10 Torr, offer excellent spatial resolution through the unburned gases and, with prompt electronic gating, avoid quenching corrections for many species. However, they suffer from radial flow and transport patterns which must be accounted for in the models; diluted flames at somewhat higher pressure, ~ 30 Torr, appear preferable. At low pressure, considerable diffusion of H atoms occurs back toward the burner surface into cool regions of the flame, and recombination at the burner surface must be included in the model.

We thank Katharina Kohse-Höinghaus and Richard Copeland for helping develop our early approach to very low pressure flames, and Kristen Steffens for help with the radial expansion experiments. We also wish to acknowledge the contributions of Professor Just to our understanding of the high temperature kinetics responsible for these low pressure flame radical and H-atom observations, and valuable discussions of both kinetics and flame diagnostics. This work was supported by the Gas Research Institute, the Air Force Office of Scientific Research and the Southern California Gas Company.

References

[1] P. Frank and Th. Just, Twentieth Symposium (International) on Combustion, p. 807. The Combustion Institute, Pittsburgh 1984.
[2] M. J. Dyer, L. D. Pfefferle, and D. R. Crosley, Appl. Opt. *29*, 111 (1990).
[3] K. Kohse-Höinghaus, J. B. Jeffries, R. A. Copeland, G. P. Smith, and D. R. Crosley, Twenty-Second Symposium (International) on Combustion, p. 1857. The Combustion Institute, Pittsburgh 1988.
[4] A. D. Sappey, D. R. Crosley, and R. A. Copeland, Appl. Phys. B *50*, 463 (1990).
[5] J. B. Jeffries, D. R. Crosley, I. J. Wysong, and G. P. Smith, Twenty-Third Symposium (International) on Combustion, p. 1847, The Combustion Institute, Pittsburgh 1990.
[6] D. E. Heard, J. B. Jeffries, G. P. Smith, and D. R. Crosley, Combust. Flame *88*, 137 (1992).
[7] D. E. Heard and J. B. Jeffries, Paper 91–21, Western States Meeting of the Combustion Institute, Boulder, CO, March 1991.
[8] J. Warnatz, in Combustion Chemistry, p. 197, W. C. Gardiner, Springer-Verlag 1984.
[9] J. A. Miller and C. T. Bowman, Prog. Energy Combust Sci. *15*, 287 (1989).
[10] R. A. Kee, J. A. Miller, and T. A. Jefferson, Sandia National Laboratory Report SAND80–8003 (1980).
[11] G. P. Smith, Comb. Flame, to be published (1992).
[12] R. J. Kee, J. F. Grcar, M. D. Smooke, and J. A. Miller, Sandia National Laboratory Report SAND85–8240 (1985).
[13] P. H. Stewart, T. Rothem, and D. M. Golden, Twenty-Second Symposium (International) on Combustion, p. 943, The Combustion Institute, Pittsburgh 1989.
[14] K. J. Rensberger, J. B. Jeffries, R. A. Copeland, K. Kohse-Höinghaus, M. L. Wise, and D. R. Crosley, Appl. Opt. *28*, 3556 (1989).
[15] D. R. Crosley and J. B. Jeffries, 7th International Symposium on Temperature, Toronto, Ontario, in press 1992.
[16] J. A. Gray and R. L. Farrow, J. Chem. Phys. *95*, 7054 (1991).
[17] D. E. Heard, D. R. Crosley, J. B. Jeffries, G. P. Smith, and A. Hirano, J. Chem. Phys. *96*, 4366 (1992).
[18] J. E. M. Goldsmith, Twenty-Second Symposium (International) on Combustion, p. 1403, The Combustion Institute, Pittsburgh 1989.
[19] D. E. Heard, J. B. Jeffries, and D. R. Crosley, Chem. Phys. Lett. *178*, 533 (1991).
[20] D. R. Crosley, Combust. Flame *78*, 153 (1989).
[21] J. B. Jeffries and D. R. Crosley, Combust. Flame *64*, 55 (1986).
[22] J. Bittner, K. Kohse-Höinghaus, U. E. Meier, and Th. Just, Chem. Phys. Lett. *126*, 567 (1986).
[23] U. E. Meier, K. Kohse-Höinghaus, and Th. Just, Chem. Phys. Lett. *126*, 567 (1986).
[24] M. F. Zabielski, L. G. Dodge, M. B. Colket, and D. J. Seery, Eighteenth Symposium (International) on Combustion, p. 1591, The Combustion Institute, Pittsburgh 1981.
[25] K. H. Eberius, K. Hoyermann, and H. Wagner, Tirteenth Symposium (International) on Combustion, p. 713, The Combustion Institute, Pittsburgh 1971.
[26] J. T. Salmon and N. M. Laurendeau, Appl. Opt. *25*, 2881 (1987).

(Received: June 11th, 1992) E 8021

Appendix G

AMPLIFIED SPONTANEOUS EMISSION MEASUREMENTS OF ATOMIC OXYGEN

AIAA 93-0047

Amplified Spontaneous Emission Measurements of Atomic Oxygen

J. B. Jeffries and M. S. Brown
SRI International
Menlo Park, CA

31st Aerospace Sciences Meeting & Exhibit
January 11-14, 1993 / Reno, NV

AMPLIFIED SPONTANEOUS EMISSION MEASUREMENTS OF ATOMIC OXYGEN

Jay B. Jeffries and Michael S. Brown
Molecular Physics Laboratory
SRI International
Menlo Park, CA 94025

Abstract

The laser-induced amplified spontaneous emission (ASE) of atomic oxygen in premixed low pressure H_2 / O_2 and CH_4 / O_2 flames has been measured. Experiments designed to determine the suitability of ASE as a thermometric probe of combustion environments have been performed. We have measured the bandwidth of the ASE signal using an etalon with the pump laser fixed at line center. These measurements are compared with model calculations of the ASE bandwidth. The ASE signal has also been recorded while scanning the pump laser for several pump laser intensities. Calculations of the ASE bandwidth reveal the sensitivity of this quantity to the excited state population and the bandwidth of the pump laser.

Introduction

Two-photon laser-induced fluorescence is often used as a means of detecting light atoms in combustion environments.[1] This technique involves exciting some of the ground state population into an excited state of the same overall parity as the ground state through two-photon absorption. Some of this excited state population relaxes to intermediate states via one photon fluorescence which is then detected. Under the proper conditions, a second physical process, amplified spontaneous emission (ASE), has been observed simultaneously with this fluorescence.[2] For light atoms, the intermediate states have a significant amount of energy relative to the ground state and therefore have no appreciable thermal population even in the elevated temperatures found in combustion environments. If the excitation rate is sufficient to move a significant population through the two-photon absorption, the lack of any thermal population in the intermediate states produces a population inversion between the excited and intermediate states. Spontaneous emission can then experience optical gain through stimulated emission. For sufficient gain, an amplified spontaneous emission signal is generated which propagates both forward and backward along the pump laser beam. The physical process of ASE is well known from studies of laser systems.[3] More recently, ASE has prompted interest as an optical diagnostic of combustion environments.[2] Atomic hydrogen,[4] oxygen,[5] carbon,[6] nitrogen[7] and chlorine[8] as well as carbon monoxide[2] have all have been detected using their ASE signal. The ASE signal is attractive as an optical diagnostic for several reasons: the spatial coherence of the emitted ASE beam implies large f# detection which yields large signal to noise ratios, only one optical access port is required, and the ASE signal can be quite large due to its nonlinear origin.

To date, the ASE studies that have been conducted have concentrated on obtaining a relative ASE signal as a function of pump laser energy, height above a burner surface or pressure of the test gas.[2,4,5,6,7,8] We are currently engaged in an experimental program designed to investigate the degree to which one can obtain quantitative information from the ASE signal. In particular we are studying the use of ASE as a thermometric probe of combustion environments. Since the two-photon pump laser interacts with a Doppler broadened transition, one anticipates that the bandwidth of the emitted ASE should include information about the temperature of the local environment. In an effort to test this idea we have recently made both measurements and calculations of the bandwidth of ASE emitted by oxygen atoms in low pressure flames as a function of temperature.

ASE Measurements

The experiments have been conducted in a low pressure chamber fitted with a flat flame McKenna burner (see Figure 1). The pump laser beam is generated by frequency doubling the output of a YAG pumped dye laser. Dielectric

mirrors were used to separate the 6 ns, doubled beam from the fundamental. The pump beam was focused into the low pressure chamber with either a 150 mm or a 500 mm focal length lens. The backward moving (counterpropagating with respect to the pump beam) ASE beam was detected using a filtered photomultiplier tube. The forward ASE beam was filtered, expanded with a negative lens and passed through an etalon. The etalon fringes were captured with an intensified CCD camera. Images of the etalon fringes were used to measure the bandwidth of the ASE while the pump laser was held fixed to line center. Excitation scans were also made by scanning the dye laser through the two-photon resonance and recording the ASE signal detected by the photomultiplier tube. Data was collected for several pump laser pulse energies ranging from 100 μJ to 800 μJ in stochiometric H_2 / O_2 and CH_4 / O_2 flames. All of the data was collected at 7 torr and at a height of 4 cm above the burner surface. Under these conditions the local environment is known to be at 1200 K for the H_2 / O_2 flame[9] and 1800 K for the CH_4 / O_2 flame.[10]

All of the measurements were made by exciting the $3p\ ^3P \leftarrow 2p\ ^3P$ two-photon transition in atomic oxygen using a pump laser tuned to 226 nm (see Figure 2). The ASE signal is generated at 845 nm following the $3s\ ^3S^\circ \leftarrow 3p\ ^3P$ one-photon transition. This system provides a good test case for quantitative ASE measurements. The two-photon absorption and photoionization cross sections[11] of oxygen atoms have been measured along with the quenching[12] and intermultiplet transfer[13] cross sections relevant to the flame environments. The fine structure spacing of the ground state is sufficiently large to ensure transitions only out of the J=2 component.

In order to extract a useful experimental temperature from the ASE bandwidth measurements, it is necessary to know some details about the two-photon pumping and the subsequent ASE emission. The ASE process is intrinsically nonlinear and attention must be paid to pump saturation, gain narrowing of the ASE signal and any ac Stark shifting or broadening that may arise. To this end we have conducted a series of experiments under different conditions

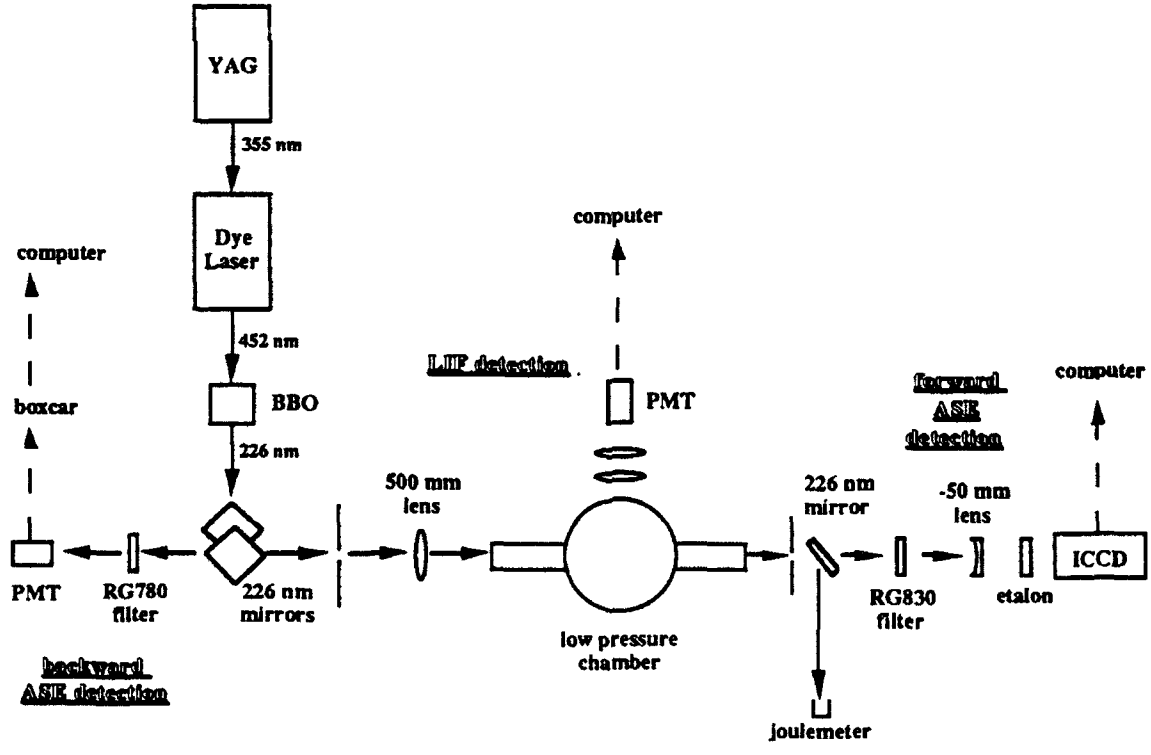

Fig. 1. Schematic of experimental arrangement for the ASE excitation and detection.

and compared the results with theoretical calculations.

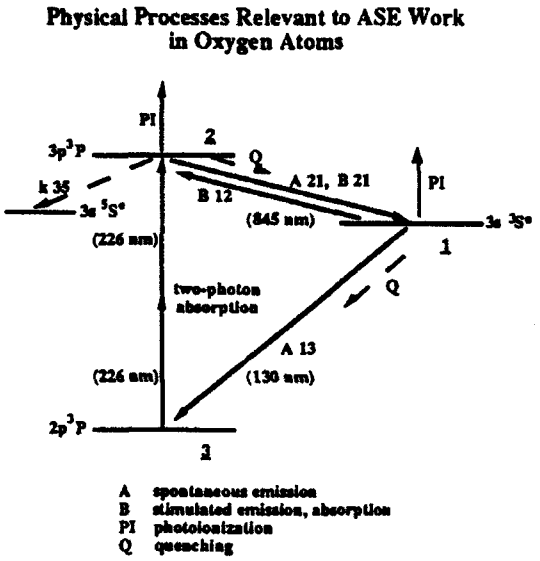

Fig. 2. Energy level diagram for the oxygen atom. Two-photon absorption at 226 nm produces the population inversion which results in ASE at 845 nm.

To better understand the pumping process we recorded a number of excitation scans. Six such scans are shown in Figures 3 and 4 as a function of pump laser intensity. These spectra were recorded in a H_2 / O_2 flame using two different focal length lenses for a range of pump laser energies. Spectra taken with a short focal length lens (150 mm) appear in Figure 3 as double peaked features. The left feature corresponds to the $3p\ ^3P_2 \leftarrow 2p\ ^3P_2$ transition while the right feature corresponds to the $3p\ ^3P_1 \leftarrow 2p\ ^3P_2$ transition. These two transitions are separated by 0.0014 nm which at 1200 K amounts to one quarter of the two-photon Doppler width. A calculation of the relative cross section of these two lines[11] indicates that they should have a relative signal strength of 3.6 : 1 with the J = 2 ← 2 transition appearing as the stronger of the two. However, in the two upper curves of Figure 3, the transitions are present with very similar strengths suggesting saturation of the J = 2 ← 2 transition. An estimate of the saturation intensity can be made using the following expression,[14]

$$W^{(2)}\,\tau = \frac{1}{2} \quad .$$

Here, τ indicates the pulsewidth of the laser and $W^{(2)}$ denotes the two-photon transition rate at saturation which is given by,[15]

$$W^{(2)} = \frac{\alpha\, I_{sat}^2}{h\,\nu} \quad .$$

The two-photon absorption cross section, Planck's constant and the frequency are denoted by α, h and ν, respectively. From the above, we estimate a saturation intensity for the J = 2 ← 2 transition of I_{sat} = 432 MW/cm^2. The upper two curves in Figure 3 were recorded with pump intensities of ~2.9 I_{sat} and ~1.0 I_{sat}, respectively.

Using a longer focal length lens (500 mm), we recorded the excitation scans which appear in Figure 4. For each of these scans the pump laser intensity is well below saturation and the spectra have a different overall appearance. The J = 1 ← 2 transition now appears relatively weak compared with the J = 2 ← 2 transition. When making quantitative bandwidth measurements it is prudent to operate in the low pump intensity limit in order to simplify the data analysis.

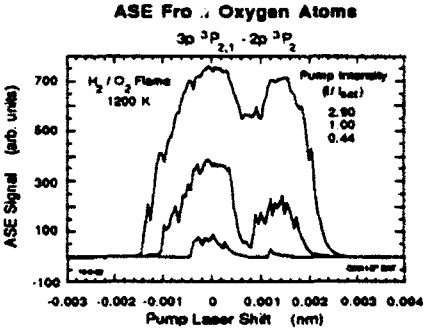

Fig. 3. ASE excitation scans taken using a 150 mm focal length lens. Saturation of the J = 2 ← 2 transition makes the J = 1 ← 2 transition appear relatively strong.

Figure 5 displays etalon fringes of ASE emission from oxygen atoms in a H_2 / O_2 flame at 1200 K. The central spot of the diffraction pattern lies just to the left of the first fringe. These fringes were recorded by summing the emission following ten pump laser shots at an intensity of 0.31 I_{sat}. The apparent noise in the fringes is due to the ASE light which passes through the etalon without any reflections. Accounting for the intrinsic bandwidth of the

etalon at the emission wavelength of 845 nm, analysis of the fringes yields an ASE bandwidth of 0.08 ± 0.04 cm^{-1}. Similar fringes were recorded in a CH_4 / O_2 flame at 1800 K using a pump intensity of 0.43 I_{sat}. The corresponding bandwidth amounts to 0.15 ± 0.04 cm^{-1}. These experimental values are plotted in Figures 6 and 7.

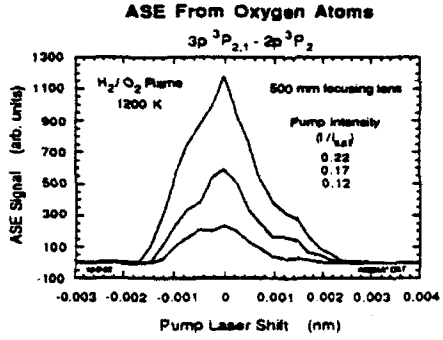

Fig. 4. ASE excitation scans taken using a 500 mm focal length lens. The $J = 2 \leftarrow 2$ transition is not saturated making the $J = 1 \leftarrow 2$ appear relatively weak.

ASE Bandwidth Calculations

In order to interpret the bandwidth measurements discussed above, we have performed calculations of the ASE signal. Previous theoretical treatment of the frequency distribution of the ASE signal did not include the finite bandwidth of the exciting pump laser which can not be neglected in the present study.[16] The calculation should be considered as a two step process in which we first determine the frequency dependent population of the excited state after two-photon absorption and then the frequency dependent gain experienced by the ASE beam as it propagates through the excited medium.

In the first step, the frequency response of the oxygen atoms is represented by the appropriate Voigt profile while the laser is represented by a Gaussian. The laser is assumed to be fixed at exact resonance and the apparent bandwidth of the pump laser during the two-photon absorption,[17] at 226 nm is taken into account. The relative population of the excited state as a function of frequency is found from the product of the Voigt profile and the laser intensity frequency distribution. Each frequency of the excited state population corresponds to an atomic velocity which is easily determined. Then each of these velocities can be converted into an ASE frequency distributed about 845 nm. In this way, the initial excited state population is

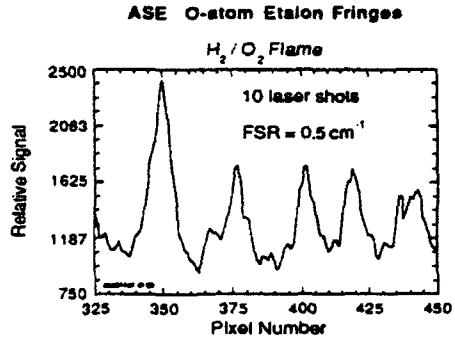

Fig. 5. Etalon fringes of the ASE at 1200 K.

found as a function of frequency and then remapped as a modified function of frequency which then experiences the gain associated with the ASE process.

In the second step, standard laser amplifier theory is used to calculate the gain coefficient for an inhomogeneously broadened system using the excited state frequency distribution found above.[18] This gain coefficient is then used in the expression for the ASE signal intensity.[18] One of the input quantities required to calculate the

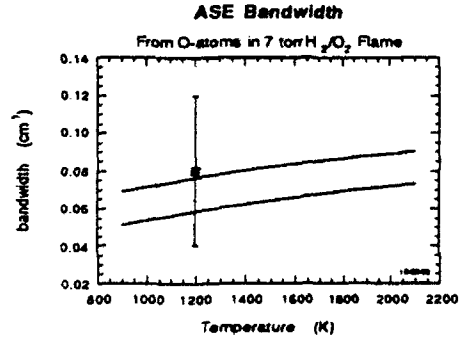

Fig. 6. Comparison of the ASE bandwidth measurement and the calculated values for a H_2 / O_2 flame.

gain coefficient is the total population inversion of the two energy levels which produce the ASE light. We estimated this population inversion by numerically integrating a system of rate equations modeling the three relevant energy

levels of the oxygen atom. As noted earlier, the cross sections for two-photon absorption, ionization, quenching and intermultiplet transfer are known for the oxygen system thus making the rate equation analysis tractable.

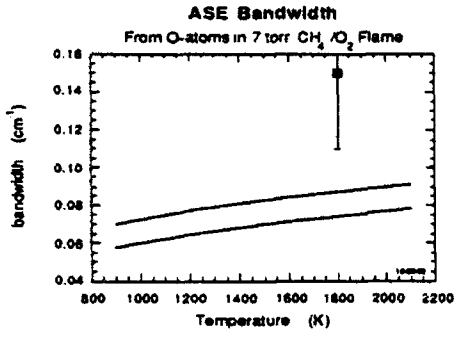

Fig. 7. Comparison of the ASE bandwidth measurement and the calculated values for a CH_4 / O_2 flame.

The results of our ASE bandwidth calculation are shown in Figure 6 for the H_2 / O_2 flame and in Figure 7 for the CH_4 / O_2 flame. The calculations were made using our measured pump laser bandwidth of 0.25 cm^{-1}. The two solid lines in Figure 6 indicate numerical results appropriate for the ground state oxygen atom concentration (2.48×10^{15} cm^{-3}) found in the H_2 / O_2 flame[19] at 1200 K. At this temperature, the two-photon Doppler width amounts to 0.55 cm^{-1} for the 226 nm pump laser. The two lines differ only in the input value of the population difference between the excited and intermediate states. The lower line corresponds to the calculated population inversion of 1.2×10^{11} cm^{-3}, while the upper line corresponds to a population inversion which is a factor of 10 smaller. The lower line represents the ideal case suggested by the rate equations while the upper line is probably closer to the truth given that several factors (including fluctuations in the pump laser intensity and inhomogeneities in the flame environment) reduce the overall population inversion obtained. The two lines appearing in Figure 7 represent similar calculations done for the oxygen atom concentration (4.96×10^{14} cm^{-3}) found in a CH_4 / O_2 flame[19] at 1800 K. The Doppler width, at 1800 K, amounts to 0.67 cm^{-1}.

As seen in Figure 6, there is good agreement between the measured and calculated ASE bandwidths for the H_2 / O_2 flame environment. However, as seen in Figure 7 there is poor agreement for the CH_4 / O_2 flame environment. At present, we do not know the reason for the disagreement. We have calculated the ac Stark broadening associated with the two-photon pumping process and find it to be insignificant at the experimental conditions. Calculations also indicate that power broadening is not significant.

The calculations do show, as expected, a dependence on the pump laser bandwidth. In Figure 8 we show the calculated results for the ASE bandwidth as a function of the dye laser bandwidth. (The bandwidth of the doubled pump beam is simply given by the product of the dye laser bandwidth and a factor of $2^{1/2}$.) This calculation was made for the conditions of the 7 torr H_2 / O_2 flame. Notice that for a dye laser bandwidth greater than the two-photon Doppler width the ASE bandwidth becomes independent of this quantity.

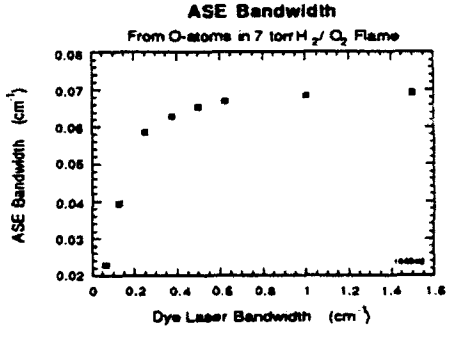

Fig. 8. The dependence of the calculated ASE bandwidth on the bandwidth of the dye laser generating the pump beam.

Conclusions

We have measured the bandwidth of oxygen atom ASE at two temperatures in low pressure flame environments. Comparison of the measurements with calculations based on a relatively simple model agree in the case of the lower temperature H_2 / O_2 flame. However, there is roughly a factor of two disagreement between the measured and calculated bandwidth for the CH_4 / O_2 flame. This dicrepancy is not understood at present. Our ongoing research is designed to resolve the difference in an effort to evaluate ASE signals as viable thermometric probes for reacting flows.

Acknowledgment

This work is supported by contract F-49620-90-C-0044 with the United States Air Force Office of Scientific Research.

References

1. A. C. Eckbreth, "Laser Diagnostics for Combustion Temperature and Species," (Abacus Press, Cambridge, MA 1988).
2. U. Westblom, S. Agrup, M. Alden, H. M. Hertz and J. E. M. Goldsmith, Appl. Phys. B, **50**, 487 (1990).
3. see for example, A. E. Siegman, "Lasers," (University Science Books, Mill Valley, CA 1986).
4. J. E. M. Goldsmith, J. Opt. Soc. Am. B, **6**, 1979 (1989).
5. M. Alden, U. Westblom and J. E. M. Goldsmith, Opt. Lett., **14**, 305 (1989).
6. M. Alden, P. E. Bengtsson and U. Westblom, Opt. Comm., **71**, 263 (1989).
7. S. Agrup, U. Westblom and M. Alden, Chem. Phys. Lett. **170**, 406 (1990).
8. A. D. Sappey and J. B. Jeffries, Appl. Phys. Lett., **55**, 1182 (1989).
9. K. Kohse-Hoinghaus, J. B. Jeffries, R. A. Copeland, G. P. Smith and D. R. Crosley, in "Twenty-Second (International) Symposium on Combustion," (The Combustion Institute, Pittsburgh, PA 1989) p. 1857.
10. K. J. Rensberger, M. J. Dyer and R. A. Copeland, Appl. Optics, **27**, 3679 (1988).
11. D. J. Bamford, L. E. Jusinski and W. K. Bischel, Phys. Rev. A, **34**, 185 (1986).
12. J. Bittner, K. Kohse-Hoinghaus, U. Meier and T. Just, Chem. Phys. Lett., **143**, 571 (1988).
13. P. J. Dagdigian, B. E. Forch and A. W. Miziolek, Chem. Phys. Lett., **148**, 299 (1988).
14. D. C. Hanna, M. A. Yuratich and D. Cotter, "Nonlinear Optics of Free Atoms and Molecules," (Springer-Verlag, Berlin 1979).
15. W. K. Bischel, B. E. Perry and D. R. Crosley, Appl. Optics, **21**, 1419 (1982).
16. L. Allen and G. I. Peters, J. Phys. A, **5**, 695 (1972).
17. B. R. Marx, J. Simons and L. Allen, J. Phys. B, **11**, L273 (1978).
18. J. T. Verdeyen, "Laser Electronics," (Prentice-Hall, Inc., Englewood Cliffs, NJ 1981).
19. G. P. Smith, in preparation.